Doctoral Dissertation

Study on All-Optical Flip-Flop using Bistable Laser Diodes with Nonlinear Couplers

(非線形カプラを有する双安定半導体レーザを用いた
全光フリップ・フロップに関する研究)

---

by

Mitsuru Takenaka

Department of Electronic Engineering
The University of Tokyo

December 2002

Dissertation Supervisor
Prof. Yoshiaki Nakano

Table of Contents

Table of
Contents

Chapter 1 Introduction

A short overview on the latest developments of bistable laser diodes (BLDs) is given. For future packet-based optical telecommunications, some optical memories will be required in all-optical routers. One of the enabling technologies for optical memory devices will be all-optical flip-flops. The BLDs have bee most promising devices to realize the all-optical flip-flops. However, there are some problems for several types of the BLDs to realize the practical all-optical flip-flops. To overcome theses problems, we propose the basic concept of a combination of the BLDs and nonlinear couplers such as directional couplers (DC), Multi-mode interferometer (MMI) couplers, and Mach-Zehnder interferometers (MZI) couplers.

1.1 Background of This Research

All-optical techniques for processing lightwave-communication signals have advanced considerably in recent years. Indeed, intensive research has produced practical all-optical devices for tasks such as routing, switching, demultiplexing, and data wavelength conversion. The output from theses devices, however, requires the continuous presence of an input signal, i.e. the output power does not latch, as shown in Fig.1.1(a). The latching capability of an optical flip-flop would allow the output to be maintained for processing at a later time; a digital, sequential means of processing would therefor be available for applications such as bit-length conversion, data-format change, demultiplixing, packet-header buffering, and retiming, as depicted in Fig.1.1(b). The flip-flop can therefore be triggered directly by signals from other all-optical gates, allowing the creation of highly functional photonic circuits without electronic-conversion components. Since most opportunities for all-optical processing exist at data rates beyond those inexpensively accessible by electronic processing, the flip-flop should operate faster than 10 Gb/s. Furthermore, for practical use in optical communication systems, the device should operate at low power levels (< 1mW) over a flexible wavelength range, and be transparent to the control-signals' polarizations.

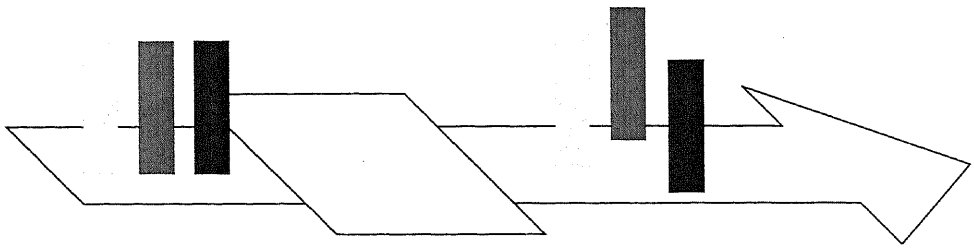

(a) without optical flip-flop

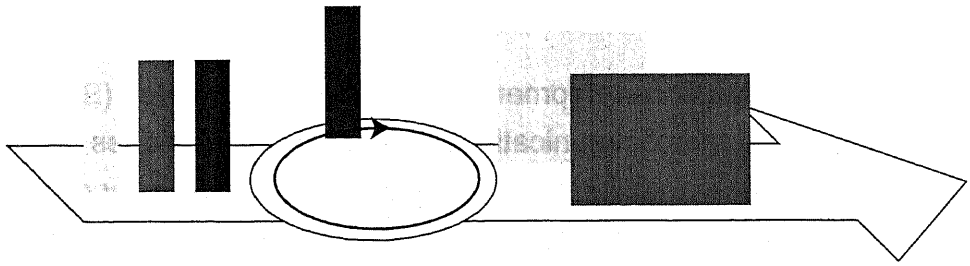

(b) with optical flip-flop

Optical functions of optical flip-flop

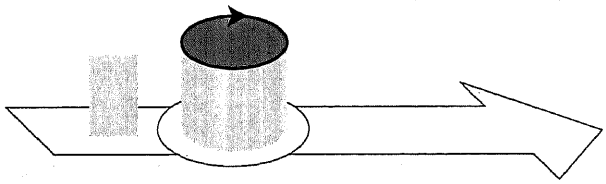

Memory

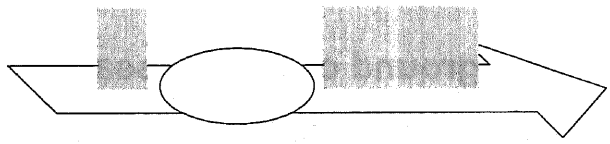

Bit-length converter

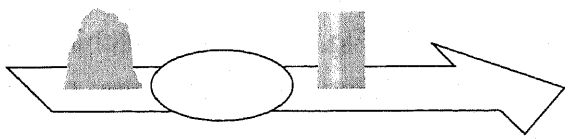

Regenerator

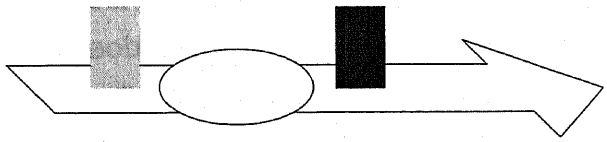

Wavelength converter

Fig.1.1 Concepts of all-optical system, (a) without optical flip-flop, (b) with optical flip-flop.

Bistable laser diodes (BLDs), for the long time, have been expected to be important elements to realize an all-optical flip-flop. BLDs have the advantage such as optical gain, low optical switching power, a high on-off ratio and large fanout. Another advantage of BLDs is that they do not need any holding optical power. There are three types of BLDs, i.e. absorptive BLDs, dispersive BLDs, and two-mode BLDs. The concise explanations about these BLDs are described as follows.

A. Absorptive BLD

LDs which have saturable absorbers in their cavity show bistability in the optical output against current curve and the optical output against optical input curve. The first bistable semiconductor laser diode with a saturable absorber was proposed by Lasher in 1964 [1]. This was demonstrated experimentally with a Fabry-Perot (FP) laser cavity [2] and a distributed feedback (DFB) laser cavity [3]. For high-speed switching, a reverse voltage is applied to the saturable absorber [4]-[7]. The repetition rate of over 5 GHz was demonstrated using voltage-controlled bistable laser diodes [7]. Digital signal regenerators and optical demultiplexers are experimentally demonstrated using the side-injection-light-controlled bistable laser diodes (SILC-BLD) [8]-[11].

B. Dispersive BLD

A resonant type LD amplifier, consisting of a normal LD biased below the laser oscillation threshold, can act as a nonlinear cavity and shows bistability in the optical input-output characteristics. This is because the active layer refractive index changes due to gain saturation by light injection. It was first discussed and demonstrated by Otsuka et al. with a FP cavity type LD amplifier [12][13]. Values of around 30 μW for switching in GaAs laser amplifiers [14], and as low as 1 μW for InGaAsP devices at 1.3 μm [15] and 1.55 μm [16], have been reported. Sharfin and Dagenais have also demonstrated the very low switching power operation of an optical switch requiring less than 1 fJ at 1.3 μm [17]. Recovery times are predicted to be the order of carrier lifetimes, i.e. a few nanoseconds at room temperature [18]. It is predicted that incorporating MQWs into the active region of the amplifier might reduce the optical and electrical power requirements, and enhance the high-frequency performance [19]. Bistability has been observed in InGaAs strained QW [20] and InGaAs/InGaAsP MQW [21] amplifiers. However, the performances are not as great as theory predicts at this moment. Bistability is also observed in a DFB LD amplifier. This was first demonstrated by Kawaguchi et al. in a 1.5 μm DFB LD [22]. Nakatsuhara et al. [23] have demonstrated all-optical set-reset operation using a nonlinear DFB waveguide, although it was not the LD structure. An optical bistability has been realized by an optical feedback structure and the optical Kerr effect. Recently, M. T. Hill et al. [24] have demonstrated an optical flip-flop based on two-coupled Mach-Zehnder interferometers that can potentially reach very high speeds.

C. Two-mode BLD

Two-mode BLD such as Polarization BLDs have recently received considerable attention because of their potential for high-speed switching. In the first report of polarization

bistability [25], an InGaAsP/InP laser was cooled down to the polarization transition temperature, which resulted in an enhancement in the TM mode gain. Tang et al. [26] predicted theoretically that LDs with two-mode bistabilities in polarization or in wavelength can be switched between the bistable states through optical input. Tang et al. demonstrated wavelength bistability experimentally. Two-section LDs will also play important roles in polarization BLD with an intracavity MQW saturable absorber [27]. This idea has been confirmed using an LD with a two-armed polarization-sensitive external cavity [28]. Kawaguchi et al. [29] have predicted theoretically that there are two kinds of polarization bistability, i.e. conventional S-shaped bistability and pitchfork bifurcation-like bistability. From the simulation of rate equations, it is predicted that the pitchfork bifurcation bistability has a major speed advantage over the conventional S-shaped bistability. This pitchfork bifurcation bistability was demonstrated by LDs with external cavities [30] and vertical-cavity surface-emitting lasers (VCSELs) [31][32]. More Recently, M. T. Hill et al. [33] have presented an all-optical set-reset flip-flop based on two coupled lasers with separate cavities and lasing at different wavelengths.

1.2 Purpose of This Research

In spite of the long research, a robust, high-speed, all-optical flip-flop applicable to optical communication systems has not yet been demonstrated. The absorptive BLDs have been used at submilliwatt powers over a 28-nm spectral range, but the carrier recombination lifetime is expected to limit repetition rates to a few GHz. Moreover, "optical-reset" is difficult. For the dispersive bistable devices, accurate signal frequency control is required and the optical frequency range over which the nonlinearity is observed is small. In addition, the extinction ratio between the ON and OFF state is usually small. Flip-flop operation based on polarization bistability in semiconductor laser is expected to be ultrafast (100 Gb/s), but requires orthogonally polarized control pulses that would be expensive to maintain in a fiber-optical system.

The purpose of this research is to give a solution to the problem mentioned before, the realization of a practical all-optical flip-flop devices using BLDs. We propose the basic concept of the combination of BLDs and nonlinear couplers such as directional couplers (DC), multi-mode interferometer (MMI) couplers, and Mach-Zehnder interferometer (MZI) couplers. The nonlinearity of theses couplers allow all-optical flip-flop operations.

1.3 Outline of This Thesis

This thesis presents a novel concept to realize all-optical flip-flops, that is the combination of the BLDs and the nonlinear couplers.

In Chapter 2, we develop the calculation methods of BLDs, that are a transfer matrix method (TMM) and a finite difference beam propagation method (FD-BPM). In Chapter 3, the basic properties of conventional absorptive BLDs are experimentally investigated. In Chapter 4, the all-optical flip-flop based on nonlinear directional couplers are proposed. The basic characteristics are experimentally investigated. In Chapter 5, we propose the absorptive BLDs with MMI couplers. The static characteristics are numerically analyzed by the FD-BPM model. In Chapter 6, a novel pitchfork bifurcation BLDs using Mach-Zehnder interferometer couplers is proposed, that has the potential for ultra high-speed switching. The bistabilities and switching characteristics are numerically analyzed by the FD-BPM model. Chapter 7 is a conclusion of this thesis.

References

[1] G. J. Lasher, "Analysis of a proposed bistable injection laser, "*Solid-State Electronics*, vol. 7, pp. 707-716, 1964.

[2] Ch. Harder, K. Y. Lau, and A. Yariv, "Bistability and pulsations in CW semiconductor lasers with a controlled amount of saturable absorption," *App. Phys. Lett.*, vol. 39, no. 5, pp. 382-384, 1981.

[3] H. Kawaguchi, K. Magari, H. Yasaka, M. Fukuda, and K. Oe, "Tunable optical-wavelength conversion using an optically triggerable multielectrode distributed feedback laser diode," *IEEE J. Quantum Electronics*, vol. QE-24, no. 11, pp. 2153-2159, 1988.

[4] S. Tarucha, and H. Okamoto, "Voltage-controlled optical bistability associated with two-dimensional exciton in GaAs-AlGaAs multiple quantum well lasers," *Appl. Phys. Lett.*, vol. 49, no. 10, pp. 543-545, 1986.

[5] H. Uenohara, H. Iwamura, and M. Naganuma, "Switching characteristics of InGaAs/InP multiquantum well voltage-controlled bistable laser diodes," *Jpn. J. Appl. Phys.*, vol. 29, no. 12, pp. L2442-L2444, 1990.

[6] H. Uenohara, Y. Kawamura, H. Iwamura, "Long-wavelength multiple-quantum-well voltage-controlled bistable laser diode," *IEEE J. Quantum Electronics*, vol. 31, no. 12, pp. 2142-2147, 1995.

[7] H. Uenohara, R. Takahashi, Y. Kawamura, H. Iwamura, "Static and dynamic response of multiple-quantum well voltage-controlled bistable laser diodes," *IEEE J. Quantum Electronics*, vol. 32, no. 5, pp. 873-883, 1996.

[8] K. Nonaka, H. Tsuda, H. Uenohara, H. Iwamura, and T. Kurokawa, "Optical nonlinear characteristics of a side-injection light-controlled laser diode with a multiple-quantum-well saturable absorption region," *IEEE Photonics. Technol. Lett.*, vol. 5, pp. 139-141, 1993.

[9] K. Nonaka, Y. Noguchi, H. Tsuda, and T. Kurokawa, "Digital signal regeneration with side-injection-light-controlled bistable laser diode as a wavelength converter," *IEEE Photonics. Technol. Lett.*, vol. 7, pp. 29-31, 1995.

[10] K. Nonaka, and T. Kurokawa, "Simultaneous time- and wavelength-domain optical demultiplexing of NRZ signals by using a side-injection-light-controlled bistable laser diode," *Electron. Lett.*, vol. 31, no. 21, pp. 1865-1866, 1995.

[11] K. Nonaka, F. Kobayashi, T. Tadokoro, K. Kishi, C. Amano, Y. Itoh, and T. Kurokawa, "Direct optical demux from 10-2.5 Gbit/s NRZ signals using a side-injection-light-controlled bistable laser diode," *Proc. 8th Eur. Conf. Integrated Optics*, pp. 470-473, 1997.

[12] K. Otsuka, and H. Iwamura, "Analysis of a mutistable semiconductor light amplifier," *IEEE J. Quantum Electronics*, vol. QE-19, no. 7, pp. 1184-1186, 1983.

[13] K. Otsuka, and S. Kobayashi, "Optical bistability and nonlinear resonance in a resonant-type semiconductor laser amplifier," *Electron. Lett.*, vol. 18, no. 7, pp. 262-263, 1983.

[14] T. Nakai, N. Ogasawara, and R. Ito, "Optical bistability in a semiconductor laser amplifier," *Jpn. J. Appl. Phys.*, vol. 22, no. 5, pp. L310-L312, 1983.

[15] W. F. Sharfin, and M. Dagenais, "Room-temperature optical bistability in InGaAsP/InP amplifiers and implications for passive devices," *App. Phys. Lett.*, vol. 46, no. 9, pp. 819-821, 1985.

[16] M. J. Adams, H. J. Westlake, M. J. O'Mahony, and I. D. Henning, "A comparison of active and passive optical bistability in semiconductors," *IEEE J. Quantum Electronics*, vol. QE-21, no. 9, pp. 1498-1504, 1985.
[17] W. F. Sharfin, and M. Dagenais, "Femtojoule optical switching in nonlinear semiconductor laser amplifiers," *App. Phys. Lett.*, vol. 48, no. 5, pp. 321-322, 1986.
[18] M. J. Adams, "Time dependent analysis of active and passive optical bistability in semiconductors, " *IEE Proc. J.*, vol. 132, no. 6, pp. 343-348, 1985.
[19] M. J. Adams, and L. D. Westbrook, "Optical bistability and nonlinear switching in quantum well amplifiers," in H. Haug, and L. Banyai (Eds.), "Optical switching in low-dimensional systems," NATO ASI Series B: Physics vol. 194, pp. 35-48, 1989.
[20] P. Likamwa, A. Miller, M. Ogawa, and R. M. Park, "All-optical bistable switching in an active InGaAs quantum-well waveguide," *IEEE Photonics. Technol. Lett.*, vol. 3, no. 6, pp. 507-509, 1991.
[21] D. A. H. Mace, M. J. Adams, and C .Seltzer, "MQW amplifier optical bistability," *Electron. Lett.*, vol. 27, no. 15, pp. 1363-1365, 1991.
[22] H. Kawaguchi, K. Inoue, T. Matsuoka, and K. Otsuka, "Bistable output characteristics in semiconductor laser injection locking," *IEEE J. Quantum Electronics*, vol. QE-21, no. 9, pp. 1314-1317, 1985.
[23] K. Nakatsuhara, T. Mizumoto, R. Munakata, Y. Kigure, and Y. Naito, "All-optical set-reset operation in a distributed feedback GaInAsP waveguide," *IEEE Photonics. Technol. Lett.*, vol. 10, no. 1, pp. 78-80, 1998.
[24] M. T. Hill, H. de Waardt, G. D. Khoe, and H. J. S. Dorren, "Fast optical flip-flop by use of Mach-Zehnder interferometers," *Microwave and Optical Technol. Lett.*, vol. 31, no. 6, pp. 411-415, 2001.
[25] Y. C. Chen, and J. M. Liu, "Polarization bistability in semiconductor lasers," *App. Phys. Lett.*, vol. 46, no. 1, pp. 16-18, 1985.
[26] C. L. Tang, A. Schremer, and T. Fujita, "Bistability in semiconductor lasers via gain saturation, " *App. Phys. Lett.*, vol. 51, no. 18, pp. 1392-1394, 1987.
[27] Y. Ozeki, J. E. Johnson, and C. L. Tang, "Polarization bistability in semiconductor lasers with intracavity multiple quantum well saturable absorber," *App. Phys. Lett.*, vol. 58, no. 18, pp. 1958-1960, 1991.
[28] Y. Ozeki, and C. L. Tang, "Polarization switching and bistability in an external cavity laser with a polarization-sensitive saturable absorber," *App. Phys. Lett.*, vol. 58, no. 20, pp. 2214-2216, 1991.
[29] H. Kawaguchi, I. H. White, J. J. Offside, and J. E. Carroll, "Ultrafast switching in polarization-bistable laser diodes," *Opt. Lett.*, vol. 17, no. 2, pp. 130-132, 1992.
[30] H. Kawaguchi, T. Irie, and M. Murakami, "Pitchfork bifurcation polarization bistability in laser diodes with external cavities," *IEEE J. Quantum Electronics*, vol. 31, no. 3, pp. 447-455, 1995.
[31] H. Kawaguchi, I. S. Hidayat, Y. Takahashi, and Y. Yamayoshi, "Pitchfork bifurcation polarization bistability in vertical-cavity surface-emitting lasers," *Electron. Lett.*, vol. 31, no. 2, pp. 109-111, 1995.
[32] H. Kawaguchi, I. S. Hidayat, "Gigahertz all-optical flip-flop operation of polarization-bistable vertical-cavity surface-emitting lasers," *Electron. Lett.*, vol. 31, no. 14, pp. 1150-1151, 1995.
[33] M. T. Hill, H. de Waardth, G. D. Khoe, H. J. S. Dorren, "All-optical flip-flop based on coupled laser diodes," *IEEE J. Quantum Electronics*, vol. 37, no. 3, pp. 405-413, 2001.

Chapter 2 Simulation Method

The simulation methods to analyze the BLDs proposed this thesis are developed. The two types of the simulation methods are adopted, i.e., a transfer matrix method (TMM) and a finite difference beam propagation method (FD-BPM). The TMM model can treat longitudinal distributions of photon density, carrier density, and refractive index, saving the calculation time. On the other hand, the FD-BPM model can treat more accurate longitudinal and lateral distributions of photon density, carrier density, and refractive index, although it takes more calculation time. The TMM model is applied to the analyses of directional coupler based BLDs, and the FD-BPM model is mainly applied to the analyses of the MMI and MZI based BLDs.

2.1 Introduction

To analyze the absorptive BLDs, a simple rate equation model has been used so far. The simplest model for absorptive bistability is the mean-field and single-mode one in the two-section LD with current biasing. This model needs only two photon rate equations and a carrier rate equation to treat the averages of the photon density and carrier density inside the cavity. However, in the case of the BLD with the nonlinear couplers, the phenomena inside the cavity are not so simple. It is very important to treat the distributions of the photon density and carrier density precisely. Therefore, we develop the two simulation method, a transfer matrix method (TMM) and a finite difference beam propagation method (FD-BPM) to analyze the proposed DC-BLD.

In the TMM [1][2], the laser structure is divided longitudinally into a number of subsections where several material and structure parameters are assumed to be constants, so the TMM can take into account logitudinal variations of photon and carrier densities, gain, and refractive index. Using the TMM, the multielectrode DFB lasers were numerically analyzed [2]. After that, to treat the dynamic characteristics of the DFB lasers, a time-dependent TMM was developed [3][4]. Because of the relatively simple formulas and the saving of the computational time, the TMM has been frequently used to analyzed various devices such as semiconductor optical amplifier (SOA) based wavelength converters [5], electroabsorp-

tion modulator-integrated DFB lasers [6][7], GCSR lasers [8], and vertical-cavity surface-emitting lasers (VCSELs) [9].

On the other hand, the FD-BPM [10] is widely used to design many kinds of guided-wave structures. It can easily treat the complicated structures and the longitudinal and lateral distributions of optical fields. Recently, the FD-BPM is applied to not only passive waveguides but also active waveguides such as LDs [11] and SOAs [12]-[14]. By adding some extra models such as the rate equations to the FD-BPM, the precise distributions of carrier densities, optical gain, and refractive index can be included to the FD-BPM.

In this section, we describe the general formulations of the this two models. The TMM is developed to analyze the DC-BLDs, and the FD-BPM with the rate equations is applied to the MMI- and MZI- BLDs.

2.2 Transfer Matrix Method

We developed the DC-BLD model taking into account longitudinal variations of carrier and photon densities, optical gain, refractive index, and lateral optical fields by time-dependent TMM. The basis of the TMM is to divide the waveguide longitudinally into a number of sections where the structural and material parameters are assumed to be homogeneous throughout each section. Moreover, to apply this model to the DC-BLD, we introduced the coupled-mode equations.

Fig.2.1 shows a schematic of the DC-BLD model. In the time-dependent TMM, the two waveguides are divided longitudinally into a number of small sections having equal length of Δz ($=v_g \Delta t$) and each section has forward and backward traveling waves and carrier density. Several material and structure parameters are assumed to be constants throughout section i in the time interval t to $t+\Delta t$ (Δt equals one section length l divided by the group velocity v_g)

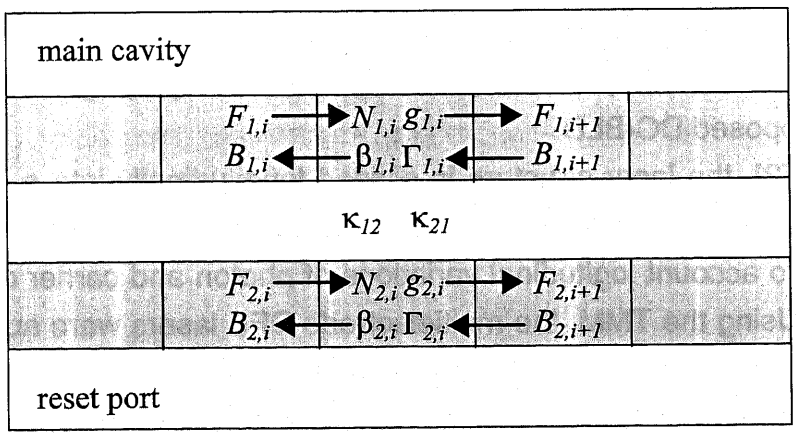

Fig.2.1 Simulation model based on the time-dependent TMM.

To evaluate the carrier density $N_{s,i}(t)$ in the section i of each waveguide (index s refers to the main cavity or the reset port, 1 or 2) at time t, the carrier rate equation is expressed as

$$\frac{dN_{s,i}}{dt} = \frac{J_{s,i}}{ed} - R(N_{s,i}) - \Gamma_{s,i} v_g g_{s,i} S_{s,i} \tag{2.1}$$

where J is the current density, e is the electron charge, d is the active region thickness, $R(N)$ is the recombination rate, Γ is the confinement factor, g is the material gain and S is the average photon density.

Using a detailed model including Auger recombination [15], the recombination rate is written as

$$R(N_{s,i}) = c_1 N_{s,i} + c_2 N_{s,i}^2 + c_3 N_{s,i}^3 \tag{2.2}$$

where c_1, c_2, and c_3 are recombination constants.

For the material gain, a realistic cubic dependence on wavelength is assumed [16]

$$g_{s,i}(N_{s,i}, \lambda) = a(N_{s,i} - N_0) - \Upsilon_1(\lambda - \lambda_N)^2 + \Upsilon_2(\lambda - \lambda_N)^3 \tag{2.3}$$

where a, γ_1, and γ_2 are gain constants, N_0 is the carrier density at transparency, λ_N is the peak wavelength, which is assumed to shift linearly with the carrier density. We set the value of λ_N to 1550 nm in the absence of any light in the DC-BLD cavity.

The average photon density in the section i is given by

$$S_{s,i} = \frac{|F_{s,i}|^2 + |F_{s,i+1}|^2 + |B_{s,i}|^2 + |B_{s,i+1}|^2}{2 v_g E} \tag{2.4}$$

where $F_{s,i}$ and $B_{s,i}$ are the modal amplitudes of the forward and backward propagating light each other, and E is the photon energy.

The spontaneous emission term contributes to the gain and nonlinear effect, so it is important that its term is included in TMM. The spontaneous emission that couples into each forward and backward propagating mode is expressed as [17]

$$\frac{J_{sp}}{|F_{s,i}|^2} F_{s,i} \tag{2.5}$$

$$\frac{J_{sp}}{|B_{s,i}|^2} B_{s,i} \tag{2.6}$$

where J_{sp} is spontaneous emission coefficient, which is written as

$$J_{sp} = \frac{1}{4} \beta_{sp} E c_2 N_{s,i}^2 dz \tag{2.7}$$

where β_{sp} is the spontaneous emission factor and $c_2 N^2$ represents the radiative spontaneous recombination.

To take into account that refractive index changes with carrier density, a linear dependent equation is assumed

$$n = n_0 + \frac{dn}{dN}N \tag{2.8}$$

where n_0 is the refractive index without any carrier injection, and dn/dN is refractive index shift coefficient, which usually takes the minus value. Therefore, equation (2.8) means that the refractive index decrease linearly as increasing the carrier density. We only consider the refractive index change of the waveguide's core, so the refractive index of the clad is fixed.

The propagation constant β and the confinement factor Γ are derived from solving the lateral mode profile. In the case of one dimensional slab waveguides, the effective refractive indices are easily calculated from the matrix approach (see Appendix C.).

A set of coupled traveling-wave transfer matrix can be derived using the slowly-varying amplitude approximations. In the time-dependent TMM, the output amplitudes $F_{s,i+1}$ and $B_{s,i}$ at time $t+\Delta t$ are calculated from the input amplitudes $F_{s,i}$ and $B_{s,i+1}$ at time t. By combination the coupled-mode theory and standard mode propagation theory, a transfer matrix for the forward propagating mode is expressed as

$$\begin{bmatrix} F_{1,i+1}(t+\Delta t) \\ F_{2,i+1}(t+\Delta t) \end{bmatrix} = \begin{bmatrix} A_1 & -j\kappa_{12}\Delta z A_1 \\ -j\kappa_{21}\Delta z A_2 & A_2 \end{bmatrix} \begin{bmatrix} F_{1,i}(t) \\ F_{2,i}(t) \end{bmatrix} \tag{2.9}$$

$$A_s = e^{\left\{\frac{1}{2}(\Gamma_{s,i}g_{s,i} - \alpha) - j\beta_{s,i}\right\}\Delta z} \tag{2.10}$$

where α the internal loss, κ_{12} and κ_{21} are the coupling coefficients, which are defined as

$$\kappa_{12} = \frac{\omega}{4Wd}\iint E_1^* E_2 (n^2 - n_2^2)\,dxdy \tag{2.11}$$

$$\kappa_{21} = \frac{\omega}{4Wd}\iint E_2^* E_1 (n^2 - n_1^2)\,dxdy \tag{2.12}$$

where ω is the optical frequency, W is the ridge waveguide width, E_1 and E_2 are the normalized lateral optical fields inside each waveguide, n, n_1 and n_2 are the lateral distributions of the refractive index, and x and y are lateral axes. The transfer matrix for the backward propagating light is expressed similarly.

The calculation procedure of the time-dependent TMM is illustrated in Fig.2.2. First, each section parameter such as the propagating lights $F_{s,i}$ and $B_{s,i}$, the carrier density $N_{s,i}$ and so on is initialized by the steady-state rate equations. It needs a little caution not to initialize $F_{s,i}$ and $B_{s,i}$ to be near zero because the spontaneous emission factors expressed as equations (2.5), (2.6) have the $1/F_{s,i}$ and $1/B_{s,i}$ term. After obtaining the next time injection current J, the carrier density $N_{s,i}$ is calculated, and this is followed by the other material and structural parameters being updated. Then, the propagation lights $F_{s,i}$ and $B_{s,i}$, are updated using the

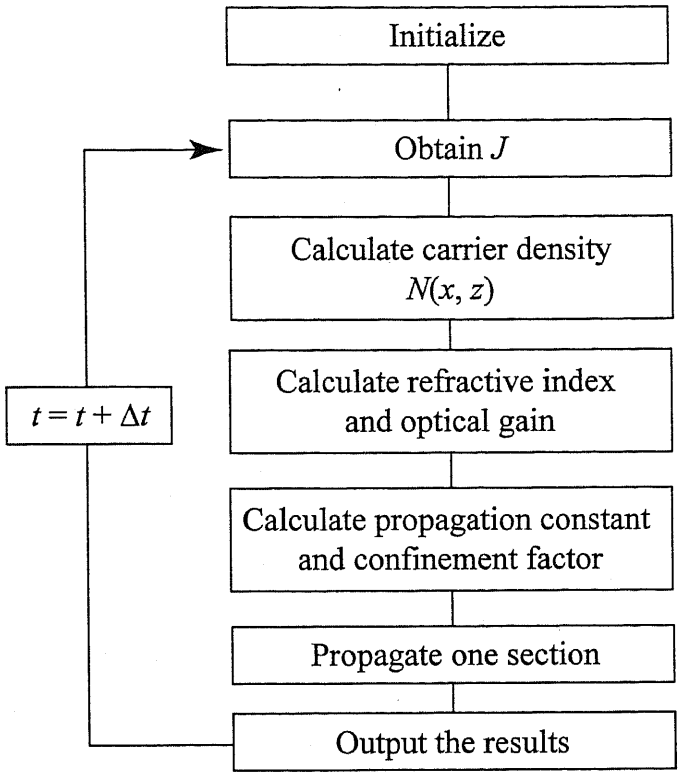

Fig.2.2 Flowchart of the calculation procedure of the time-dependent TMM. The propagation light and the other section parameters such as carrier density, refractive index, gain, propagation constant and confinement factor are updated at each time increment Δt.

transfer matrices (equation (2.9)). Finally, the output power is calculated, and the whole procedure is repeated at each time increment Δt.

2.3 Beam Propagation Method

In this section, we developed a finite difference beam propagation method (FD-BPM) for precise and flexible analyses of the static characteristics of the MMI- and MZI-BLDs. This model takes into account accurate distributions of photon and carrier densities, optical gain and refractive index inside the cavity. This modified FD-BPM model is especially effective to analyze the two-mode bistability.

To describe the propagation through the waveguides, the wave equation for a TE mode derived from Maxwell's equations should be solved. The scalar Helmholz equation for a TE-polarized light propagating a planar waveguide in the direction of z axis becomes

$$\frac{\partial^2 E}{\partial z^2} + \frac{\partial^2 E}{\partial x^2} + k_0^2 n E = 0 \tag{2.13}$$

where $E(x, z)$ is space-dependent electric field, $n(x, z)$ the space-dependent refractive index, k_0 the wave vector in vacuum and a temporal dependence of $exp(j\omega t)$ is assumed. This equation can be reduced to the paraxial wave equation which is

$$E(x,z) = \phi(x,z)exp(-j\beta_0 z) \tag{2.14}$$

$$2j\beta_0\frac{\partial\phi}{\partial z} = \frac{\partial^2\phi}{\partial x^2} + (k_0^2 n^2 - \beta_0^2)\phi \tag{2.15}$$

where β_0 is a reference propagation constant. Equation (2.15) is obtained by neglecting the second order derivatives of E with z, i.e. using a slowly varying envelope approximation. It is solved using finite differences in the transverse ($x=i\Delta x$) direction and a Crank-Nicolson scheme for the longitudinal ($z=j\Delta z$) coordinate. After a bit of algebra, the discrete equations are expressed as

$$\begin{aligned}&\eta^-_{i-1,j+1}\phi_{i-1,j+1} + \xi^-_{i,j+1}\phi_{i,j+1} + \eta^-_{i+1,j+1}\phi_{i+1,j+1} \\ &\quad = \eta^+_{i-1,j}\phi_{i-1,j} + \xi^+_{i,j}\phi_{i,j} + \eta^+_{i+1,j}\phi_{i+1,j}\end{aligned} \tag{2.16}$$

where

$$\eta^{\pm}_{i,j} = \pm\frac{1}{(\Delta x)^2}, \tag{2.17}$$

$$\xi^{\pm}_{i,j} = \mp\frac{2}{(\Delta x)^2} + \frac{4j\beta_0}{\Delta z} \pm k_0^2(n_{i,j}^2 - n_{eff}^2), \tag{2.18}$$

in which $\beta_0 = k_0 n_{eff}$. Since equations (2.16) - (2.18) leads to a tridiagonal matrix, equation (2.16) can be solved by the standard technique such as the Thomas algorithm [18].

In order to avoid nonphysical reflections from the computational window edges, Hadley's transparent boundary condition [19] is implemented.

Because the equation (2.15) includes only the forward propagating light, reflections are neglected inside the cavity. We consider only reflections on the cleaved facets. The forward and backward propagating fields are calculated separately and both fields are coupled each other at the cleave facets only [11].

We also take photon-carrier interaction into account. To evaluate the carrier density $N(x,z)$, the steady-state carrier rate equation in the case of the two-mode bistability is expressed as

$$\frac{J}{ed} = R(N) + \Gamma v_g g_1 S_1 + \Gamma v_g g_2 S_2 \tag{2.19}$$

where J is the current density, e the electron charge, d the thickness of the active layer, R the recombination rate, Γ the confinement factor, v_g the group velocity, g the material gain and S the photon density (the subscripts 1 and 2 refer to the two modes, respectively). The recombination rate is written as the same equation in case of the TMM (See equation (2.2)).

For the unsaturated material gain g_0, a linear dependence on carrier density is assumed

$$g_0(N) = a(N - N_0) \tag{2.20}$$

where a is gain constants, N_0 the carrier density at transparency.

The two-mode bistability of the MMI- and MZI-BLDs originates in cross gain saturation, so it is necessary that this effect is included in bistability analysis. The saturated gains for the two modes are related to the unsaturated gain g_0 through the photon densities of the two modes as follows.

$$g_1(N) = \frac{g_0}{1 + \varepsilon_{11}S_1 + \varepsilon_{12}S_2}$$
$$g_2(N) = \frac{g_0}{1 + \varepsilon_{22}S_2 + \varepsilon_{21}S_1} \tag{2.21}$$

where ε_{11}, ε_{22} and ε_{12}, ε_{21} are the self-saturation and the cross-saturation coefficients, respectively.

Refractive index change is taken into account using a linear dependent equation (2.8).

The L-I characteristics are calculated self-consistently as described in Fig.2.3. First, eigenmodes field profile are injected into the input ports instead of spontaneous emission because our BPM model can not treat spontaneous emission. Theses fields are propagated inside the cavity one round. Then, the carrier density is calculated from the carrier rate equation (2.19). The complex dielectric constant (i.e. refractive index and optical gain)

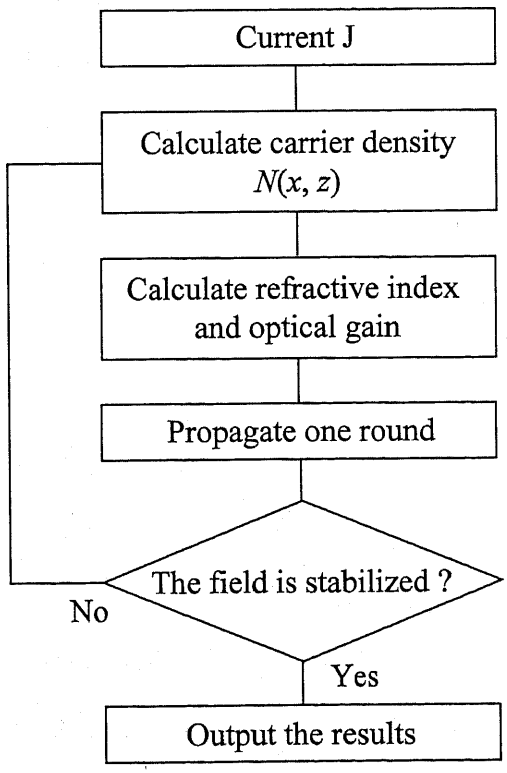

Fig.2.3 Numerical procedure of the FD-BPM with the carrier rate equation.

are calculated from the obtained carrier density, then the one-round field propagation is calculated again. This procedure is repeated until the field change becomes small enough after one round-trip.

2.4 Parameters

The parameters used in the TMM and FD-BPM are shown in Table.2.1. We consider an InGaAsP multi quantum well (MQW) structure whose band gap energy is around 1.55 μm.

To analyze two-mode bistability, self-gain saturation and cross-gain saturation should be included into the calculations. However, the exact value of the gain saturation coefficients are unknown yet. Based on the fact that the a relative value of the cross-gain saturation coefficient to the self-gain saturation coefficient is important, we assume the self-saturation coefficient as 8.0×10^{-17} cm^3 and the cross-saturation coefficient is twice as large.

Table.2.1 Parameters used in this simulation.

Symbol		Value	
λ	(μm)	1.55	Wavelength
n_0		3.27	Refractive index (core)
		3.25	Refractive index (clad)
d	(μm)	0.2	Thickness of active region
N_0	(cm^{-3})	0.83×10^{18}	Carrier density at transparency
α	(cm^{-1})	20	Internal loss
v_g	(cms^{-1})	7.89×10^{9}	Group velocity
a	(cm^2)	4.63×10^{-16}	Gain constant
γ_1	(cm^{-3})	7.4×10^{12}	
γ_2	(cm^{-4})	3.15×10^{17}	
c_1	(s^{-1})	0.23×10^{9}	Recombination coefficient
c_2	(cm^3s^{-1})	1.0×10^{-10}	
c_3	(cm^6s^{-1})	5.0×10^{-28}	
dn/dN	(cm^3)	-1.33×10^{-20}	Refractive index shift coefficient
ε_{11}, ε_{22}	(cm^3)	8.0×10^{-17}	self-saturation coefficient
ε_{12}, ε_{21}	(cm^3)	1.6×10^{-16}	cross-saturation coefficient

2.5 Conclusion

In this chapter, we developed the simulation methods to analyze the DC-, MMI-, MZI-BLDs. The two types of the simulation methods are adopted, i.e., a transfer matrix method (TMM) and a finite difference beam propagation method (FD-BPM). The TMM model can treat longitudinal distributions of photon density, carrier density, and refractive index, saving the calculation time. Moreover, it was extended to treat directional couplers by the coupled-mode theory. The TMM is applied to analyze the basic characteristics of the DC-BLD. On the other hand, the FD-BPM with the carrier rate equation was developed for the MMI- and MZI-BLDs. It can treat more accurate longitudinal and lateral distributions of photon density, carrier density, and refractive index, although it takes more calculation time. Theses simulation models will be used in the following chapter to analyze the bistable characteristics of the proposed BLDs.

References

[1] G. Björk, and O. Nilsson, "A new exact and efficient numerical matrix theory of complicated laser structures: Properties of asymmetric phase-shifted DFB lasers," *J. Lightwave Technol.* vol. LT-5, pp. 140-146, 1987.

[2] M. G. Davis, and R. F. O'Dowd, "A transfer matrix-based analysis of multielectrode DFB lasers," *IEEE Photonics. Technol. Lett.*, vol. 3, pp. 603-605, 1991.

[3] M. G. Davis, and R. F. O'Dowd, "A new large-signal dynamic model for multielectrode DFB lasers based upon the transfer matrix method," *IEEE Photonics. Technol. Lett.*, vol. 4, pp. 838-840, 1992.

[4] M. G. Davis, and R. F. O'Dowd, "A transfer matrix method based large-signal dynamic model for multielectrode DFB lasers," *IEEE J. Quantum Electronics*, vol. 30, no. 11, pp. 2458-2466, 1994.

[5] M. Saitoh, B. Ma, and Y. Nakano, "Static and dynamic characteristics analysis of all-optical wavelength conversion using directionally coupled semiconductor optical amplifiers," *IEEE J. Quantum Electronics*, vol. 36, no. 8, pp. 984-990, 2000.

[6] Y. Kim, H. Lee, J. Lee, J. Han, T. W. Oh, and J. Jeong, "Chirp characteristics of 10-Gb/s electroabsorption modulator integrated DFB lasers," *IEEE Photonics. Technol. Lett.*, vol. 36, no. 8, pp. 900-908, 2000.

[7] Y. Kim, S. Nam, and J. Jeong, "Yield estimation of 10-Gb/s electroabsorption modulator-integrated DFB lasers due to chirp," *IEEE Photonics. Technol. Lett.*, vol. 14, no. 4, pp. 447-449, 2002.

[8] O. A. Lavrove, and D. J. Blumenthal, "Detailed transfer matrix method-based dynamic model for multisection widely tunable GCSR lasers," *J. Lightwave Technol.* vol. 18, no. 9, pp. 1274-1282, 2000.

[9] S. F. Yu, "An improved time-domain traveling-wave model for vertical-cavity surface-emitting lasers," *IEEE J. Quantum Electronics*, vol. 34, no. 10, pp. 1938-1948, 1998.

[10] Y. Chung, and N. Dagli, "An assessment of finite difference beam propagation method," *IEEE J. Quantum Electronics*, vol. 26, no. 8, pp. 1335-1339, 1990.

[11] H. K. Bissessur, F. Koyama, and K. Iga, "Modeling of oxide-confined vertical-cavity surface-emitting lasers," *IEEE J. Select. Topics in Quantum Electronics*, vol. 3. pp. 344-352, 1997.

[12] M. Y. Hong, Y. H. Chang, A. Dienes, J. P. Heritage, P. J. Delfyett, S. Dijaili, and F. G. Peterson, "Femtosecond self- and cross-phase modulation in semiconductor laser amplifiers," *IEEE J. Select. Topics in Quantum Electronics*, vol. 2. pp. 523-539, 1996.

[13] N. K. Das, Y. Yamayoshi, and H. Kawaguchi, "Analysis of basic four-wave mixing characteristics in a semiconductor optical amplifier by the finite-difference beam propagation method," *IEEE J. Quantum Electronics*, vol. 36, no. 10, pp. 1184-1192, 2000.

[14] N. K. Das, T. Kawazoe, Y. Yamayoshi, and H. Kawaguchi, "Analysis of optical phase-conjugate characteristics of picosecond four-wave mixing signals in semiconductor optical amplifiers," *IEEE J. Quantum Electronics*, vol. 37, no. 1, pp. 55-61, 2001.

[15] R. Olshansky, C. B. Su, J. Manngin, and W. Powazinik, "Measurement of radiative and nonradiative recombination rates in InGaAsP and AlGaAs light sources," *IEEE J. Quantum Electronics*, vol. QE-20, pp. 838-854, 1984.

[16] A. E. Willner and W. Shieh, "Optimal spectral and power parameters for all-optical wavelength shifting: Single state, fanout, and cascadability," *J. Lightwave Technol.* vol. 13, pp. 771-781, 1995.

[17] K. Petermann, "Calculated spontaneous emission factor for double-heterostructure injection lasers with gain-induced waveguiding," *IEEE J. Quantum Electronics*, vol. QE-15, pp. 566-570, 1979.
[18] W. H. Press, S. A. Teukolsky, W. T. Vetterling, and B. P. Flannery, *Numerical recipes*, Cambridge University Press, 1992.
[19] G. R. Hardley, "Transparent boundary condition for the beam propagation method," *IEEE J. Quantum Electronics*, vol. 28, pp. 363-370, 1992.

Chapter 3 Absorptive Bistable Laser Diode

The basic properties of BLDs with saturable absorbers were experimentally evaluated in this chapter. The fabrication procedure of the saturable absorber were developed to get a high isolation resistance between gain and absorption regions. The proper length of the saturable absorber was experimentally decided. Moreover, the maximum device length to get a clear hysteresis was obtained. To overcome this restriction, we studied a multi-sectioned saturable absorber, which allowed shorter absorber length than normal one. The characteristics of optical set operation such as polarization and wavelength dependences were investigated. Finally, the effect of a reverse voltage applied to the saturable absorber was evaluated. The knowledge obtained here were useful for realization of a novel all-optical flip-flop based on the absorptive BLD.

3.1 Introduction

A bistable laser consisting of a Fabry-Perot injection laser whose plated p contact is divided into two electrically isolated portions was proposed by Lasher in 1964 [1]. An inversion is produced in one portion by an injection current, but the other portion is biased at a negligible current or a reverse voltage, which then acts as a saturable absorber. A saturable absorber is defined as a material whose absorption decreases with the increase of incident radiation intensity. The LDs with saturable absorbers, i.e., the absorptive LDs show bistability in the optical-output-versus-current (L-I) curve and in the optical-output-versus-optical-input (L-P) curve. A typical hysteresis characteristics of the absorptive BLD is shown in Fig.3.1. The photon density versus excitation ratio was calculated from the rate equation. In the OFF state of the absorptive BLD, there is only spontaneous emission from the gain region. Since the light level is low, light traveling in the waveguide between the reflecting ends will be strongly absorbed and there will be no laser action. In the ON state, the device operates as a laser. The population in the absorber is inverted by optical pumping from the gain regions so that it is essentially transparent to the laser radiation. The quasi-Fermi level in the gain region decreases as it goes from the OFF state to the ON state, while, in the absorber, it increases. After Lasher's proposal, a clear hysteresis in absorptive BLDs were

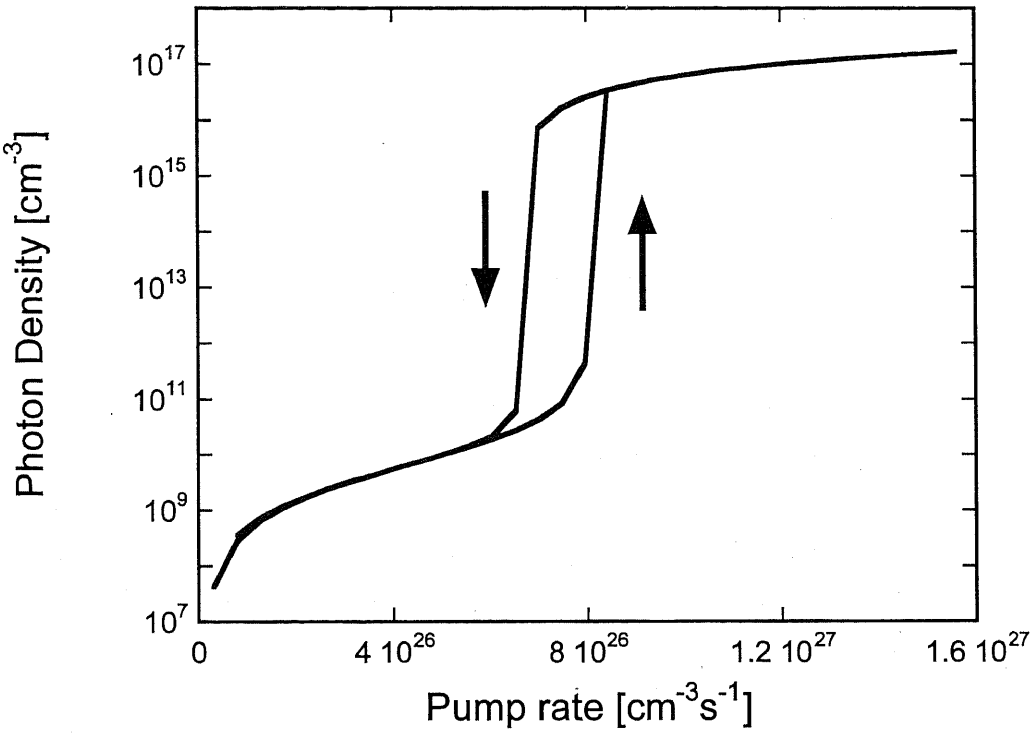

Fig.3.1 Typical hysteresis characteristic of the absorptive BLD calculated from the rate equations. The photon density versus excitation rate is plotted.

experimentally demonstrated by Yariv et al [2]-[6]. Now, the saturable absorbers have been used for not only BLDs, but also mode-locked semiconductor lasers [7]-[11], clock recovery [12][13] and regeneration [14].

In this chapter, we evaluated the basic characteristics of BLDs based on saturable absorbers, which were helpful to novel all-optical flip-flops proposed the following chapters. In Section 3.2, the fabrication procedure of the conventional absorptive BLDs is mentioned. In Section 3.3, we study the proper length of the saturable absorber to obtain the clear hysteresis. In Section 3.4, the multi-sectioned saturable absorber are developed, that shown more effective nonlinear absorption than conventional one. In Section 3.5 and Section 3.6, the optical set characteristics and the effect of the reverse voltage applied to the saturable absorber are investigated, respectively. Conclusions are given in Section 3.7.

3.2 Fabrication of Absorptive BLD

First, we started to study the fabrication procedure of the saturable absorber for the absorptive BLDs. We used the normal ridge-waveguide Fabry-Perot LD structure. The LD layer structure is shown in Fig.3.2, which was grown on n-InP substrates by metal organic vapor phase epitaxy (MOVPE, AIXTRON: 1409). The MOVPE had the double injection sys-

tem and that was able to grow the multi layer structure precisely. The active layer was 0.8% compressively-strained InGaAsP MQW (5 layers) whose band gap energy was around 1. 55 μm. Both the well and barrier thickness was 10 nm. The 120 nm InGaAsP SCH layers (λ_g = 1.25 μm) were equipped at the both sides of the MQW layer. The upper cladding layer was 1000 nm p-InP including 3nm InGaAsP etch-stop layer (λ_g = 1.25 μm), and that was followed by 200 nm p+InGaAs contact layer to provide a ohmic contact through a electrode. To fabricate the absorptive BLD using this wafer, we adopted the conventional process of the ridge waveguide LDs.

(i) Patterning: A stripe pattern was made by photolithography. Photo-resist (Shipley: S1805) was spin-coated on the InP substrate. The rotation speed of the spinner was 1st: 500 rpm (5 sec.), 2nd: 6000 rpm (40 sec.). The pre-baking for 10 min. at 90 °C was following. After the UV exposure for around 3 sec., 10 sec. development by NMD-3 was following. For successful liftoff process to open the current injection window of the ridge waveguide, the wafer didn't be post-baked.

(ii) Wet-etching: The ridge waveguides were formed by chemical wet-etching. The InGaAs cap layer was etched by H_2SO_4 : H_2O_2 : H_2O = 1 : 1: 5 solution (30 sec., 5 °C). Then, the p-InP upper clad was etched by 20 % HCl solution (3 min., R.T.). The etching was stopped by the InGaAsP etch-stop layer.

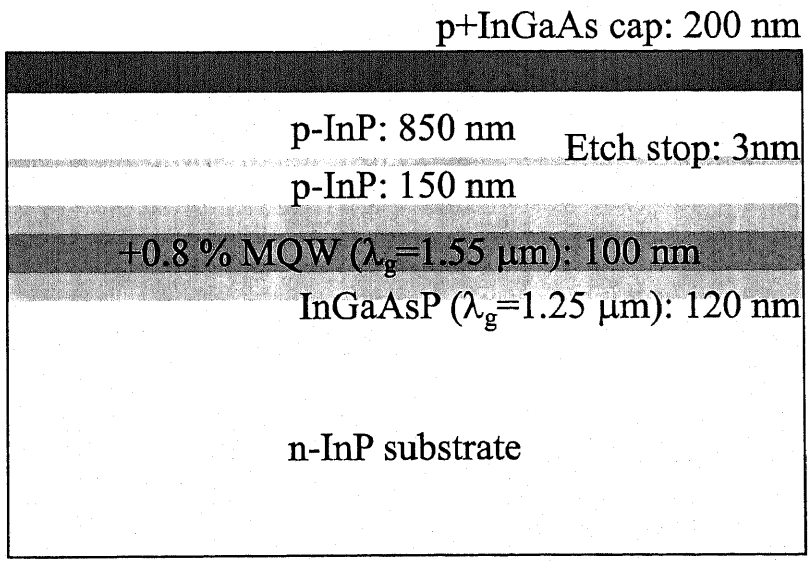

Fig.3.2 The LD layer structure used in this paper, which was grown on a n-InP substrate by MOVPE (AIXTRON: 1409). The active layer was 0.8 % compressive strain MQW (5 layers, λ_g = 1.55 μm), had 120 nm InGaAsP SCH layers (λ_g = 1.25 μm) at both sides. The upper p-InP layer included the InGaAsP etch-stop layer (λ_g = 1.25 μm), and that was followed by the p+InGaAs contact layer.

(iii) Liftoff: After Al_2O_3 current-blocking layer (100 nm) was deposited by electron-beam (EB) evaporation, the liftoff was incorporated to open the window for current injection. For the liftoff, the wafer was soaked in boiling acetone (10 min.) and ultrasonic vibrating acetone (20 min.).

(iv) Electrode formation: The Ti (30 nm) / Au (150 nm) p-contact electrodes were deposited by EB evaporation.

(v) Saturable absorber formation: The saturable absorber was formed by etching the electrode. The separator pattern was made by photolithography. Photo-resist (Tokyo Ohka kogyo: OFPR-800 50CP) was spin-coated on the wafer. The rotation speed of the spinner was 1st: 500 rpm (5 sec.), 2nd: 4000 rpm (40 sec.). The pre-baking for 30 min. at 90 °C was following. After the UV exposure for around 11 sec., the NMD-3 development (1 min.) and the post-baking (30 min., 90 °C) were following. The Au layer was etched by I : KI : H_2O = 1 g : 2 g : 50 g solution (1 min., R. T.). The Ti layer was etched by 63 buffered HF (23 sec., R. T.). To get high isolation resistance between the gain and absorption regions, the InGaAs cap layer was etched using H_2SO_4 : H_2O_2 : H_2O = 1 : 1: 5 solution (1 min., 5 °C).

Griding: The wafer was gridded into 120 μm thickness to cleave it easily. Finally, the Ti (30 nm) / Au (150 nm) electrode was deposited on the back of the wafer.

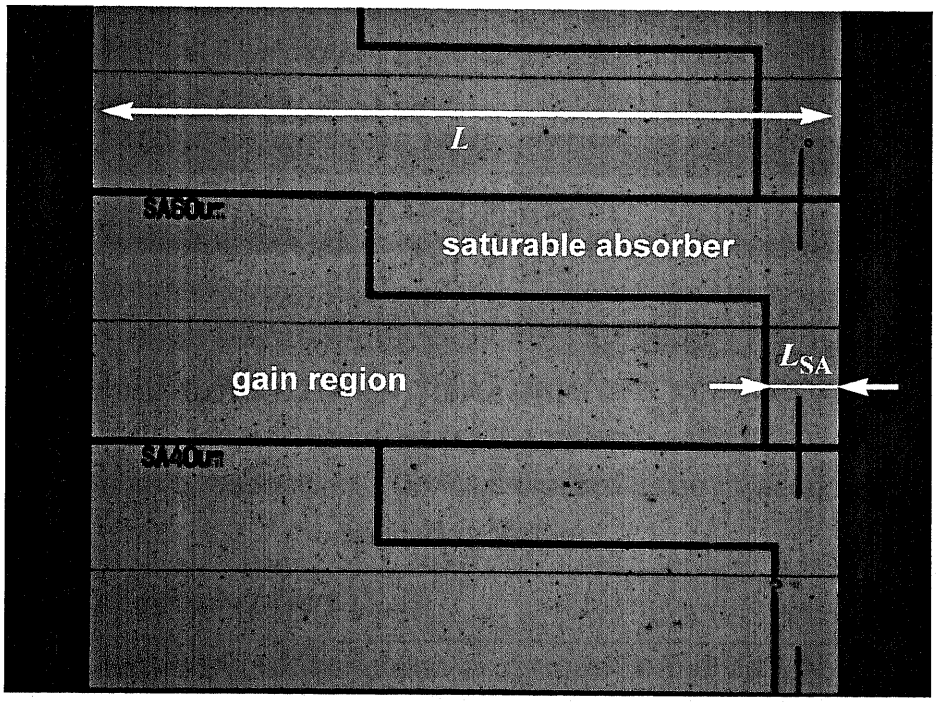

Fig.3.3 Microscopic view of the fabricated BLDs. The device length L was varied from 500 μm to 2500 μm, and the saturable absorber length L_{SA} was varied from 20 μm to 150 μm.

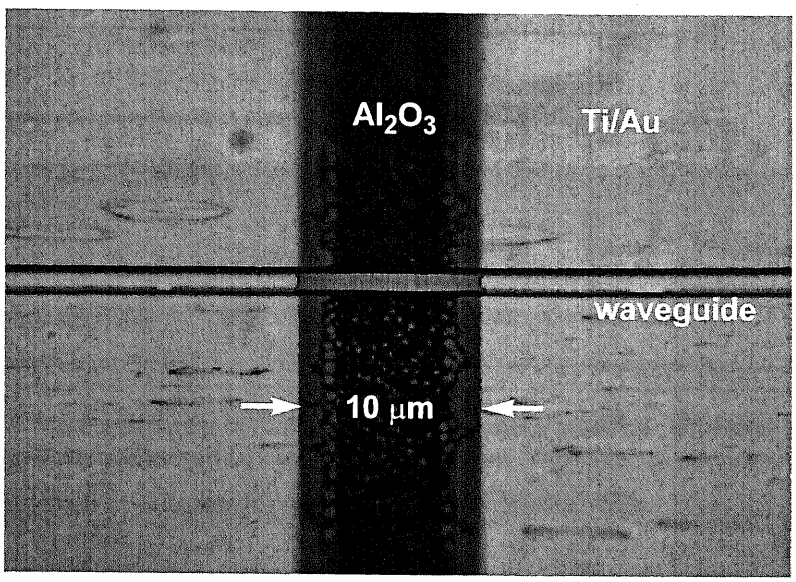

Fig.3.4 Microscopic photograph (×1000) of the electrode separation region. The width of separation region was around 10 μm. The isolation resistance was around 15 kΩ.

The microscopic top view photograph of the fabricated BLDs is shown in Fig.3.3. To investigate the proper saturable absorber length, the cavity length L was varied from 500 μm to 2500 μm, and the saturable absorber length L_{SA} was varied from 20 to 150 μm. The saturable absorber was equipped with the edge of the fabricated LDs. The saturable absorber was realized to separate the electrode of the gain region and the saturable absorption region. The microscopic photograph of the separation region is shown in Fig.3.4. The width of the separator was around 10 μm. The current-blocking region, Al_2O_3, appeared by removing the Ti/Au electrode. The isolation resistance between the gain region and the saturable absorber was around 15 kΩ that was large enough to obtain the clear hysteresis. In the following sections, the all devices were measure at CW operation (20 °C), and we used tapered fibers for coupling the lights.

3.3 Length of Saturable Absorber

For stable operations, the width of hysteresis loop require more than 3 mA. The saturable absorber length affects the characteristics of the absorptive BLDs. To obtain proper saturable absorber length, we measured the hysteresis characteristics of the fabricated absorptive BLD.

We prepared the saturable absorbers whose length L were around 20 μm - 150 μm. The total lengths of the BLDs L_{SA} were 500 μm - 2500 μm. For convenience, we defined SA ratio as the ratio of the saturable absorber length to the total length, i.e., L_{SA}/L. The SA ratio

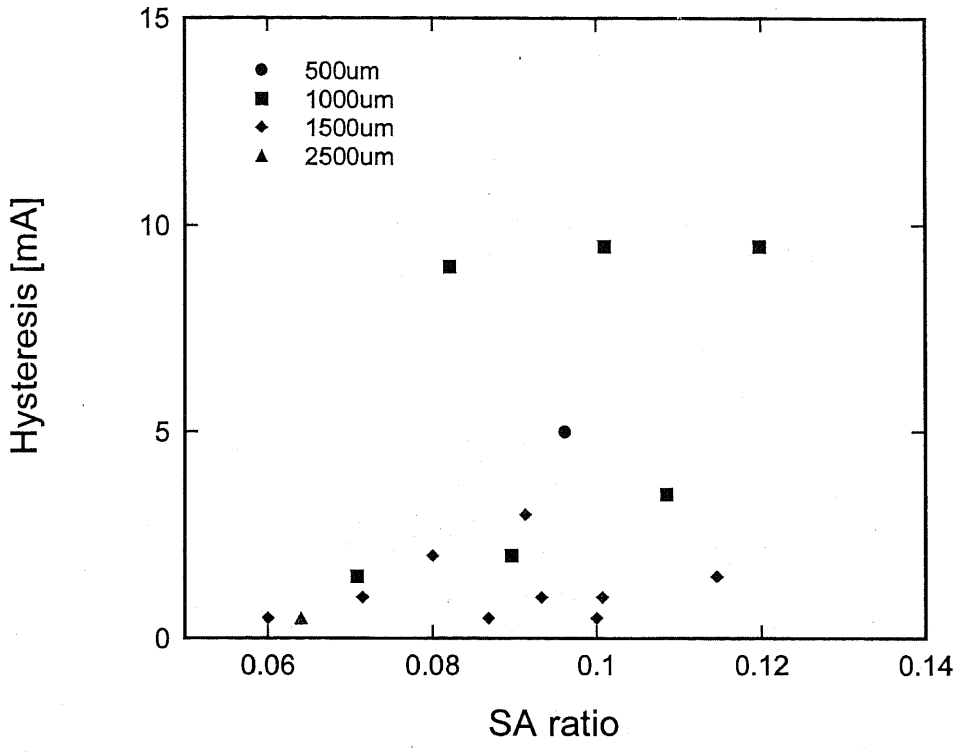

Fig.3.5 SA ratio dependence of hysteresis width. The hysteresis widths were around 3 mA in that case that SA ratio was around 0.1. The hysteresis was not observed when the device length was larger than 2000 μm.

dependence of the hysteresis width is depicted in Fig.3.5. The lasing wavelength of the absorptive BLDs was around 1.55 μm. No voltage or no current were applied to the saturable absorbers. In the case that the total device length was less than 1500 μm, the hysteresis loops were clearly observed. The width of hysteresis loop was about 3 mA, as the SA ratio was 0.1. On the other hand, the hysteresis could not appear in the case that the device lengths were larger than 2000 μm. From theses results, it was concluded that the total device length should be within 1500 μm, and the optimal length of the saturable absorber was around 10% of the device length.

3.4 Multi-sectioned Saturable Absorber

We could not obtain hysteresis of the BLD whose length was more than 2000 μm. This result originated from that the lasing wavelength was red-shifted and the carrier redistribution between the gain region and absorption region decayed. The small carrier redistribution led to the small saturable absorption, so the hysteresis disappeared.

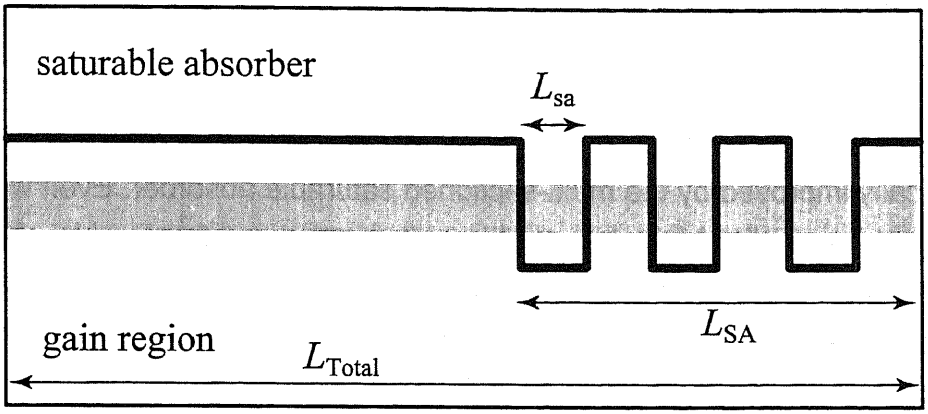

Fig.3.6 Schematic view of multi-sectioned saturable absorber. The total absorber section length L_{SA} was fixed to 500 μm. The number of division was varied from 2 to 5 so that the SA ratio did not change from 0.1.

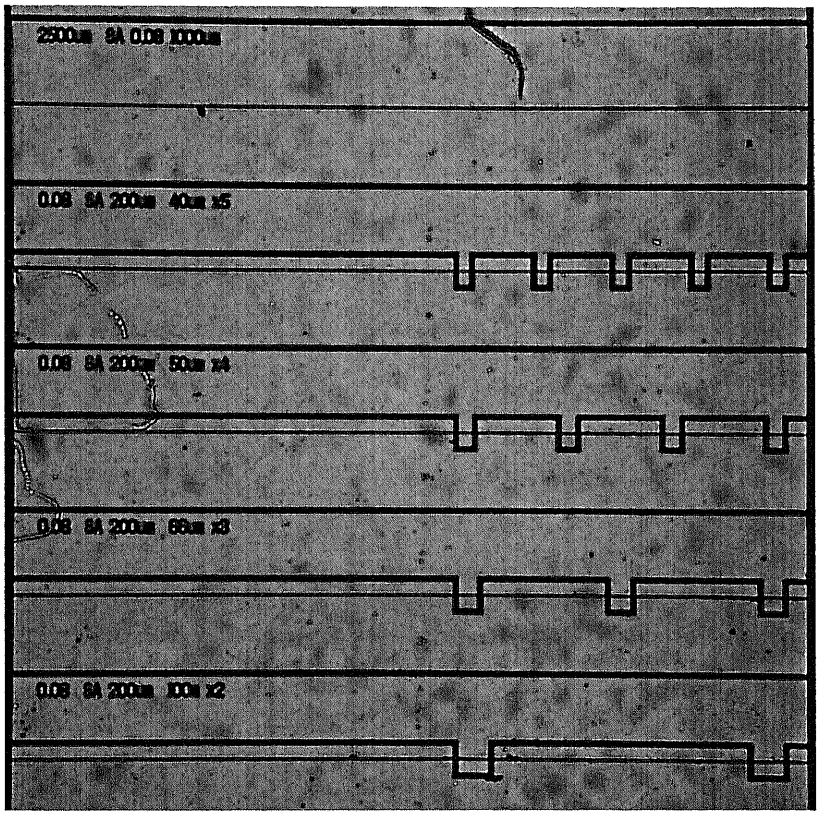

Fig.3.7 Microscopic photograph (×200) of the fabricated multi-sectioned saturable absorber.

To overcome this restriction, we adopted a multi-sectioned saturable absorber sketched as Fig.3.6. The carrier redistribution can be enhanced by dividing the saturable absorber into small sections [15][16].

Using the same procedure of the normal saturable absorber, we fabricated the multi-sectioned saturable absorber shown in Fig.3.7. The L_{SA} length was fixed at 500 μm & 1000 .

μm, and the number of division and the length of the small absorber section L_{sa} were varied so that the SA ratio did not change from 0.1.

The L-I characteristic in the case that the device length was 2350 μm were shown in Fig.3.8. We didn't applied any voltage or current to the saturable absorbers. The hysteresis was dramatically improved by the multi-sectioned saturable absorber. Even when the saturable absorber was divided into two sections, the recovery of saturable absorption was clearly observed. Using the multi-sectioned saturable absorber, we could realize absorptive BLD, irrespective of the device length. The multi-sectioned saturable absorbers had more effective saturable absorption than normal one, so the hysteresis width was larger than normal one. Fig.3.9 shows SA ratio dependence of hysteresis width of the BLDs with multi-sectioned saturable absorbers. The hysteresis widths were more than 3 mA, although the SA ratios was 0.1 (cf. Fig.3.5).

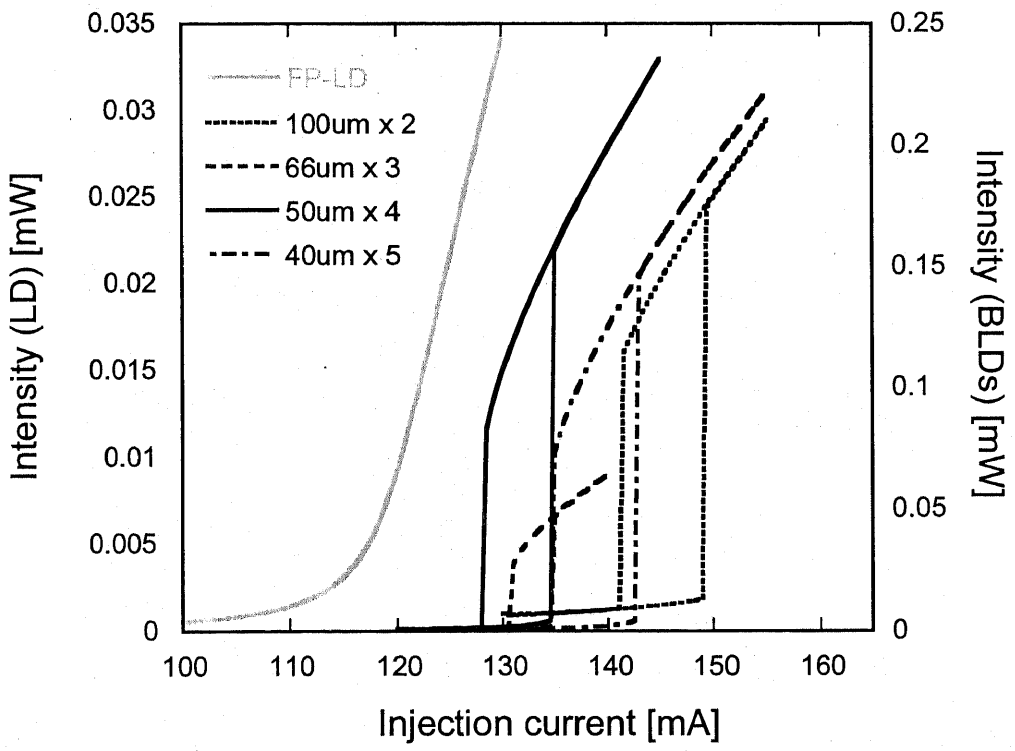

Fig.3.8 L-I characteristics of the multi-sectioned saturable absorber BLD. The device length was 2350 μm. The hysteresis was drastically improved, and the clear bistability was observed.

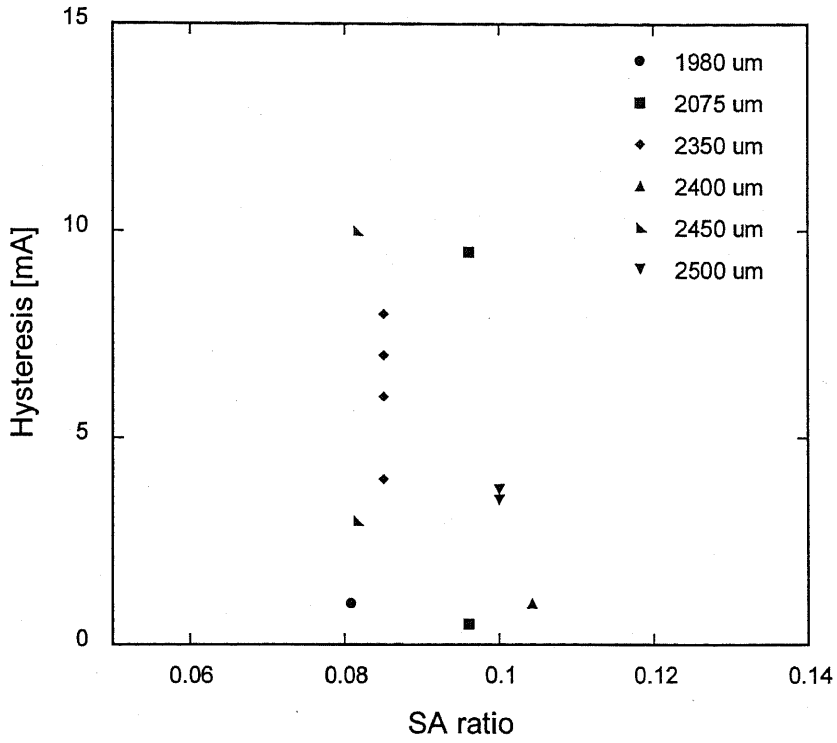

Fig.3.9 SA ratio dependence of hysteresis width of the BLDs with multi-sectioned saturable absorber. The bistability was clearly observed although the device length was more than 2000 μm. Almost all device shown the hysteresis width more than 3 mA.

3.5 Optical Turn-on Characteristics

An absorptive BLD can be turned on by injecting the set signal into the saturable absorber. The input light makes photo-generated carrier and saturates the absorption. Therefore, the turn-on characteristics have dependences on polarization and wavelength of the set signal. In this section, the basic properties of the optical set operation were experimentally investigated. In both cases, any voltage or current were not applied to the saturable absorbers.

The fabricated BLD had the compressively strained MQW that TE modes had much larger optical gain than TM modes. The polarization dependence of the turn-on operation is shown in Fig.3.10. The lasing wavelength of the BLDs was around 1550 nm. The input lights were 1555 nm CW lights from the wavelength tunable LD source. The TE mode set signal turned the BLD on at -4 dBm. On the other hand, the TM mode could not turn it on because the saturable absorber had no absorption for TM modes.

The MQW whose bandgap energy was around 1550 nm also had wavelength dependence. Fig.3.11 shows the wavelength dependence of the turn-on power. The set signal was TE-polarized CW light. The switching power had a minimum point that was estimated

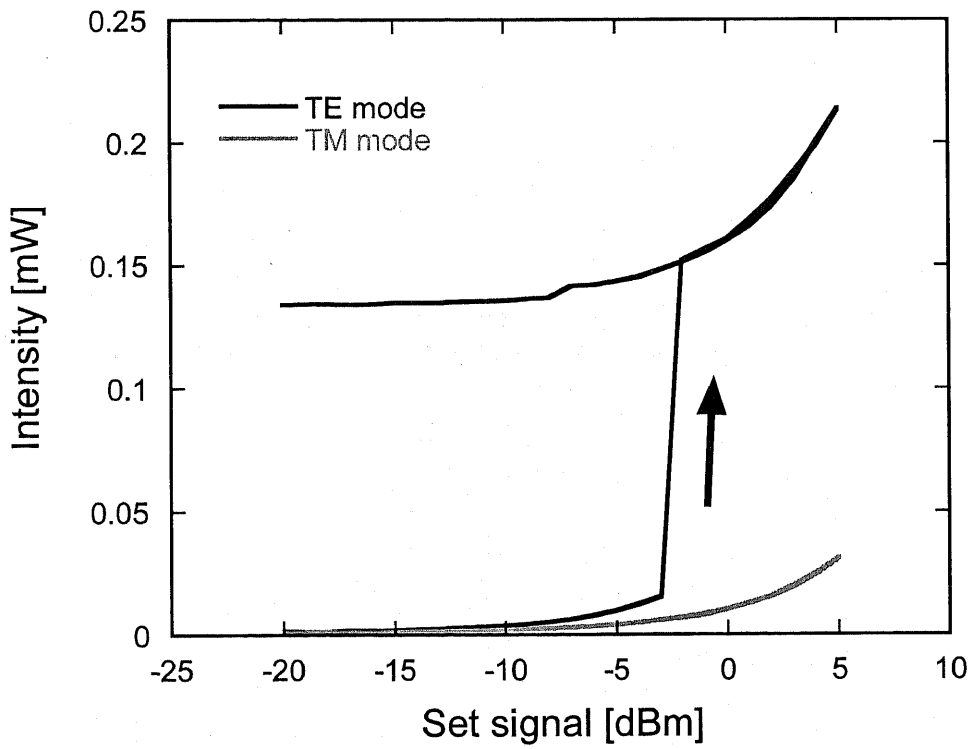

Fig.3.10 Polarization dependence of turn-on characteristics. The input lights were 1555 nm CW lights. Only the TE mode could turn the BLD on because of the polarization dependence of the MQW.

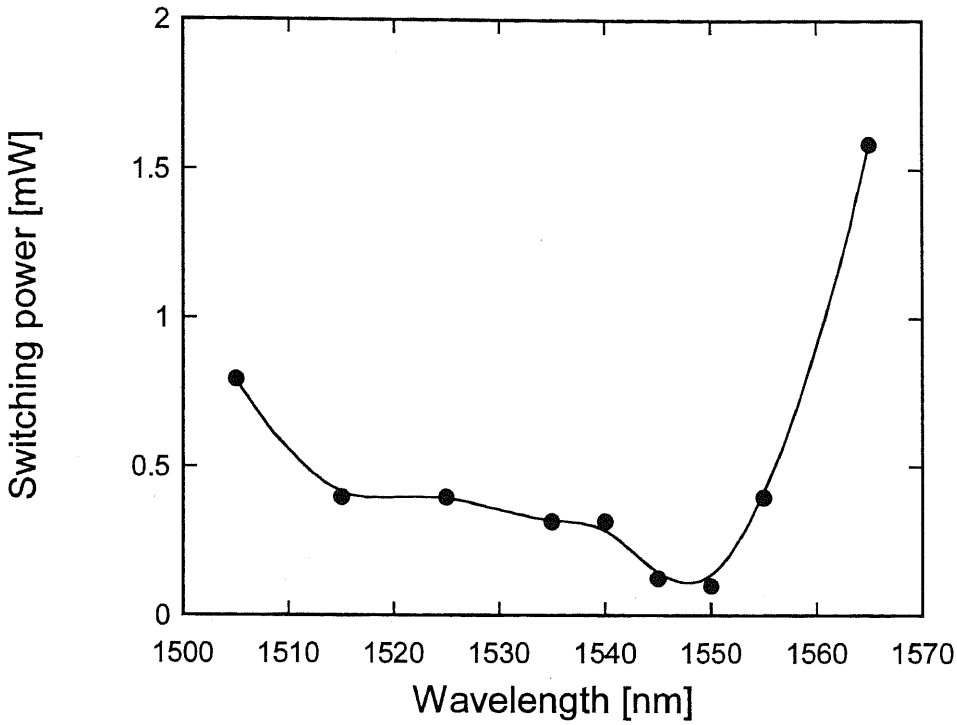

Fig.3.11 Wavelength dependence of turn-on power. The set signal was TE-polarized light. The optical set was realized over 50 nm bandwidth. The switching power had a minimum point at around the exciton peak.

as a exciton peak wavelength, 1550 nm. As the wavelength was far from the exciton peak, the switching power increased. Especially, the larger power was needed at the longer wavelength from the exciton peak because the absorption of the saturable absorber decayed rapidly. On the other hand, there was flat dependence at shorter wavelength from the exciton peak. The bandwidth was larger than 50 nm on condition that the switching power was less than 1 mW.

In both the cases, the input powers included the coupling loss that was estimated to around 10 dB, so the minimum turn-on power was less than 0.1 mW.

3.6 Reverse Voltage Dependence

In the previous sections, we didn't apply the reverse voltage to the saturable absorber. However, to achieve a high-speed operation, the reverse voltage should be applied to the saturable absorber. The reverse bias voltage allows faster turn-off switching speed due to the shorter carrier sweep-out time by the applied electric field [17]-[19]. At the same time, the absorption coefficient and the absorption band edge of the saturable absorption region are changed by applied voltage because of the quantum confined Stark effect (QCSE) [20] in the semiconductor QW structures. The fabricated BLD shown clear hysteresis character-

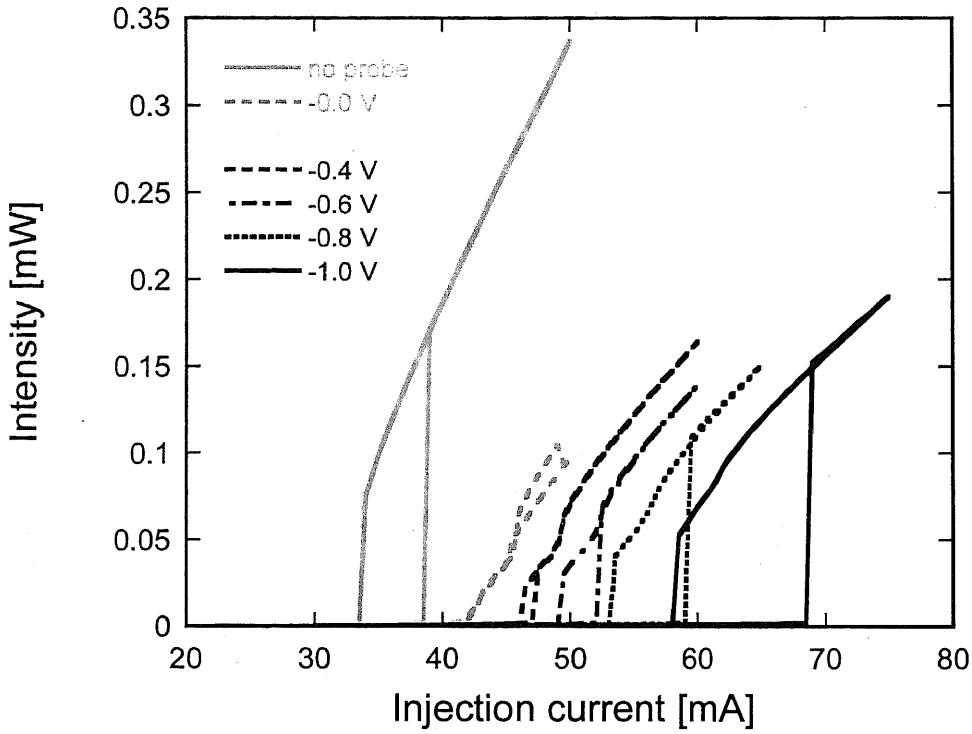

Fig.3.12 Reverse voltage dependence of the hysteresis characteristics. The applied voltage to the saturable absorber was varied from 0 V to -1 V. The threshold and the hysteresis width increased with the increase of the reverse voltage.

istics and good controllability with applied voltage to the saturable absorption region, as seen in Fig.3.12. The total device length and the saturable absorber length were 500 μm and 50 μm, respectively. The turn-on threshold current changed from 38 mA to 68 mA, and the hysteresis width from 4 mA to 10 mA by the applied voltage change from 0 V to -1 V. The hysteresis was not observed in the case that the applied voltage was within -0.2 V. That is because the absorption edge was too far from the lasing wavelength at around 0 V reverse voltage. This phenomenon was often observed in the case of strained MQWs that has sharp absorption edges.

From these results, the reverse voltage should be around -1 V to obtain the clear hysteresis and the high-speed switching. Moreover, we can shorten the length of the saturable absorber, that leads to the small switching power.

3.7 Conclusion

In this Chapter, we experimentally investigated the basic properties of the absorptive BLDs. By developing the fabrication procedure of the saturable absorber, a high isolation resistance between the gain and absorption regions was obtained around 15 kΩ, that led to the clear hysteresis. The proper length of the saturable absorber was experimentally

decided to be 10 % of the total device length. Moreover, the device length should be less than 1500 μm to get the clear bistability. To overcome this restriction, we studied a multi-sectioned saturable absorber, which allowed shorter absorber length than normal one. The characteristics of optical set operation such as polarization and wavelength dependences were investigated. Only the TE-polarized light could turn the BLD on because of the compressive strain MQW's polarization dependence. The optical set was obtained by the TE-polarized light over 50 nm wavelength bandwidth. Finally, the effect of the reverse voltage applied to the saturable absorber was evaluated for the high-speed switching. Due to the QCSE, the threshold current and hysteresis width increased as increasing the reverse voltage. The knowledge obtained in this chapter were helpful for realization of a novel all-optical flip-flop based on the absorptive BLD proposed in the following chapters.

References

[1] G. J. Lasher, "Analysis of a proposed bistable injection laser, "*Solid-State Electronics*, vol. 7, pp. 707-716, 1964.

[2] Ch. Harder, K. Y. Lau, and A. Yariv, "Bistability and pulsations in CW semiconductor lasers with a controlled amount of saturable absorption," *App. Phys. Lett.*, vol. 39, no. 5, pp. 382-384, 1981.

[3] Ch. Harder, K. Y. Lau, and A. Yariv, "Bistability and negative resistance in semiconductor lasers," *App. Phys. Lett.*, vol. 40, pp. 124-126, 1982.

[4] K. Y. Lau, Ch. Harder, and A. Yariv, "Dynamical switching characteristic of a bistable injection laser," *App. Phys. Lett.*, vol. 40, pp. 198-200, 1982.

[5] K. Y. Lau, CH. Harder, and A. Yariv, "Interaction of a bistable injection laser with an external optical cavity," *App. Phys. Lett.*, vol. 40, pp. 369-371, 1982.

[6] Ch. Harder, K. Y. Lau, and A. Yariv, "Bistability and pulsations in semiconductor lasers with inhomogeneous current injection," *IEEE J. Quantum Electronics*, vol. QE-18, no. 9, pp. 1351-1361, 1982.

[7] J. P. Van der Ziel, W. T. Tsang, R. A. Logan, R. M. Mikulyak, and W. M. Augustyniak, "Subpicosecond pulses from passively mode-locked GaAs buried optical guide semiconductor lasers," *App. Phys. Lett.*, vol. 39, pp. 525-527, 1981.

[8] D. J. Jones, L. M. Zhang, J. E. Carroll, and D. D. Marcenac, "Dynamics of monolithic passive mode locked semiconductor lasers," *IEEE J. Quantum Electronics*, vol. 31, pp. 1051-1058, 1995.

[9] T. Hoshida, H. F. Liu, M. Tsuchiya, Y. Ogawa, and T. Kamiya, "Subharmonic hybrid mode-locking of a monolithic semiconductor laser," *IEEE J. Selct. Topics Quantum Electronics*, vol. 2, pp. 514-522, 1996.

[10] S. Arahira, Y. Katoh, D. Kunimatsu, and Y. Ogawa, "Stabilization and timing jitter reduction of 160 GHz colliding-pulse mode-locked laser diode by subharmonic-frequency optical pulse injection," *IEICE Trans. on Electron.*, vol. E83-C, pp. 966-973, 2000.

[11] H. C. Bao and H. F. Liu, "Amplitude noise of subharmonically hybrid mode-locked pulses generated from a monolithic semiconductor laser," *IEEE Photonics. Technol. Lett.*, vol. 14, pp. 6-8, 2002.

[12] K. Vlachos, G. Theophilopoulos, A. Hatziefremidis, and H. Avramopoulos, "30 Gb/s all-optical clock recovery circuit," *IEEE Photonics. Technol. Lett.*, vol. 12, no. 6, pp. 705-707, 2000.

[13] V. Mikhailov, and P. Bayvel, "All-optical multiwavelength clock recovery using integrated semiconductor amplifier array module," *Electron. Lett.*, vol. 37, no. 4, pp. 232-234, 2001.

[14] K. Inoue, "Technique to compensate waveform distortion in a gain-saturated semiconductor optical amplifier using a semiconductor saturable absorber," *Electron. Lett.*, vol. 34, no. 4, pp. 376-378, 1998.

[15] H. Kawaguchi, K. Magari, H. Yasaka, M. Fukuda, and K. Oe, "Tunable optical-wavelength conversion using an optically triggerable multielectrode distributed feedback laser diode," *IEEE J. Quantum Electronics*, vol. QE-24, no. 11, pp. 2153-2159, 1988.

[16] A. Paradisi, and I. Montrosset, "Numerical modeling of bistable laser diodes with saturable absorbers," *IEEE J. Quantum Electronics*, vol. 27, no. 3, pp. 817-823, 1991.

[17] T. Odagawa, T. Machida, K. Tanaka, T. Sanada, and K. Wakao, "Fast optical flip-flop operations of bistable laser diodes," *Trans. IEICE*, vol. J74-C-I, pp. 465-479, 1991.
[18] H. Uenohara, Y. Kawamura, and H. Iwamura, "Long-wavelength multiple-quantum-well voltage-controlled bistable laser diodes," *IEEE J. Quantum Electronics*, vol. 31, no. 12, pp. 2142-2147, 1995.
[19] H. Uenohara, R. Takahashi, Y. Kawamura, and H. Iwamura, "Static and dynamic response of mutiple-quantum-well voltage-controlled bistable laser diodes," *IEEE J. Quantum Electronics*, vol. 32, no. 5, pp. 873-883, 1996.
[20] G. Bastard, E. E. Mendez, L. L. Chang, and L. Esaki, "Variational calculations on a quantum well in an electric field," *Phys. Rev. B*, vol. 28, pp. 3241-3245, 1983.

Chapter 4 DC Bistable Laser Diode

A novel all-optical flip-flop device using a directionally coupled bistable laser diode (DC-BLD) is proposed and demonstrated in this chapter. From the analyses using the TMM and FD-BPM models, we predict that the DC-BLD can be used for an all-optical flip-flop device under the condition of asymmetrical current injection to the directional coupler. The proposed DC-BLD is fabricated using the conventional fabrication procedure of LDs. To separate the electrode of the directional coupler, an oblique electron-beam evaporation technique is developed, and the electrodes of the directional coupler are electrically isolated without any lithography. By measuring the fabricated DC-BLD, we make sure the all-optical flip-flop operation by the nonlinear effect of the directional coupler with sufficiently small input optical power level around 0 dBm.

4.1 Introduction

A BLD based on saturable absorption has a simple two-section structure and easily gets a stable bistability as compared with other bistable devices based on dispersive bistability or pitchfork polarization bistability. Moreover, the absorptive BLD has inherent advantages such as optical gain, low optical switching power, a high on-off ratio and large fanout. These features were experimentally confirmed in Chapter 3.

In the basic configuration, the absorptive BLD biased close to it threshold can be switched on by injection of an optical set pulse, while a negative electric pulse has been used to turn off the laser. However, the lack of an optical switch-off (or reset) feature would undermine the device prospects because future optical systems are likely to employ all optical schemes.

Two physical effects have been used in the past to achieve the optical resetting. Inoue and One [1] exploited the frequency beating between an optical reset pulse and the mode of a free-running BLD. Another way to optically switch off a BLD is to use the gain quenching effect. A light pulse is injected into the device and is amplified by the gain medium, thus reducing the available gain for the BLD mode to a level low enough to annihilate a sustained oscillation. All-optical set-reset operation based on this effect was shown by the BLD

intracavity-coupled to a vertical-cavity surface-emitting laser (VCSEL) [2]. However, the problems have still remained that the demonstrated devices have needed precise wavelength tuning or a complicated fabrication process.

4.2 BLD with Nonlinear Directional Coupler

To overcome the problem to turn off the absorptive BLD by light injection, we decide to connect the BLD with some nonlinear coupler. The semiconductor materials such as InGaAsP/InP has large nonlinear effects, so we can easily introduce the nonlinear coupler to the semiconductor device.

There are so many types of nonlinear couplers such as directional coupler (DC), multimode interference (MMI) coupler, and Mach-Zehnder interference (MZI) coupler. The nonlinear directional coupler (NLDC), in particular, has been studied intensely because it has possibilities for all-optical devices such as switching, demultiplexing, wavelength converter and so on. The NLDC was firstly suggested and analyzed theoretically by Jensen [3] in 1982, and later demonstrated experimentally in a multiple quantum well (MQW) structure by Li Kam Wa et al [4]. The device has been investigated in many materials, for example, optical fibers [5]-[7], AlGaAs waveguides [8]-[11] and InGaAsP optical amplifiers. All-optical switching [12] and all-optical wavelength converter [13]-[17] were demonstrated by directionally coupled semiconductor optical amplifiers based on InGaAsP materials. Moreover, the possibilities of the NLDCs are expected to be extended by the asymmetrical configurations. The bistable devices and the optical logical devices are investigated using the asymmetrical NLDCs [18]-[20]. In the following sections, we investigated a novel BLD structure with the asymmetrical NLDC to realize the all-optical flip-flop device.

4.3 Proposal of DC-BLD

We propose all-optical flip-flop using a BLD with a directional coupler. A schematic view of the directionally-coupled bistable laser diode (DC-BLD) is shown in Fig.4.1. The DC-BLD is composed of a main cavity and a reset port connected with each other through a directional coupler. The main cavity shows S-shaped bistability due to a saturable absorber equipped at the end of the waveguide, so the DC-BLD has a same structure of a conventional BLD based on saturable absorption except for the reset port connected by the directional coupler. Because all waveguides are composed of active waveguides such as a MQW laser diode structure, the directional coupler has large nonlinear effects, for example, refractive index change and gain quenching.

The ON state of the proposed DC-BLD corresponds to the laser oscillation of the main cavity. In the OFF state of the DC-BLD, there is only spontaneous emission from the gain

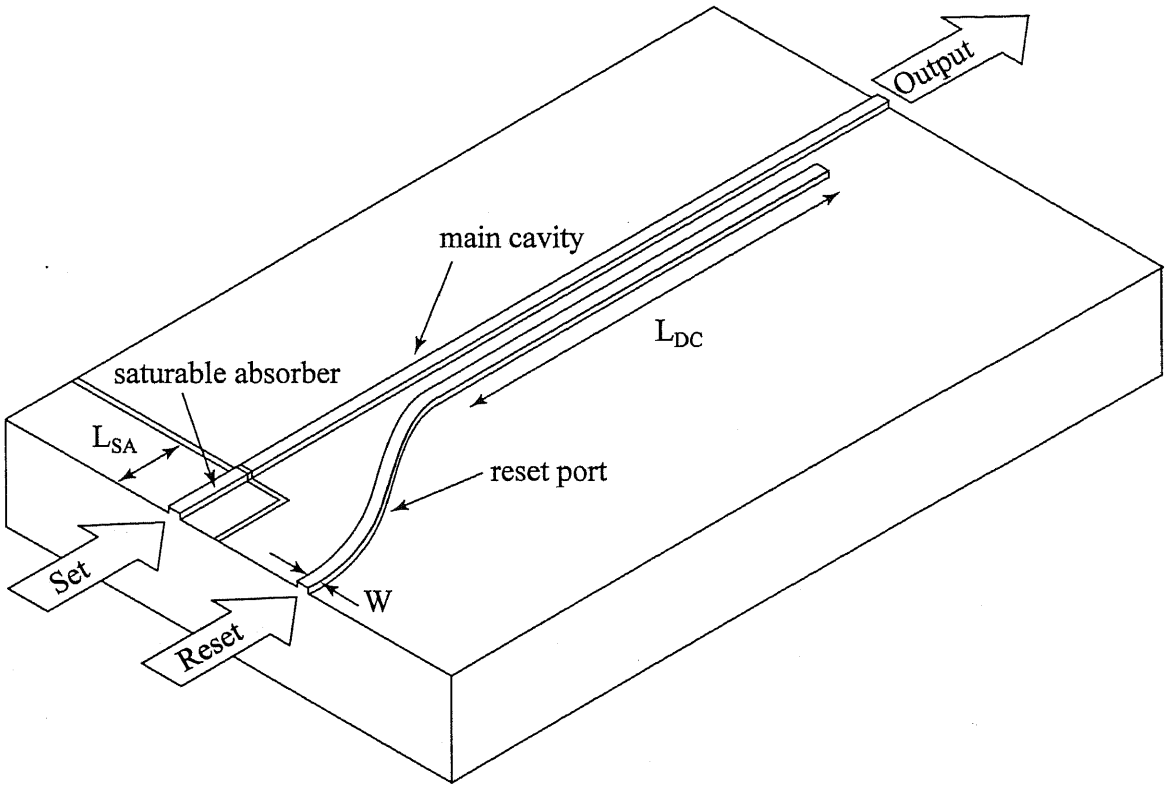

Fig.4.1 Schematic view of the DC-BLD, which is composed of a main cavity and a reset port connected with each other through a directional coupler. A saturable absorber is equipped at the end of the main cavity to get a hysteresis characteristic.

region. Because of the low light level, the spontaneous emission will be strongly absorbed by the saturable absorber section and there will be no laser action. When the optical set-signal is injected into the main cavity, the absorption of the saturable absorber becomes smaller, and the main cavity starts the laser radiation. In other words, the DC-BLD goes from the OFF state to the ON state. On the other hand, the external optical injection into the reset port terminates the laser oscillation due to momentary extraction of lasing light to the reset port by the nonlinear directional coupler. Even when the reset-signal is terminated, the recovered absorption of the saturable absorber prevent the main cavity from lasing again. In this way, the nonlinear directional coupler enable the BLD to be optically turn off, and we can realize an all-optical flip-flop using the DC-BLD.

4.4 Basic Properties of Directional Coupler

If two waveguides are sufficiently close such that their fields overlap, light can be coupled from one into the other. Optical power can be transferred between the waveguides, an effect that can be used to make optical couplers and switches. The basic properties of a directional coupler are presented in this section. Consider two parallel planar waveguides

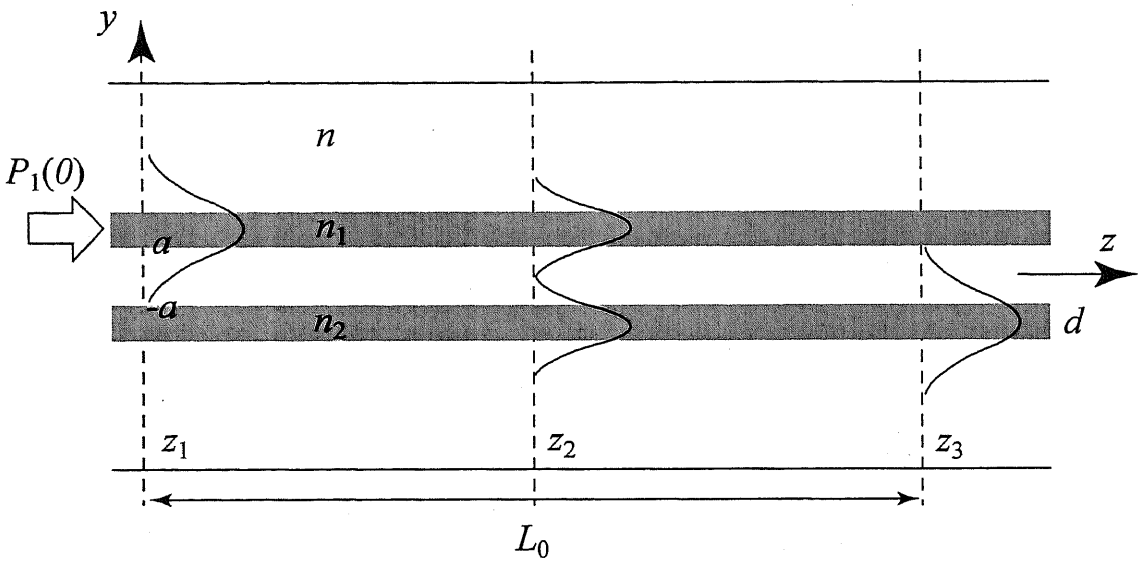

Fig.4.2 Coupling between two parallel planar waveguides. At z_1 light is mostly in waveguide1, at z_2 it is divided equally between the two waveguides, and at z_2 it is mostly in waveguide 2.

made of two slabs of width d, separation $2a$, and refractive indices n_1 and n_2 embedded in a medium of refractive index n slightly smaller than n_1 and n_2, as illustrate in Fig.4.2. Each of the waveguides is assumed to be single-mode. The separation between the waveguides is such that the optical field outside the slab of one waveguide (in the absence of the other) overlaps slightly with the slab of the other waveguide.

The formal approach to studying the propagation of light in this structure is to write Maxwell's equations in the different regions and use the boundary conditions to determine the modes of the overall system. These modes are different from those of each of the waveguides in isolation. An exact analysis is difficult and is beyond the scope of this paper. However, for weak coupling, a simplified approximate theory, known as coupled-mode theory, is usually satisfactory.

The coupled-mode theory assumes that the modes of each of the waveguides, in the absence of the other, remain approximately the same, say $E_1(y)\exp(-j\beta_1 z)$ and $E_2(y)\exp(-j\beta_2 z)$, and that coupling modifies the amplitudes of theses modes without affecting their transverse spatial distributions or their propagation constants, where E_1 and E_2 are the normalized lateral optical fields inside each waveguide, β_1 and β_2 are the propagation constants of each mode. The amplitudes of the modes of waveguides 1 and 2 are therefore functions of z, $A_1(z)$ and $A_2(z)$. The theory aims at determining $A_1(z)$ and $A_2(z)$ under appropriate boundary conditions.

Coupling can be regarded as a scattering effect. The field of waveguide 1 is scattered from waveguide 2, creating a source of light that changes the amplitude of the field in waveguide 2. The field of waveguide 2 has a similar effect on waveguide 1. An analysis of this mutual interaction leads to two coupled differential equations that govern the variation of the amplitudes $A_1(z)$ and $A_2(z)$.

It can be shown that the amplitudes $A_1(z)$ and $A_2(z)$ are governed by two coupled first-order differential equations (Coupled-mode equations, see Appendix A.)

$$\begin{aligned} \frac{dA_1}{dz} &= -j\kappa_{12} exp(j\Delta\beta z) A_2(z) \\ \frac{dA_2}{dz} &= -j\kappa_{21} exp(-j\Delta\beta z) A_1(z) \end{aligned} \tag{4.1}$$

where

$$\Delta\beta = \beta_1 - \beta_2 \tag{4.2}$$

is the phase mismatch per unit length and

$$\begin{aligned} \kappa_{12} &= \frac{1}{2}(n_2^2 - n^2)\frac{k_0^2}{\beta_1}\int_a^{a+d} E_1(y)E_2(y)dy \\ \kappa_{21} &= \frac{1}{2}(n_1^2 - n^2)\frac{k_0^2}{\beta_2}\int_{-a-d}^{-a} E_2(y)E_1(y)dy \end{aligned} \tag{4.3}$$

are coupling coefficients.

We see from (4.1), that the rate of variation of $A_1(z)$ is proportional to $A_2(z)$, and vice versa. The coefficient of proportionality is the product of the coupling coefficient and the phase mismatch factor $\exp(j\Delta\beta z)$.

Assuming that the amplitude of light entering waveguide 1 is $A_1(0)$ and that no light enters waveguide 2, $A_2(0) = 0$, then (4.1) can be solved under these boundary conditions, yielding the harmonic solution

$$\begin{aligned} A_1(z) &= A_1(0) exp\left(j\frac{\Delta\beta z}{2}\right)\left(cos\gamma z - j\frac{\Delta\beta}{2\gamma} sin\gamma z\right) \\ A_2(z) &= A_1(0)\frac{\kappa_{12}}{j\gamma} exp\left(-j\frac{\Delta\beta z}{2}\right) sin\gamma z \end{aligned} \tag{4.4}$$

where

$$\gamma^2 = \left(\frac{\Delta\beta}{2}\right)^2 + \kappa^2 \tag{4.5}$$

and

$$\kappa = (\kappa_{12}\kappa_{21})^{1/2}. \tag{4.6}$$

The optical power $P_1(z) \propto |A_1(z)|^2$ and $P_2(z) \propto |A_2(z)|^2$ are therefore

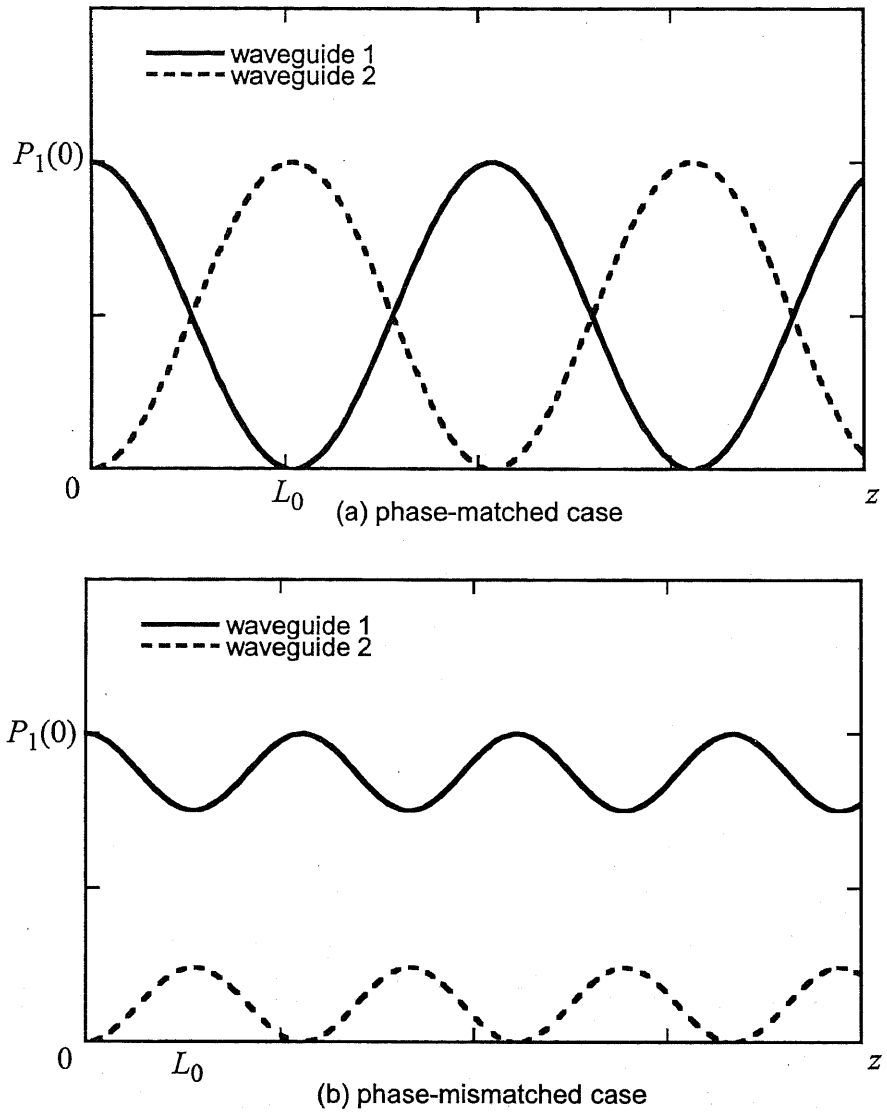

Fig.4.3 Exchange of power between waveguide 1 and waveguide 2 in (a) phase-matched case, and (b) phase-mismatched case. The optical power $P_1(0)$ is injected to waveguide-1.

$$P_1(z) = P_1(0)\left[\cos^2\gamma z + \left(\frac{\Delta\beta}{2\gamma}\right)^2 \sin^2\gamma z\right]$$

$$P_2(z) = P_1(0)\frac{|\kappa_{12}|^2}{\gamma^2}\sin^2\gamma z \qquad (4.7)$$

Thus power is exchanged periodically between the two guides. The period is $2\pi/\gamma$. Power conservation requires that $\kappa_{12} = \kappa_{21}$.

When the waveguides are identical, i.e., $n_1 = n_2$, $\beta_1 = \beta_2$,and $\Delta\beta = 0$, the two guided waves are said to be phase matched. Equations (4.7) then simplify to

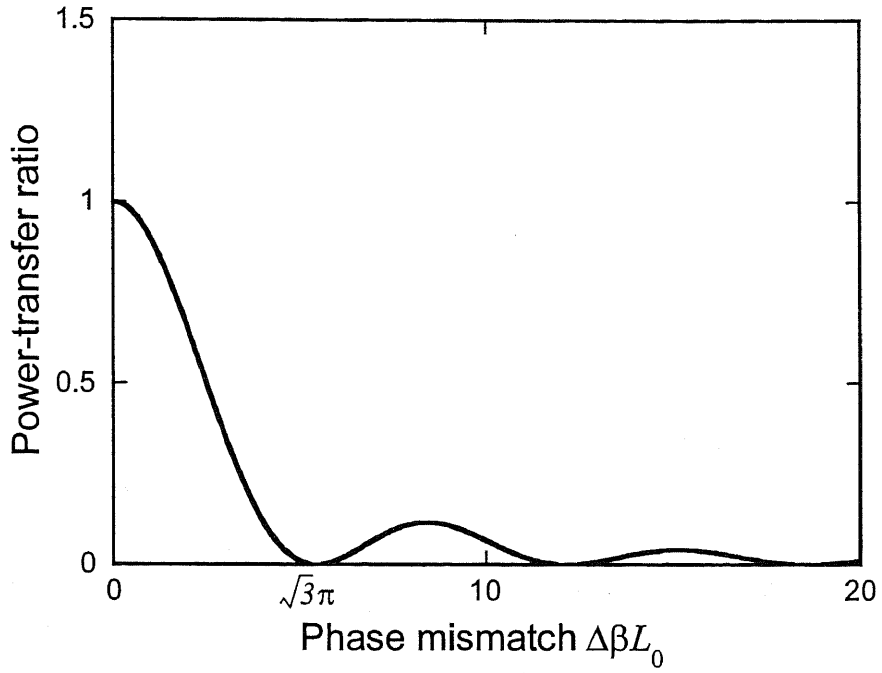

Fig.4.4 Dependence of the power transfer ratio $\Im = P_2(L_0)/P_1(0)$ on the phase mismatch parameter $\Delta\beta L_0$. The waveguide length is chosen such that for $\Delta\beta = 0$ (the phase-matched case), maximum power is transferred to waveguide 2, i.e., $\Im = 1$.

$$P_1(z) = P_1(0)\cos^2\kappa z$$
$$P_2(z) = P_1(0)\sin^2\kappa z \qquad (4.8)$$

The exchange of power between the waveguides can then be complete, as illustrated in Fig.4.3 (a). At a distance $z = L_0 = \pi/2\kappa$, called the coupling length, the power is transferred completely from waveguide 1 to waveguide 2. The power exchange in the phase-mismatched case is also shown in Fig.4.3 (b). The input power is not transferred completely from waveguide 1 to waveguide 2 in the phase-mismatched case. It is important property that the coupler length $L_0 = \pi/2\gamma$ is shorter than the phase-matched case.

A waveguide coupler of fixed length, $L_0 = \pi/2\kappa$, for example, changes its power-transfer ratio if a small phase mismatch $\Delta\beta$ is introduced. Using (4.7) and (4.5), the power-transfer ratio $\Im = P_2(L_0)/P_1(0)$ may be written as a function of $\Delta\beta$,

$$\Im = \left(\frac{\pi}{2}\right)^2 sinc\left\{\frac{1}{2}\left[1+\left(\frac{\Delta\beta L_0}{\pi}\right)^2\right]^{1/2}\right\} \qquad (4.9)$$

where $\mathrm{sinc}(x) = \sin(\pi x)/(\pi x)$. Fig.4.4 illustrates the dependence of the power-transfer ratio $\Im$ on the mismatch parameter $\Delta\beta L_0$. The ratio has a maximum value of unity at $\Delta\beta L_0 = 0$, decrease with increase $\Delta\beta L_0$, and then vanishes when $\Delta\beta L_0 = \sqrt{3}\pi$. The dependence of

the transferred power on the phase mismatch have been utilized in making all-optical devices such as switches [12], and wavelength converters [16].

4.5 Design of Directional Coupler

In the previous section, we mentioned the basic properties of a directional coupler. The coupling characteristics can be controlled by changing the refractive index of one waveguide. We use this effect to realize the DC-BLD. In this section, the design of the DC-BLD, mainly the directional coupler section is described.

The coupling length L_0 is affected by the waveguide parameters such as refractive indices of core and clad, ridge width, and gap between coupled waveguides. The refractive index of the clad is not changed so much because the ridge height is usually fixed at around 1.0 μm. Therefore, we consider the clad index is the constant value, 3.24. The refractive index of core is decreased as increasing the carrier density in the active layer, as mentioned in Equation (2.8). In the case of the material parameters listed in Table.2.1, the core index at the lasing state is around 3.25 - 3.255. In this cae, the coupling lengths versus the gaps and the ridge widths can be calculated using $L_0 = \pi/2\kappa$, as shown in Fig.4.5. By decreasing the gap, the coupling lengths gradually decrease because the modal overlap between the coupled waveguides becomes large. We can see same tendency in the case of the ridge width. The fabrication tolerance of the directional coupler is large when the gap and ridge width is small, because the directional coupler with small gap is close to a zero-gap directional coupler, i.e., a MMI coupler. The core index dependences on the coupler length are also calculated for the convenience of designing directional couplers (see Appendix B.).

For the DC-BLD, the directional coupler is designed to be the one coupling length. The width of the ridge waveguide is usually around 2.0 μm to satisfy the single-mode operation, so the coupling length is decided to be around 1000 μm from Fig.4.5 (a), when the core index is 3.25 and the gap is 3 μm.

These parameters that the gap and the ridge width are 3.0 μm and 2.0 μm are proper values to fabricate the directional coupler actually, so we adopt these values for the analyses by Transfer Matrix Method, mentioned in the next section.

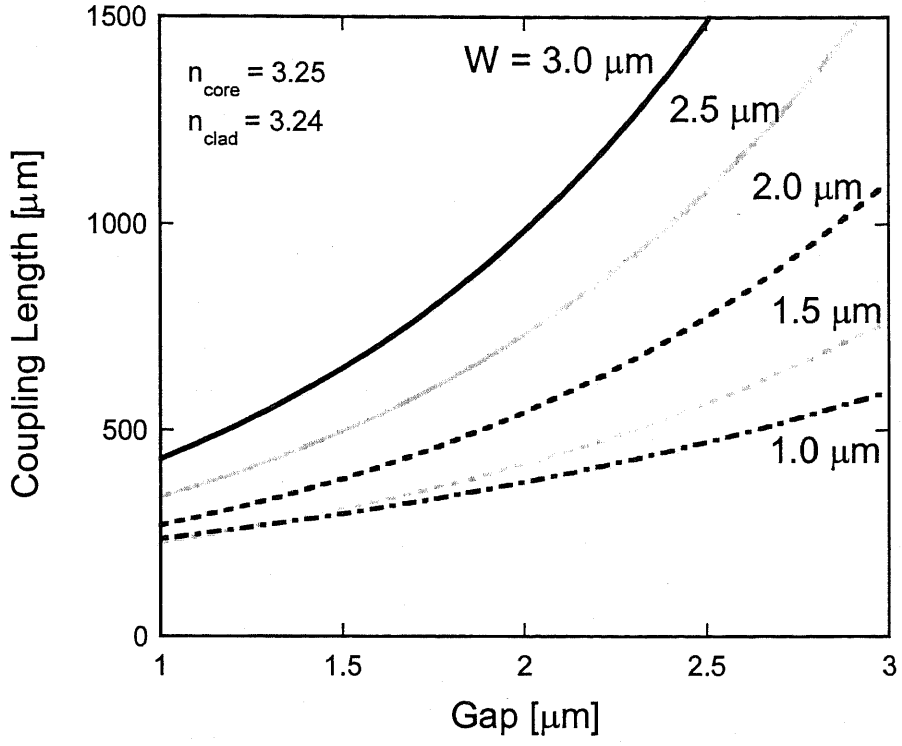

(a) Refractive index of core = 3.25

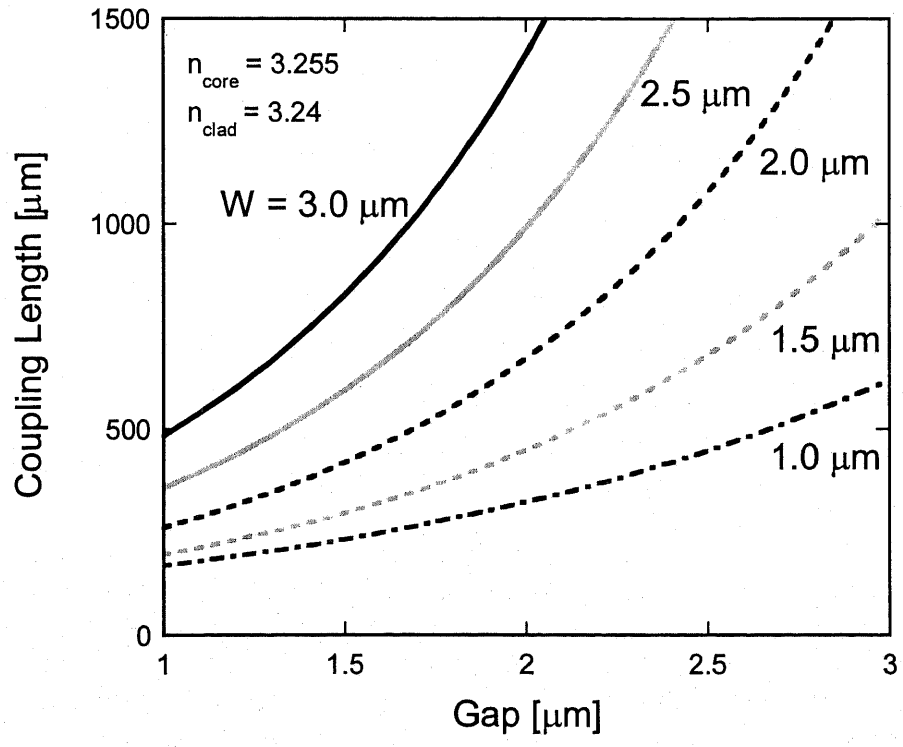

(b) Refractive index of core = 3.255

Fig.4.5 Coupling length of directional coupler versus gap between the coupled waveguides in the case that (a) $n_{core} = 3.25$, (b) $n_{core} = 3.255$.

4.6 Bistability Analysis by TMM

In this section, we analyzed the static bistable characteristics of the DC-BLD using the Transfer Matrix Method developed in Section 2.2. The schematic view of the proposed DC-BLD was illustrated in Fig.4.1. The design of the directional coupler section was described in the previous section, that the ridge width was 2 μm, the gap between the coupled waveguides was 3.0 μm, and the length of the directional coupler was one coupling length, 1000 μm. The input and output ports length were assumed to be 200 μm. Therefore, the total length of the DC-BLD was around 1400 μm. The waveguides were assumed to be made from InGaAsP material active waveguides, whose bandgap was around 1.55 μm. The material parameters used in the following analyses were listed in Table.2.1.

In the TMM, the waveguides are divided longitudinally into a number of small sections. We assumed that the length of each section was 50 μm. Therefore, the DC-BLD cavity was divided to 28 sections in this case.

A. Hysteresis characteristics

First, we analyzed the L-I characteristic of the main cavity. Fig.4.6 shows bistable behavior of the DC-BLD with the saturable absorber, 0, 100, 200 μm, in the case of pumping only the main cavity. The lasing wavelength was assumed to be 1.55 μm. Because the reset port is not pumped, the coupling coefficients of the directional coupler is almost zero. Therefore, the main cavity behaves as like as the single waveguide LD. Due to the saturable absorber equipped with the edge of the main cavity, a bistable loop occurs in the characteristics of the main cavity. As increasing the length of the saturable absorber, the hysteresis width and the threshold current increased. To obtain stable hysteresis, the saturable absorber length should be around 10 % of the total device length (see Section 3.3). Therefore, the length of saturable absorber was set to be 200 μm. The saturable absorber section was homogeneously pumped by injection current density, 0.1 kA/cm^2 in following analyses. In this case, the ON current and OFF current were 3.5 kA/cm^2, and 3.2 kA/cm^2, respectively. The injection current of the main cavity should be within the hysteresis loop for all-optical flip-flop operation, so we adopted 3.3 kA/cm^2 to 3.4 kA/cm^2 as the bias current. The width of this bias condition corresponded to around 2.4 mA. Under this bias condition, the refractive index of core determined by the current density in the active layer was around 3.250, so the directional coupler had one coupling length (if symmetrical configuration, i.e., the two waveguides had same indices, 3.250) as designed in Section 4.5.

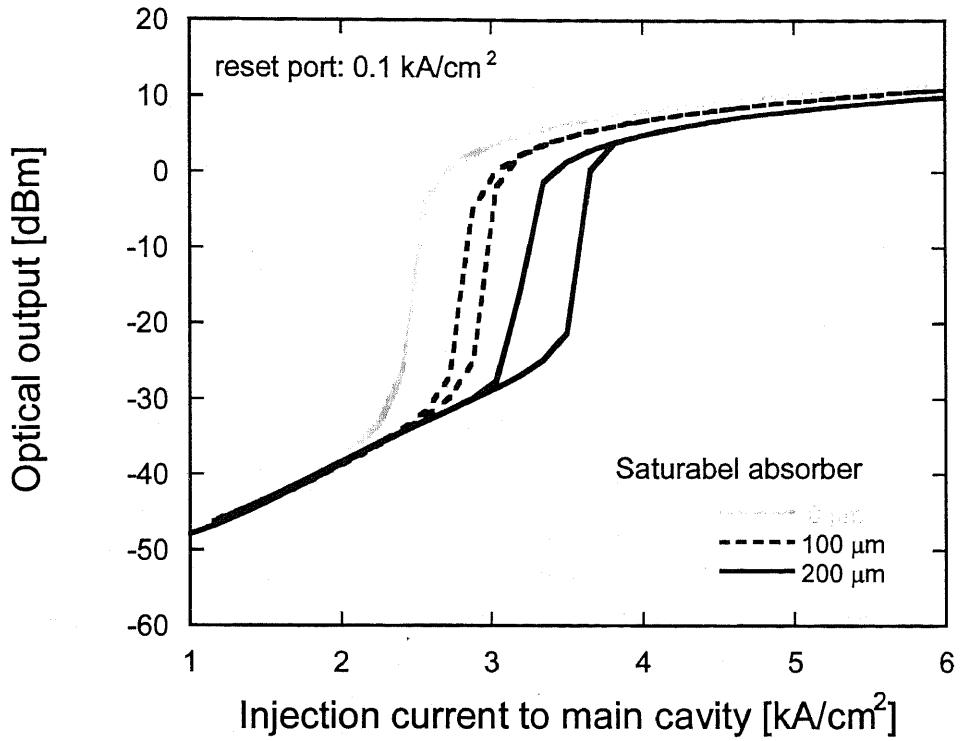

Fig.4.6 Bistable behavior of the proposed DC-BLD with the saturable absorber, 0, 100, 200 μm, biased 0.1 kA/cm^2. The injection current density of the reset port was fixed as 0.1 kA/cm^2.

B. Optical turn-on characteristics

Fig.4.7 shows optical turn-on operation of the DC-BLD. As like the hysteresis analyses, the reset port was biased at 0.1 kA/cm^2. Therefore, the only main cavity was considered. The set signal was injected to the main cavity. The wavelength of the set signal was assumed to be 1.55 μm, which was same as the lasing wavelength. When the optical set-signal was injected, the saturable absorber had smaller optical loss, then the main cavity biased inside the hysteresis loop started lasing. This turn-on phenomenon is well-known through the previous researches. The DC-BLD was transferred to the ON state at -20 dBm to -10 dBm optical injection, and it kept the ON state after the optical injection was eliminated. The optical power for the optical turn-on decreased, when the bias current of the main cavity was increased. The reason is that the difference between the bias current and the ON current became small. The output power at the ON state also increased from -3 dBm to 0 dBm, as increasing the bias current. If the high output power is desired, the bias current should be near to the ON current for the normal BLDs (The same thing is not applied for the DC-BLD, see Section 4.6 D.).

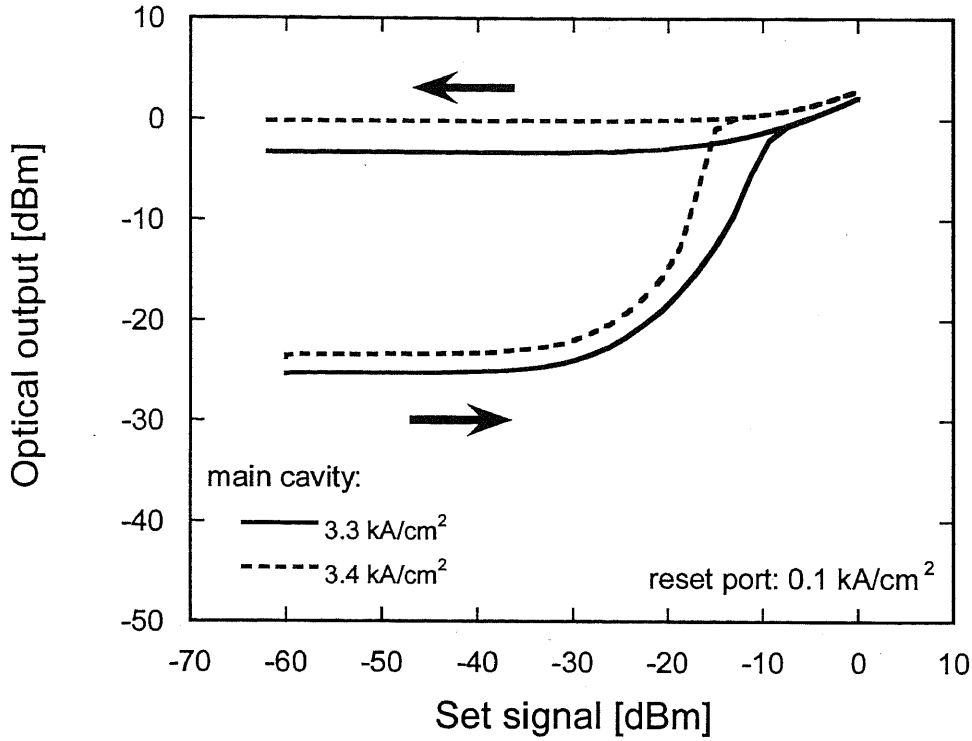

Fig.4.7 Optical turn-on operation of the DC-BLD by injecting the set-signal into the main cavity. The reset port was biased at 0.1 kA/cm^2. The length of saturable absorber was 200 μm. As increasing the bias current of the main cavity, the power for turn-on decreased.

C. Electrical-off characteristics

For the all-optical flip-flop operation using the DC-BLD, the bias current of the reset port is important. To obtain the bias condition of the reset port, the phenomena of the DC-BLD was analyzed in the case of injecting the current to the reset port. If no current is injected to the reset port, the coupling coefficient is small, and the optical power doesn't exchange between the adjacent waveguides. If the current to the reset port is increased, the difference of the current densities (simultaneously, the refractive indices) between the two coupled waveguides decreases, and the coupling coefficient increases. Therefore, the coupling coefficient can be controlled by the current to the reset port. The coupling coefficient of the directional coupler affects the characteristic of the main cavity. The increase of the coupling coefficient extracts the lasing light from the main cavity to the reset port, so the electrical turn-off operation can be realized. Fig.4.8 shows the electrical turn-off operation of the DC-BLD by increasing the current to the reset port. The injection current density of the main cavity was fixed to be 3.3 kA/cm^2 (solid line) and 3.4 kA/cm^2 (broken line), and the DC-BLD was set to the ON state by the set-pulse at the beginning of the calculation. Increasing the current density of the reset port, the intensity of the main cavity rapidly decreased, and the

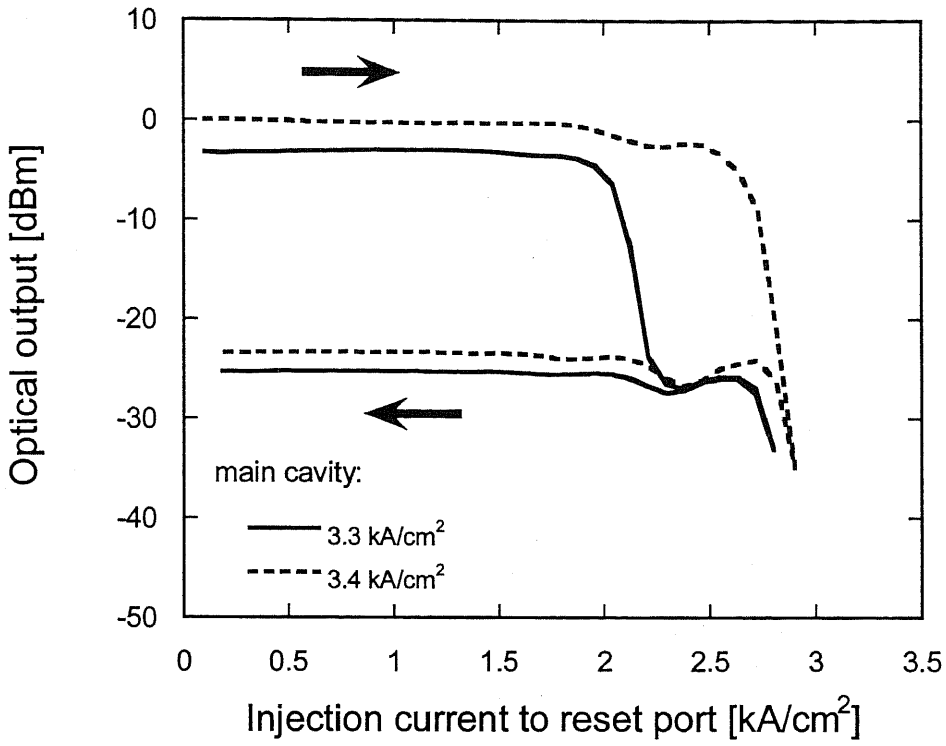

Fig.4.8 Electrical turn-off operations of the DC-BLD by the current to the reset port. The bias condition of the main cavity was 3.3 kA/cm^2 (solid line) and 3.4 kA/cm^2 (broken line). The bias currents of the reset port can be determined from this results.

laser radiation stopped for the reason of the coupling coefficient increase. The turn-off currents were 2.0 kA/cm^2 (solid line) and 2.7 kA/cm^2 (broken line). The change of the turn-off currents was around 12 mA by the change of the bias current of the main cavity, 2.4 mA. Therefore, it is very important to keep the current of the main cavity constant for the stable operation. From Fig.4.8, the bias conditions of the reset port for all-optical flip-flop operation were decided as 1.9 kA/cm^2 and 2.6 kA/cm^2 respectively, which were slightly smaller than the current density that terminated the laser radiation. Instead of the current, the light signal injected to the reset port will produce the photo-carriers inside the reset port and turn the DC-BLD off. In this way, we can determine the bias conditions of the main cavity and the reset port to get the all-optical flip-flop operation.

D. All-optical flip-flop characteristics

In the previous sections, we mentioned how to determine the bias currents of the main cavity and reset port to obtain the all-optical flip-flop operation. Using this conditions, the all-optical flip-flop characteristics were calculated as shown in Fig.4.9. The main cavity and the reset port was biased at (main, reset) = (3.3 kA/cm^2, 1.9 kA/cm^2) and (3.4 kA/cm^2, 2.6 kA/cm^2), respectively. The set signal and the reset signal were assumed to be 1.55 μm, CW

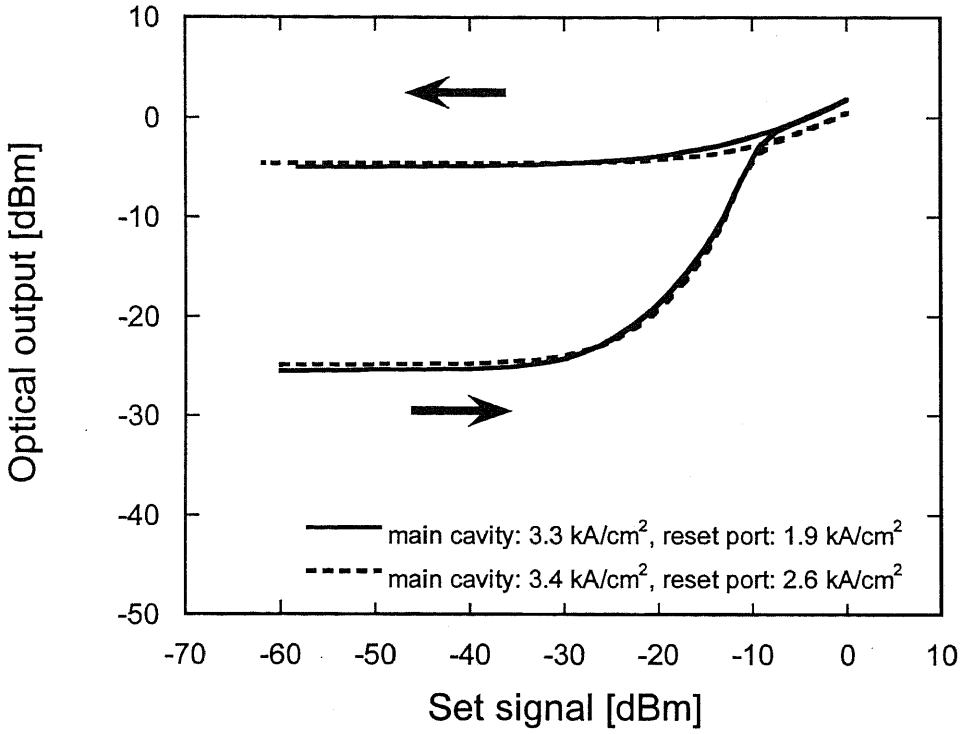

(a) Optical turn-on characteristics

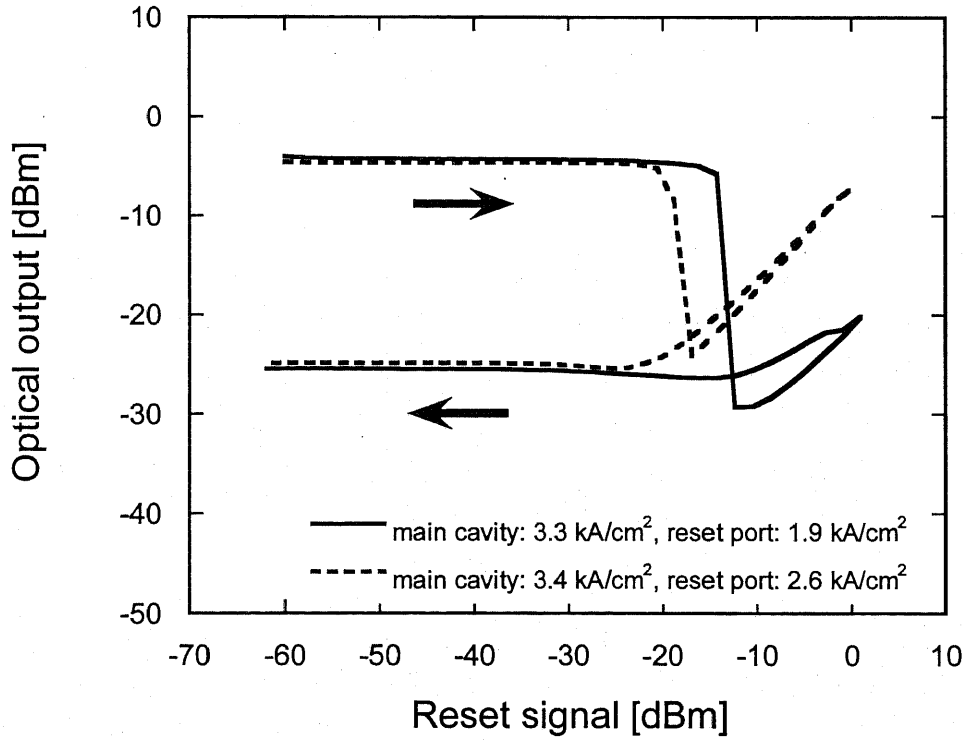

(b) Optical turn-off characteristics

Fig.4.9 All-optical flip-flop characteristics of the DC-BLD, (a) optical turn-on characteristics and (b) optical turn-off characteristics. The bias conditions were (main, reset) = (3.3, 1.9) and (3.4, 2.6) kA/cm^2, respectively.

light. The optical turn-on characteristics should be re-calculated because the bias condition of the reset port was different from that mentioned in Section 4.6 B. The current of the reset port was increased to more than 1.9 kA/cm^2 in this section. The optical turn-on characteristics were shown in Fig.4.9 (a). The turn-on powers were around -10 dBm in both bias conditions. These characteristics of both bias conditions were almost same in spite of the different bias currents (cf. Fig.4.7). Both output power at the ON state were degraded to - 5 dBm, because the part of the lasing light leaked to the reset port.

Fig.4.9 (b) shows the optical turn-off operation of the DC-BLD by injecting the optical reset signal to the reset port. The situation was same as the case of the electrical turn-off operation at the beginning of the calculation. The reset signal was increased instead of the current density. Like the current injection, the photo-generated carriers enlarged the coupling of the directional coupler. The output light emitted from the main cavity decreased by -20 dBm to -10 dBm reset-signal. In the optical turn-off operation, not only increase of coupling the directional coupler but also the gain saturation is contributed to switch the DC-BLD off. After the rapid decay, the output power increased again as increasing the reset signal, that were the amplified reset signals.

The optical powers for the set and reset operations were also calculated. Fig.4.10 (a) shows the optical powers in the case that the main cavity biased at 3.3 kA/cm^2, and Fig.4.10 (b) shows the case of 3.4 kA/cm^2. The all-optical flip-flop operation was achieved at the 0.4 kA/cm^2 range of the reset port current. The 0.4 kA/cm^2 was equivalent to 9.6 mA, so the tolerance of the reset port current was large enough to control. In both the cases, the turn-on power was under -10 dBm and almost independent on the bias currents. On the other hand, the turn-off power was gradually decreased from 10 dBm to 0 dBm by the reset port current. Therefore, the bias current of the reset port is as large as possible to reduce the reset power. The turn-off power was not same as the power that stopped the laser radiation, -20 dBm to -10 dBm in Fig.4.9 (b), because the coupling coefficient change was not large enough at these levels.

In this way, the basic properties of the DC-BLD were analyzed by the TMM model. We confirmed that the nonlinear directional coupler enabled the absorptive BLD to be turn off by the light injection, and the DC-BLD were useful for the all-optical flip-flop devices.

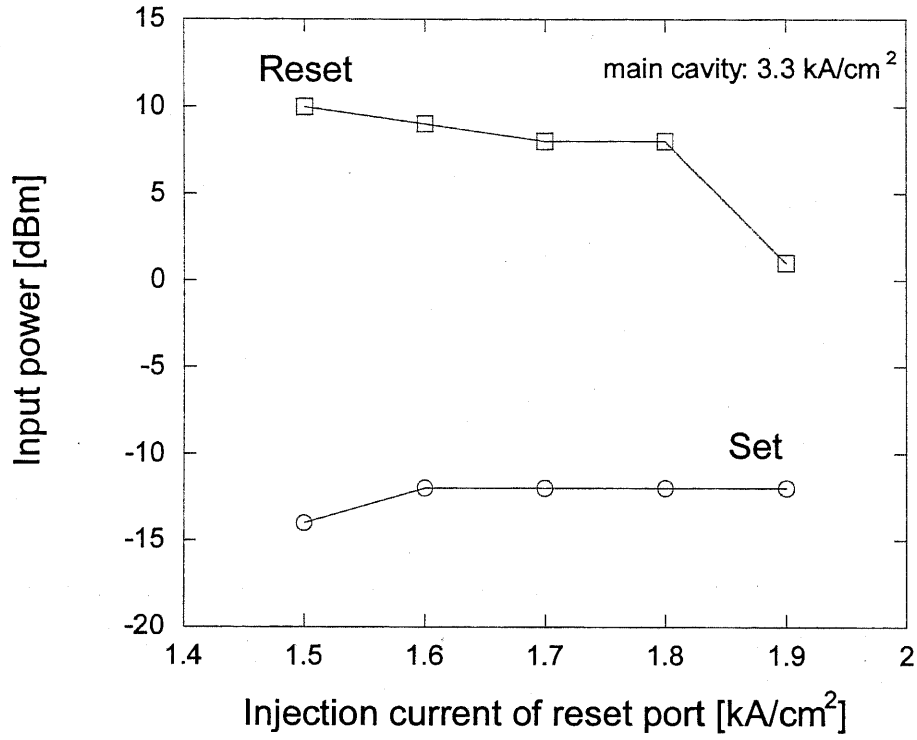

(a) main cavity: 3.3 kA/cm^2

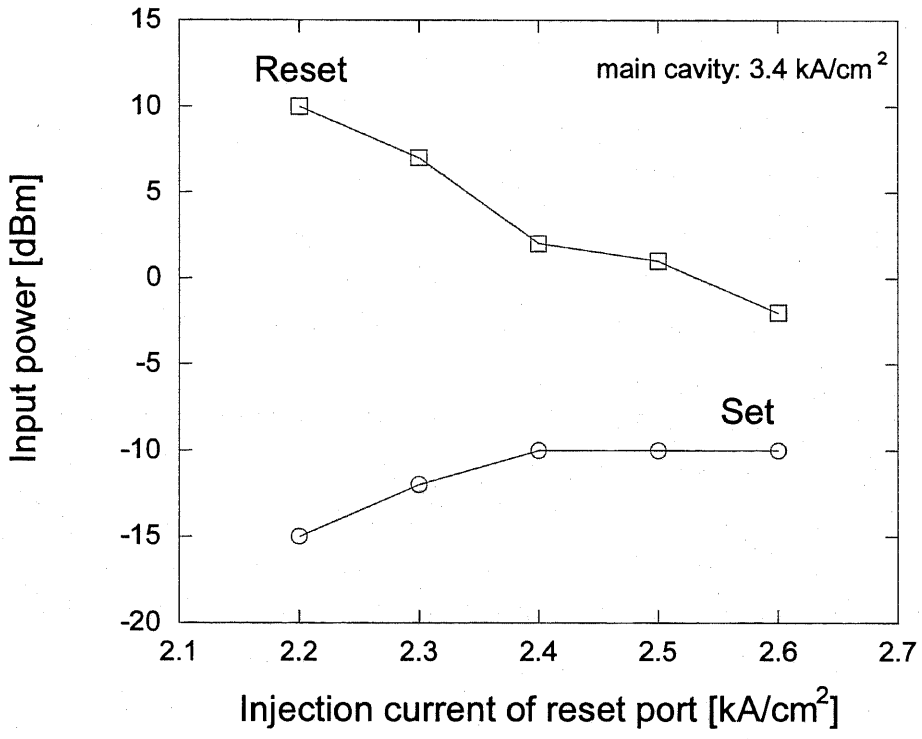

(b) main cavity: 3.4 kA/cm^2

Fig.4.10 Optical powers for the set and reset operations. The all-optical flip-flop operation was obtained at the 0.4 kA/cm^2 range of the reset port current. The turn-on power was less than -10 dBm, and the turn-off power was gradually decreased from 10 dBm to 0 dBm, as increasing the reset port current.

4.7 Bistability Analysis by FD-BPM

We also analyzed the static bistable characteristics of the DC-BLD by the developed finite difference beam propagation method (FD-BPM). In the case of the TMM, some approximations were needed to treat the DC-BLD precisely. However, the asymmetrical directional coupler based on SOAs shows very complicated phenomena, so we should confirm whether the approximations of the TMM is right. On the other hand, using the FD-BPM, we can more easily analyze the precise distribution of photon densities, carrier densities, optical gain, refractive index inside the cavity and the complicated phenomena of the asymmetrical nonlinear coupler. From this reason, we confirmed the results obtained by the TMM, using the FD-BPM analyses.

In the FD-BPM analyses, the refractive index at the lasing state was calculated to be around 3.255 (cf. 3.250 in the TMM analyses). If the gap between the coupled waveguides are set to 3 μm, the coupling length is estimated to be more than 1500 μm from Fig.4.5 (b). To shorten the coupling length, the gap should be smaller than the TMM case. In the following analyses, the gap was designed to be 2 μm. In this case, the one coupling length L_{DC} was 725 μm and the ridge width W was 2 μm. The length of the saturable absorber was 50 μm, that was around 10 % of the total length. An InGaAsP waveguide structure whose band gap energy was around 1.55 μm was studied here. The parameters used in this simulation are shown in Table.2.1.

The calculation region of the FD-BPM was 1000 μm × 20 μm, that was divided into a number of 0.3 μm × 0.1 μm blocks. The FD-BPM model can not treat the spontaneous emissions, so -60 dBm lights were injected to the waveguides instead of the spontaneous emissions.

A. Hysteresis characteristic

As like the TMM case, we firstly calculated the L-I characteristic of the DC-BLD. Fig.4.11 shows the bistable behavior of the DC-BLD in the case of pumping only the main cavity. Because of the saturable absorber, the hysteresis occurred in the characteristic of the main cavity. The output power at the OFF state was around -60 dBm, because the -60 dBm lights were injected instead of the spontaneous emissions. The injection current of the main cavity should be within the hysteresis loop for the all-optical flip-flop operation, so we adopted 2.15 kA/cm^2 as the bias current. The threshold current was smaller than the TMM case, because the internal loss was assumed to be 0 cm^{-1} in the FD-BPM model.

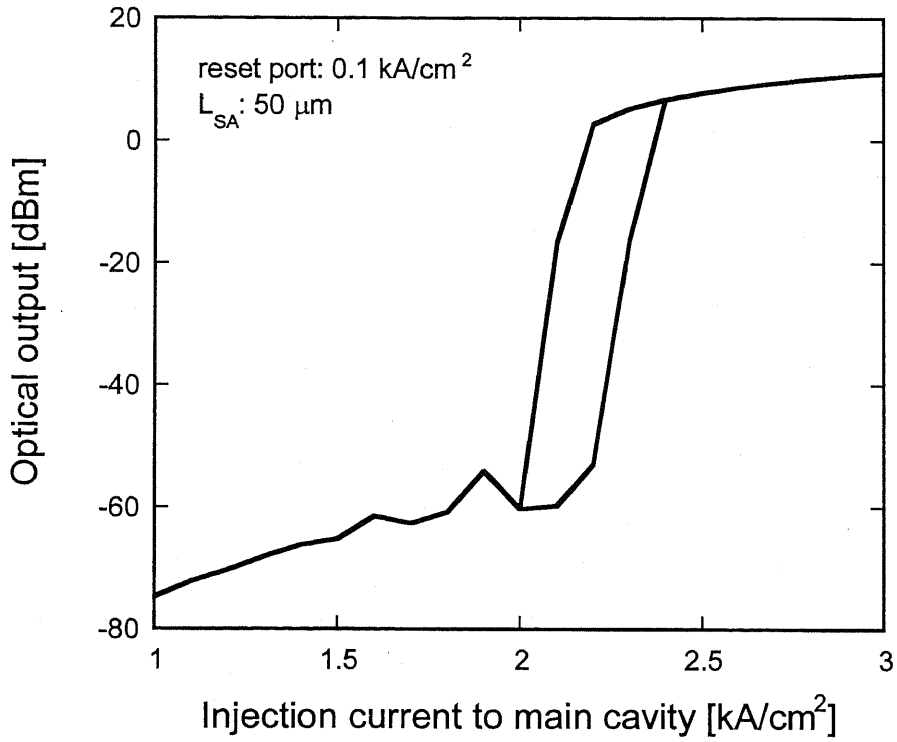

Fig.4.11 Bistable behavior of the proposed DC-BLD with the saturable absorber, 50 μm, biased 0.1 kA/cm^2. The injection current density of the reset port was fixed as 0.1 kA/cm^2.

B. Optical turn-on characteristic

The light injected to the main cavity can switch the DC-BLD on. Fig.4.12 shows the optical turn-on operation of the DC-BLD. The set signal was injected to the main cavity, that was assumed to be 1.55 μm CW light. The reset port was biased at 0.1 kA/cm^2, so the coupling of the directional coupler could be neglected. Due to the saturated absorption, the main cavity under 2.15 kA/cm^2 bias condition started lasing by the set-signal above -10 dBm. The output power after lasing had some fluctuations because the convergence time of the simulation was not long enough.

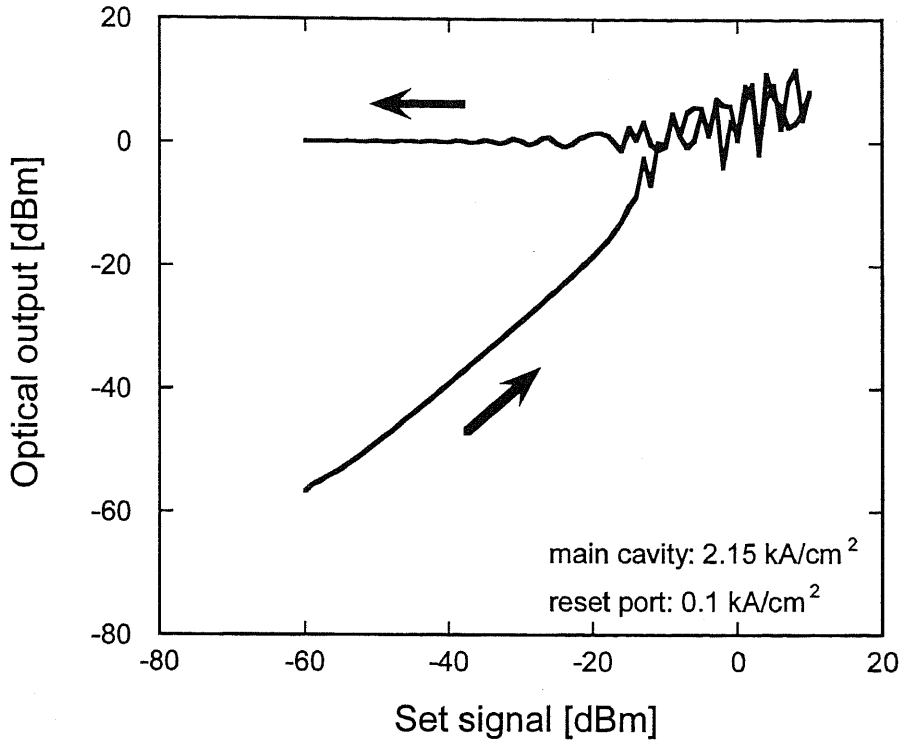

Fig.4.12 Optical turn-on operation of the DC-BLD by injecting the set-signal into the main cavity. The reset port was biased at 0.1 kA/cm^2. The length of saturable absorber was 50 μm.

C. Electrical turn-off characteristic

The coupling coefficient of the directional coupler can be controlled by the current to the reset port, and this effect was used for the electrical turn-off operation as shown in Fig.4.8. We could confirmed the same results using the FD-BPM. Fig.4.13 shows the turn-off operation of the DC-BLD by the current injection to the reset port. The injection current density of the main cavity was fixed at 2.15 kA/cm^2 and the DC-BLD was set to the ON state at the beginning of the calculation. Increasing the current density of the reset port, the output power from the main cavity rapidly decreased above 1.0 kA/cm^2 and the laser radiation stopped for the reason of the coupling coefficient increase. We already know how to decide the bias current of the reset port to obtain the all-optical flip-flop operation. From Fig.4.13, the bias condition of the reset port for all-optical flip-flop operation was decided as 0.8 kA/cm^2 which is slightly smaller than the current density that terminated the laser radiation. In the same way as the TMM case, we could decide the bias current of the main cavity and the reset port.

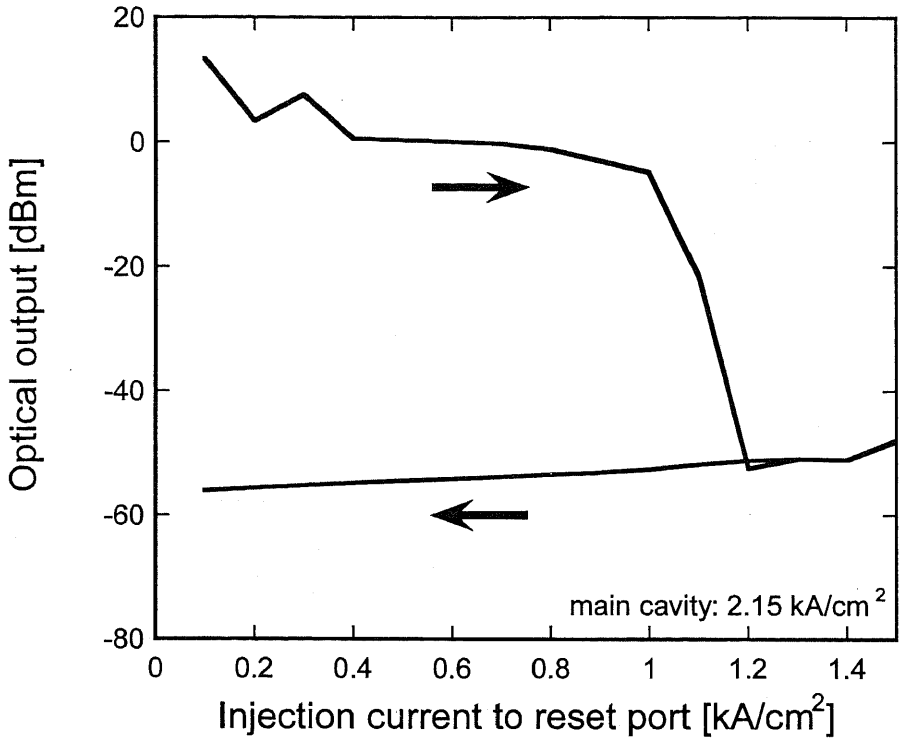

Fig.4.13 Electrical turn-off operations of the DC-BLD by the current to the reset port. The bias condition of the main cavity was 2.15 kA/cm^2. The bias currents of the reset port can be determined from this results.

D. All-optical flip-flop characteristic

At the bias condition mentioned above, the optical reset can be realized. The set signal and the reset signal was assumed to be 1.55 μm, CW light. The optical set operation is shown in Fig.4.14 (a). The set signal around -10 dBm turn the DC-BLD on.

Fig.4.14 shows the turn-off operation of the DC-BLD by the optical reset signal injected into the reset port. The intensity of the reset-signal was increased instead of the current. The output intensity of the main cavity decreased by 0 dBm reset-signal because the photo-generated carrier enlarged the coupling coefficient of the directional coupler like the injection current. After eliminating the reset-signal, the recovered absorption of the saturable absorber prevented the DC-BLD from lasing again.

In this way, we could confirm the results from the TMM model. The all-optical flip-flop operation was also predicted by the FD-BPM model.

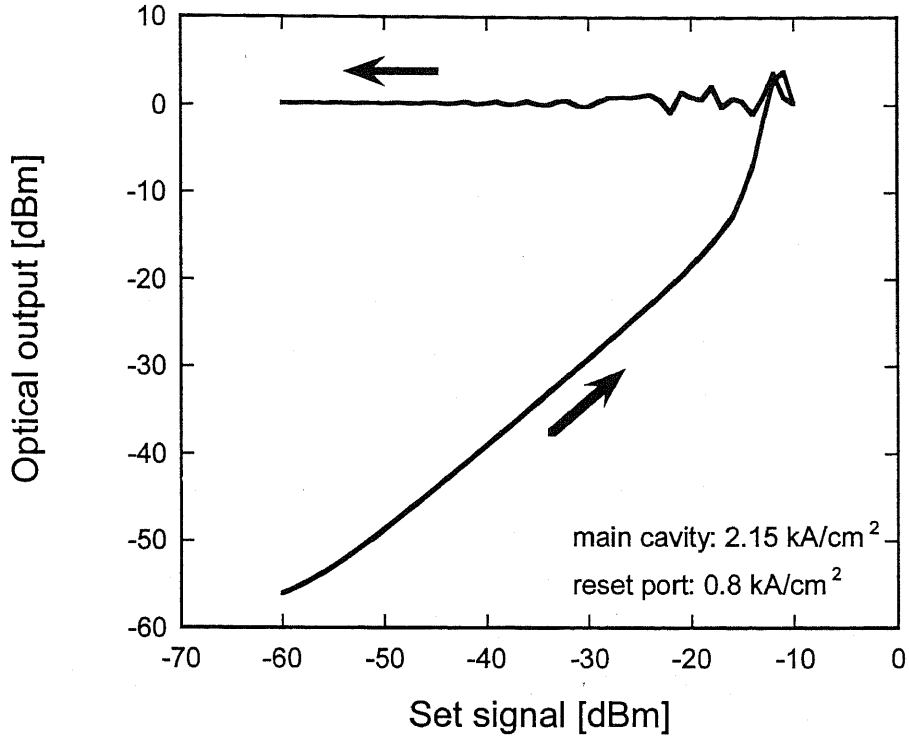

(a) Optical turn-on characteristic

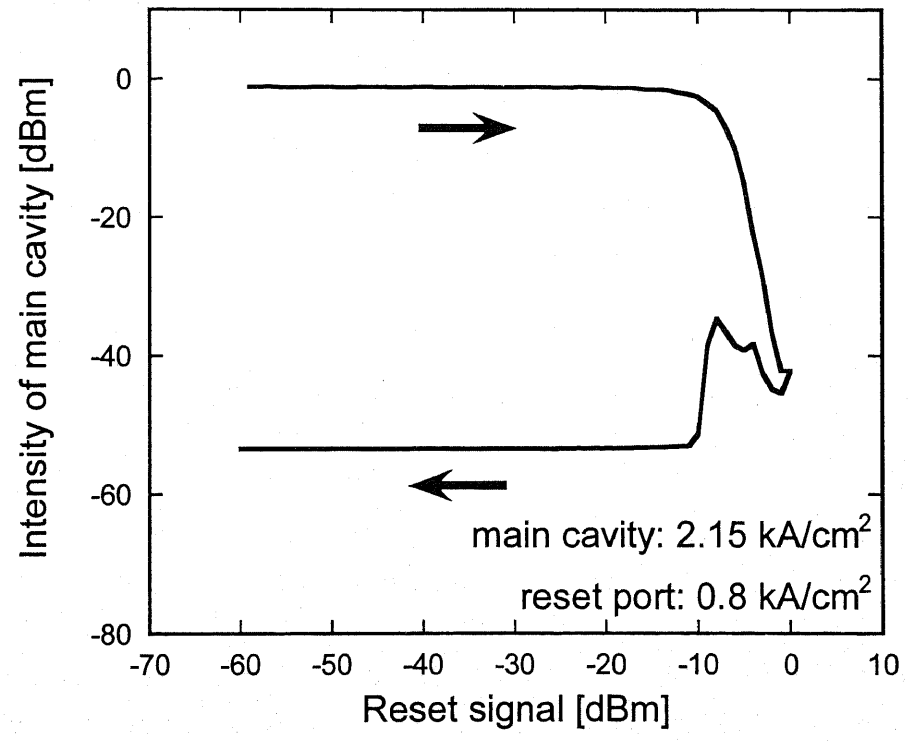

(b) Optical turn-off characteristic

Fig.4.14 All-optical flip-flop characteristics of the DC-BLD, (a) optical turn-on characteristics and (b) optical turn-off characteristics. The bias conditions of the main cavity and the reset port were 2.15, and 0.8 kA/cm^2, respectively. The turn-on power was around -10 dBm. The laser radiation was stopped by 0 dBm reset signal.

4.8 Fabrication of DC-BLD

In the previous section, we analyzed the proposed DC-BLD by the TMM and FD-BPM models. Both models predicted that the DC-BLD was useful for the all-optical flip-flop operation. In this section, we mentioned the fabrication procedure of the DC-BLD.

The DC-BLD has an almost same structure of conventional LDs. The multiple layer structure as an LD including a 0.8% compressively-strained InGaAsP MQW active layer whose band gap energy was around 1.55 μm was grown on an n-InP substrate by metal-organic vapor phase epitaxy (MOVPE). The layer structure was same as depicted in Fig.3.2. The DC-BLD was prepared by following the conventional fabrication procedure of ridge-waveguide LDs as shown in Fig.4.15.

(i) Patterning: A directional coupler pattern was made by photolithography. Photo-resist (Shipley: S1805) was spin-coated on the InP substrate. The rotation speed of the spinner was 1st: 500 rpm (5 sec.), 2nd: 6000 rpm (40 sec.). The pre-baking for 10 min. at 90 °C was following. After the UV exposure for around 3 sec., 10 sec. development by NMD-3 was following. For successful Al_2O_3 liftoff process to open the current injection window of the ridge waveguide, the wafer didn't be post-baked.

(ii) Wet-etching: The ridge waveguides were formed by chemical wet-etching. The InGaAs cap layer was etched by H_2SO_4 : H_2O_2 : H_2O = 1 : 1: 5 solution (30 sec., 5 °C). Then, the p-InP upper clad was etched by 20 % HCl solution (3 min., R. T.). The etching was stopped by the InGaAsP etch-stop layer.

(iii) Liftoff: After Al_2O_3 current-blocking layer (100 nm) was deposited by electron-beam (EB) evaporation, the liftoff was incorporated to open the window for current injection. For the liftoff, the wafer was soaked in boiling acetone (10 min.) and ultrasonic vibrating acetone (20 min.).

(iv) Electrode formation: The Ti (30 nm) / Au (150 nm) p-contact electrodes were deposited by EB evaporation. The electrode materials were deposited at 75-degree incident angle to separate the electrodes between the main cavity and reset port.

(v) Saturable absorber formation: The saturable absorber was formed by etching the electrode. The separator pattern was made by photolithography. Photo-resist (Tokyo Ohka kogyo: OFPR-800 50CP) was spin-coated on the wafer. The rotation speed of the spinner was 1st: 500 rpm (5 sec.), 2nd: 4000 rpm (40 sec.). The pre-baking for 30 min. at 90 °C was following. After the UV exposure for around 11 sec., the NMD-3 development (1 min.) and the post-baking (30 min., 90 °C) were following. The Au layer was etched by I : KI : H_2O = 1 g : 2 g : 50 g solution (1 min., R. T.). The Ti layer was etched by 63 buffered HF (23 sec., R. T.). To get high isolation resistance between the gain and absorp-

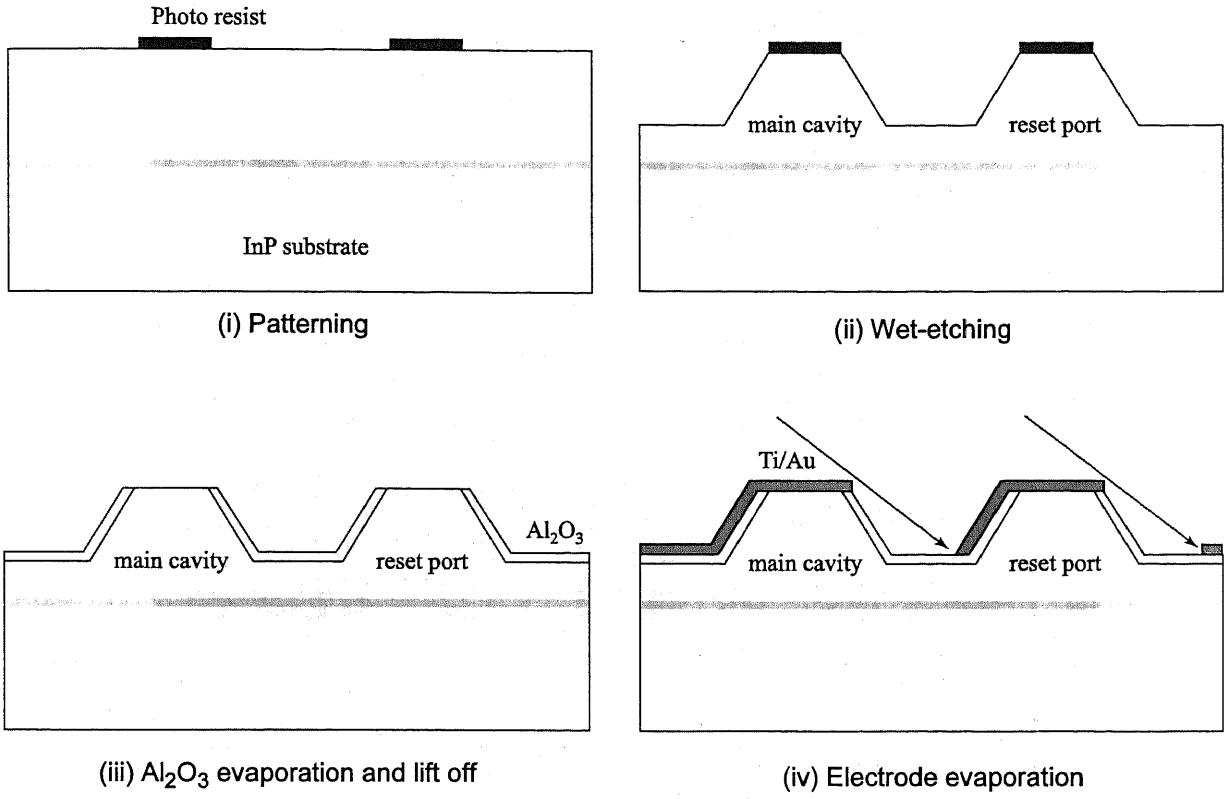

Fig.4.15 Fabrication procedure of DC-BLD, that is almost same as that for the conventional ridge-waveguide LDs. The oblique EB evaporation technique (iv) was developed to separate the electrode of the two adjacent waveguides.

tion regions, the InGaAs cap layer was etched using H_2SO_4 : H_2O_2 : H_2O = 1 : 1: 5 solution (1 min., 5 °C).

(vi) Griding: The wafer was gridded into 160 μm thickness to cleave it easily. Finally, the Ti (30 nm) / Au (150 nm) electrode was deposited on the back of the wafer.

To obtain the all-optical flip-flop operation using the DC-BLD, the electrode of the two coupled waveguides should be electrically isolated to inject currents separately. For this purpose, we used oblique electron-beam evaporation (Fig.4.15 (iv)). The electrode material, Ti/Au, was deposited at 75-degree incident angle which was larger than the waveguide's mesa angle. Therefore, the mesa shaded the region between the coupled waveguides from Ti/Au evaporation. In this way, the two adjacent waveguides of the directional coupler were electrically isolated without any lithography. A SEM photograph of the directional coupler (Fig.4.16) shows that the electrode was successfully separated. Moreover, one waveguide had a s-bend section to widen the region of the reset port electrode, so we can easily contact to the reset port electrode which has enough width.

The microscopic photograph of the DC-BLD fabricated by the process mentioned above is shown in Fig.4.17. The width of the ridge waveguides were designed to be around 2 μm.

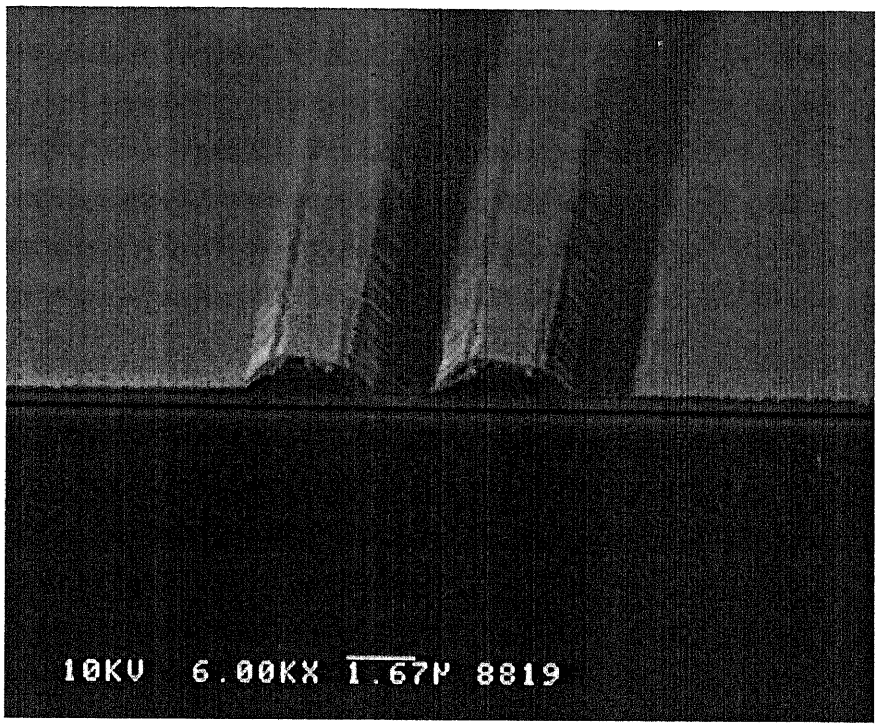

Fig.4.16 A SEM photograph of the directional coupler section whose electrodes were successfully separated.

The directional coupler length was fixed to be 750 μm, but the gap of the directional coupler was varied from 2.4 μm to 3.2 μm. The length of saturable absorber at the end of the main cavity was 150 μm, that was about 10 % of the total length, 1300 μm. The reset port was bended to separate the two inputs. The gap between the two input ports was 50 μm.

4.9 Evaluation of DC-BLD

In this section, we experimentally evaluated the basic characteristics of the DC-BLD. The properties predicted by the numerical analyses were confirmed by the measurements. The all devices were bonded on the Cu or AlN submounts, that were attached to the heatsink whose temperature was kept at 20 °C by the peltiert cooler. The characteristics of the DC-BLD were evaluated at CW operation, and the optical input and output powers were coupled using standard single-mode tapered fibers. The coupling loss of the tapered fiber was estimated to be around 10 dB in our experiments. To contact each electrode, the micro-probe with Karr Suss probehead PH100 was used.

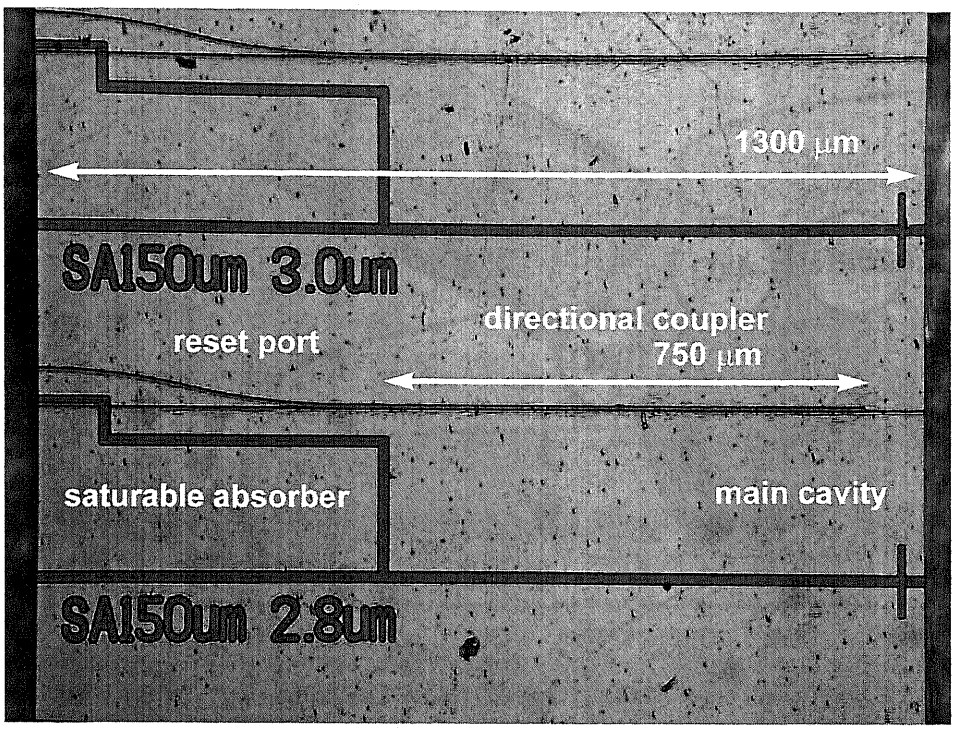

Fig.4.17 The top view of the fabricated DC-BLD. The ridge width was around 2 μm. The gap and length of the directional coupler section were 2.4 - 3.2 μm and 750 μm, respectively. The saturable absorber length was 150 μm. The reset port was bended to separate the two input ports

A. Isolation resistance

First, we evaluated the each isolation resistance between the electrodes, which affected the device properties. The resistances were measured by digital multimeter. The contact resistance between the micro-probe and the electrode was around 10 Ω, which was small enough not to disturb the measurements.

The measurement results of the isolation resistance were illustrated in Fig.4.18. The resistance between the main cavity and the saturable absorber affected the hysteresis of the BLDs. If the resistance is small, the BLD never show the clear hysteresis. To obtain high resistance, the p-InGaAs cap layer of the separation region was etched. The measured resistance was around 40 kΩ. This value was enough for the hysteresis.

The isolation resistance between the main cavity and reset port is very important to inject currents separately. To get the all-optical flip-flop, the main cavity and reset port should be biased at the different currents. As described in the previous section, we used the self-alignment technique to separate the electrodes. We obtained that the isolation resistance between the coupled waveguides was around 4 kΩ, being larger enough for pumping them separately.

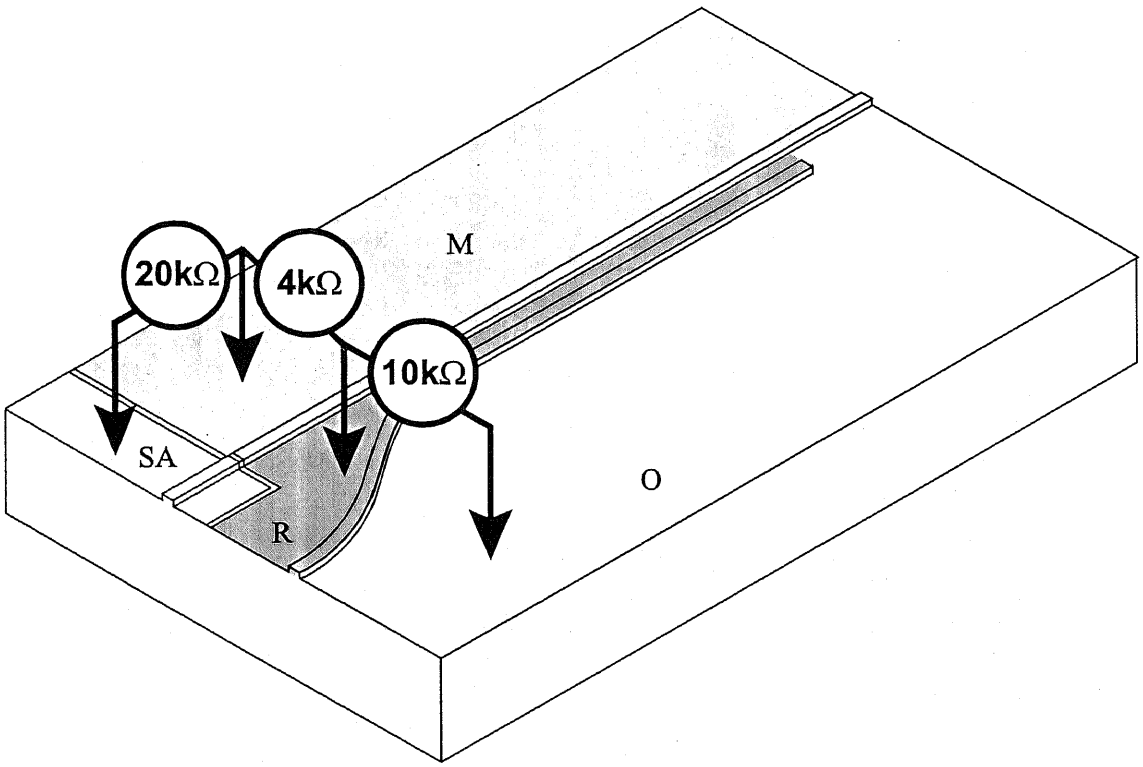

Fig.4.18 Isolation resistance of the DC-BLD. Each electrode was named M: main cavity, R: reset port, SA: saturable absorber, and O: other. The resistance between the main cavity and reset port was around 4 kΩ. The resistance between the saturable absorber and main cavity was around 20 kΩ. These resistance was large enough for the DC-BLD.

We also measured the resistance between the reset port electrode (R) and the adjacent one (O). Interestingly, the resistance was not 0 Ω, but 10 kΩ.

We measured the L-I characteristics of the fabricated DC-BLD to make sure the electrode separation. The DC-BLD without any saturable absorbers was prepared for this measurement. Either main cavity or reset port was pumped. Fig.4.19 and show the L-I characteristics in the case of injecting current to the main cavity (a) and reset port (b), respectively. In Fig.4.19 (a), the main cavity started lasing at 90 mA injection current, while the reset port emitted just only small spontaneous emission. Otherwise, in Fig.4.19 (b), the reset port did not lase in spite of its large amplified spontaneous emission because the reset port had small Fabry-Perot resonance cavity. The spontaneous emission from the main cavity was much smaller than the reset port. The intensity ratio of the main cavity to the reset port was more than 40 dB at 150 mA injection current respectively, so the isolation resistance between the main cavity and reset port was large enough for the independent forward bias.

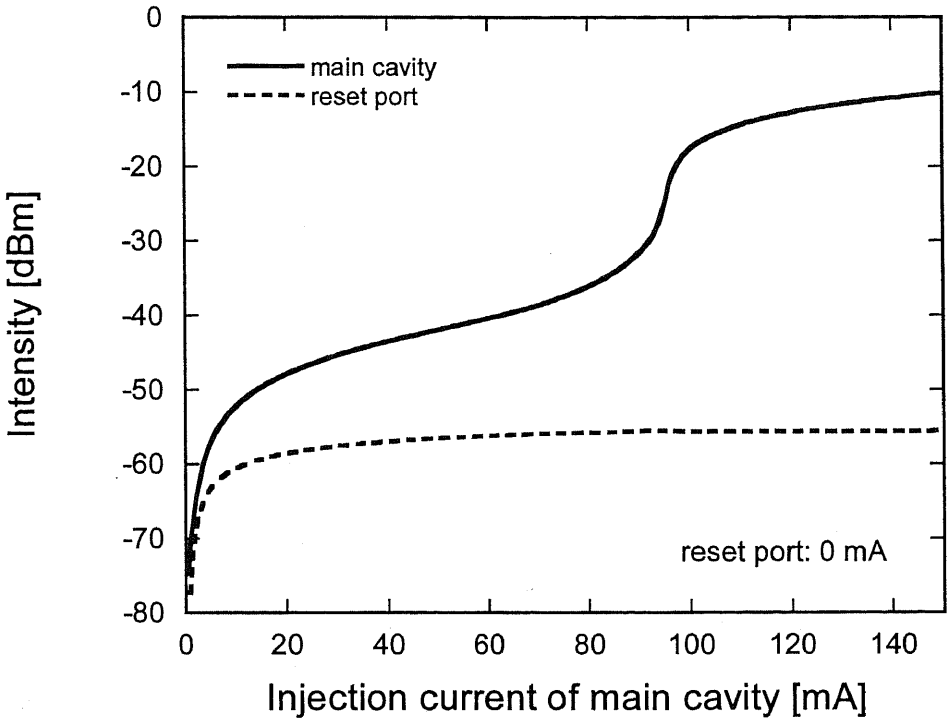

(a) Pumping only main cavity

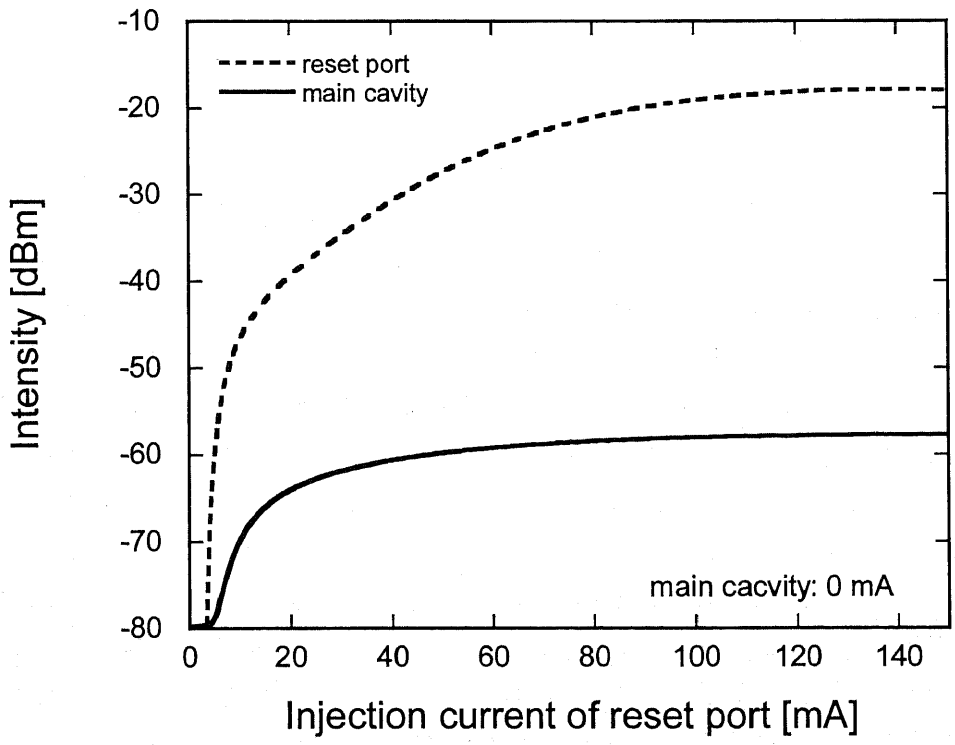

(b) Plumping only reset port

Fig.4.19 L-I characteristics of the DC-BLD in the case of injecting the current to the main cavity and reset port, respectively. The output power ratios between the two waveguides were more than 40 dB, so the isolation resistance was large enough.

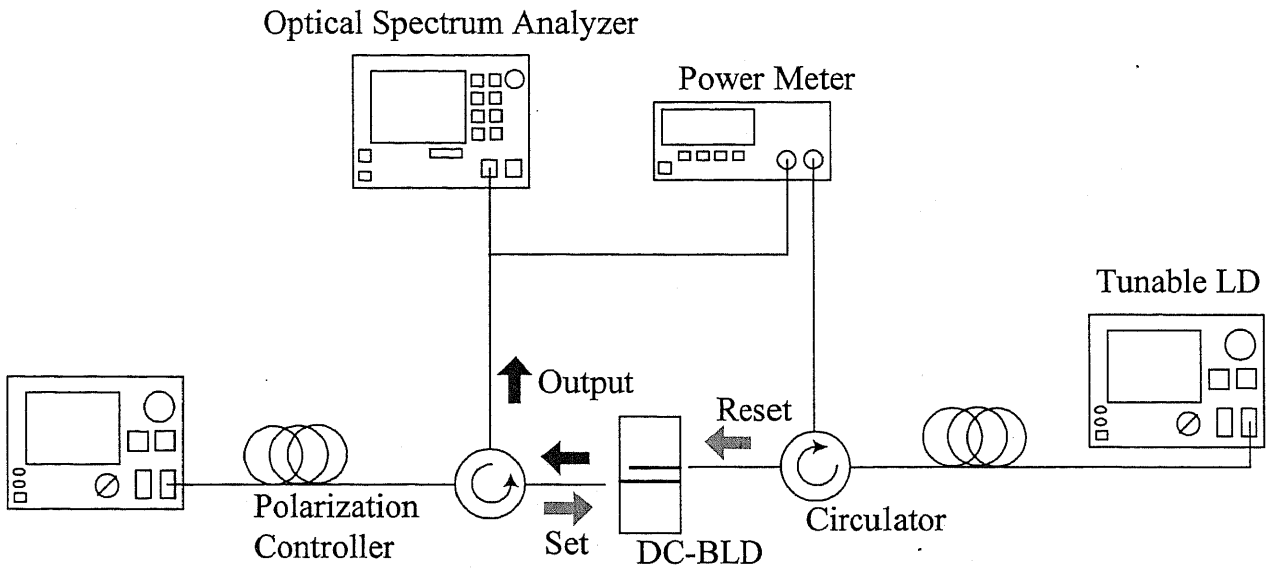

Fig.4.20 Measurement setup for the DC-BLD. The set signal was injected from the opposite side of the reset signal. The output was extracted through a circulator. Each element such as optical-power meter, OSA, and tunable LDs was controlled by PC through GP-IB interface.

B. Hysteresis characteristic

The basic properties predicted by the numerical analyses were measured to prove the all-optical flip-flop operation of the DC-BLD. The measurement setup is shown in Fig.4.20. We used two wavelength tunable LDs (Anritsu: MG9638A, Photonetics: Tunics-PR) for the set and reset signal source. The set and reset signal was guided by single-mode fibers and coupled into the DC-BLD through the tapered fibers. The input signals were tuned to the TE-polarized lights by the polarization controllers. In the analyses, the set and reset signal was injected from the same side. However, the distance between the two output ports was only 50 μm, that was too near for accessing by two tapered fibers simultaneously. From this reason, the set signal was inputted from the opposite side. Using a optical circulator, the output was measured from the same port. The output powers were monitored by a optical multimeter (Hewlett Packard: 8153A). The spectrum was measured by an optical spectrum analyzer (Ando: AQ-6315). To bias the waveguides, we used two current sources (ILX ligth-wave: LDP-3811, LDP-3220). All measurement components are controlled by a personal computer through GP-IB interfaces.

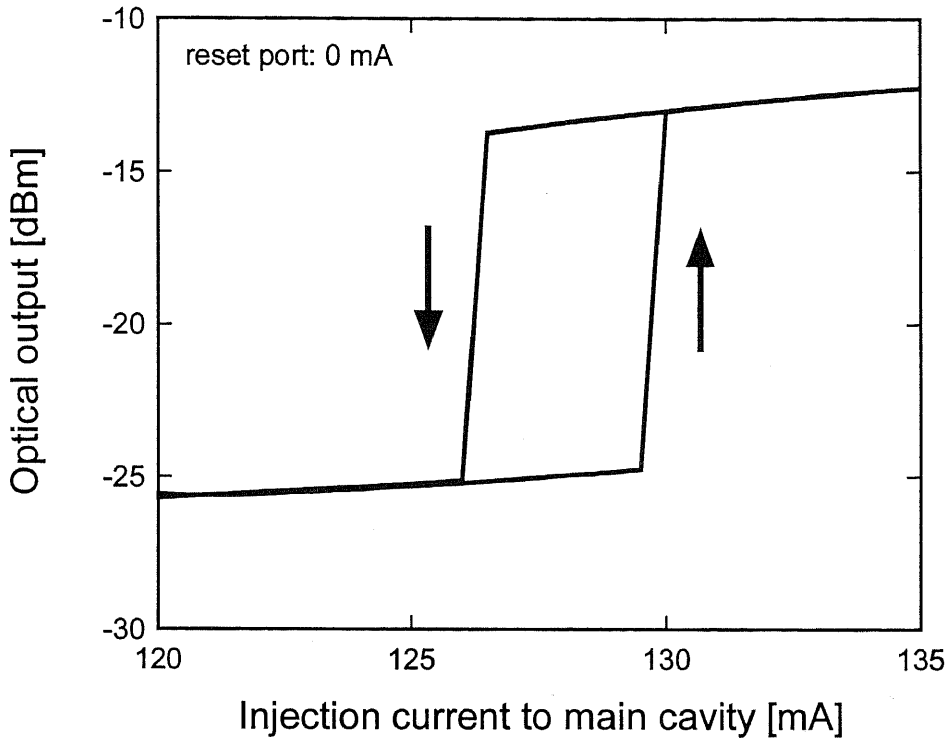

Fig.4.21 Hysteresis loop of the DC-BLD. The current was injected to only the main cavity. The turn-on and turn-off currents were 130 mA and 126 mA, respectively.

First, the hysteresis characteristic was evaluated. Due to the saturable absorption, the DC-BLD exhibited the bistable lasing behavior. Fig.4.21 shows the hysteresis of the DC-BLD in the case of pumping the main cavity only. The current of the reset port was zero. The hysteresis was very clear owing to the high isolation resistance between the gain and absorption regions. The turn-on and turn-off currents were 130 mA and 126 mA, respectively. The injection current of the main cavity should be within hysteresis loop in order to make use of the bistable switching. Therefore, we adopted 128 mA as the bias current to the main cavity.

The lasing spectrum was shown in Fig.4.22. The DC-BLD had several Fabry-Perot longitudinally multi-mode lasing modes. The lasing wavelength at 128 mA was around1563 nm. The peak wavelength was slightly red-shifted because the absorption of the saturable absorber and the thermal effect by the currents.

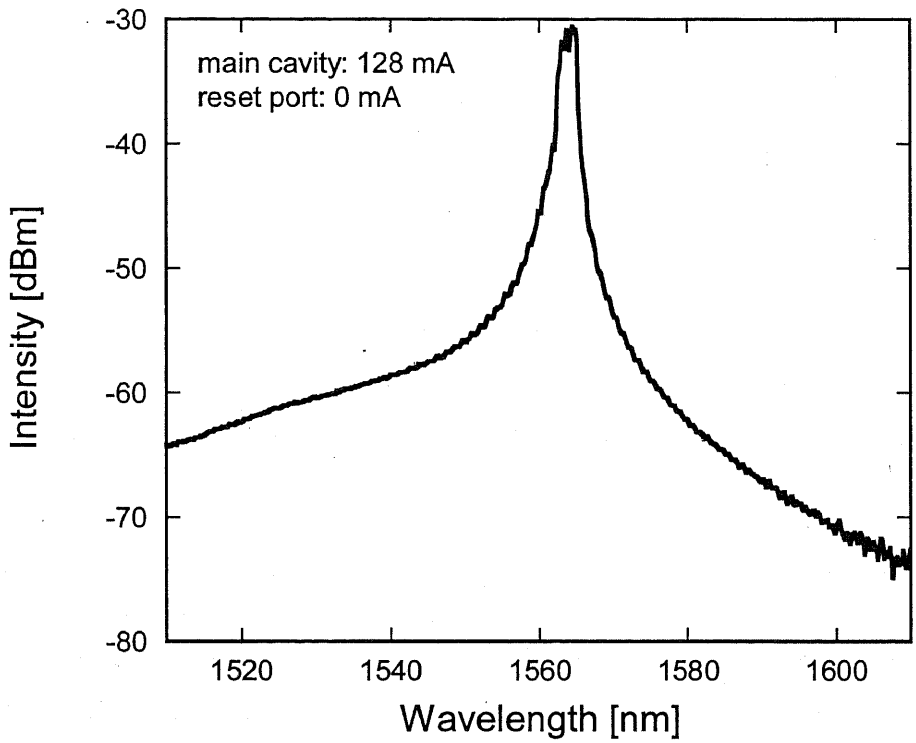

Fig.4.22 The lasing spectrum of the DC-BLD biased at 128 mA. The reset port was not pumped. The lasing wavelength was around 1563 nm.

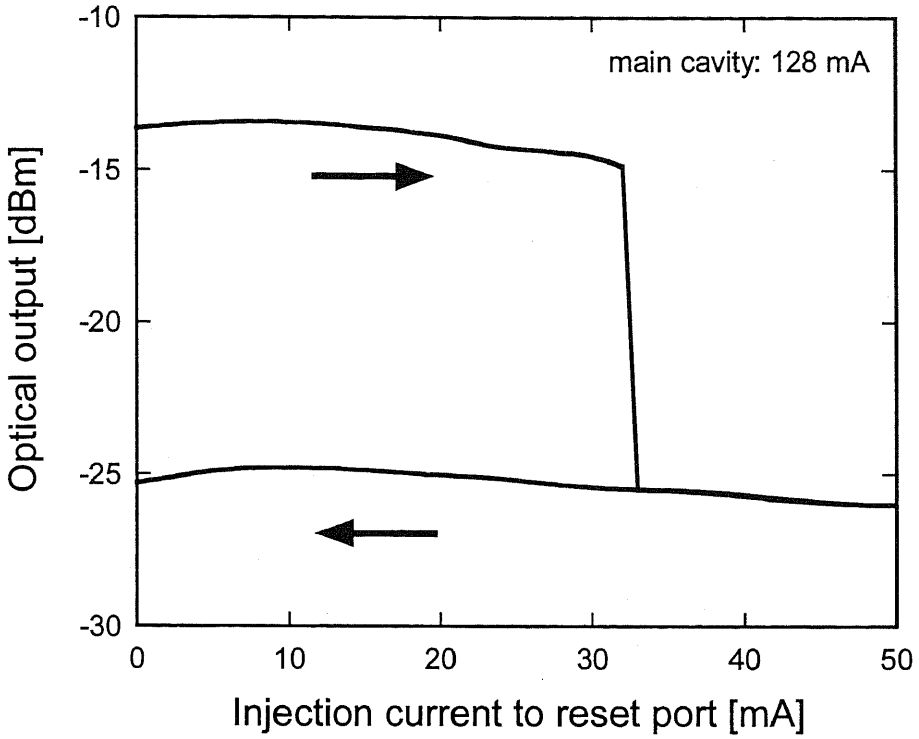

Fig.4.23 Electrical turn-off operation of the DC-BLD. The main cavity was biased at 128 mA. Due to increasing the coupling coefficient of the directional coupler, the laser radiation was stopped.

C. Electrical turn-off characteristic

To decide the bias current of the reset port, the electrical turn-off characteristic should be measured as predicted by the numerical results. The coupling coefficient of the directional coupler is controllable through the injection current into the reset port waveguide. Fig.4.23 shows the electrical turn-off operation; the DC-BLD, set the ON state at the beginning, turned the OFF state due to increasing coupling of the directional coupler by the current injection to the reset port. The output stays the OFF state even if the current was turned back down. From Fig.4.23, the bias condition of the reset port for the all-optical flip-flop operation was determined to be 33 mA, slightly smaller value than that terminated the laser oscillation.

D. All-optical flip-flop characteristic

At the bias condition mentioned above, the DC-BLD can work as an all-optical flip-flop. We used 1560 nm TE-polarized light as both the set and reset signals. The optical turn-on characteristic is shown in Fig.4.24 (a). The set optical input above 6 dBm switched the DC-BLD on due to absorption reduction. Since the power included coupling loss, the actual power necessary was expected to be below 0 dBm.

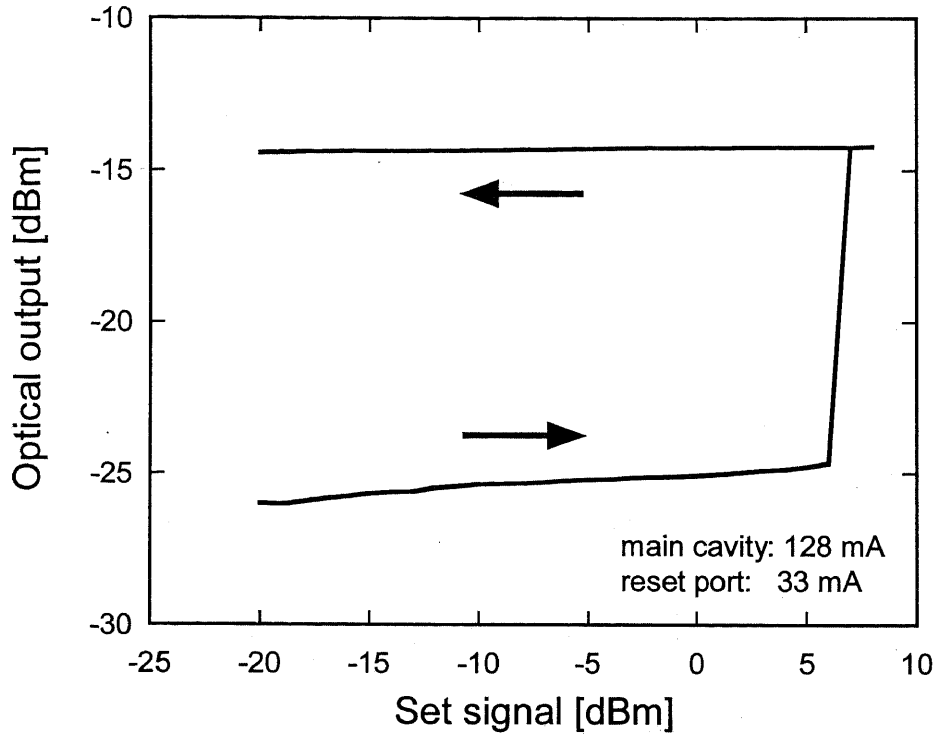

(a) Optical turn-on characteristic

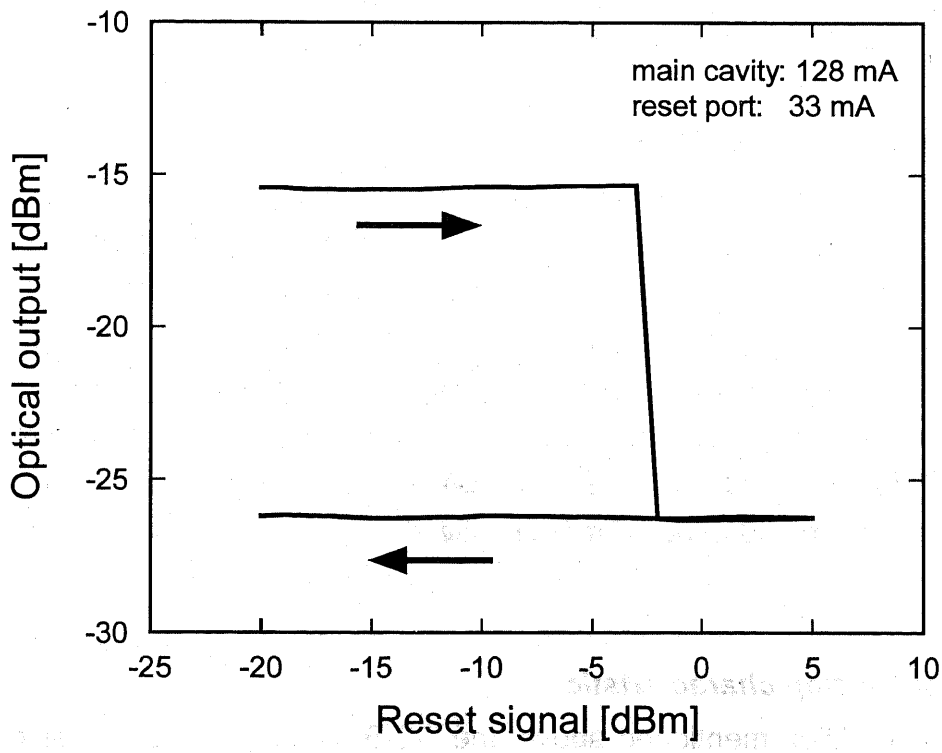

(b) Optical turn-off characteristic

Fig.4.24 All-optical flip-flop characteristic of the DC-BLD. The main cavity and reset port were biased at 128 mA and 33 mA, respectively. The turn-on power and turn-off power were 6 dBm and -3 dBm, respectively.

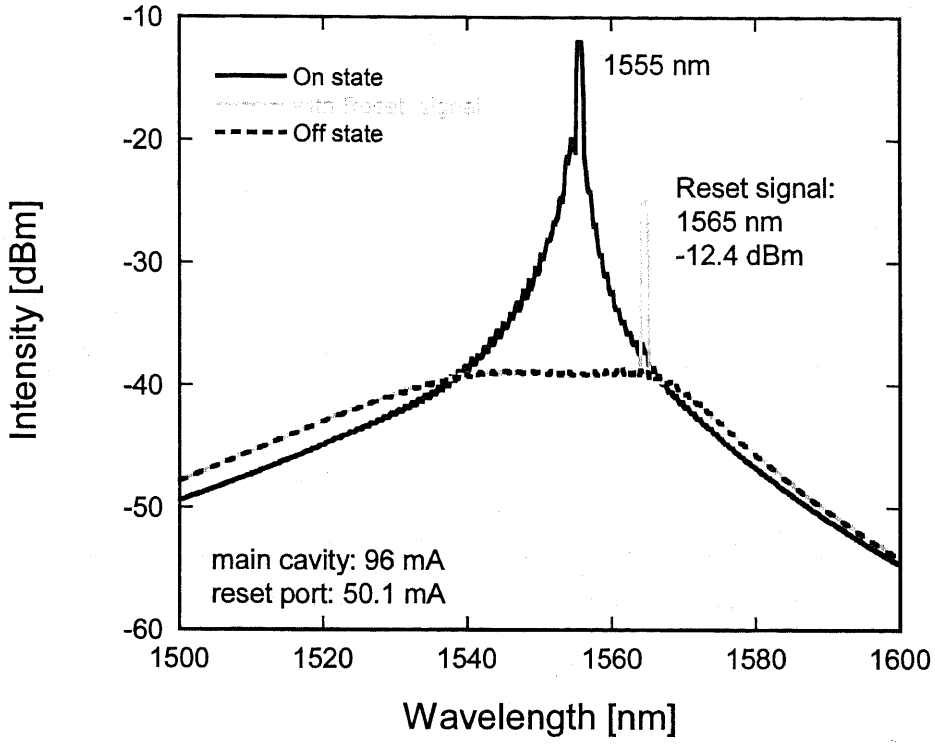

Fig.4.25 Spectra change during the reset operation. The main cavity and reset port were biased at 96 mA and 50.1 mA, respectively. The DC-BLD was turned off by the -12.4 dBm reset signal. The lasing spectrum changed to only the spontaneous emissions by the reset signal.

At the same bias currents as the set operation, the optical reset operation was demonstrated. Fig.4.24 (b) shows the optical turn-off characteristic by the light injection to the reset port. The photo-carriers generated by reset light absorption enlarged the coupling coefficient of the directional coupler, like in the case of current injection, thus increasing the optical loss of the main cavity to stop lasing. The turn-off power including the fiber coupling loss was around -3 dBm. After the optical reset input was eliminated, the recovered absorption of the saturable absorber prevented the DC-BLD from lasing again. The extinction ratio was more than 10 dB.

The typical spectra change during the reset operation were shown in Fig.4.25. In this device, the main cavity and the reset port were biased at 96 mA and 50.1 mA, respectively. The lasing wavelength was 1555 nm. The reset light (-12.4 dBm, 1565 nm) switched the DC-BLD off. Fig.4.25 show that the lasing spectrum changed to only the spontaneous emissions by the reset signal.

In this way, the basic characteristics of the DC-BLD was experimentally evaluated. The experimental results corresponded with the numerical analyses by the TMM and FD-BPM models, and we demonstrated that the proposed DC-BLD worked as the all-optical flip-flop.

4.10 Estimation of Maximum Switching Speed

The switching speed between the ON and OFF states is one of the most important factor of all-optical flip-flop devices. In the case of the DC-BLD, the maximum switching speed is limited by relaxation oscillation frequency as like direct modulation of LDs.

In general, the relaxation oscillation frequency f_r is expressed as

$$f_r = \frac{1}{2\pi}\sqrt{\frac{\partial G}{\partial N}\cdot\frac{S_0}{\tau_{ph}}} \tag{4.10}$$

where $\partial G/\partial N$ is differential gain, S_0 photon density, τ_{ph} photon lifetime.

The modal gain G is written as

$$G(N) = \Gamma\frac{c}{n_r}a(N-N_0) \tag{4.11}$$

where Γ confinement factor, c light speed in vacuum, n_r effective refractive index, a gain constant, N carrier density, N_0 the carrier density at transparency.

From equation (4.11), the differential gain is calculated as

$$\frac{\partial G}{\partial N} = \Gamma\frac{c}{n_r}a. \tag{4.12}$$

The photon lifetime means the photon trapping time inside the cavity and are expressed as

$$\frac{1}{\tau_{ph}} = \frac{c}{n_r}\left(\alpha+\frac{1}{2L}ln\frac{1}{R^2}\right) \tag{4.13}$$

where α internal loss, L is cavity length, R power reflectivity.

The relaxation oscillation frequency of the DC-BLD can be calculated using equations (4.10) - (4.13) and the result is shown in Fig.4.26. We use the almost same parameters listed in Table.2.1, i.e., c = 3.0 × 10^{10} [cm·s^{-1}], n_r = 3.25, α = 20 [cm^{-1}], R = 0.3, Γ = 0.4, a = 4.63 × 10^{-16} [cm^2]. The photon density at lasing state is estimated to be 1.0 × 10^{14} [cm^{-3}]. The relaxation oscillation frequency of the DC-BLD is around 1 GHz to 2 GHz. The DC-BLD fabricated in Section 4.9 had 1300 μm cavity length, so the maximum switching speed is estimated to be around 1 GHz. The relaxation oscillation frequency was decayed as compared with normal LDs, because the photon density at the ON state was decreased by coupling to the reset port. Therefore, the higher differential gain materials and the smaller device are required for high speed switching. By the improvement in there points, the relaxation oscillation frequency can be increased to around 10 GHz.

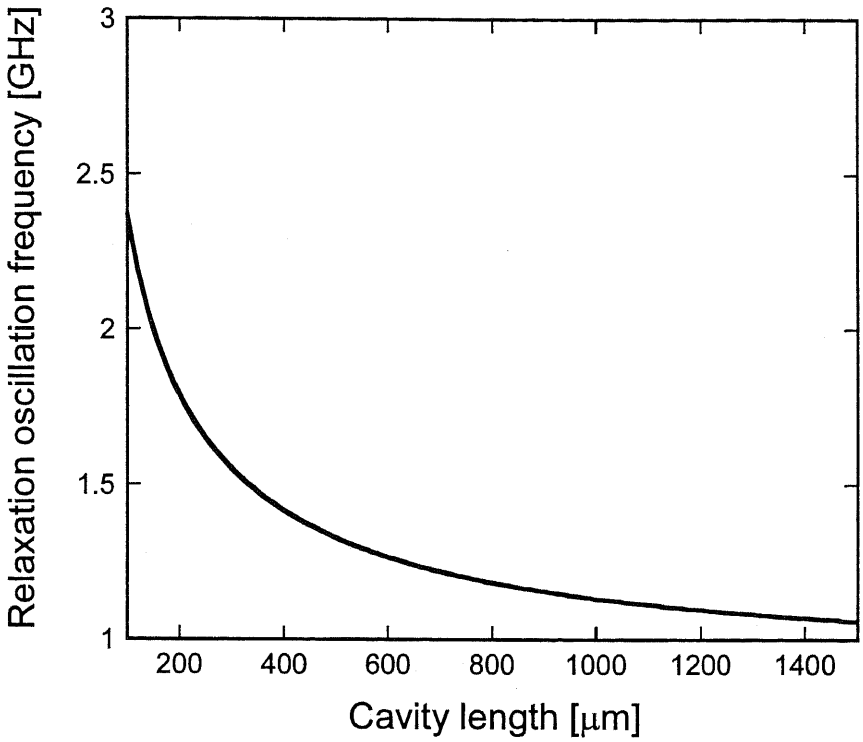

Fig.4.26 Relaxation oscillation frequency versus cavity length of the DC-BLD. The maximum switching speed of the fabricated DC-BLD was estimated to be around 1 GHz.

4.11 Reduction of Device Length

To enlarge the relaxation oscillation frequency, the device size of the DC-BLD should be as small as possible. Moreover, the turn-off power is estimated to be decreased because of the short reset port.

The DC-BLD fabricated in Section 4.8 was divided in the two parts, i.e. the directional coupler section and the port section. Each section should be shortened.

The directional coupler length was designed to 750 μm in Section 4.8. The coupler length can be shortened by the narrower gap directional coupler. As shown in Fig.4.5 (b), the one coupling length is less than 300 μm if the gap and the ridge width are 1.0 μm and 2.0 μm, respectively. In the case of the forward-mesa type ridge waveguide, the gap is narrower than the photo-resist pattern after the formation of the mesa. Therefore, the 1.0 μm gap can be realized. The self-align electrode separation by the oblique EB evaporation was also demonstrated for the 1.0 μm gap directional coupler.

The S-bend port (i.e., reset port) length was around 500 μm because the offset between the two input ports was designed to be 50 μm at the cleaved facet. This offset was decided by obtaining the wide electrode for the reset port. The radius of the S-bend can not be

changed from 1000 μm to avoid excess losses. However, the S-bend length can be reduced to be 200 μm by 10 μm port offset. In this case, the electrode for the reset port was too narrow to contact electrically. To solve this problem, it is needed to bridge between the electrode R (see Fig.4.18) and the electrode O. The photolithography and Ti/Au evaporation incorporating a liftoff process will realize the electrode bridge.

The total device length: the input port (200 μm) + the directional coupler (300 μm) + the output port (50 μm), i.e. around 500 μm can be realized.

We also analyzed the basic characteristics of the short DC-BLD. We used the FD-BPM model because the TMM model could not treat the strong coupling accurately. The one coupler length was calculated to be 183 μm in this case because the higher carrier density led to the smaller refractive index. The port lengths were set to be 100 μm. The parameters used here were same as the other analyses, which were listed in Table.2.1.

A. Hysteresis characteristics

The L-I characteristics of the DC-BLD with 0, 10, 20, 30 μm saturable absorbers were shown in Fig.4.27. The saturable absorber was biased at 0.1 kA/cm^2. The reset port was

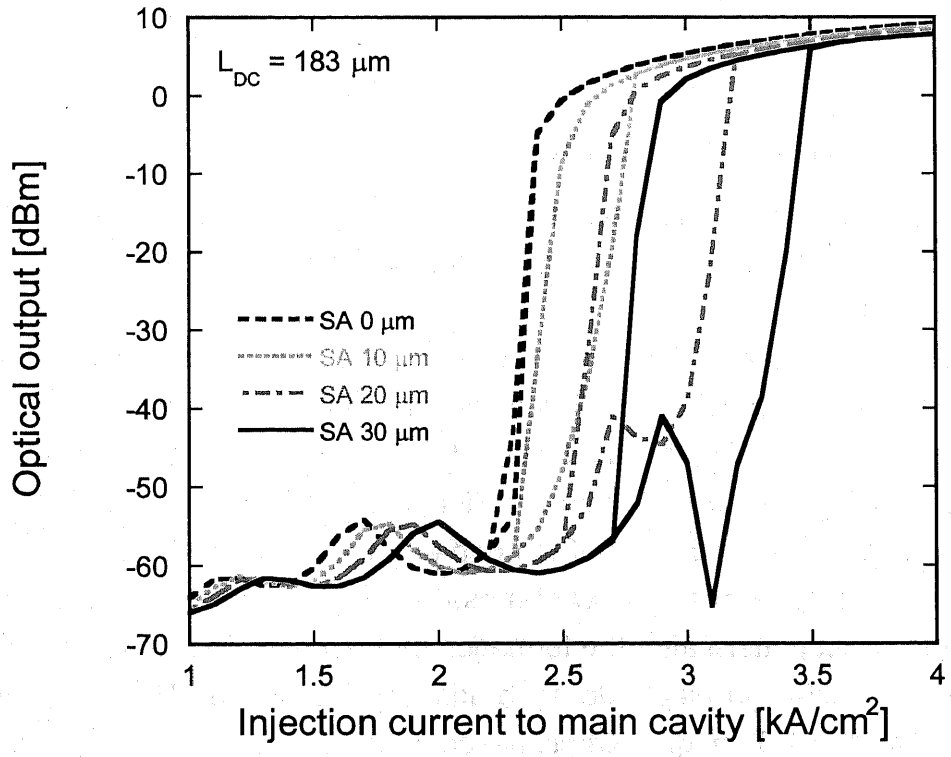

Fig.4.27 Bistable behavior of the short DC-BLD with the saturable absorber, 0, 10, 20, 30 μm, biased 0.1 kA/cm^2. The coupler length was 183 μm, and the port lengths were 100 μm. The injection current density of the reset port was fixed as 0.1 kA/cm^2.

not pumped, so we only consider the main cavity. As increasing the saturable absorber length, the threshold current and hysteresis width became large. For stable operation, we adopted 30 μm as the saturable absorber length. The bias current of the main cavity was decided to be 2.95 kA/cm^2 from this result.

B. Electrical turn-off characteristic

To decide the reset port current for the all-optical flip-flop operation, the electrical turn-off characteristic was calculated as shown in Fig.4.28. While the L-I characteristics didn't show a sharp change, the electrical reset was predicted as same as Fig.4.13. From this result, the bias current of the reset port was decided to be 0.5 kA/cm^2.

C. All-optical flip-flop characteristics

Using the bias currents acquired above, the all-optical flip-flop can be realized. The set signal and the reset signal were assumed to be 1.55 μm, CW light. Fig.4.29 (a) shows the set operation of the short DC-BLD. The set power was around -10 dBm, that was same the long DC-BLD. The reset operation was also analyzed as shown in Fig.4.29 (b). The reset

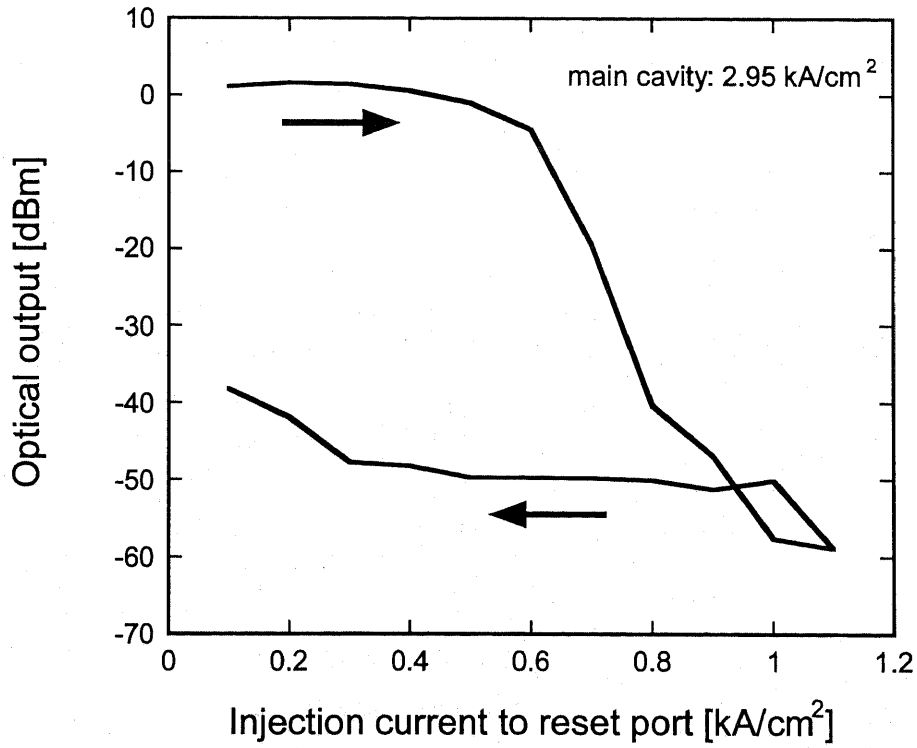

Fig.4.28 Electrical turn-off operations of the short DC-BLD by the current to the reset port. The bias condition of the main cavity was 2.95 kA/cm^2. The bias currents of the reset port can be determined from this results.

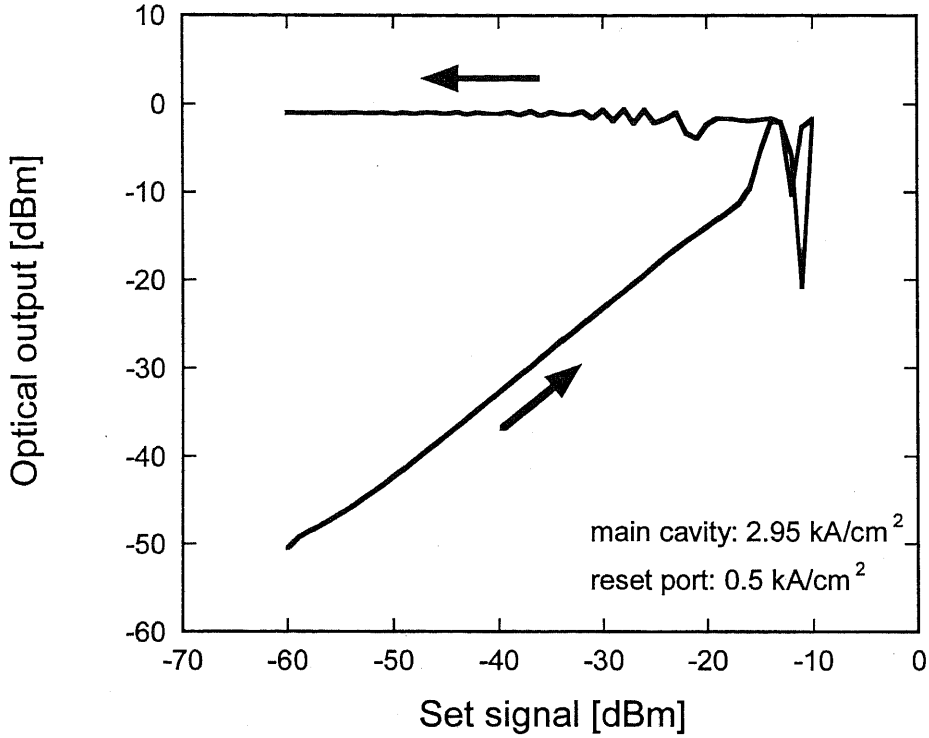

(a) Optical turn-on characteristic

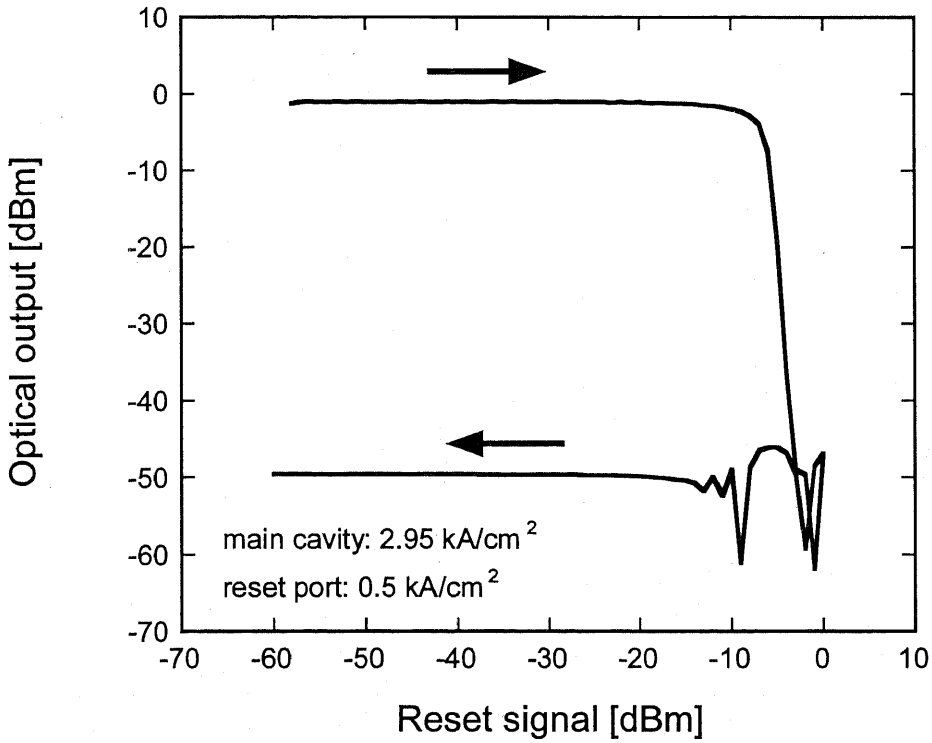

(b) Optical turn-off characteristic

Fig.4.29 All-optical flip-flop characteristics of the short DC-BLD, (a) optical turn-on characteristics and (b) optical turn-off characteristics. The bias conditions of the main cavity and the reset port were 2.95, and 0.5 kA/cm^2, respectively. The turn-on power was around -10 dBm. The laser radiation was stopped by 0 dBm reset signal.

characteristic was almost same as the long DC-BLD, and the reset power was less than 0 dBm.

In this way, the FD-BPM analyses also predicted the all-optical flip-flop operation by the short cavity DC-BLD, whose directional coupler length was around 180 μm. The higher switching speed will be realized by this short cavity DC-BLD.

4.12 Conclusion

In this chapter, we have proposed and demonstrated a novel all-optical flip-flop device using a directionally coupled bistable laser diode (DC-BLD). The all-optical flip-flop operation was numerically predicted using the TMM and FD-BPM models. Under the asymmetrical bias conditions, the nonlinearity of the directional coupler enabled the DC-BLD to realize the optical turn-off operation.

The DC-BLD was also fabricated using the conventional fabrication procedure of LDs. To separate the electrode of the directional coupler, we developed an oblique electron-beam evaporation technique. The electrodes of the directional coupler were electrically separated without any lithography.

We experimentally evaluated the basic characteristics of the fabricated DC-BLD, that were predicted by the numerical analyses. The optical reset, that was difficult for the conventional absorptive BLDs, was obtained with optical power level around 0 dBm. The optical set was simultaneously achieved, and the all-optical flip-flop operation was successfully demonstrated.

The maximum switching speed was estimated to be limited by the relaxation oscillation frequency, that was calculated to be around a few GHz for the fabricated DC-BLD in this chapter. However, the switching speed can be improved by the higher differential gain materials and smaller devices. We also predicted that the device length of the DC-BLD could be reduced to be around 400 μm by the FD-BPM analyses.

From these results, the usefulness of the basic concept of the absorptive BLDs with the nonlinear coupler was proved for the all-optical flip-flop devices.

References

[1] K. Inoue, and K. Oe, "Optical triggered off-switching in a bistable laser diode using a two-electrode DFB-LD," *Electron. Lett.*, vol. 24, no. 9, pp. 512-513, 1988.

[2] F. Rober, D. Fortusini, and C. L. Tang, "All-optical set-reset operation of a bistable semiconductor laser intracavity-coupled to a vertical-cavity surface-emitting laser," *IEEE Photonics. Technol. Lett.*, vol. 12, no. 5, pp. 465-467, 2000.

[3] S. M. Jensen, "The nonlinear coherent coupler," *IEEE J. Quantum Electronics*, vol. QE-18, no. 10, pp. 1580-1583, 1982.

[4] P. Li Kam Wa, J. E. Sitch, N. J. Mason, J. S. Roberts, and P. N. Robson, "All-optical multiple quantum well waveguide switch," *Electron. Lett.*, vol. 21, pp. 26-28, 1985.

[5] S. R. Friberg, Y. Silberberg, M. K. Olivier, M. J. Andrejco, M. A. Saifi, and P. W. Smith, "Ultrafast all optical switching in a dual core fiber nonlinear coupler," *Appl. Phys. Lett.*, vol. 51, pp. 1135-1137, 1987.

[6] J. Wilson, G. I. Stegeman, and E. M. Wright, "Soliton switching in an erbium doped nonlinear fiber coupler," *Opt. Lett.*, vol. 16, pp. 1653-1655, 1991.

[7] R. A. Betts, T. Tjugiarto, Y. L. Xue, and P. L. Chu, "Nonlinear refractive index in erbium doped optical fiber," *IEEE J. Quantum Electronics*, vol. 27, pp. 908-913, 1991.

[8] P. LiKamWa, A. Miller, C. B. Park, J. S. Roberts, and P. N. Robson, "All-optical switching of picosecond pulse in a GaAs quantum well waveguide coupler," *Appl. Phys. Lett.*, vol. 57, no. 18, pp. 1846-1848, 1990.

[9] P. LiKamWa, A. Miller, J. S. Roberts, and P. N. Robson, "130 ps recovery of all-optical switching in a GaAs multi quantum well directional coupler," *Appl. Phys. Lett.*, vol. 58, no. 19, pp. 2055-2057, 1991.

[10] R. T. Sahara, S. G. Hummel, W. H. Steier, and P. D. Dapkus, "AlGaAs waveguide optically controlled directional coupler latch," *J. Lightwave Technol.*, vol. 11, no. 10, pp. 1533-1538, 1993.

[11] A. Villeneuve, K. Al-Hemyari, J. U. Kang, C. N. Ironside, J. S. Aitchison, and G. I. Stegeman, "Demonstration of all-optical demultiplexing at 1555 nm with an AlGaAs directional coupler," *Electron. Lett.*, vol. 29, no. 8, pp. 721-722, 1993.

[12] D. A. O. Davies, "Nonlinear switching in InGaAsP laser amplifier directional couplers biased at transparency," *Electron. Lett.*, vol. 29, pp. 1710-1711, 1993.

[13] B. Ma, Y. Nakano, and K. Tada, "Novel all-optical wave length converter using coupled semiconductor optical amplifiers," *Proc. Conf. Lasers and Electro-Optics (CLEO'98)*, pp. 477-478, San Fransisco, USA, May, 1998.

[14] B. Ma, M. Tabei, and Y. Nakano, "All-optical wavelength converter based on directionally-coupled semiconductor optical amplifiers," *Proc. ISLC'98*, postdeadline paper PD-8, Nara, Japan, 1998.

[15] B. Ma, Y. Nakano, and K. Tada, "All-optical wavelength converter based on coupled semiconductor optical amplifiers," *Proc. Integrated Photonics Research (IPR'98)*, pp. 164-166, Victoria, Canada, March, 1999.

[16] B. Ma, and Y. Nakano, "Realization of all-optical wavelength converter based on directionally coupled semiconductor optical amplifiers," *IEEE Photonics. Technol. Lett.*, vol. 11, pp. 188-190, 1999.

[17] B. Ma, and Y. Nakano, "Gain characteristics of codirectionally coupled semiconductor optical amplifier for polarity-noninverted digital wavelength conversion," *Electron. Lett.*, vol. 35, pp. 1560-1561, 1999.

[18] Chin-Chun Yang, and A. J. S. Wang, "Asymmetric nonlinear coupling and its applications to logic functions," *IEEE J. Quantum Electronics*, vol. 28, no. 2, pp. 479-487, 1992.
[19] C. Thirstrup, "Optical bistability in a nonlinear directional coupler," *IEEE J. Quantum Electronics*, vol. 31, no. 12, pp. 2101-2106, 1995.
[20] K. Z. Nóbrega, M. G. da Silve, A. S. B. Sombra, "Multistable all-optical switching behavior of the asymmetric nonlinear directional coupler," *Opt. Commun.*, vol. 173, pp. 413-421, 2000.

Chapter 5 MMI Bistable Laser Diode

We propose a novel BLD with active multi-mode interference (MMI) cavity. 2×2 MMI is designed as input light totally couples to a cross port. A bistable switching can be realized between two cross-coupled modes associated with gain saturation. Static characteristics of the MMI-BLD are analyzed using a finite difference beam propagation method (FD-BPM) scheme. The carrier is considered by the carrier rate equation. This model gives accurate distributions of photon and carrier densities, optical gain and refractive index inside the cavity. The condition for two-mode bistability, stability and extinction ratio of bistable switching are investigated. Carrier density difference inside the MMI coupler is small enough, so the instability effects such as filamentation never occur and the MMI-BLD has stable lasing. We predict that the MMI-BLD shows bistable switching between the two cross-coupled modes by injecting light, which can be used as all-optical flip-flop or optical memory.

5.1 Introduction

In the previous chapter, we have proposed the DC-BLD and demonstrated the all-optical flip-flop operation by overcoming the optical reset problem. However, the DC-BLD had the slightly complicated characteristics because the phenomena of the asymmetrical nonlinear directional coupler were not so simple.

In this chapter, we propose a novel two-mode BLD that has a symmetrical multi-mode interference (MMI) cavity and a simple operation principle. An active MMI-LDs have been mainly studied by Hamamoto et al. for high output power lasers [1]-[3] and ring lasers with MMI coupler [4]. We design 2×2 MMI as input light totally couples to a cross port. S-shaped two-mode bistability between two cross-coupled modes can be realized associated with gain saturation. Kawaguchi et al. [5] predicted theoretically that two-mode bistability has two types, i.e., conventional S-shaped bistability and pitchfork bifurcation bistability. S-shaped (hysteresis) polarization bistability was firstly reported by Chen and Liu [6] using InGaAsP/InP LD. Various attempts [7]-[11] of two-mode bistability in LDs followed this result, however only hysteresis like bistability with small widths of the hysteresis loops have been observed. The S-shaped two-mode bistability with a saturable absorber was clearly

demonstrated using the cross-coupled laser [12] based on a hybrid device proposed by Lasher and Fowler [13]. However this bistable laser had a slightly complicated structure. On the other hand, pitchfork bifurcation polarization bistability was experimentally demonstrated in LDs with external cavities [14] and vertical-cavity surface-emitting lasers (VCSELs) [15][16], and they shown high-speed switching. However, these devices needs a polarizer to take out one mode or a precise optimization of LD structure. This bistability of the MMI-BLD that occurs between same transverse electric (TE) modes is not polarization bistability, so we don't need any polarizers, external cavity and optimized LD structures for two orthogonally polarized modes. Moreover, the proposed device has a simple structure that matched to the conventional LD fabrication technique.

We use a finite difference beam propagation method (FD-BPM) to analyze static characteristics of the MMI-BLD. This model takes into account accurate distributions of photon and carrier densities, optical gain and refractive index inside the cavity. Two-mode bistability of the MMI-BLD is precisely investigated. In Section 5.2, the basic properties of multimode waveguides are described. In Section 5.3 & 5.4, the proposal and design of the MMI-BLD are mentioned. In Section 5.5, simulation results on two-mode bistability and all-optical flip-flop operation in the MMI-BLD are described. In Section 5.6, the limitation of the maximum repetancy frequency of the MMI-BLD is investigated. Conclusions are given in Section 5.7.

5.2 Basic Properties of MMI Coupler

Multi-mode interference couplers [17]-[19] have found a considerable interest in recent years. They feature compactness, high design tolerances, a large optical bandwidth and polarization insensitivity when strongly guided structures are used [20][21]. Currently, MMI's are used as 3 dB power splitters and combiners [22], as mode converter[23], as power splitters with free selection of power splitting ratio [24], as multileg-splitters, that can act as 1×N, 1×N, or N×N [25]-[27] splitters and they have recently been used for wavelength-multiplexing [28].

A basic principle of the MMI coupler is "self-imaging". The self-imaging of periodic objects illuminated by coherent light was first described more than 150 years ago [29]. Self-focusing (graded index) waveguides can also produce periodic real images of an object [30]. The principle can be stated as follows: Self-imaging is a property of multi-mode waveguides by which an input field profile is reproduced in single or multiple images at periodic intervals along the propagation direction of the guide.

The central structure of an MMI device is a waveguide designed to support a large number of modes (typically ≥ 3). In order to launch light into and recover light from that multi-

mode waveguide, a number of access (usually single-moded) waveguides are placed at its beginning and at its end. Such devices are generally referred to as N×M MMI couplers, where N and M are the number of input and output waveguides respectively.

A full-modal propagation analysis is probably the most comprehensive theoretical tool to describe self-imaging phenomena in multi-mode waveguides. In not only supplies the basis for numerical modelling and design, but it also provides insight into the mechanism of multi-mode interference. Other approaches make use of ray optics [31], hybrid methods [32], or BPM type simulations. To describe the basic properties of MMI coupler, we follow here the guided-mode propagation analysis (MPA), proposed first in [33] for the formulation of the periodic imaging.

Self-imaging may exist in three-dimensional multi-mode structures, for which MPA combined with two-dimensional (finite-element or finite-difference methods) cross-section calculations can provide a useful simulation tool [34]. However, the current trend of etch-patterning produces step-index waveguides, which are, in general, single-moded in the transverse direction. As the lateral dimensions are much larger than the transverse dimensions, it is justified to assume that the modes have the same transverse behavior everywhere in the waveguide. The problem can thus be analyzed using a two-dimensional (lateral and longitudinal) structure, such as the one depicted in Fig.5.1, without losing generality. The analysis hereafter is based on such a 2-D representation of the multi-mode waveguide, which can be obtained from the actual 3-D physical multi-mode waveguide by several techniques, such as the effective index method (EIM) [35] or the spectral index method (SIM) [36].

A. Propagation constants

Fig.5.1 shows a step-index multi-mode waveguide of width W_M, ridge (effective) refractive index n_r and cladding (effective) refractive index n_c. The waveguide supports m lateral modes (as shown in Fig.5.2) with mode numbers ν = 0, 1, ... (m-1) at a free-space wavelength λ_0. The lateral wavenumber $k_{y\nu}$ and the propagation constant β_ν are related to the ridge index n_r by the dispersion equation

$$k_{y\nu}^2 + \beta_\nu^2 = k_0^2 n_r^2 \tag{5.1}$$

with

$$k_0 = \frac{2\pi}{\lambda_0} \tag{5.2}$$

$$k_{y\nu} = \frac{(\nu+1)\pi}{W_{e\nu}} \tag{5.3}$$

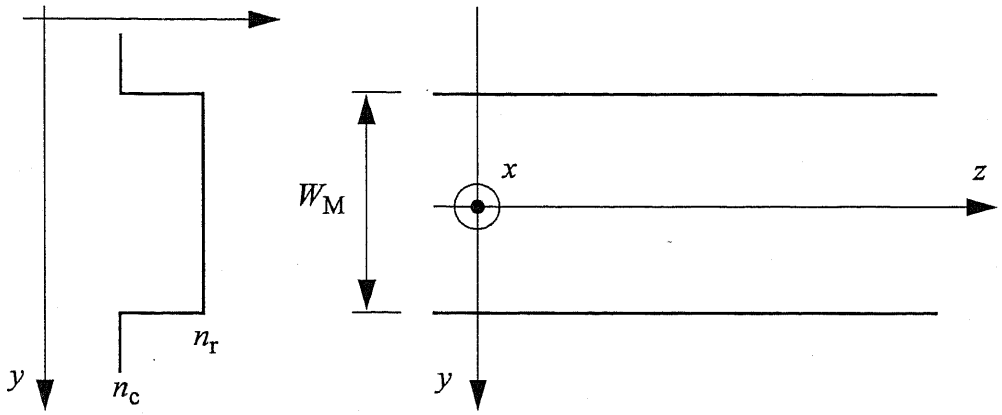

Fig.5.1 Two-dimensional representation of a step-index multi-mode waveguide; (effective) index lateral profile (left), and top view of ridge boundaries and coordinate system (right).

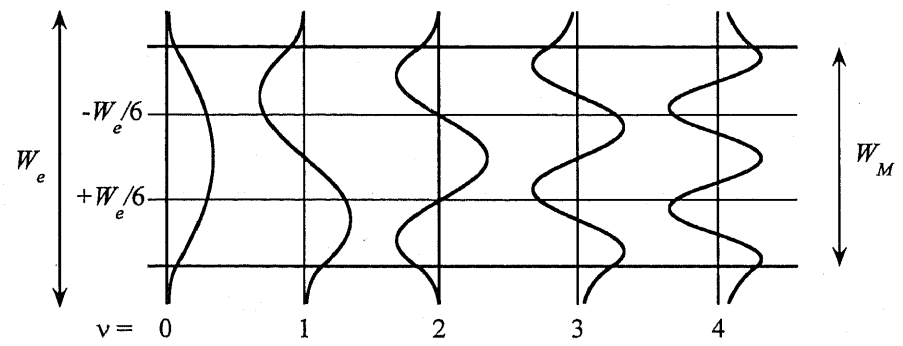

Fig.5.2 Example of amplitude-normalized lateral field profiles $\varphi_\nu(y)$ in a step-index multi-mode waveguide that support five TE modes. The parameters are n_r = 3.255, n_c = 3.24, W_M = 12 μm, and λ = 1.55 μm.

where the "effective" width W_{ev} takes into account the (polarization-dependent) lateral penetration depth of each mode field, associated with the Goos-Hähnchen shifts at the ridge boundaries. For high-contrast waveguides, the penetration depth is very small so that $W_{ev} \approx W_M$. In general, the effective widths W_{ev} can be approximated by the effective width W_{e0} corresponding to the fundamental mode [37], (which shall be noted for W_e simplicity):

$$W_{e\nu} \approx W_e = W_M + \left(\frac{\lambda_0}{\pi}\right)\left(\frac{n_c}{n_r}\right)^{2\sigma}(n_r^2 - n_c^2)^{-\frac{1}{2}} \tag{5.4}$$

where σ = 0 for TE and σ = 1 for TM. By using the binomial expansion with $k_{y\nu}^2 \ll k_0^2 n_r^2$, the propagation constants β_ν can be deduced from (5.1)-(5.3)

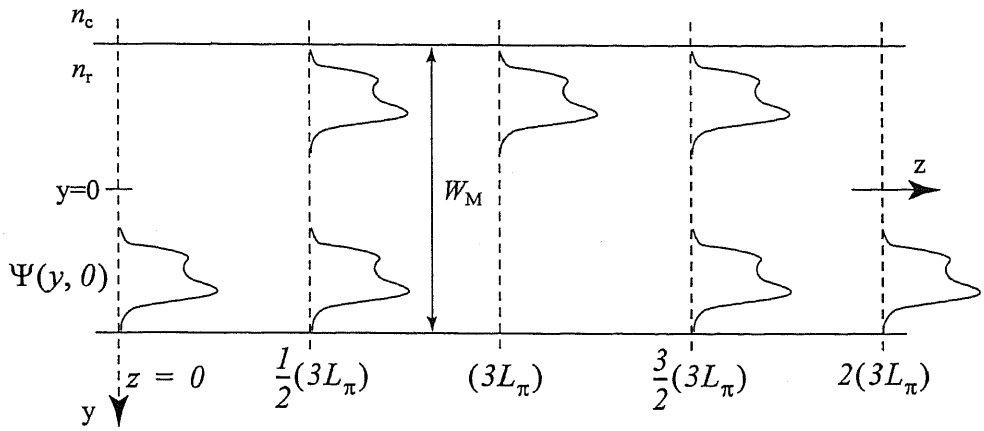

Fig.5.3 Multi-mode waveguide showing the input field $\Psi(y,0)$, a mirrored single image at $(3L_\pi)$, a direct image at $2(3L_\pi)$, and two-fold images at $\frac{1}{2}(3L_\pi)$ and $\frac{3}{2}(3L_\pi)$.

$$\beta_\nu \approx k_0 n_r - \frac{(\nu+1)^2 \pi \lambda_0}{4 n_r W_e^2}. \tag{5.5}$$

Therefore, the propagation constants in a step-index multimode waveguide show a nearly quadratic dependence with respect to the mode number ν.

By defining L_π as the beat length of the two lowest-order modes

$$L_\pi = \frac{\pi}{\beta_0 - \beta_1} \approx \frac{4 n_r W_e^2}{3\lambda_0} \tag{5.6}$$

the propagation constants spacing can be written as

$$\beta_0 - \beta_1 \approx \frac{\nu(\nu+2)\pi}{3L_\pi} \tag{5.7}$$

B. Guided-mode propagation analysis

An input field profile $\Psi(y, 0)$ imposed at $z = 0$ and totally contained with W_e (Fig.5.3), will be decomposed into the modal field distributions $\Psi_\nu(y)$ of all modes:

$$\Psi(y, 0) = \sum_\nu c_\nu \varphi_\nu(y) \tag{5.8}$$

where the summation should be understood as including guided as well as radiative modes. The field excitation coefficients c_ν can be estimated using overlap integrals

$$c_\nu = \frac{\int \Psi(y, 0)\varphi_\nu(y)dy}{\sqrt{\int \varphi_\nu^2(y)dy}} \tag{5.9}$$

based on the field-orthogonality relations.

If the "spatial spectrum" of the input field $\Psi(y, 0)$ is narrow enough not to excite unguided modes, (a condition satisfied for all practical applications), it may be decomposed into the guided modes alone

$$\Psi(y, 0) = \sum_{\nu=0}^{m-1} c_\nu \varphi_\nu(y). \tag{5.10}$$

The field profile at a distance z can then be written as a superposition of all the guided mode field distributions

$$\Psi(y, z) = \sum_{\nu=0}^{m-1} c_\nu \varphi_\nu(y) exp[j(\omega t - \beta_\nu z)]. \tag{5.11}$$

Taking the phase of the fundamental mode as a common factor out of the sum, dropping it and assuming the time dependence $\exp(j\omega t)$ implicit hereafter, the field profile $\Psi(y, z)$ becomes

$$\Psi(y, z) = \sum_{\nu=0}^{m-1} c_\nu \varphi_\nu(y) exp[j(\beta_0 - \beta_\nu z)]. \tag{5.12}$$

A useful expression for the field at a distance $z = L$ is then found by substituting (5.7) into (5.12)

$$\Psi(y, z) = \sum_{\nu=0}^{m-1} c_\nu \varphi_\nu(y) exp\left[j\frac{\nu(\nu+2)\pi}{3L_\pi}L\right]. \tag{5.13}$$

The shape of $\Psi(y, z)$, and consequently the types of images formed, will be determined by the modal excitation c_ν, and the properties of the mode phase factor

$$exp\left[j\frac{\nu(\nu+2)\pi}{3L_\pi}L\right]. \tag{5.14}$$

The following properties will prove useful in later derivations:

$$\nu(\nu+2) = \begin{cases} even\ for\ \nu\ even \\ odd\ for\ \nu\ odd \end{cases} \tag{5.15}$$

and,

$$\varphi_\nu(-y) = \begin{cases} \varphi_\nu(y)\ for\ \nu\ even \\ \varphi_\nu(-y)\ for\ \nu\ odd \end{cases} \tag{5.16}$$

the latter being a consequence of the structural symmetry with respect to the plane $y = 0$.

C. Single images

By inspecting (5.13), it can be seen that $\Psi(y, L)$ will be an image of $\Psi(y, 0)$ if

$$exp\left[j\frac{\nu(\nu+2)\pi}{3L_\pi}L\right] = 1\ or\ (-1)^\nu. \tag{5.17}$$

The first condition means that the phase changes of all the modes along L must differ by integer multiples of 2π. In this case, all guided modes interfere with the same relative phases as in $z = 0$; the image is thus a direct replica of the input field. The second condition means that the phase changes must be alternatively even and odd multiples of π. In this case, the even modes will be in phase and the odd modes in antiphase. Because of the odd symmetry stated in (5.16), the interference produces an image mirrored with respect to the plane $y = 0$.

Taking into account (5.15), it is evident that the first and second condition of (5.17) will be fulfilled at

$$L = p(3L_\pi) \text{ with } p = 0, 1, 2, \ldots \tag{5.18}$$

for p even and p odd, respectively. The factor p denotes the periodic nature of the imaging along the multi-mode waveguide. Direct and mirrored single images of the input field $\Psi(y, 0)$ will therefore be formed by general interference at distances z that are, respectively, even and odd multiples of the length $(3L_\pi)$, as shown in Fig.5.3. It should be clear at this point that the direct and mirrored single images can be exploited in bar- and cross-couplers, respectively.

D. Multiple images

Next, we investigate multiple imaging phenomena, which provide the basis for a broader range of MMI couplers.

In addition to the single images at distances given by (5.18), multiple images can be found as well. Let us first consider the images obtained half-way between the direct and mirrored image positions, i.e., at distances

$$L = \frac{p}{2}(3L_\pi) \text{ with } p = 1, 3, 5, \ldots \tag{5.19}$$

The total field at these lengths is found by substituting (5.19) into (5.13)

$$\Psi\left(y, \frac{p}{2}3L_\pi\right) = \sum_{\nu=0}^{m-1} c_\nu \varphi_\nu(y) \exp\left[j\nu(\nu+2)p\left(\frac{\pi}{2}\right)\right] \tag{5.20}$$

with p an odd integer. Taking into account the property of (5.15) and the mode field symmetry conditions of (5.16), (5.20) can be written as

$$\begin{aligned}\Psi\left(y, \frac{p}{2}3L_\pi\right) &= \sum_{\nu \text{ even}} c_\nu \varphi_\nu(y) + \sum_{\nu \text{ odd}} (-j)^p c_\nu \varphi_\nu(y) \\ &= \frac{1+(-j)^p}{2}\Psi(y, 0) + \frac{1-(-j)^p}{2}\Psi(-y, 0)\end{aligned} \tag{5.21}$$

The last equation represents a pair of images of $\Psi(y, 0)$, in quadrature and with amplitudes $1/\sqrt{2}$, at distances $z = \frac{1}{2}(3L_\pi), \frac{3}{2}(3L_\pi), \ldots$ as shown in Fig.5.3. This two-fold imaging can be used to realize 2×2 3-dB coupler.

E. Restricted interference

Thus far, no restrictions have been placed on the modal excitation. The selective excitation allow new interference mechanisms through shorter periodicities of the mode phase factor of (5.14).

By noting that

$$mod_3[\nu(\nu+2)] = 0 \text{ for } \nu \neq 2, 5, 8, \ldots \tag{5.22}$$

it is clear that the length periodicity of the mode phase factor of (5.14) will be reduced three times if

$$c_\nu = 0 \text{ for } \nu = 2, 5, 8, \ldots \tag{5.23}$$

Therefore, single (direct and inverted) images of the input field are now obtained at (cf. (5.18))

$$L = p(L_\pi) \text{ with } p = 0, 1, 2, \ldots \tag{5.24}$$

provided that the modes $\nu = 2, 5, 8, \ldots$ are not excited in the multi-mode waveguide. By the same token, two-fold images are found at $(p/2)L_\pi$ with p odd.

One possible way of attaining the selective excitation of (5.23) is by launching an even symmetric input field $\Psi(y, 0)$ (for example, a Gaussian beam) at $y = \pm W_e/6$. At these positions, the modes $\nu = 2, 5, 8, \ldots$ present a zero with odd symmetry, as shown in Fig.5.2. The overlap integrals of (5.9) between the (symmetric) input field and the (antisymmetric) mode fields will vanish and therefore $c_\nu = 0$ for $\nu = 2, 5, 8, \ldots$ Obviously, the number of input waveguides is in this case limited to two.

When the selective excitation of (5.23) is fulfilled, the modes contributing to the imaging are paired, i.e. the mode pairs 0-1, 3-4, 6-7, ... have similar relative properties. (For example, each even mode leads its odd partner by a phase difference of $\pi/2$ at $z = L_\pi/2$: the 3-dB length, by a phase difference of π at $z = L_\pi$: the cross-coupler length, etc.). This mechanism will be therefore called paired interference.

5.3 Proposal of MMI-BLD

The proposed MMI-BLD schematic view is shown in Fig.5.4. The all waveguides including the MMI coupler have active layer structure as conventional stripe LDs, so the proposed BLD has an active MMI cavity. The 2×2 MMI cavity is designed as input light totally couples

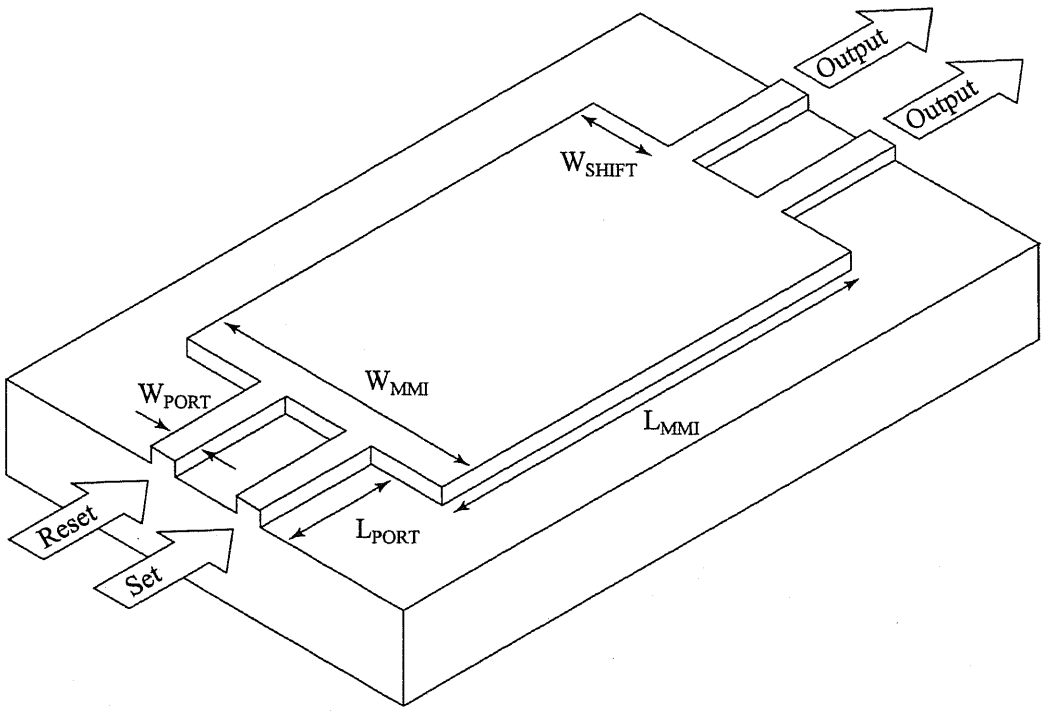

Fig.5.4 Schematic view of the 2×2 MMI-BLD designed as input light totally couples to a cross port. Each size is follows, W_{MMI} is 12 μm, L_{MMI} is 540 μm, W_{SHIFT} is 2.7 μm, L_{PORT} is 100 μm, W_{PORT} is 2 μm.

to a cross port, i.e. a cross-coupled MMI coupler. The MMI-BLD designed here supports two cross-coupled modes that propagate a round trip between the two diagonal ports, therefore the two cross-coupled modes are lasing modes of the MMI-BLD. The cross-coupled modes suppress each other through the gain saturation because the modal profiles of them overlap inside the MMI coupler. The gain saturation between the two modes leads to two-mode bistability. The all-optical flip-flop will be obtained by injecting a set or reset signal into each input port depicted as Fig.5.4.

5.4 Design of MMI Coupler

In this section, we investigate the design of the MMI coupler section for the MMI-BLD. The BLD proposed here includes a MMI coupler designed as the cross-coupled MMI coupler inside the laser cavity. The basic MMI couplers have the cross coupling properties as shown in Fig.5.3. Generally, the high-mesa waveguides are used for the MMI couplers because of their compactness. However, reflections inside the MMI couplers [19], [38]-[40] can be extremely effective for the BLD properties. Therefore, the ridge waveguide is adopted as the MMI-BLD. The reflection at the ridge waveguide's wall is very small since the refractive index difference between a waveguide's core and clad is below 1 %. In the

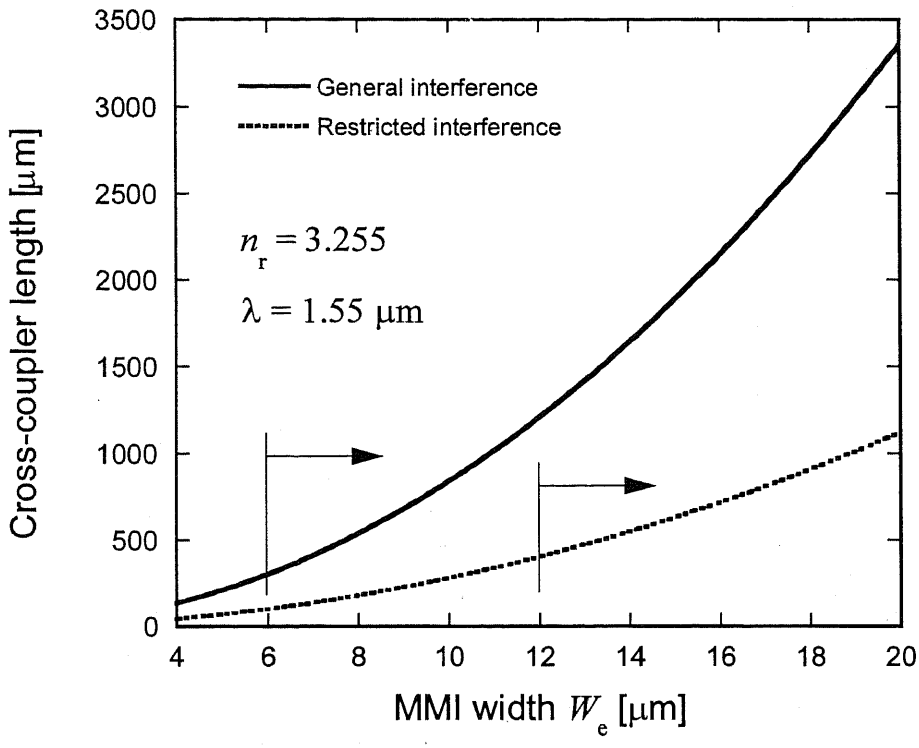

Fig.5.5 The cross-coupler length of MMI coupler with effective MMI width W_e. Solid line: general interference case, dotted line: restricted interference case. Refractive index of core n_r is 3.255, and the operation wavelength λ is 1.55 μm.

case of the active ridge waveguide that includes InGaAsP MQW (λ_g = 1.55 μm) structure, the indices of core and clad are estimated to be around 3.255 and 3.24, respectively. For the single-mode condition, the width of the ridge waveguide except for the MMI section is around 2 μm.

The cross-coupler lengths in the general interference and the restricted interference case are expressed as (5.18) and (5.24). Fig.5.5 shows the cross-coupler length with the effective MMI width. The solid line and the dotted line indicate the general interference and the restricted interference case, respectively. In general, there are two type of 3-dB or cross-coupled MMI, i.e. General interference type and Restricted interference type shown in Fig.5.6. The general interference type can reduce the MMI width, however it needs longer coupler length than the restricted interference type. To reduce the coupling between the adjacent ports, the gap between the two ports should be larger than 2 μm. To fulfill this restriction, the MMI width should be larger than 6 μm (the general interference type) or 12 μm (the restricted interference type) because the ridge width is 2 μm. The minimum lengths of two type MMIs are not so different shown as Fig.5.5. However, the cross-coupled MMI can not be realized very well in the general interference MMI because the number of modes

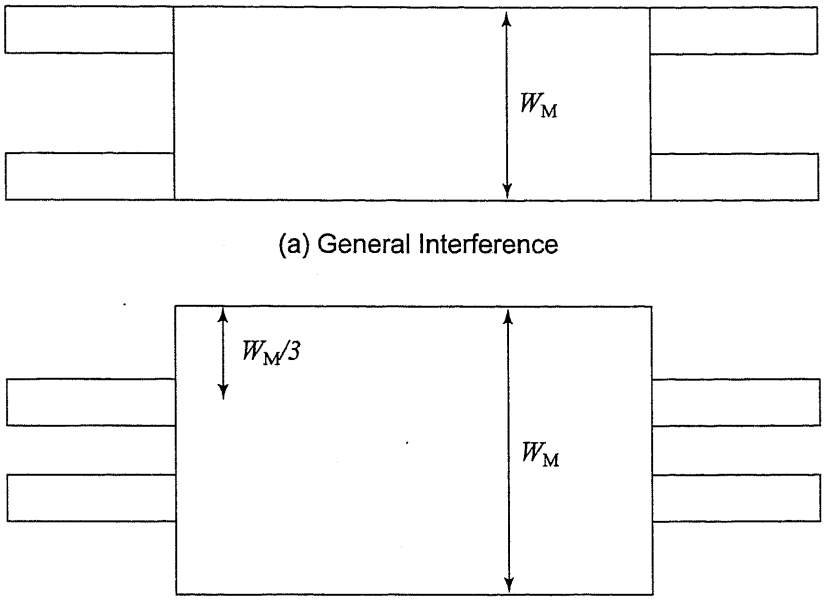

(a) General Interference

(b) Restricted Interference

Fig.5.6 Two types of the cross-coupled MMI, (a) General interference type, (b) Restricted interference type. For selective excitation, the ports of the restricted interference type are shifted from the side edge of MMI coupler.

is too small for self-imaging in the small index step waveguides. Fig.5.7 shows the number of modes in the case that the indices of core and clad are 3.255 and 3.24 respectively. There are only 3-modes in the 6-μm width multi-mode waveguide. The field propagations of the general interference cross-coupled MMIs are calculated by FD-BPM (Fig.5.8). The cross coupler lengths are 550 μm (W_M= 6 μm) and 820 μm (W_M= 8 μm), respectively. The coupler lengths are larger than the theoretical value in Fig.5.5 because the strong confinement such as high-mesa waveguides is assumed in the theory. The non-perfect self-imaging lead to the leak of the input light to the bar port, and the extinction ratio of the cross state degenerates into around 10 dB. The extinction ratio of the cross coupler is one of the most important factor for the MMI-BLD to keep the modal independence, so the general interference MMIs are not suitable for the MMI-BLD.

The restricted interference MMI take the advantage with respect to the extinction ratio. The restricted interference MMI needs large W_M more than 12 μm, which allow more modes. Actually, there are 5-modes in the case of W_M = 12 μm (see Fig.5.7). The higher extinction ratio can be obtained because of better self-imaging than the general interference MMI. From this reason, we adopt the restricted interference type (Fig.5.6 (a)) for the MMI-BLD. The width of the MMI is determined to be the minimum value shown in Fig.5.5, i.e. 12 μm. The modal profiles in the 12-μm width MMI are depicted in Fig.5.2, and the effective refractive indices calculated by the matrix approach (see Appendix C.) are listed in

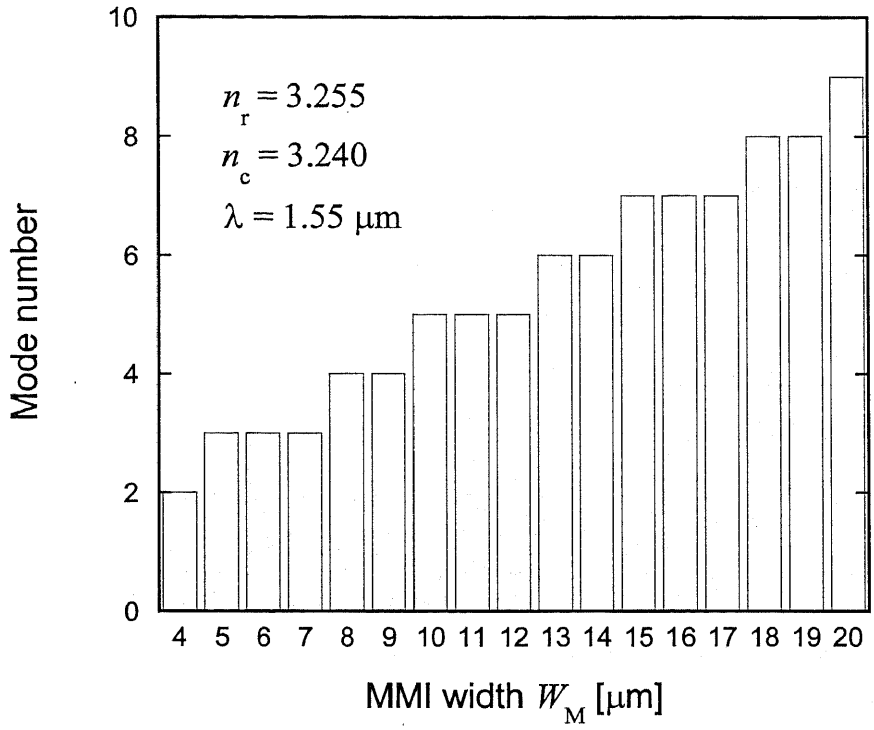

Fig.5.7 Number of modes in the ridge waveguides with MMI width W_M. Refractive indices of core n_r and clad n_c is 3.255 and 3.240 respectively, and the operation wavelength λ is 1.55 μm.

Table.5.1. The TE modes have almost same indices of TM modes, so the polarization dependence of the MMI coupler can be neglected.

Table.5.1 Effective refractive indices of 12-μm width MMI. The refractive indices of core n_r and clad n_c is 3.255 and 3.240 respectively, and the operation wavelength λ is 1.55 μm.

Mode order	n_{TE}	n_{TM}
0th	3.25450	3.25450
1st	3.25301	3.25301
2nd	3.25055	3.25055
3rd	3.24720	3.24719
4th	3.24312	3.24311

The field propagations are also calculated by FD-BPM. Fig.5.9 shows the two cross-coupled modes injected from the left side of the MMI coupler. We assume that the operation wavelength is 1.55 μm and the refractive indices of core and clad are 3.255, 3.24. We call mode-1 (Fig.5.9 (a)) and mode-2 (Fig.5.9 (b)) as the two cross-coupled modes. The cross coupler length is 540 μm (W_M = 12 μm), and each port length is 100 μm. The ports may be

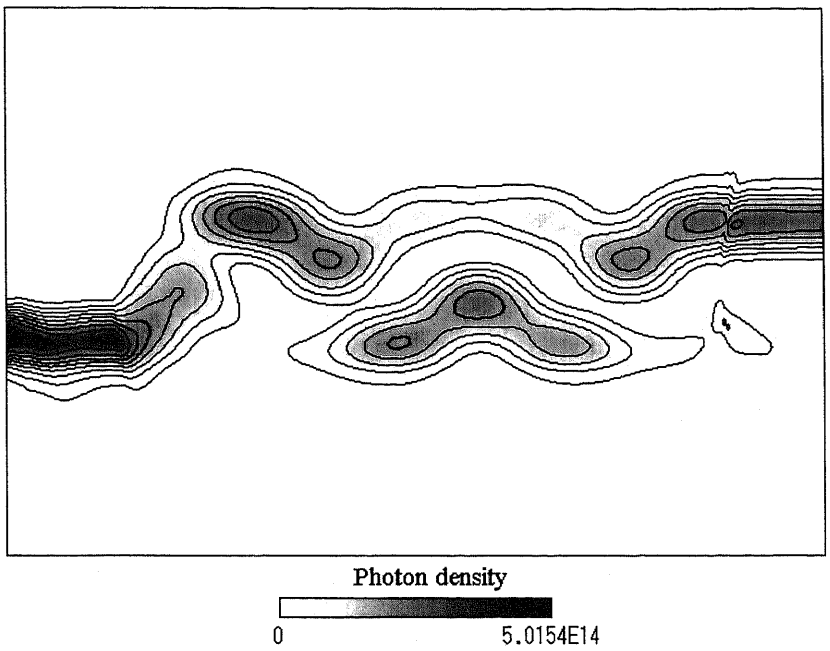

(a) W_M = 6 μm, L_M = 550 μm (General interference).

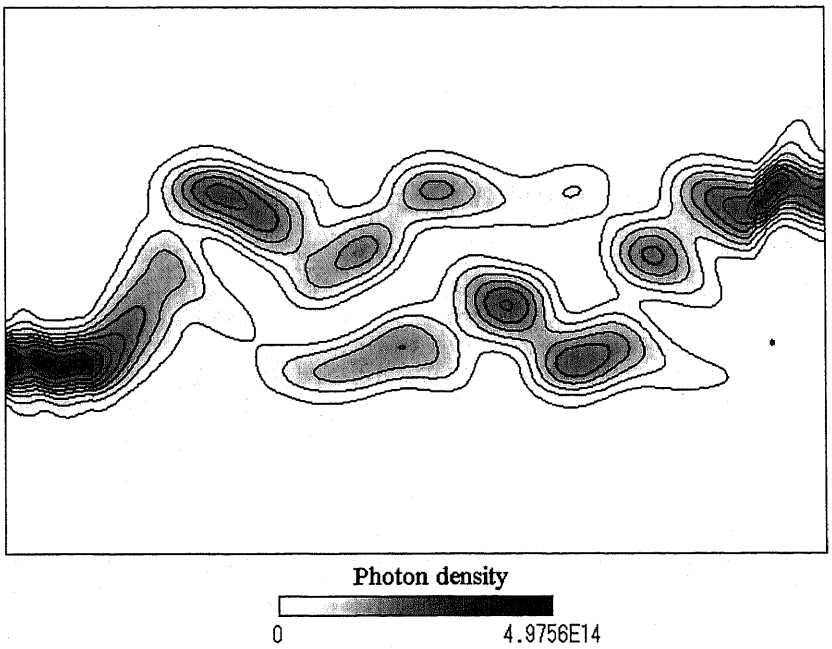

(b) W_M = 8 μm, L_M = 820 μm (General interference).

Fig.5.8 The field propagation (photon density [cm^{-3}]) of the general interferometer cross-coupled MMI calculated by FD-BPM, (a) W_M = 6 μm, (b) W_M = 8 μm. The cross coupler lengths are (a) 550 μm, (b) 820 μm. The port width is 2 μm, the refractive indices of core n_r and clad n_c is 3.255 and 3.240 respectively, and the operation wavelength λ is 1.55 μm.

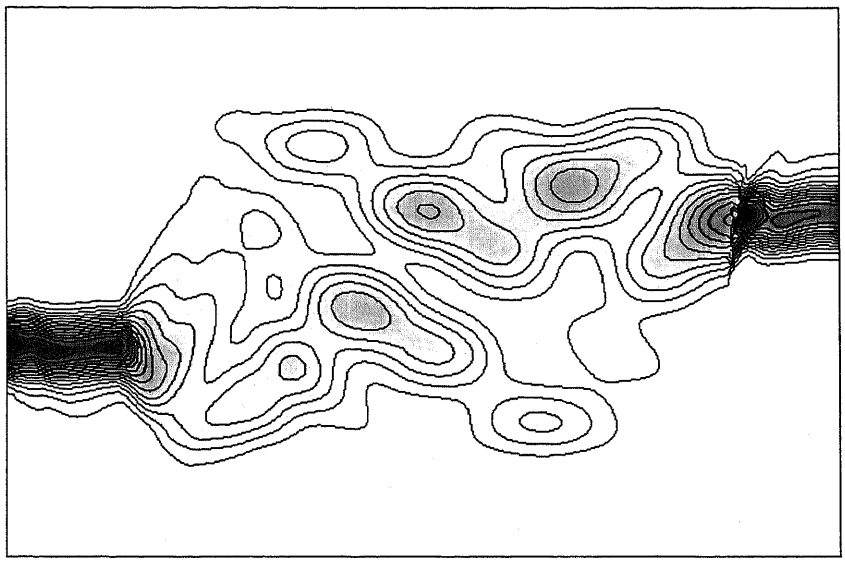

(a) mode-1

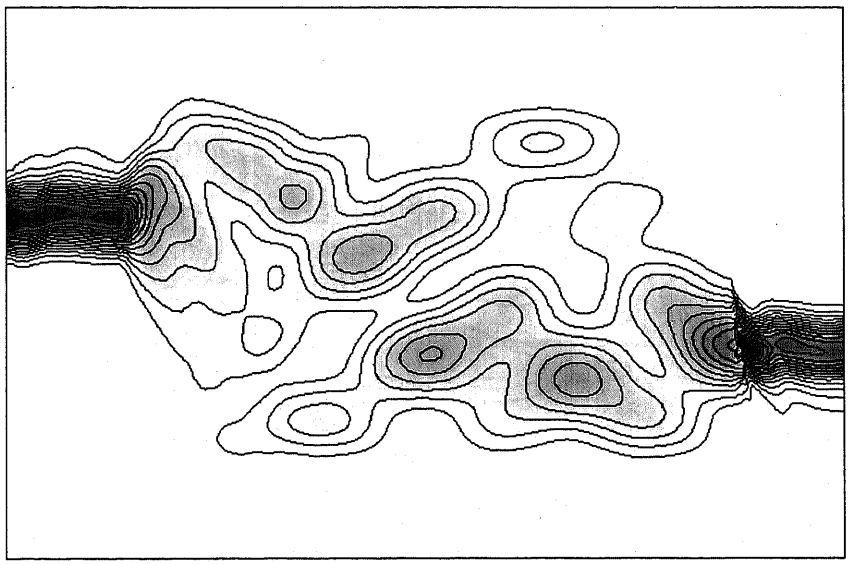

(b) mode-2

Fig.5.9 Propagation characteristics of the cross-coupled MMI for (a) mode-1 and (b) mode-2. Photon density [cm-3] distributions of the injected lights that propagate toward right-hand side from left-hand side are shown. The total power of the injected light is 0 dBm. The cross coupler lengths is 540 μm, and the MMI width is 12 μm. The port width is 2 μm, the refractive indices of core n_r and clad n_c is 3.255 and 3.240 respectively, and the operation wavelength λ is 1.55 μm.

equipped at $y = \pm W_e/6$, however W_M is slightly smaller than W_e. Therefore, we should adjust the port shift W_{SHIFT} to 2.7 μm (see Fig.5.4). The extinction ratio is improved to be around 20 dB. The schematic view of the MMI-BLD and each size are depicted in Fig.5.4. The two-mode bistability will occur between the cross-coupled modes, i.e. mode-1, and mode-2. In the following section, we discuss the bistability of the MMI-BLD designed here.

5.5 Bistability Analysis

The modeling of a MMI coupler for bistability analyses requires a little cautions because several modes inside the coupler interfere with each other. Moreover, the behavior of an active MMI coupler has been not well known yet. An active semiconductor waveguides has large nonlinear effects that lead MMI-BLD to complicated phenomena. We also consider the overlap between the two cross-coupled modes to analyze the bistability through cross gain saturation. Therefore, we chose FD-BPM developed in Section 2.3, which can easily treat complicated distributions of photon, refractive index, and gain inside the cavity.

A. General theory of two-mode bistability

The main origin of the bistability observed in two-mode lasers may be considered to arise from the gain saturation. If a laser oscillating in two different modes, the cross gain saturation between the two modes arises. To the lowest order in the nonlinearity, the saturated gains in the case of two modes are expressed as equations (2.21) in Section 2.3. Two possible characteristics situations, weak coupling and strong coupling are derived from the rate equation analysis [41]-[44].

To the lowest order in the nonlinearity, the saturated gain $g_i(I)$ of a particular mode (i) of an idealized laser is related to the unsaturated gain g_{i0} through the mode intensity I_i and saturation parameter I_{isat} as follows.

$$g_i(I) = \frac{g_{i0}}{1 + \varepsilon_{ii} I_i} \tag{5.25}$$

where $\varepsilon_{ii} = 1/I_{isat}$. When $\varepsilon_{ii} I_i \ll 1$, $g_i(I)$ can be rewritten as follows.

$$g_i(I) = g_{i0}(1 - \varepsilon_{ii} I_i) \tag{5.26}$$

In the case of two modes, mode 1 and mode 2, the rate of change of one-mode intensity also depends on the intensity of the other:

$$\frac{dI_1}{dt} = g_1 I_1 (1 - \varepsilon_{11} I_1 - \varepsilon_{12} I_2) \tag{5.27}$$

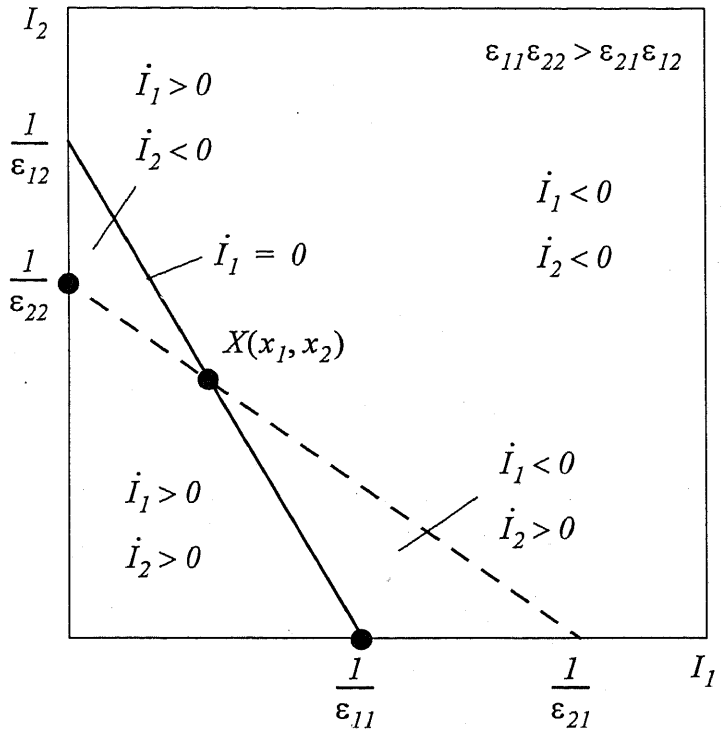

Fig.5.10 Diagram for light intensities I_1 and I_2 of two-mode oscillation in the case of $\varepsilon_{11}\varepsilon_{22} > \varepsilon_{21}\varepsilon_{12}$ (weak coupling).

$$\frac{dI_2}{dt} = g_2 I_2(1 - \varepsilon_{21} I_1 - \varepsilon_{22} I_2) \tag{5.28}$$

where ε_{11} and ε_{22} are self-saturation and ε_{12} and ε_{21} are cross-saturation coefficients. The stability of such a gain-coupled two-mode laser system can be analyzed in the phase plane (I_1, I_2). Equations (5.27) and (5.28) for the steady state give

$$I_1 = 0 \text{ or } \varepsilon_{11} I_1 + \varepsilon_{12} I_2 = 1 \tag{5.29}$$

$$I_2 = 0 \text{ or } \varepsilon_{21} I_1 + \varepsilon_{22} I_2 = 1 \tag{5.30}$$

since $\dot{I}_1 = 0$ and $\dot{I}_2 = 0$, where the dot denotes the time derivative.

We draw a graph with I_1 as the abscissa and I_2 as the ordinate, as in Fig.5.10. Then (5.29) gives the I_2 axis and the solid slant line, while (5.30) gives the I_1 axis and the broken line. It can be seen from (5.29) that $\dot{I}_1 = 0$ on the solid slant line, while $\dot{I}_1 < 0$ above the line on the right and $\dot{I}_1 > 0$ below it on the left. The condition for I_2 is similar with regard to the broken line. Therefore, the time variations of I_1 and I_2 in the four domains partitioned by the two slant lines are shown in Fig.5.10. It is thus found that the states satisfying the steady-

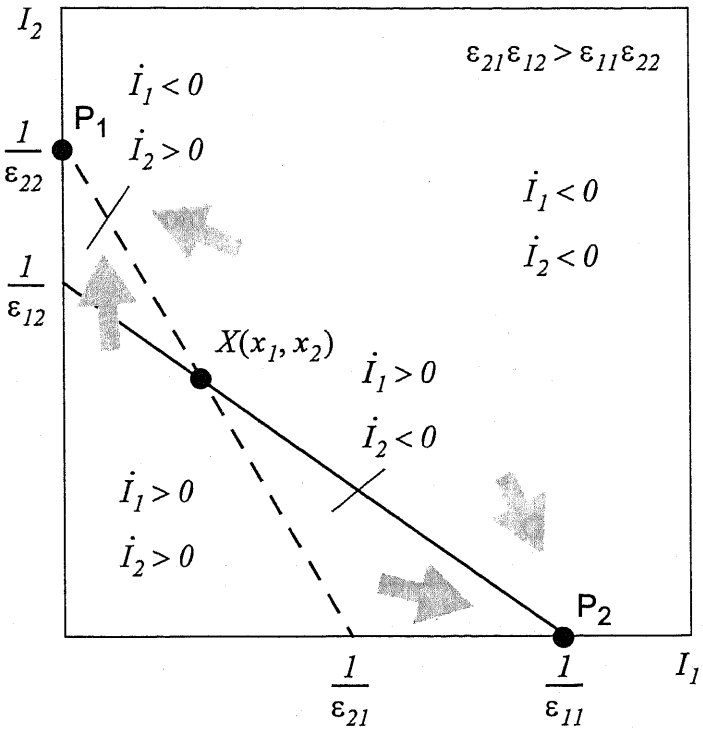

Fig.5.11 Diagram for light intensities I_1 and I_2 of two-mode oscillation in the case of $\varepsilon_{21}\varepsilon_{21} > \varepsilon_{11}\varepsilon_{22}$ (strong coupling). In this case, there are two stable points, P_1 and P_2, and bistability will occur

state conditions simultaneously are given by the three black points in Fig.5.10, of which the stable point is $X(x_1, x_2)$:

$$x_1 = (\varepsilon_{12} - \varepsilon_{22}) / (\varepsilon_{21}\varepsilon_{12} - \varepsilon_{11}\varepsilon_{22}) \tag{5.31}$$

$$x_2 = (\varepsilon_{21} - \varepsilon_{11}) / (\varepsilon_{21}\varepsilon_{12} - \varepsilon_{11}\varepsilon_{22}) \tag{5.32}$$

It should be noted that this holds for the weak-coupling case.

Two possible characteristic situations, weak coupling and strong coupling can occur. If $\varepsilon_{11}\varepsilon_{22} > \varepsilon_{12}\varepsilon_{21}$ (weak coupling), in general, there can be stable one- or two-mode operation. If X is below the I_1 axis ($x_1 > 0$, $x_2 < 0$), only mode 1 will oscillate. If $x_1 > 0$, $x_2 > 0$, stable simultaneous two-mode oscillation will result. If $x_1 < 0$, $x_2 > 0$, the laser will oscillate only in mode 2.

Bistability will occur if $\varepsilon_{12}\varepsilon_{21} > \varepsilon_{11}\varepsilon_{22}$ (strong coupling). In this case, if X is in the first quadrant of the phase plane as shown in Fig.5.11, the laser is bistable. Also, in this case, if $x_1 > 0$, $x_2 < 0$, mode 2 will oscillate; if $x_1 < 0$, $x_2 > 0$, mode 1 will oscillate. Thus, in the strong-coupling case, only one of the modes oscillates, the other mode being suppressed. In the resulting steady state, therefore, the laser does not oscillate simultaneously in two modes,

but it oscillates in only one of the modes. At the stable point P_1 in Fig.5.11, it oscillates in mode 1, while at P_2 it oscillates in mode 2. Which of the bistabie states is reached is dependent on the initial conditions, as can be seen from the arrows in Fig.5.11.

Without going into the details of the numerical calculations, we can say several characteristics of gain saturation parameters from the symmetry properties of the crystal alone [45]. In the case of InGaAsP with cubic symmetry, the relationship between a self-saturation coefficient and a cross-saturation coefficient for the TE modes is described as follows.

$$\begin{aligned} \varepsilon_{12}(\omega_1 = \omega_0, \omega_2 = \omega_0) &= 2 \times \varepsilon_{11}(\omega_0) \\ \varepsilon_{21}(\omega_2 = \omega_0, \omega_1 = \omega_0) &= 2 \times \varepsilon_{22}(\omega_0) \end{aligned} \tag{5.33}$$

where ω_1 and ω_2 are angular frequencies of the two TE modes, respectively. It is important that the two modes have the same frequency because the cross-saturation coefficient is significant only around $\omega_1 = \omega_2$ and it vanishes otherwise [46].

In the case of the MMI-BLD which we propose, the two-mode bistability will occur between the cross-coupled modes shown in Fig.5.9. The two modes, i.e. mode-1 and mode-2 are symmetrical and have the same lasing frequency, so we assume that equations (5.33) are always satisfied. Therefore, the strong coupling condition for two-mode bistability is locally fulfilled. However the two cross-coupled modes have spatially different distributions inside the MMI cavity. In other words, the overlap between the two modes is not 100 %. When the overlap is smaller than 100 %, effective cross-saturation coefficient as the whole MMI cavity becomes smaller. The overlap as the whole cavity between the two modes can be estimated using a following equation.

$$(overlap) = \frac{\iint \sqrt{P_1(x,z)P_2(x,z)}(dx)dz}{\sqrt{\iint P_1(x,z)(dx)dz} \cdot \sqrt{\iint P_2(x,z)(dx)dz}} \tag{5.34}$$

where P_1 and P_2 are power distribution of the two modes inside the MMI cavity calculated by FD-BPM, respectively. In the case of the proposed MMI-BLD, the overlap between the two modes is below 100 %, so it is necessary to evaluate correctly whether the effective cross gain saturation is large enough for two-mode bistability. In these points, we should investigate the two-mode bistability condition.

B. Analysis of bistable switching (without saturable absorber)

The parameters used in this paper are shown in Table.2.1. We consider an InGaAsP Multi Quantum Well (MQW) structure whose band gap energy is around 1.55 μm. The gain saturation is affected by many factors such as material, strain, and MQW structure. The gain saturation coefficients of InGaAs or InGaAsP materials are measured to be 2.0×10^{-17} - 6.0×10^{-17} cm^3 [47][48]. In the two-mode bistability, the relative value of the gain satura-

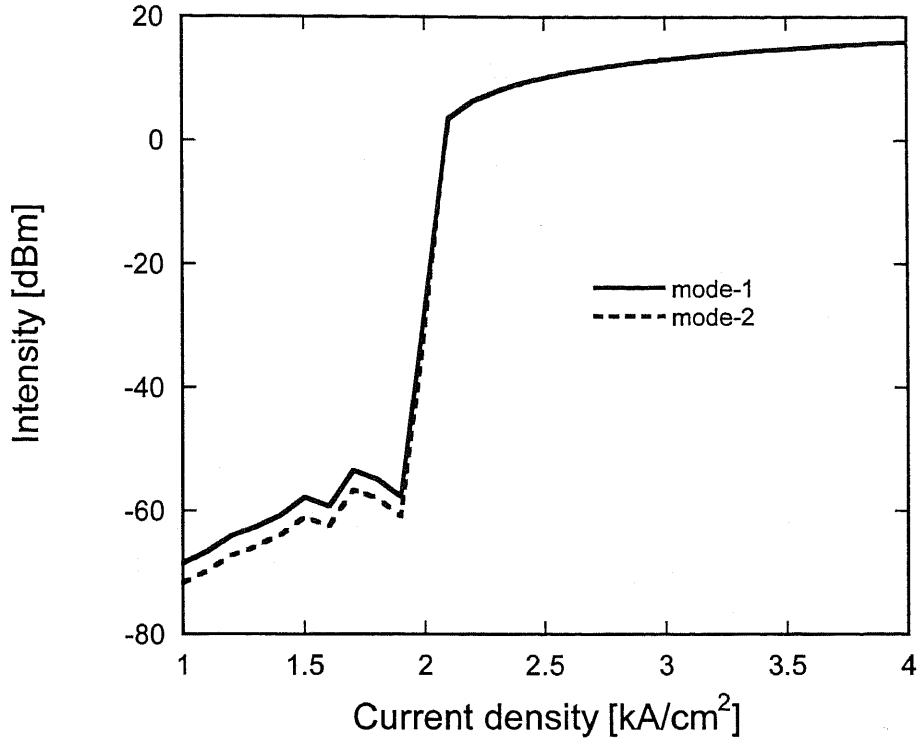

Fig.5.12 L-I characteristic of the MMI-BLD with no saturable absorber. The injected lights for mode-1 and mode-2 are 55 dBm and 60 dBm. There is no bifurcation point between the two cross-coupled mode, so the MMI-BLD doesn't have pitchfork bifurcation bistability.

tion coefficient is more important than absolute value, so we assume 8.0×10^{-17} cm^3 as the self-saturation coefficient and the cross-saturation coefficient is derived from equations (5.33). While we also analyzed 1.0 - 10.0×10^{-17} cm^3 as self-saturation coefficient, the bistability characteristics were almost same as 8.0×10^{-17} cm^3. So we show the results of only the 8.0×10^{-17} cm^3 case.

There are the two oscillating modes in the MMI-BLD shown in Fig.5.9. The overlap between mode-1 and mode-2 is around 60 % by calculating equation (5.34). The L-I characteristic in the case of uniform current injection is shown Fig.5.12. The light injection power to mode-1 is 55 dBm that is 5 dBm larger than mode-2, so if the MMI cavity has enough overlap between mode-1 and mode-2, pitchfork bifurcation bistability, i.e. mode-1 starts lasing and mode-2 is suppressed through cross gain saturation, will appear. However, the L-I characteristic in Fig.5.12 has no bifurcate points. We also calculate L-I characteristics with self-saturation coefficients varied from 1.0×10^{-17} - 1.6×10^{-16} cm^3, but these characteristics never show pitchfork bifurcation. From this results, we conclude that the mode overlap of the MMI cavity designed here is too small for pitchfork bifurcation bistability and the saturable absorber will be needed to get two-mode bistability.

C. Analysis of bistable switching (with saturable absorber)

If the MMI-BLD has some saturable absorbers at its ports, the effective self gain saturation of each mode becomes small [49], so this effect leads to satisfy the strong coupling condition.

If absorbers are included and have saturation characteristics similar to the gain medium, then the two-mode rate equations can be written as

$$\frac{dI_1}{dt} = \left(\frac{g_1}{1+\varepsilon_{11}I_1+\varepsilon_{12}I_2} - \frac{a_1}{1+\varepsilon_{a11}I_1+\varepsilon_{a12}I_2}\right)I_1 \tag{5.35}$$

$$\frac{dI_2}{dt} = \left(\frac{g_2}{1+\varepsilon_{21}I_1+\varepsilon_{22}I_2} - \frac{a_2}{1+\varepsilon_{a21}I_1+\varepsilon_{a22}I_2}\right)I_2. \tag{5.36}$$

The first and second terms in parentheses describe the saturation behavior of the gain and the saturable absorber, respectively. The stability problem is analyzed by solving the above equations in the steady state and then examining the stability of each steady-state solution. In the steady-state, (5.35) and (5.36) become

$$I_1 = 0 \text{ or } G_1(I_1, I_2) = 0 \tag{5.37}$$

where $G_1(I_1, I_2) = \dfrac{g_1}{1+\varepsilon_{11}I_1+\varepsilon_{12}I_2} - \dfrac{a_1}{1+\varepsilon_{a11}I_1+\varepsilon_{a12}I_2}$

$$I_2 = 0 \text{ or } G_2(I_1, I_2) = 0 \tag{5.38}$$

where $G_2(I_1, I_2) = \dfrac{g_2}{1+\varepsilon_{21}I_1+\varepsilon_{22}I_2} - \dfrac{a_2}{1+\varepsilon_{a21}I_1+\varepsilon_{a22}I_2}$.

Similar to the case without saturable absorbers, $G_1(I_1, I_2) = 0$ and $G_2(I_1, I_2) = 0$ represent two straight lines on the I_1-I_2 phase plane as shown in Fig.5.13. With some further manipulation, $G_1(I_1, I_2) = 0$ and $G_2(I_1, I_2) = 0$ could be arranged

$$G'_1(I_1, I_2) = \frac{g_1}{1+\varepsilon'_{11}I_1+\varepsilon'_{12}I_2} - a_1 = 0 \tag{5.39}$$

$$G'_2(I_1, I_2) = \frac{g_2}{1+\varepsilon'_{21}I_1+\varepsilon'_{22}I_2} - a_2 = 0 \tag{5.40}$$

where

$$\varepsilon'_{11} = \varepsilon_{11} - \frac{g_1}{a_1}\varepsilon_{a11} \tag{5.41}$$

$$\varepsilon'_{22} = \varepsilon_{22} - \frac{g_2}{a_2}\varepsilon_{a22} \tag{5.42}$$

$$\varepsilon'_{12} = \varepsilon_{12} - \frac{g_1}{a_1}\varepsilon_{a12} \tag{5.43}$$

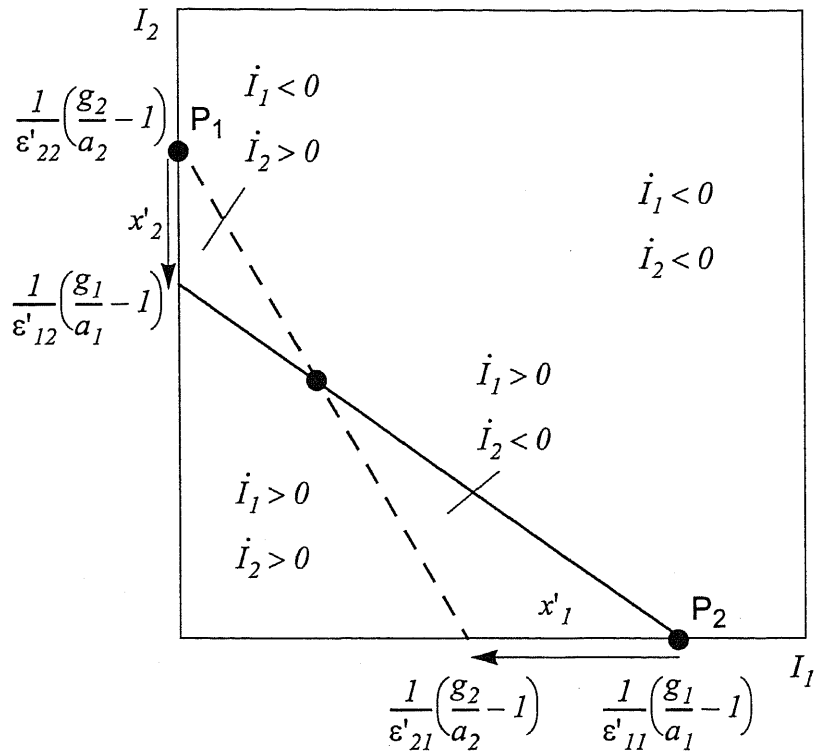

Fig.5.13 Diagram for light intensities I_1 and I_2 of two-mode oscillation in the case of existenece of saturable absorber. In this case shown as this diagram, two-mode bistability occur.

$$\varepsilon'_{21} = \varepsilon_{21} - \frac{g_2}{a_2}\varepsilon_{a21}. \tag{5.44}$$

The conditions for the stability are then summarized in the following. The conditions are almost same as that without saturable absorber. Define

$$\begin{aligned} x'_1 &= \frac{1}{\varepsilon'_{21}}\left(\frac{g_2}{a_2}-1\right) - \frac{1}{\varepsilon'_{11}}\left(\frac{g_1}{a_1}-1\right) \\ x'_2 &= \frac{1}{\varepsilon'_{12}}\left(\frac{g_1}{a_1}-1\right) - \frac{1}{\varepsilon'_{22}}\left(\frac{g_2}{a_2}-1\right) \end{aligned} \tag{5.45}$$

1) $x'_1<0$ and $x'_2>0$: oscillation at mode 1.
2) $x'_1>0$ and $x'_2<0$: oscillation at mode 2.
3) $x'_1>0$ and $x'_2>0$: simultaneous oscillation at both mode 1 and mode 2.
4) $x'_1<0$ and $x'_2<0$: bistability.

Situation 4) shown in Fig.5.13 concludes that the necessary condition for the bistability is

$$\varepsilon'_{21}\varepsilon'_{12} > \varepsilon'_{11}\varepsilon'_{22}. \tag{5.46}$$

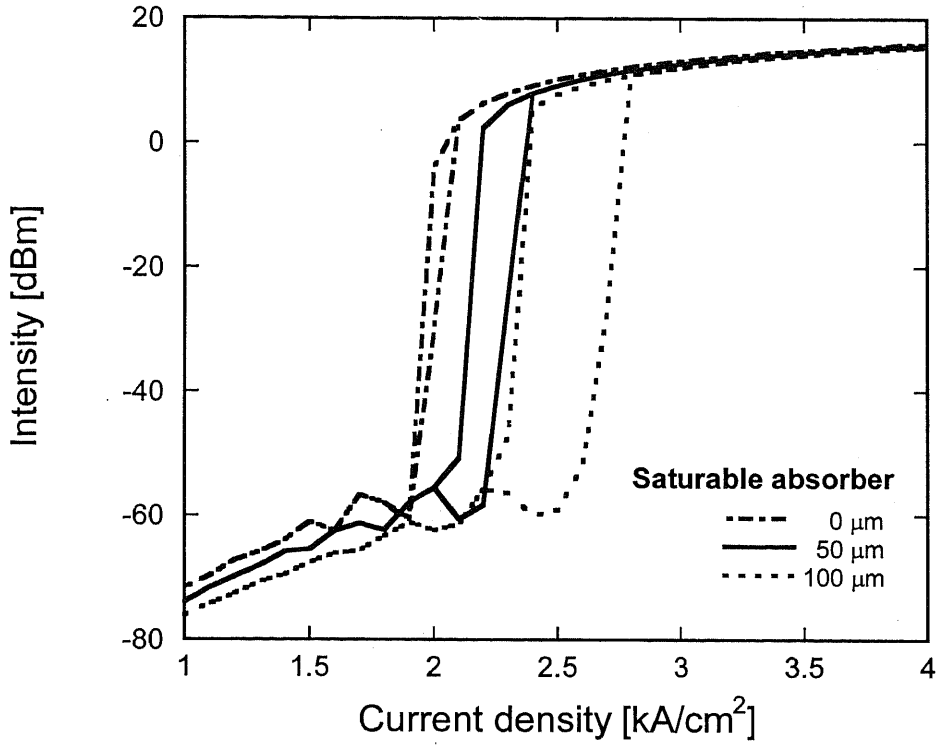

Fig.5.14 L-I characteristics of the MMI-BLD with saturable absorbers, 0, 50, 100 μm. The saturable absorbers are biased 0.1 kA/cm^2. The MMI-BLD shows S-shaped bistability for nonlinear absorption of saturable absorbers as increasing the absorber length.

From (5.41) - (5.44), this condition could still hold even when $\varepsilon_{21}\varepsilon_{12} < \varepsilon_{11}\varepsilon_{22}$. Therefore, the interplay between the gain and absorption saturations makes the condition, $\varepsilon_{21}\varepsilon_{12} < \varepsilon_{11}\varepsilon_{22}$, able to cause two-mode bistability.

The saturable absorbers equipped at the end of the output ports reduce the effective self-saturation coefficient of the whole cavity and the bistability condition, i.e. equation (5.46) is satisfied. Fig.5.14 shows L-I characteristics with the length of the saturable absorber (biased at 0.1 kA/cm^2) being 0, 50, 100 μm, respectively. By increasing the saturable absorber length, the lasing threshold and the width of the hysteresis loop increase due to nonlinear absorption. The injection current of the gain region should be within the hysteresis loop in order to make user of the two-mode bistability. We adopt 50 μm as the saturable absorber length and 2.1 kA/cm^2 as the bias current density of the gain region in following analyses.

External light injection to mode-1 saturates the absorption to mode-1 small, and then the mode-1 starts the laser radiation (we say it ON state). At the same time, the cross gain saturation and the absorption to mode-2 by the saturable absorber suppress mode-2. Simi-

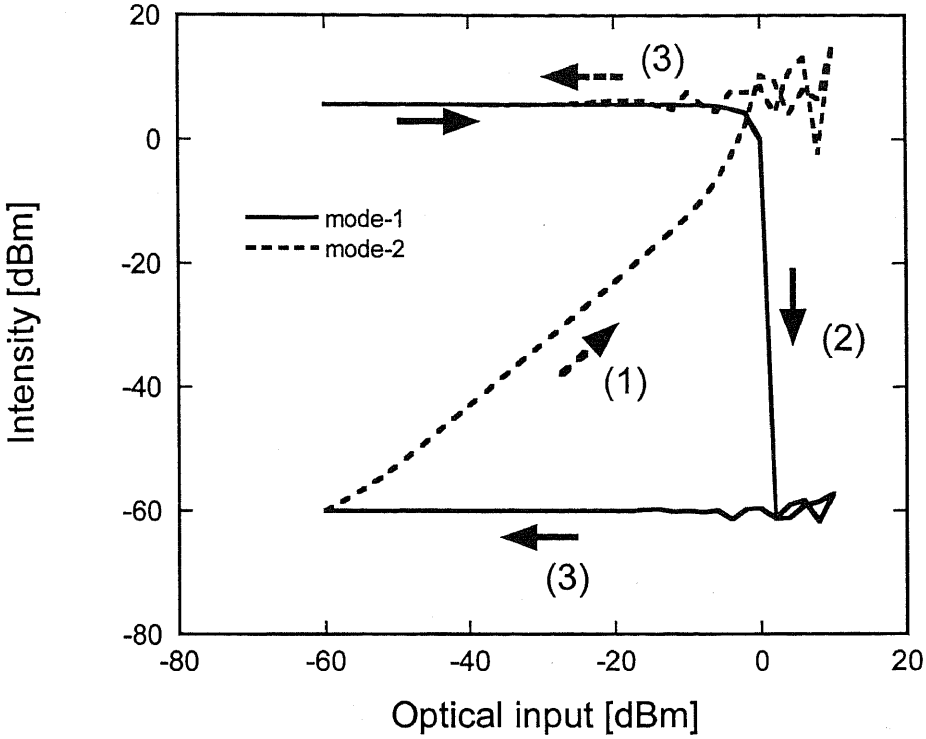

Fig.5.15 Bistable switching characteristics of the MMI-BLD. The length of saturable absorber is 50 μm. The current densities of the absorption and gain region are fixed at 0.1 kA/cm^2 and 2.1 kA/cm^2, respectively. The switching between the two cross-coupled mode occurs by 0 dBm light injection to mode-2.

larly, the light injection to mode-2 at the ON state suppresses mode-1 through cross gain saturation, and stops the laser oscillation. Simultaneously, the absorption of mode-2's saturable absorber decreases by the light injection to result in lasing of mode-2 (OFF state). Even when the light injection is terminated, cross gain saturation and recovered absorption of mode-1's saturable absorber prevent mode-1 from lasing again. In this way, all-optical flip-flop operation in the MMI-BLD is realized. Fig.5.15 shows this bistable switching characteristics. The MMI-BLD is set to the ON state by set-pulse at the beginning of the calculation. Increasing the light injection into mode-2 (1) suddenly results in extinction of mode-1 (2) at around 0 dBm, thus switching the MMI-BLD into the OFF state. When the light injection is eliminated, it keeps the OFF state (3).

The photon density distributions of the ON and OFF states inside the cavity are shown in Fig.5.16 (a), (b). These distributions are almost same as those which the waveguide has uniform refractive index (Fig.5.9 (a), (b)), and mode-1 and mode-2 keep the modal shapes after lasing.

Fig.5.17 and Fig.5.18 show distributions of carrier density and refractive index in the case of the ON state, respectively. Because there are strong stimulated emission at the large

optical intensity points, the carrier distribution becomes uneven, i.e. spatial hole-burning occurs. Inside the MMI coupler, the range of the carrier density is 8.8×10^{17} to 9.2×10^{17} cm^{-3}. This difference of carrier density leads to the uneven distribution of refractive index, 3.2535 to 3.254 inside the MMI coupler. The range of refractive index is small enough for the tolerance of the MMI coupler, so the spatial hole-burning don't make some unstable operation such as filamentation, and the laser radiations of mode-1 and mode-2 exist stably. The photon density at the output cross section is plotted by logarithm to Fig.5.19. The refractive index profile is also shown. The cross-talk to mode-2 from mode-1 lasing at the ON state is less than -15 dB, so the bistable switching of the MMI-BLD has high extinction ratio.

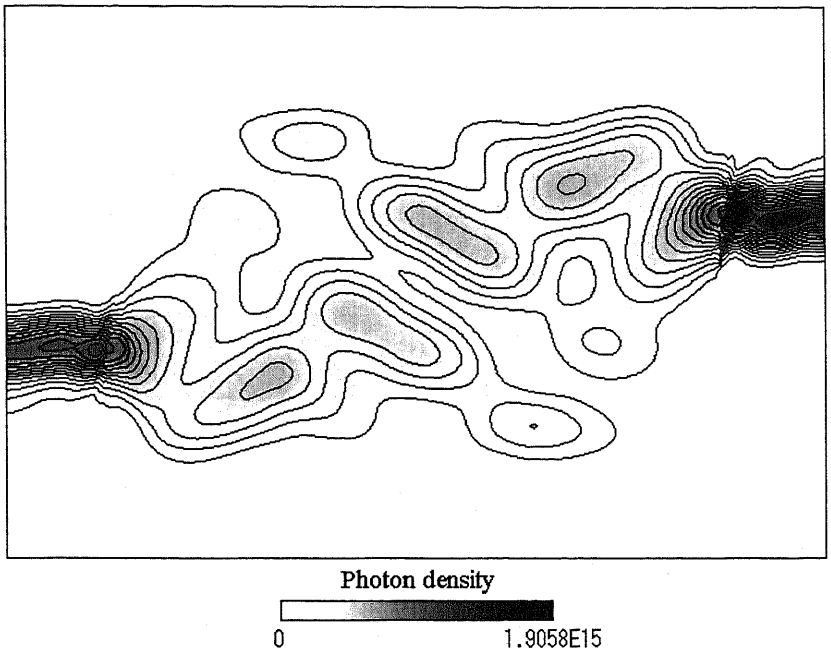

(a) ON state (lasing: mode-1).

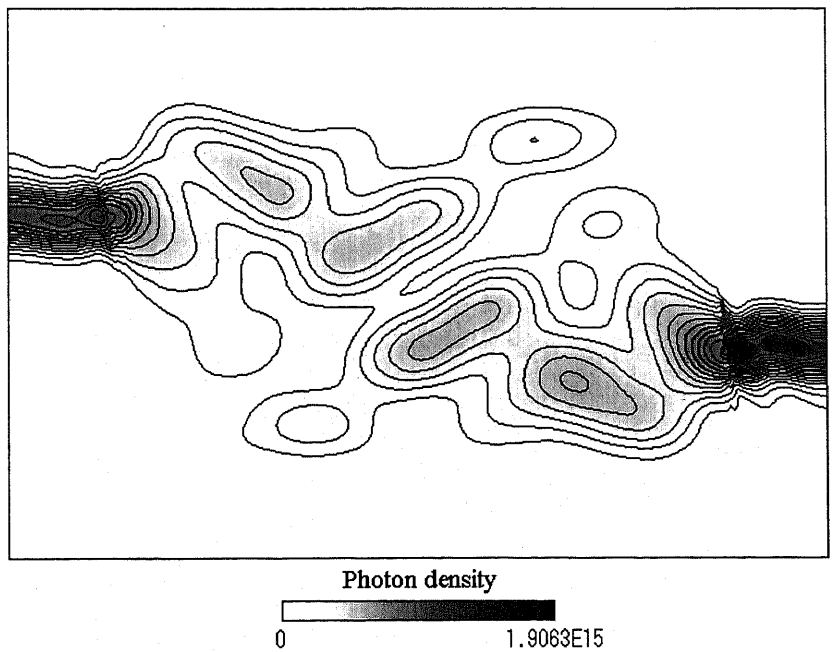

(b) OFF state (lasing: mode-2).

Fig.5.16 Photon density [cm^{-3}] distributions of the MMI-BLD at (a) mode-1 and (b) mode-2. Theses distributions are almost same as the propagation characteristics of the MMI cavity, and the modal shape is well kept after lasing.

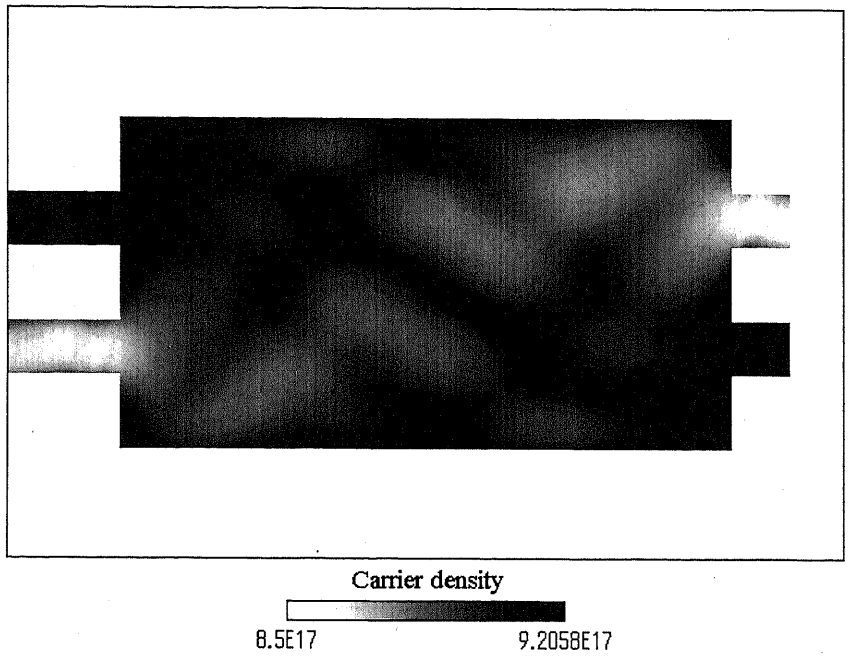

Fig.5.17 Carrier density [cm^{-3}] distributions of the MMI-BLD lasing at mode-1. Carrier density less than 8.5×10^{17} cm^{-3} is omitted to emphasize the difference inside the MMI cavity, so the absorption regions of the output ports are shown as blank. Spatial hole-burning occurs because the uneven field distribution of mode-1. The range of the carrier density inside the MMI coupler is 8.8×10^{17} cm^{-3} to 9.2×10^{17} cm^{-3}.

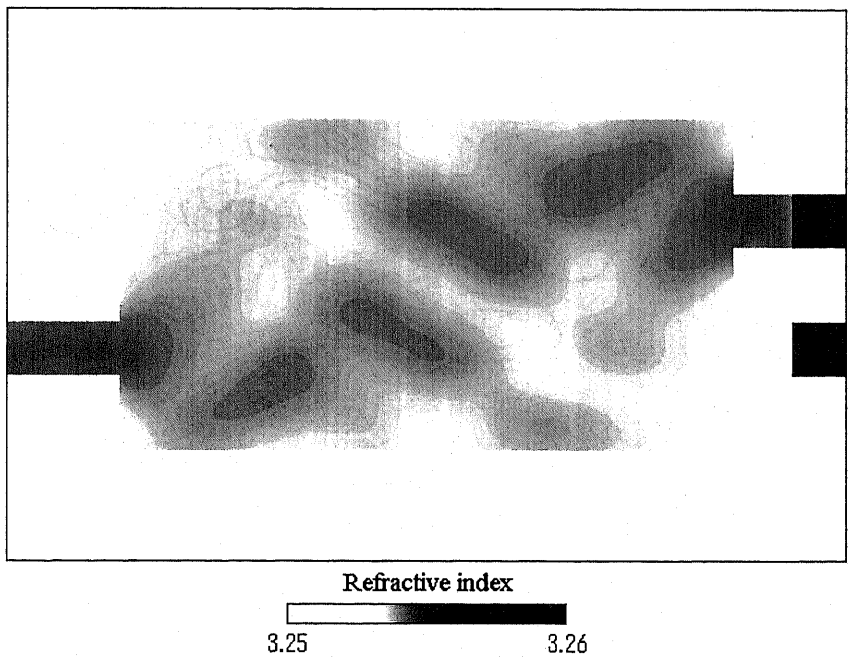

Fig.5.18 Refractive index distributions of the MMI-BLD lasing at mode-1. Refractive index less than 3.25 is omitted as blank to emphasize the difference inside the MMI cavity. Spatial hole-burning makes the uneven distribution of refractive index. The range of the refractive index inside the MMI coupler is 3.2535 to 3.254.

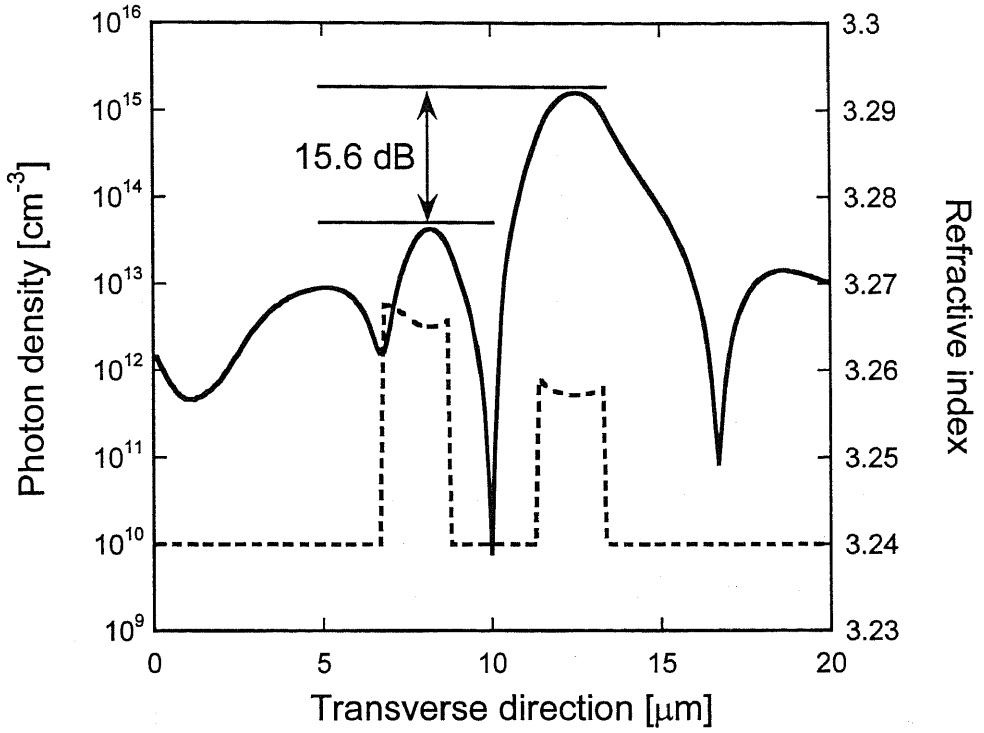

Fig.5.19 The photon density [cm^{-3}] at the output cross section in the case of mode-1 lasing. The cross-talk to mode-2 from mode-1 is less than -15 dBm, so the MMI-BLD has high extinction ratio of bistable switching.

5.6 Estimation of Maximum Switching Speed

The switching speed between the ON and OFF states is one of the most important factor of all-optical flip-flop devices. In the case of the DC-BLD, we estimate that the maximum switching speed is limited by relaxation oscillation frequency, i.e. around 10 GHz. On the other hand, the change of carrier density inside the active MMI coupler is suppressed in the case of the MMI-BLD, because mode-1 and mode-2 has the overlap inside the MMI coupler. The share of part of carriers between mode-1 and mode-2 suppresses the change of carrier density between the ON and OFF states, and make the maximum switching speed more than the relaxation oscillation frequency.

In general, the relaxation oscillation frequency f_r is expressed as

$$f_r = \frac{1}{2\pi}\sqrt{\frac{\partial G}{\partial N}\cdot\frac{S_0}{\tau_{ph}}} \tag{5.47}$$

where $\partial G/\partial N$ is differential gain, S_0 photon density, τ_{ph} photon lifetime.

The modal gain G is written as

$$G(N) = \Gamma \frac{c}{n_r} a(N - N_0) \tag{5.48}$$

where Γ confinement factor, c light speed in vacuum, n_r effective refractive index, a gain constant, N carrier density, N_0 the carrier density at transparency.

From equation (5.48), the differential gain is calculated as

$$\frac{\partial G}{\partial N} = \Gamma \frac{c}{n_r} a. \tag{5.49}$$

The photon lifetime means the photon trapping time inside the cavity and are expressed as

$$\frac{1}{\tau_{ph}} = \frac{c}{n_r}\left(\alpha + \frac{1}{2L} ln \frac{1}{R^2}\right) \tag{5.50}$$

where α internal loss, L is cavity length, R power reflectivity.

The relaxation oscillation frequency of the MMI-BLD can be calculated using equations (5.47) - (5.50) and the result is shown in Fig.5.20. We use the almost same parameters listed in Table.2.1, i.e., c = 3.0 × 10^{10} [cm·s^{-1}], n_r = 3.25, α = 20 [cm^{-1}], R = 0.3, Γ = 0.4, a = 4.63 × 10^{-16} [cm^2]. The photon density at lasing state is estimated to be 2.0 × 10^{15} [cm^{-3}] from Fig.5.16. The relaxation oscillation frequency of the MMI-BLD is around 5 GHz, because the cavity length is around 700 - 800 μm. The parameters used in this analyses are not special values, so the relaxation oscillation frequency is not so high. If using high differential gain materials, the relaxation oscillation frequency can be increased to around 10 GHz.

In normal BLDs, the switching speed is limited by the relaxation oscillation frequency. However, the switching speed of the MMI-BLD can be over the relaxation oscillation frequency, because the changes of the carrier densities are suppressed by the mode overlapping. If the overlap between mode-1 and mode-2 is 100 %, the maximum switching speed is limited by the photon lifetime expressed as equation (5.50). We needs to be careful to treat the internal loss α in the case of all-optical switching. Usually, the internal loss means extra waveguide loss such as free carrier absorption, i.e., it don't include the optical gain from stimulated emissions. However, the carrier injection is not changed in the case of optical switching, so the modes receive optical gains during switching. From this reason, the internal loss in equation (5.50) (in this case, α takes a minus value, i.e., gain) needs to be treat accurately. The photon density and carrier density during switching are obtained to be 2.0 × 10^{15} [cm^{-3}] and 9.0 × 10^{17} [cm^{-3}] from Fig.5.16 and Fig.5.17. The carrier density at transparency N_0 is 8.3 × 10^{17} [cm^{-3}], and the unsaturated modal gain is calculated to be around 13 [cm^{-1}] from equation (5.48). The self-saturation coefficient ε_s is assumed to be

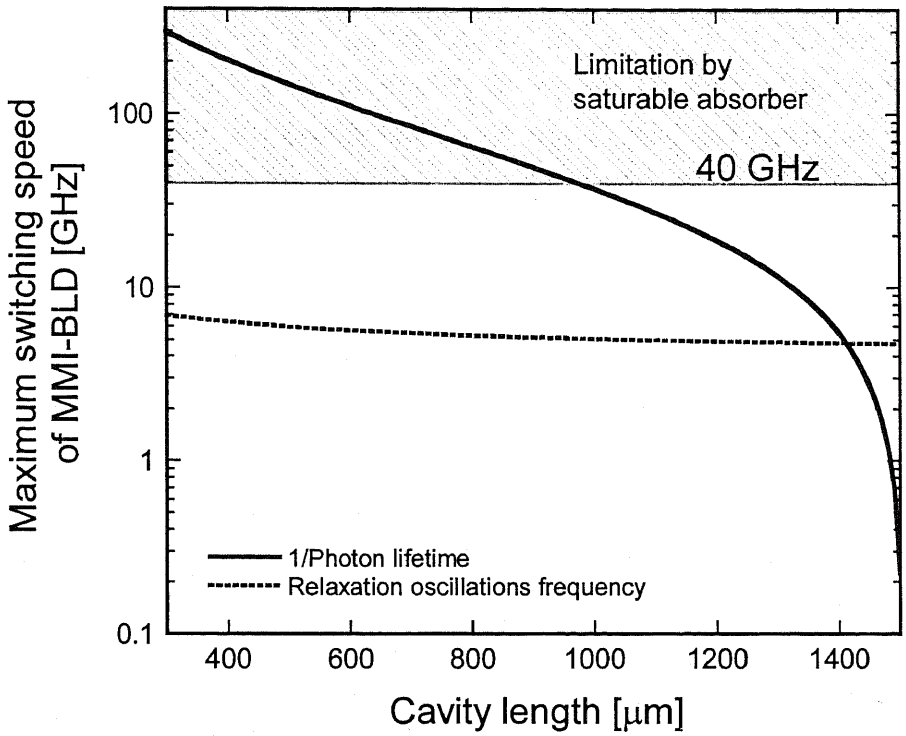

Fig.5.20 The estimated maximum switching speed of the MMI-BLD. The solid line shows the limitation by photon lifetime, and the dotted line shows the limitation by relaxation oscillation frequency. The shadow region means the limitation by saturable absorber. The switching speed is estimated to be inside the enclosed region by the solid and dotted lines.

0.8×10^{-16} [cm^3], and the cross-saturation coefficient ε_c is calculated to be 1.6×10^{-16} [cm^3] from the relation (5.33). The gain saturation factor is expressed as

$$\frac{1}{1+\varepsilon_s S_0+\varepsilon_c S_0}, \tag{5.51}$$

and calculated to be around 0.7, i.e., the modal gain is reduced to 8 [cm^{-1}] by the gain saturation.

To calculate the photon lifetime from equation (5.50), we take -8 [cm^{-1}] as the internal loss α (in the simulation, we neglect the extra optical loss such as free carrier absorption). In this way, we can calculate the photon lifetime during optical switching and estimate the maximum switching speed of the MMI-BLD. The maximum speed ($1/\tau_{ph}$) limited by the photon lifetime (solid line) with cavity length is plotted in Fig.5.20 with the relaxation oscillation frequency (dotted line). The photon lifetime is ultra-fast below 10 psec. if the cavity length is small. The switching speed can be estimated to be inside the enclosed region by the solid and dotted line. However, the maximum speed is limited by the carrier lifetime of the saturable absorbers, which is around 40 GHz in the reverse bias condition. From Fig.5.20, $1/\tau_{ph}$ is

over 40 GHz if the cavity length is smaller than 1000 μm. Since the MMI cavity length is around 700 μm - 800 μm, the maximum speed is limited by the saturable absorber in the MMI-BLD case. From this results, we can conclude that the switching speed is around 5 GHz (relaxation oscillation limitation) to 40 GHz (saturable absorber limitation). The switching speed approaches 40 GHz, if the two cross-coupled modes has more overlap. As shown here, the MMI-BLD has the possibility of high-speed switching more than 10 GHz.

5.7 Conclusion

We have proposed and investigated a novel BLD with active 2×2 MMI coupler cavity designed as input light totally couples to a cross port. A bistable switching can be realized between the two cross-coupled modes associated with gain saturation. Static characteristics of the MMI-BLD are analyzed using FD-BPM which includes photon-carrier interaction through the carrier rate equation. This model gives accurate distributions of photon and carrier densities, optical gain and refractive index inside the cavity. The strong coupling condition for two-mode bistability, stability of lasing and extinction ratio are investigated. The MMI-BLD with saturable absorbers shows two-mode bistability and can be switched by 0 dBm optical injection. Carrier density difference inside the MMI coupler is small enough, so the instability effects such as filamentation never occur and the MMI-BLD has stable laser radiation. The modal shape is kept after lasing and extinction ratio is expected to be more than 15 dB. We predict that the MMI-BLD shows bistable switching between the two cross-coupled modes by light injection, which can be used as all-optical flip-flop or optical memory.

We also discuss about the switching speed of the MMI-BLD. There are three limitation factors of maximum switching speed, i.e. relaxation oscillation frequency, photon lifetime, and carrier lifetime of the saturable absorbers. In the case that the cavity length is less than 1000 μm, the maximum speed is limited by relaxation oscillation frequency and the saturable absorber, and the switching speed is estimated to be around 5 to 40 GHz.

References

[1] K. Hamamoto, E. Gini, C. Holtmann, and H. Melchior, "Single transverse mode active multimode interferometer InGaAsP/InP laser diode," *Electron. Lett.*, vol. 34, no. 5, pp. 462-464, 1998.

[2] K. Hamamoto, E. Gini, C. Holtmann, H. Melchior, and T. Sasaki, "Active multimode interferometer laser diode demonstrated via 1.48 μm high power application," *Electron. Lett.*, vol. 36, no. 2, pp. 138-139, 2000.

[3] K. Hamamoto, E. Gini, C. Holtmann, and H. Melchior, "Single-transverse-mode active multi-mode-interferometer 1.45 μm high power laser diode," *Applied Physics B, Laser and Optics.*, vol. 73, pp. 571-574, 2001.

[4] H. S. Kim, Y. S. Kwon, S. Hong, "Square ring laser diode with MMI coupler cavity," *IEEE Photonics. Technol. Lett.*, vol. 9, no. 5, pp. 584-586, 1997.

[5] H. Kawaguchi, I. H. White, M. J. Offside, and J. E. Carrol, "Ultrafast switching in polarization-bistable laser diodes," *Opt. Lett.*, vol. 17, no. 2, pp. 130-132, 1992.

[6] Y. C. Chen, and J. M. Liu, "Polarization bistability in external cavity semiconductor lasers," *Appl. Phys. Lett.,* vol. 46, pp. 16-18, 1985.

[7] T. Fujita, A. Schremer, and C. L. Tang, "Polarization bistability in external cavity semiconductor lasers," *Appl. Phys. Lett.,* vol. 51, pp. 392-394, 1987.

[8] B. Rheinländer, A. Klehr, O. Ziemann, V. Gottschalch, and G. Oelgart, "Room temperature polarization bistability in 1.3 μm InGaAsP/InP ridge waveguide lasers," *Opt. Commun.,* vol. 80, pp. 259-261, 1991.

[9] A. Klehr, A. Bärwolff, R. Müller, M. Voß, J. Sacher, W. Elsässer, and E. O. Göbel, "Ultrafast polarisation switching in ridge-waveguide laser diodes," *Electron. Lett.*, vol. 27, pp. 1680-1682, 1991.

[10] Y. Ozeki, J. E. Johnson, and C. L. Tang, "Polarization bistability in semiconductor lasers with intracavity multiple quantum well saturable absorber," *Appl. Phys. Lett.,* vol. 58, pp. 1958-1960, 1991.

[11] Y. Ozeki, and C. L. Tang, "Polarization switching and bistability in an external cavity laser with a polarization-sensitive saturable absorber," *Appl. Phys. Lett.,* vol. 58, pp. 2214-2216, 1991.

[12] B. B. Jian, "Continuous-wave operation of monolithic two-mode optical flip-flop with etched laser mirrors," *Electron. Lett.*, vol. 32, no. 20, pp. 1923-1925, 1996.

[13] G. J. Lasher, and A. B. Fowler, "Mutually quenched injection lasers as bistable devices," *IBM J. Res. Dev.,* vol. 8, pp. 471-475, 1964.

[14] H. Kawaguchi, T. Irie, and M. Murakimi, "Pitchfork bifurcation polarization bistability in laser diodes with external cavities," *IEEE J. Quantum Electronics*, vol. 31, no. 3, pp. 447-455, 1995.

[15] H. Kawatuchi, I. S. Hidayat, Y. Takahashi, and Y. Yamayoshi, "Pitchfork bifurcation polarisation bistability in vertical-cavity surface-emitting lasers," *Electron. Lett.*, vol. 31, no. 2, pp. 109-111, 1995.

[16] H. Kawatuchi, and I. S. Hidayat, "Gigahertz all-optical flip-flop operation of polarisation-bistable vertical-cavity surface-emitting lasers," *Electron. Lett.*, vol. 31, no. 14, pp. 1150-1151, 1995.

[17] O. Bryngdahl, "Image formation using self-imaging techniques," *J. Optic. Soc. Amer.,* vol. 63, pp. 416-419, 1973.

[18] R. Ulrich and T. Kamiya, "Resolution of self-images in planar optical waveguides," *J. Optic. Soc. Amer.,* vol. 68, no. 5, pp. 583-592, 1978.

[19] L. B. Soldano and E. C. M. Pennings, "Optical multimode interference devices based on self-imaging: Principles and applications," *J. Lightwave Technol.,* vol. 13, pp. 615-627, 1995.

[20] R. J. Deri, E. C. M. Pennings, A. Scherer, A. S. Gozdz, C. Caneau, N. C. Andreadakis, V. Shah, L. Curtis, R. J. Hawkins, J. B. D. Soole, and J. I. Song, "Ultracompact monolithic integration of balanced, polarization diversity photodetectors," *Proc. ECOC'92*, pp. 457-460, Berlin, Germany, Sept. 1992.

[21] P. A. Besse, M. Bachmann, H. Melchior, L. B. Soldano, and M. K. Smit, "Optical bandwidth and fabrication tolerances of multimode interference couplers," *J. Lightwave Technol.,* vol. 12, pp. 1004-1009, 1994.

[22] M. Bachmann, M. K. Smit, P. A. Besse, E. Gini, H. Melchior, and L. B. Soldano, "Polarization-insensitive low-voltage optical waveguide switch using InGaAsP/InP four-port Mach-Zehnder interferometer," *Proc. Tech. Dig. OFC/IOOC'93*, pp. 32-33, San. Jose, CA, Feb. 1993.

[23] J. Leuthold, J. Echner, E. Gamper, P. A. Besse, and H. Melchior, "Multimode interference couplers for the conversion and combining of zero- and first-order modes," *J. Lightwave Technol.,* vol. 16, no. 7, pp. 1228-1239, 1998.

[24] P. A. Besse, E. Gini, M. Bachmann, and H. Melchior, "New 1 × 2 multimode interference couplers with free selection of power splitting ratios," *Proc. ECOC'94*, pp. 669-672, Firenze, Italy, Sept. 1994.

[25] J. M. Heaton, R. M. Jenkins, D. R. Wight, J. T. Parker, J. C. H. Birbech, and K. P. Hilton, "Novel 1-to-*N* way integrated optical beam splitters using symmetric mode mixing in GaAs/AlGaAs multimode waveguides," *Appl. Phys. Lett.,* vol. 61, pp. 1754-1756, 1992.

[26] L. B. Soldano, F. B. Veermann, M. K. Smit, B. H. Verbeek, A. H. Dubost, and E. C. M. Pennings, "Planar monomode optical couplers based on multimode interference effects," *J. Lightwave Technol.,* vol. 10, pp. 1843-1845, 1992.

[27] P. A. Besse, M. Bachmann, and H. Melchior, "Phase relations in multimode Mach-Zehnder interferometer based on multimode interference couplers and their applications to generalized integrated Mach-Zehnder optical switches," *Proc. European Conf. Integrated Opt. ECIO'93*, pp. 2.21-2.23, Neuchâtel, Switzerland, Apr. 1993.

[28] M. R. Paiam. C. F. Janz, R. I. MacDonald, and J. N. Broughton, "Compact planar 980/1550 nm wavelength multi/demultiplexer based on multimode interference," *IEEE Photonics. Technol. Lett.*, vol. 7, pp. 1180-1182, 1995.

[29] H. F. Talbot, "Facts relating to optical science No. IV," *London, Edinburgh Philosophical Mag., J. Sci.,* vol. 9, pp. 401-407, 1836.

[30] D. Marcuse, *Light Transmission Optics.* New York: Van Nostrand Reinhold, 1972.

[31] R. Ulrich, and G. Ankele, "Self-imaging in homogeneous planar optical waveguides," *Appl. Phys. Lett.,* vol. 27, no. 6, pp. 337-339, 1975.

[32] D. C. Chang, and E. F. Kuester, "A hybrid method for paraxial beam propagation in multimode optical waveguides," *Trans. Microwave Theory Tech.,* vol. MTT-29, no. 9, pp. 923-933, 1981.

[33] R. Ulrich, "Light-propagation and imaging in planar optical waveguides," *Nouv. Rev. Optique,* vol. 6, no. 5, pp. 253-262, 1975.

[34] C. M. Weinert, and N. Agrawal, "Three-dimensional simulation of multimode interference devices," *Proc. Integr. Phot. Res. (IPRC)*, pp. 287-289, San Francisco, Feb. 1994.

[35] R. M. Knox and P. P. Toulios, "Integrated circuits for the millimeter through optical frequency range," *Proc. Symp. Submillimiter Waves*, pp. 497-516, J. Fox, Ed., New York, Mar./Apr. 1970.
[36] P. N. Robson, and P. C. Kendall, Eds., *Rib Waveguide Theory by the Spectral Index Method*, Optoelectronic Series, Research Studies Press Ltd. New York: Wiley, 1990.
[37] N. S. Kapany, and J. J. Burke, *Optical Waveguides.* New York: Academic, 1972.
[38] E. C. M. Pennings, R. van Roijen, M. J. N. van Stralen, P. J. de Waard, R. G. M. P. Koumans, and B. H. Verbeek, "Reflection properties of multimode interference devices," *IEEE Photonics. Technol. Lett.*, vol. 6, no. 6, pp. 715-718, 1994.
[39] Y. Shibata, S. Oku, M. Yamamoto, N. Yashimoto, and M. Naganuma, "Quantitative analysis of optical reflection in a multimode interference 3 dB coupler using a low-coherence interferometric reflectometer," *Electron. Lett.*, vol. 32, no. 24, pp. 2266-2268, 1996.
[40] D. Erasme, L. H. Spiekman, C. G. P. Herben, M. K. Smit, and F. H. Groen, "Experimental assessment of the reflection of passive multimode interference couplers," *IEEE Photonics. Technol. Lett.*, vol. 9, no. 12, pp. 1604-1606, 1997.
[41] W. E. Lamb, "Theory of an Optical Maser," *Phys. Rev.,* vol. 134, no. 6A, pp. A1429-A1450, 1964.
[42] K. Shimoda, *Introduction to Laser Physics.* Berlin: Springer-Verlag, 1984.
[43] M. Yamada, "Transverse and longitudinal mode control in semiconductor injection lasers," *IEEE J. Quantum Electronics*, vol. QE-19, no. 9, pp. 1365-1380, 1983.
[44] C. L. Tang, A. Schremer, and T. Fujita, "Bistability in two-mode semiconductor lasers via gain saturation," *Appl. Phys. Lett.,* vol. 51, no. 18, pp. 1392-1394, 1987.
[45] Y. R. Shen, *The Principle of Nonlinear Optics.* New York: Wiley, 1984.
[46] Y. Takahashi, A. Neogi, and H. Kawaguchi, "Polarization-dependence nonlinear gain in semiconductor lasers," *IEEE J. Quantum Electronics*, vol. 34, no. 9, pp. 1660-1682, 1996.
[47] J. Shimizu, H. Yamada, S. Murata, A. Tomita, M. Kitamura, and A. Suzuki, "Optical-confinement-factor dependencies of the *K* factor, differential gain, and nonlinear gain coefficient for 1.55 μm InGaAs/InGaAsP MQW and strained-MQW lasers," *IEEE Photonics. Technol. Lett.*, vol. 3, no. 9, pp. 773-776, 1991.
[48] H. Yasaka, K. Takahata, N. Yamamoto, and M. Naganuma, "Gain saturation coefficients of strained-layer multiple quantum-well distributed feedback lasers," *IEEE Photonics. Technol. Lett.*, vol. 3, no. 10, pp. 879-882, 1991.
[49] C. F. Lin, and P. C. Ku, "Analysis of stability in two-mode laser systems," *IEEE J. Quantum Electronics*, vol. 32, pp. 1377-1382, 1996.

Chapter 6 MZI Bistable Laser Diode

We propose a novel BLD with a Mach-Zehnder interferometer (MZI) coupler. The MZI has semiconductor optical amplifiers (SOAs) in its arms. There are two orthogonal modes that propagate between a two cross ports of the MZI. A bistable switching can be realized between two cross-coupled modes associated with gain saturation. Static characteristics of the MZI-BLD are analyzed using a finite difference beam propagation method (FD-BPM) scheme. The carrier is considered by the carrier rate equation. This model gives accurate distributions of photon and carrier densities, optical gain and refractive index inside the cavity. From the analyses, it is predicted that the MZI-BLD shows pitchfork bifurcation bistability since the cross-coupled modes have 100 % overlap in the SOA regions. There is no change of carrier density between the ON and OFF states, so the switching speed is estimated to be around 100 GHz. We predict that the MZI-BLD shows bistable switching between the two cross-coupled modes by injecting light, which can be used as all-optical flip-flop or optical memory.

6.1 Introduction

In the previous chapter, we have proposed the MMI-BLD predicted to show the all-optical flip-flop operation. However, the MMI-BLD needs the saturable absorber to obtain two-mode bistability because the two cross-coupled modes of the MMI-BLD didn't have the overlap enough for pitchfork bifurcation bistability. So, the MMI-BLD has the problem that the maximum switching speed is limited by the carrier lifetime of the saturable absorber, i.e. around 40 GHz.

In this chapter, we extend the concept of the MMI-BLD, and propose a novel two-mode BLD that has a Mach-Zehnder interferometer (MZI) with semiconductor optical amplifiers (SOAs) in its arms. MMI-SOAs have been mainly studied for high-speed TDM telecommunication devices such as all-optical switching [1]-[7], multiplexing [8], demultiplexing [9]-[14], wavelength conversion [15]-[18], and regeneration [19]-[21]. We use 2×2 MZI-SOA configuration as BLDs. We call it a MZI-BLD. The MZI-BLD has two orthogonal modes that propagate between the two diagonal cross ports. Because the two cross-coupled modes have

100 % overlap in the SOA regions, pitchfork bifurcation bistability can be realized associated with gain saturation. Pitchfork bifurcation bistability was theoretically predicted by Kawaguchi et al [22] and experimentally demonstrated in LDs with external cavities [23] and vertical-cavity surface-emitting lasers (VCSELs) [24][25]. In pitchfork bifurcation bistability, when a LD is oscillation in two modes, the output intensities of these modes bifurcate at a critical point as increasing the LD current, and only one mode oscillates. If an optical input is injected with the opposite mode to the oscillating one, the oscillating mode changes to that of the input. The pitchfork bifurcation BLDs realized until now have been polarization bistability, so they needs a polarizer to take out one mode. The MZI-BLD proposed in this chapter shows the bistability between same polarized modes (usually TE modes), i.e. the bistability of the MZI-BLD is not polarization bistability. The output power of the ON sate and OFF state emit from two adjacent output ports, respectively. Moreover, we can user mature techniques for integrated semiconductor devices to fabricate the proposed MZI-BLD.

We use a finite difference beam propagation method (FD-BPM) to analyze static characteristics of the MZI-BLD. This model takes into account accurate distributions of photon and carrier densities, optical gain and refractive index inside the cavity. Pitchfork bifurcation bistability of the MZI-BLD is precisely investigated. In Section 6.2, the concept of the MZI-BLD is proposed. In Section 6.3, the design of the MZI-BLD is described. In Section 6.4, the basic modal properties of the MZI-BLD are investigated. In Section 6.5, simulation results on pitchfork bifurcation bistability and all-optical flip-flop operation in the MZI-BLD are described. In Section 6.6, the limitation of the maximum switching speed is estimated. In Section 6.7, some ideas to get the modal stability are mentioned. Conclusions are given in Section 6.8.

6.2 Proposal of MZI-BLD

The MZI-BLD proposed here has the same structure as MZI-SOA. The schematic view of the MZI-BLD is shown in Fig.6.1. The MZI-BLD comprises two SOAs with in its arms, and two 3-dB multi-mode interference (MMI) splitters. The waveguides except for the SOA regions are composed of passive waveguides, so the only SOA regions are injected currents and provide optical gains. If there is no phase difference between the two SOA arms, the light injected into one input port totally couples to a cross port. In this situation, the MZI-BLD supports two cross-coupled modes that propagate a round trip between the two diagonal ports, therefore we can separate the lasing modes of the MZI-BLD into this two orthogonal modes. The cross-coupled modes suppress each other through the gain saturation because the modal profiles of them overlap in the SOA arms. The overlap in the SOA arms

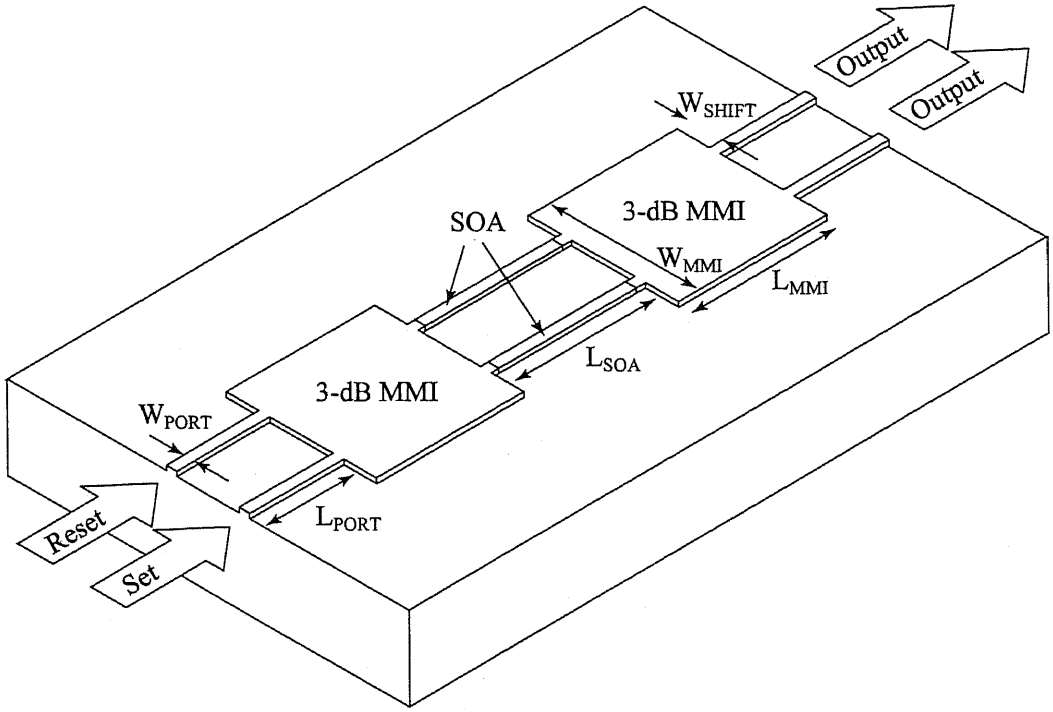

Fig.6.1 Schematic view of the 2×2 MZI-BLD with SOAs in its arms. 3-dB MMI coupler are used to concatenate the waveguides of a MZI structure. In the case of ridge-waveguide structure, each size is follows, W_{MMI} is 20 μm, L_{MMI} 650 μm, W_{SHIFT} 5.6 μm, L_{SOA} 300 μm, L_{PORT} 100 μm, W_{PORT} 2 μm.

is 100 %, so the gain saturation between the two modes leads to pitchfork bifurcation bistability. The all-optical flip-flop will be obtained by injecting a set or reset signal into each input port depicted as Fig.6.1.

6.3 Design of MZI-BLD

In this section, we investigate the design of the MZI-BLD. First, we discuss on 3-dB MMI couplers. We already described the basic properties of MMI couplers in Section 5.2. The 3-dB MMI coupler can be achieved at the length of $3L_\pi/2$ (General interference case) or $L_\pi/2$ (Restricted interference case). To reduce the MMI length, the high-mesa waveguide is preferable. However, we adopt the ridge waveguide structure in this chapter, because the FD-BPM developed for the bistability analyses is not so suitable for the high-mesa structure. We use the Restricted interference MMI coupler to make the coupler length as short as possible.

The cross coupler MMI was already designed in Section 5.4 in the case of W_{MMI} = 12 μm. From the basic properties of MMI couples, the 3-dB MMI coupler is obtained at the half length of the cross coupler MMI. Fig.6.2 shows the field propagation of 3-dB MMI coupler

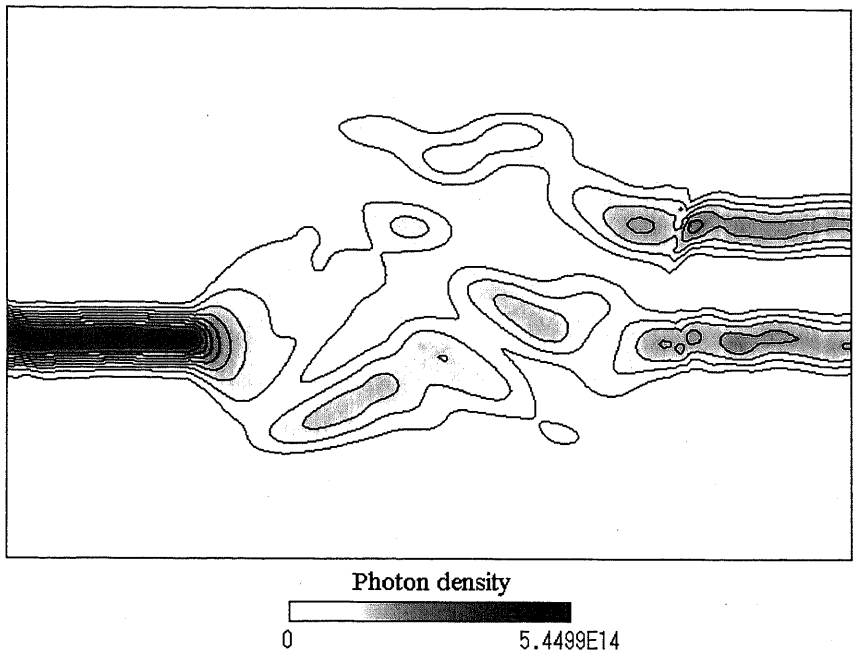

Fig.6.2 The field propagation (photon density [cm^{-3}]) of the restricted interferometer 3-dB MMI coupler calculated by FD-BPM. Each parameter of the MMI coupler is follow, W_{MMI} = 12 μm, L_{MMI} = 263 μm, and W_{SHIFT} = 3.0 μm. The port width is 2 μm, the refractive indices of core n_r and clad n_c is 3.27 and 3.24 respectively, and the operation wavelength λ is 1.55 μm.

(W_{MMI} = 12 μm) calculated by FD-BPM. The designed parameters of the length and the port shift are slightly changed, since the core's refractive index is changed from 3.255 to 3.27 for passive waveguides. The refractive index of clad is 3.24. We assume that the operation wavelength is 1.55 μm. The each parameters of the 3-dB MMI coupler is follows, W_{MMI} 12 μm, L_{MMI} 263 μm, W_{SHIFT} 3.0 μm, and W_{PORT} 2.0 μm. The power difference between the two output ports is around 0.02 %, so the nearly perfect 3-dB MMI coupler can be obtained.

The MZI-BLD can be realized using the two 3-dB MMI coupler and two SOAs with Mach-Zehnder interferometer's arms. The SOAs are equipped to provide optical gains, which are 300-μm long active regions whose bandgap are around 1.55 μm. The integration of active waveguides and passive waveguides has been realized by Selective Area Growth (SAG) [26] or butt-joint technique [27].

The field propagations of MZI-BLD are also calculated by FD-BPM. If the two SOA arms have same phase shift, there are two orthogonal cross-coupled modes that propagate a round trip between the two diagonal ports. Fig.6.3 shows the two cross-coupled modes injected from the left side of the MZI-BLD. We call mode-1 (Fig.6.3 (a)) and mode-2 (Fig.6.3 (b)) as the two cross-coupled modes. The pitchfork bifurcation bistability will occur between

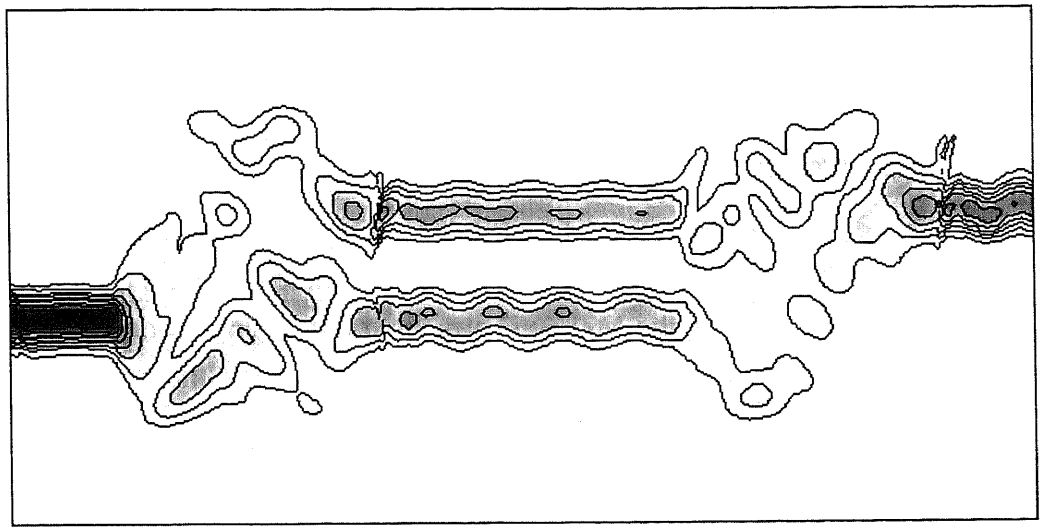

(a) mode-1

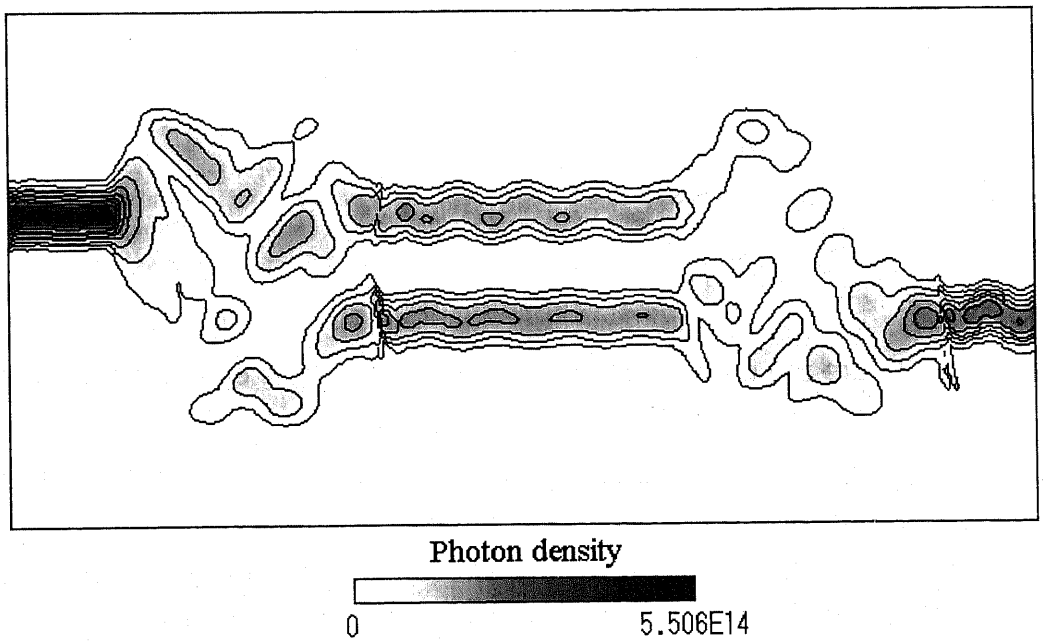

(b) mode-2

Fig.6.3 Propagation characteristics of the MMI-BLD for (a) mode-1 and (b) mode-2. Photon density [cm-3] distributions of the injected lights that propagate toward right-hand side from left-hand side are shown. The total power of the injected light is 0 dBm. The 3-dB MMI lengths is 263 μm, and the width is 12 μm. The length of SOA regions are 300 μm. The port width is 2 μm, the refractive indices of core n_r and clad n_c is 3.27 and 3.240 respectively, and the operation wavelength λ is 1.55 μm.

this cross-coupled modes, i.e. mode-1, and mode-2. In the following sections, we discuss the basic modal properties of the MZI-BLD and the bistability of the MMI-BLD designed here.

6.4 Basic Modal Properties of MZI-BLD

In the previous section, we mentioned about the design of the MZI-BLD and the two cross-coupled modes. We adopted the two cross-coupled modes as the orthogonal modes of the MZI-BLD. However, in fact, the MZI-BLD has the many lasing modes besides the two cross-coupled modes. In this section, we describe about the basic modal properties of the MZI-BLD and the propriety of adopting the two cross-coupled modes as the lasing modes.

A. The MZI-BLD transfer function

To analyze the modal properties, the transfer function of the MZI-BLD should be formulated. First, we describe the transfer function of 3-dB MMI couplers. The transfer function of each input port is shown in Fig.6.4. The amplitudes of electrical fields are expressed by A_0 and B_0, which are complex numbers. When the light is injected into one port, the output lights have same power, but different phase by $\pi/2$. The total transfer function can be obtained by linear combination of the transfer function of each port, which is express as

$$\begin{bmatrix} A_1 \\ B_1 \end{bmatrix} = \begin{bmatrix} \frac{1}{\sqrt{2}} e^{j\left(\frac{\pi}{2}+\theta_0\right)} & \frac{1}{\sqrt{2}} e^{j\theta_0} \\ \frac{1}{\sqrt{2}} e^{j\theta_0} & \frac{1}{\sqrt{2}} e^{j\left(\frac{\pi}{2}+\theta_0\right)} \end{bmatrix} \begin{bmatrix} A_0 \\ B_0 \end{bmatrix} \tag{1}$$

where A_1 and B_1 are the output from 3-dB coupler, and θ_0 is common phase shift inside the coupler.

The whole transfer function is derived by two series of 3-dB coupler transfer matrix (1). Here, we assume that the two Mach-Zehnder arms has no phase difference and no optical gains or losses. Under this assumption, transfer matrix of the Mach-Zehnder arms is just only an unit matrix, and the transfer function of the MZI-BLD is expressed as

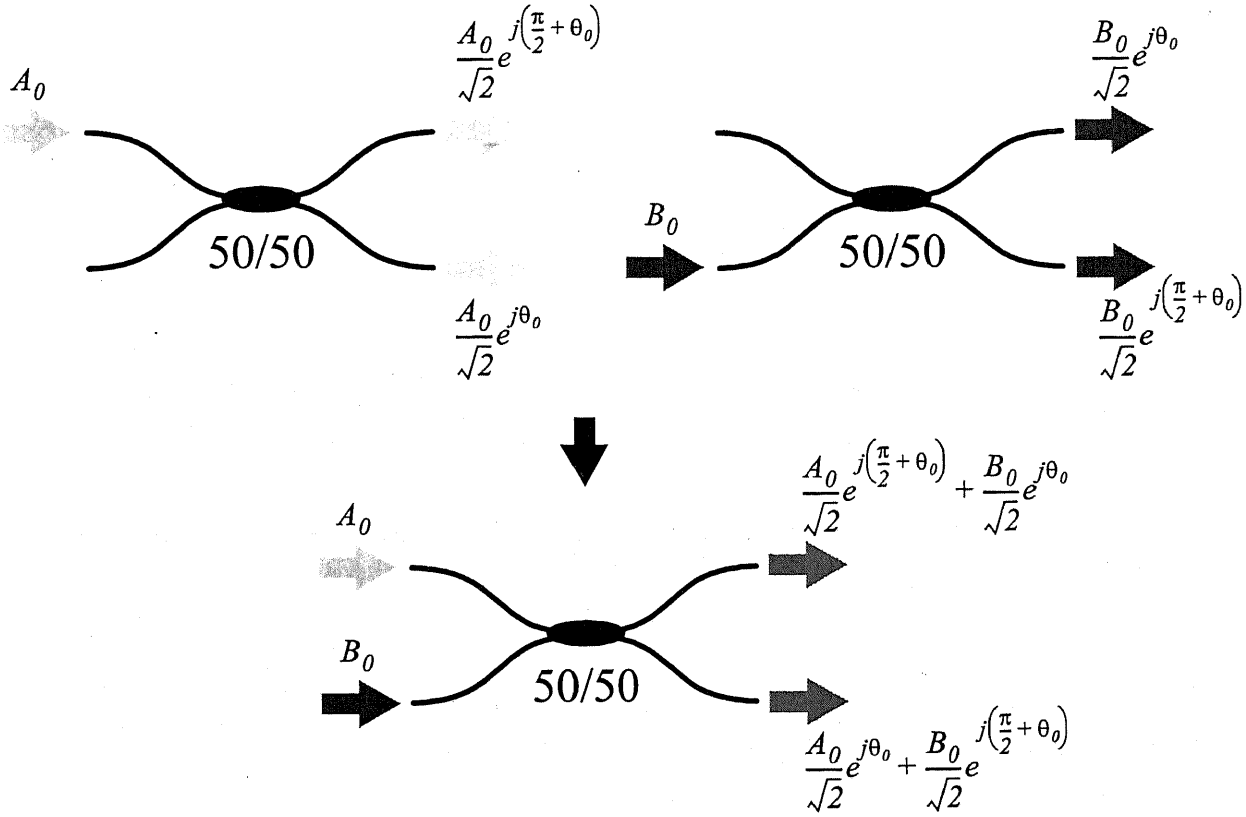

Fig.6.4 Transfer functions of 3-dB MMI coupler. The light injected to one port is divided into two same power light through 3-dB MMI coupler whose phase are different $\pi/2$. By liner combination law of each input port transfer functions, the whole transfer function of 3-dB MMI coupler is obtained.

$$\begin{bmatrix} A_2 \\ B_2 \end{bmatrix} = \begin{bmatrix} \frac{1}{\sqrt{2}}e^{j\frac{\pi}{2}} & \frac{1}{\sqrt{2}} \\ \frac{1}{\sqrt{2}} & \frac{1}{\sqrt{2}}e^{j\frac{\pi}{2}} \end{bmatrix} \begin{bmatrix} 1 & 0 \\ 0 & 1 \end{bmatrix} \begin{bmatrix} \frac{1}{\sqrt{2}}e^{j\frac{\pi}{2}} & \frac{1}{\sqrt{2}} \\ \frac{1}{\sqrt{2}} & \frac{1}{\sqrt{2}}e^{j\frac{\pi}{2}} \end{bmatrix} \begin{bmatrix} A_0 \\ B_0 \end{bmatrix} \quad (2)$$

$$= \begin{bmatrix} 0 & e^{j\frac{\pi}{2}} \\ e^{j\frac{\pi}{2}} & 0 \end{bmatrix} \begin{bmatrix} A_0 \\ B_0 \end{bmatrix}$$

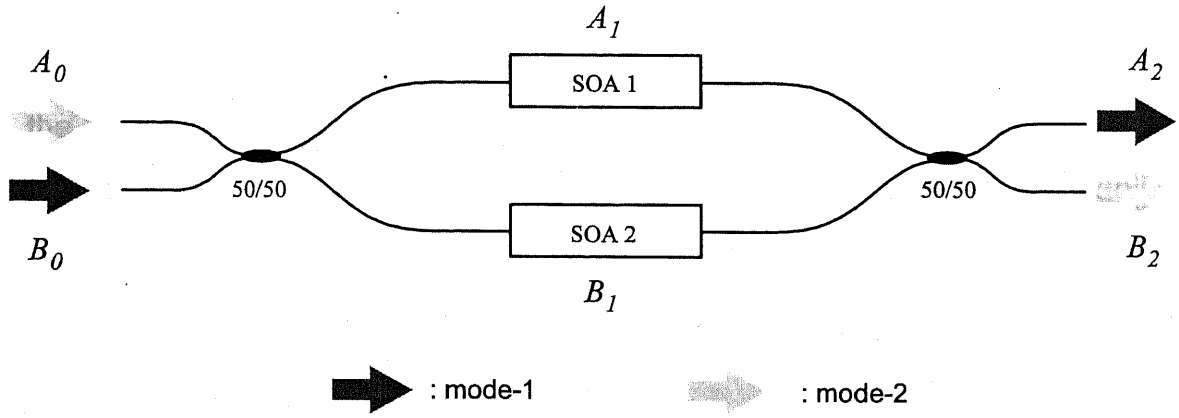

Fig.6.5 Transfer function of the MZI-BLD. If the Mach-Zehnder arms have no phase difference, there are two orthogonal cross-coupled modes in the MZI-BLD.

where A_2 and B_2 are the output from the MZI-BLD, and the common phase shift θ_0 is assumed to be 0. Eventually, the total transfer function is expressed as

$$A_2 = e^{j\frac{\pi}{2}} B_0$$
$$B_2 = e^{j\frac{\pi}{2}} A_0 \tag{3}$$

From equation (3), it is proven that the light injected into one port is outputted from a cross port, i. e. the two cross-coupled modes exist in the MZI-BLD as depicted in Fig.6.5. The one cross-coupled mode is not affected by another one, so the two cross-coupled modes are orthogonal modes. Therefore, we can conclude that the MZI-BLD has two orthogonal lasing modes, mode-1 and mode-2. We assumed that there are no phase change difference and no gain (or loss) at the SOA arms. Any lasing modes can be expressed by this two orthogonal modes.

One lasing mode is express by linear combination of mode-1 and mode-2, and the electrical fields of the Mach-Zehnder arms is derived by equation (1),

$$A_1 = \frac{A_0}{\sqrt{2}} e^{j\frac{\pi}{2}} + \frac{B_0}{\sqrt{2}} \tag{4}$$

$$B_1 = \frac{A_0}{\sqrt{2}} + \frac{B_0}{\sqrt{2}} e^{j\frac{\pi}{2}} \tag{5}$$

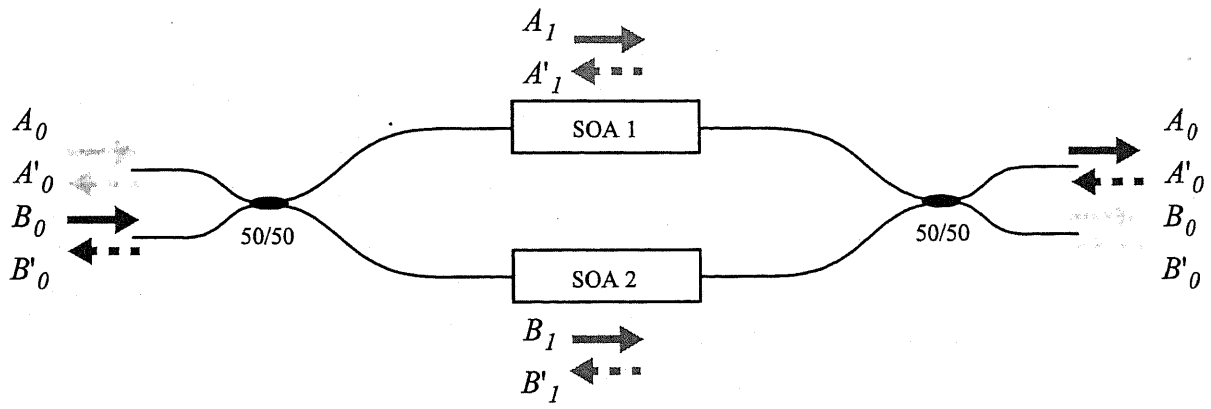

Fig.6.6 Lasing mode of the MZI-BLD, which is expressed by linear combination of two orthogonal cross-coupled modes, mode-1 and mode-2. The power distributions of both arms are completely same for any lasing modes.

$$A'_1 = \frac{A'_2}{\sqrt{2}} e^{j\frac{\pi}{2}} + \frac{B'_2}{\sqrt{2}} \tag{6}$$

$$B'_1 = \frac{A'_2}{\sqrt{2}} + \frac{B'_2}{\sqrt{2}} e^{j\frac{\pi}{2}} \tag{7}$$

where A'_1, A'_2, B'_1 and B'_2 are electrical fields of backward propagating light (i.e. propagating from the right-hand side to the left-hand side) shown in Fig.6.6.

Under the assumption that power reflectivity is 100 %, $A'_2 = B_0 e^{j\pi/2}$, $B'_2 = A_0 e^{j\pi/2}$ are derived from equation (3), therefore the backward propagating electrical fields of the Mach-Zehnder arms are expressed

$$A'_1 = e^{j\frac{\pi}{2}} \left(\frac{A_0}{\sqrt{2}} + \frac{B_0}{\sqrt{2}} e^{j\frac{\pi}{2}} \right) \tag{8}$$

$$B'_1 = e^{j\frac{\pi}{2}} \left(\frac{A_0}{\sqrt{2}} e^{j\frac{\pi}{2}} + \frac{B_0}{\sqrt{2}} \right). \tag{9}$$

Immediately, the following equations are obtained from (4), (5), (8), (9),

$$\begin{aligned} |A_1|^2 &= |B'_1|^2 \\ |B_1|^2 &= |A'_1|^2 \end{aligned} \tag{10}$$

From equation (10), the relation between the total powers inside the SOA arms is obtained.

$$\begin{aligned}(Total\ power\ of\ SOA1) &\equiv |A_1|^2 + |A'_1|^2 \\ &= |B_1|^2 + |B'_1|^2 \equiv (Total\ power\ of\ SOA2)\end{aligned} \tag{11}$$

In short, equation (11) means that one Mach-Zehnder arm has completely same power of the other arm for the any lasing modes. The same power distribution at the SOA region leads to same gain for any lasing modes, so every modes expressed by linear combination of mode-1 and mode-2 have same threshold for lasing, and they are able to be lasing mode of the MZI-BLD. This characteristic can be compared with VCSELs. If VCSELs have pure circular structure, they can take any polarized light as a lasing mode.

At the analyses mentioned above, we assumed that the SOA regions with Mach-Zehnder arms had no phase difference and no optical gain and the reflectivities at the facets are 100 %. At the lasing state, the total gain is equal to the total loss, when the lasing mode propagates a round trip. The mirror losses at the facet is compensated by the gain of the SOAs, i.e. we can consider that the SOAs have no gains and the mirrors have no losses. If this assumptions is correct, the last assumption that the SOA regions have no phase difference is also correct. The case that the SOA regions have some phase difference means the power distributions of the two SOAs is different. In this case, the modal gain becomes small, i.e. the threshold current becomes large. Therefore, this mode can not start lasing. As the result of this reason, the SOAs should have no phase difference at the lasing state.

In this section, we described the lasing modes of the MZI-BLD. We can select the any set of the two orthogonal lasing modes, however for practical use, we adopt mode-1 and mode-2 as the orthogonal lasing mode set shown in Fig.6.3. In the next section, the pitchfork bifurcation bistability between mode-1 and mode-2 is mentioned.

6.5 Bistability Analysis

To analyze the pitchfork bifurcation bistability of the MZI-BLD, the FD-BPM with the rate equations developed in Section 2.3 is used. This model was also useful for the MMI-BLD analyses mentioned in the previous chapter. The overlap between the two cross-coupled modes can be analyzed with no special assumption by the FD-BPM. The distributions of carrier density, gain (or loss), and refractive index are also treated precisely at following analyses.

A. Requirement for pitchfork bifurcation bistability

We already discussed the general theory of two-mode bistability in Section 5.5. Again, we review the requirement for pitchfork bifurcation bistability, briefly.

To realize the pitchfork bifurcation bistability, the strong coupling condition [28]- [30] must be satisfied,

$$\varepsilon_{12}\varepsilon_{21} > \varepsilon_{11}\varepsilon_{22}, \tag{12}$$

where ε_{11} and ε_{22} are self-saturation and ε_{12} and ε_{21} are cross-saturation coefficients.

By the symmetry properties of InGaAsP cubic crystal, the relationship between a self-saturation coefficient and a cross-saturation coefficient for the TE modes is described as follows [31].

$$\begin{aligned} \varepsilon_{12}(\omega_1 = \omega_0, \omega_2 = \omega_0) &= 2 \times \varepsilon_{11}(\omega_0) \\ \varepsilon_{21}(\omega_2 = \omega_0, \omega_1 = \omega_0) &= 2 \times \varepsilon_{22}(\omega_0) \end{aligned} \tag{13}$$

where ω_1 and ω_2 are angular frequencies of the two TE modes, respectively. It is important that the two modes have the same frequency because the cross-saturation coefficient is significant only around $\omega_1 = \omega_2$ and it vanishes otherwise [32].

In the case of the MZI-BLD, the strong coupling condition (12) is only considered at the SOA regions. As shown in Fig.6.3, the overlap between mode-1 and mode-2 is 100 % at the SOA regions. As the result of 100 % modal overlap and equation (13), the strong coupling condition is always satisfied, and the MZI-BLD shows pitchfork bifurcation bistability.

B. Analysis of bistable switching

The parameters used in this paper are shown in Table.2.1. We consider an InGaAsP Multi Quantum Well (MQW) structure whose band gap energy is around 1.55 μm. The gain saturation is affected by many factors such as material, strain, and MQW structure. However, in pitchfork bifurcation bistability, the relative value of the gain saturation coefficient is more important than absolute value, so we assume 8.0×10^{-17} cm^3 as the self-saturation coefficient and the cross-saturation coefficient is derived from equations (13), which are same value as the MMI-BLD analyses.

First, the L-I characteristic of the MZI-BLD is calculated. If the BLD has a pitchfork bifurcation bistable characteristic, one mode starts lasing and suppresses the other mode at a bifurcate point. Some fluctuation of the BLD decide which mode starts lasing. In the calculation, the light injection to mode-1 is 5 dB larger than mode-2 (-60 dBm) instead of fluctuations. Fig.6.7 shows the L-I characteristic of the MZI-BLD. The injection currents of both the SOAs are same in the following analyses. Increasing the current injection to the two SOA regions, the L-I characteristic shows the bifurcate point around 3.4 kA/cm^2, and mode-1 starts laser radiation and suppresses mode-2. Above 4.0 kA/cm^2, mode-2 is perfectly suppressed to the spontaneous emission level (the -60 dBm light injection is used instead of the real spontaneous emission in the FD-BPM model). To get the pitchfork bifurcation

bistability, the bias current should be above the bifurcate point. Therefore, we adopt 4.0 kA/cm^2 as the injection current of the SOA regions.

The lasing states can be controlled by an external light injection to mode-1 and mode-2. The MZI-BLD starts lasing at mode-1 (we call it the ON state), if the light signal near the lasing wavelength is injected to mode-1. At the same time, the lasing mode-1 suppresses mode-2 through the cross gain saturations shown as Fig.6.7. Similarly, the light injection to mode-2 at the ON state suppresses mode-1 through cross gain saturation, and stops the laser oscillation. Simultaneously, mode-2 starts lasing instead of mode-1. In this way, an optical flip-flop operation can be realized. The flip-flop operation by the external light injection is shown in Fig.6.8. In the beginning of the calculation, the MZI-BLD is set to the ON state. The bistable switching occurs above 0 dBm light injection to mode-2, i.e. the MZI-BLD is switched from the ON state to the OFF state.

The photon densities of the ON state and the OFF state inside the cavity are shown in Fig.6.9 (a), (b). The bistable switching shown in Fig.6.8 occurs between this two states. The photon distributions between the two Mach-Zehnder arms are almost same, so the carrier

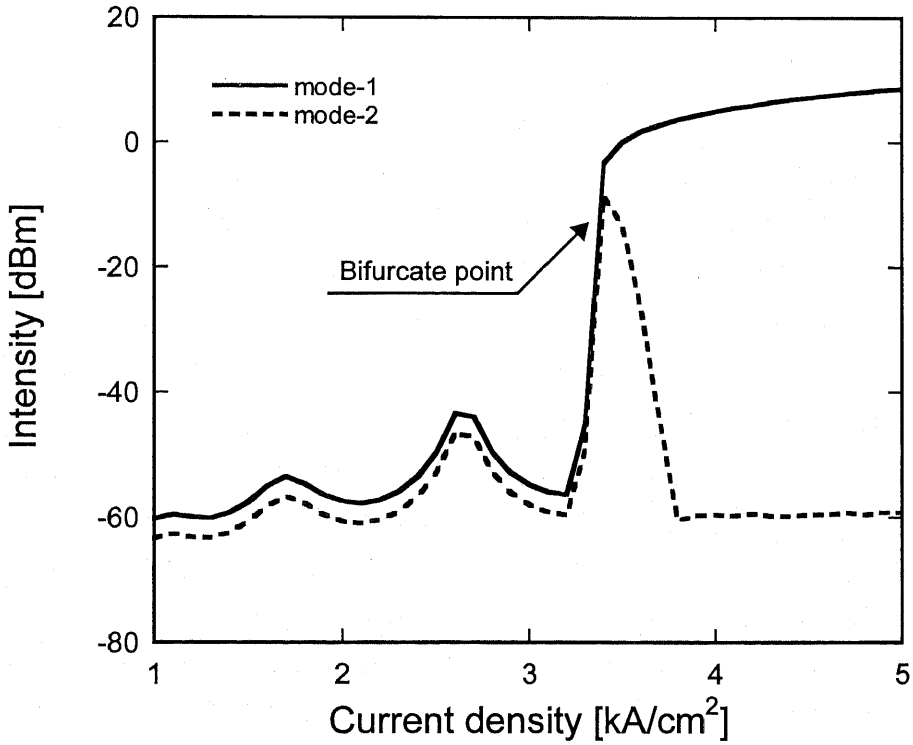

Fig.6.7 Pitchfork bifurcation bistable characteristic of the MZI-BLD. The self-saturation coefficient is 8.0×10^{-17} cm^3. The light injection to mode-1 instead of the spontaneous emission is -55 dBm, which is 5 dB larger than mode-2, -60 dBm. At the bifurcation points (3.4 kA/cm^2), mode-1 starts lasing, and mode-2 is suppressed through the cross gain saturation.

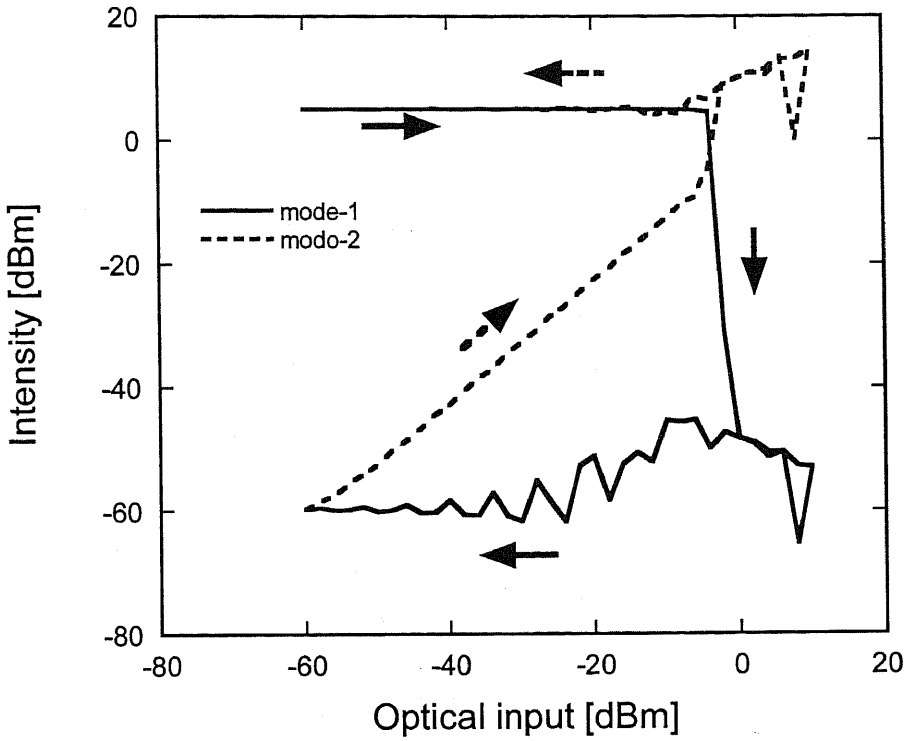

Fig.6.8 Bistable switching characteristics of the MZI-BLD. The current densities of the SOA regions are fixed at 4.0 kA/cm^2. The switching between the two cross-coupled mode occurs by 0 dBm light injection to mode-2.

densities have also no difference between the SOA regions. The carrier distribution of the SOA arms is shown in Fig.6.10. The passive waveguide regions such as the 3-dB MMI couplers and the input and output ports are shown as blank. The two SOA arms have almost same carrier distributions. The distributions of refractive indices are also calculated from the carrier distributions shown in Fig.6.11. The SOA regions have no different distributions of refractive index, because of small difference of carrier densities. Refractive index less than 3.249 is omitted to emphasize the difference inside the SOA regions. The passive waveguides such as the 3-dB MMI couplers and four ports whose indices are 3.27 are shown as black color. From this results, the assumption that there is no phase difference at the Mach-Zehnder arms is confirmed.

In this section, the bistable characteristics of the MZI-BLD are discussed. It is numerically predicted that the MZI-BLD shows pitchfork bifurcation bistability, and all-optical flip-flop devices can be realized. In the next section, we mention the potential of a high-speed operation of the MZI-BLD.

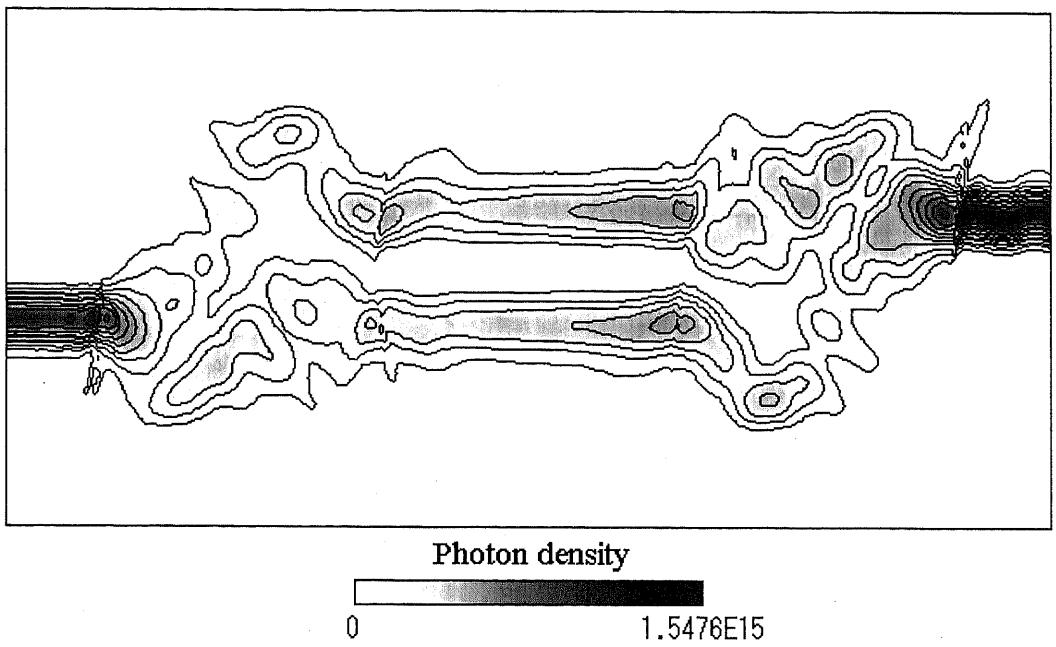

(a) ON state (lasing: mode-1).

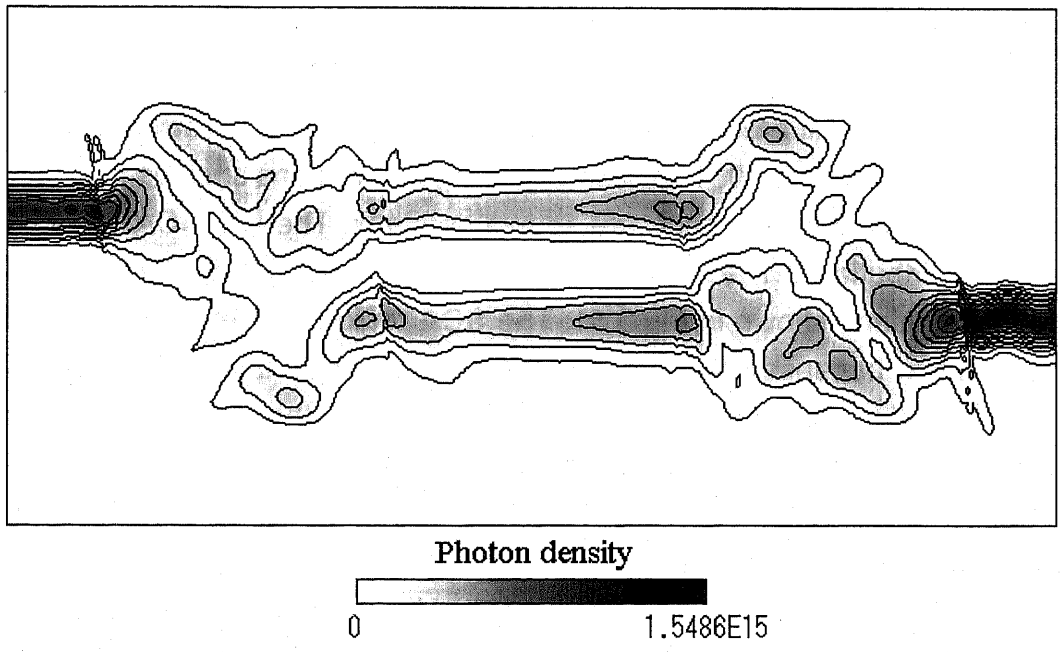

(b) OFF state (lasing: mode-2).

Fig.6.9 Photon density [cm^{-3}] distributions of the MMI-BLD at (a) the ON state and (b) the OFF state. The bistable switching between two states occurs by the external light injection.

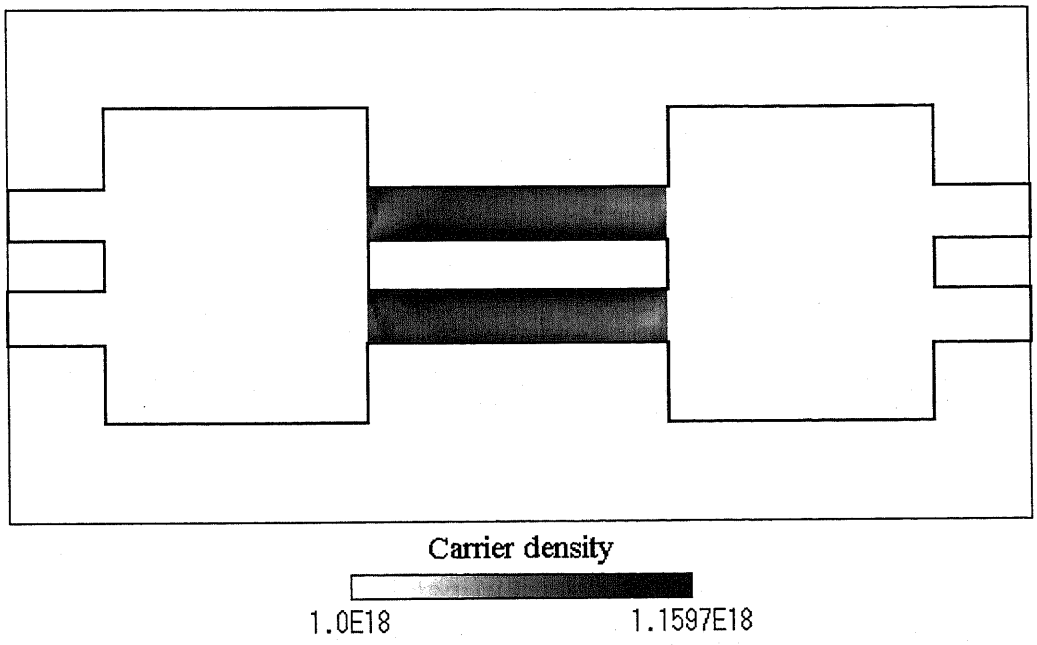

Fig.6.10 Carrier density [cm^{-3}]
distributions of the MZI-BLD lasing at mode-1. The 3-dB MMI coupler and the input and output ports are passive waveguides, so they are shown as blank. There is almost no difference of the carrier densities between the two SOA arms.

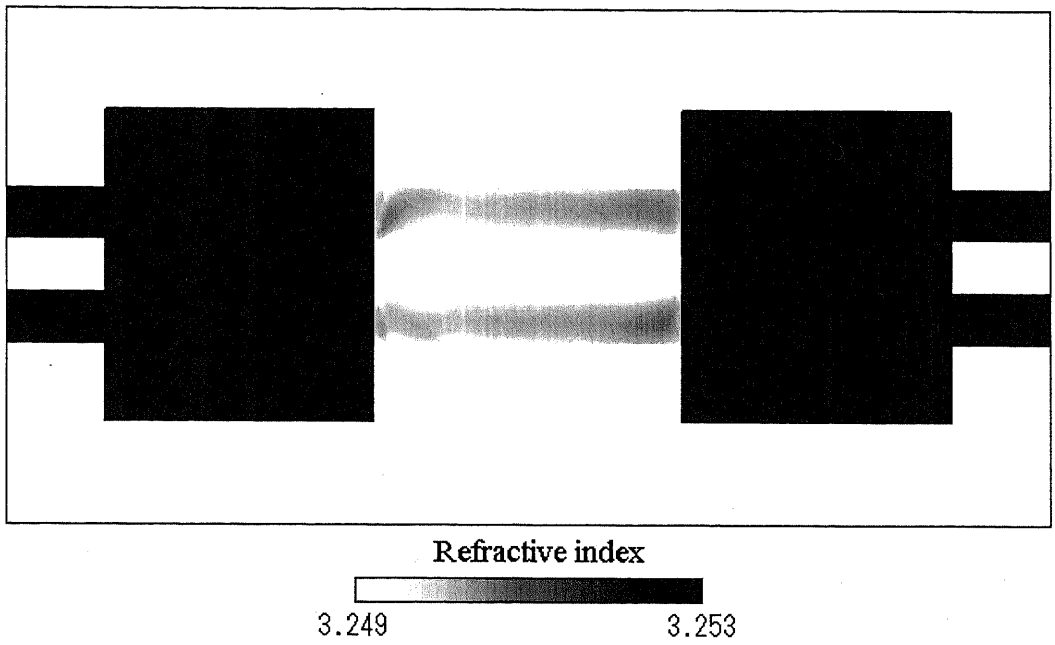

Fig.6.11 Refractive index distributions of the MZI-BLD lasing at mode-1. Refractive index less than 3.249 is omitted as blank to emphasize the difference inside the SOA regions. The 3-dB MMI coupler and the four ports are passive waveguides and have the constant refractive index, 3.27, which are shown as black color. The SOA arms have almost same refractive index distributions.

6.6 Estimation of Maximum Switching Speed

The switching speed between the ON and OFF states is one of the most important factor of all-optical flip-flop devices. In the case of the DC-BLD, we estimated that the maximum switching speed was limited by relaxation oscillation frequency, i.e. around 10 GHz. In the case of the MMI-BLD, the maximum switching speed was estimated to be around 10 GHz - 40 GHz. The suppression of the carrier density change inside the active MMI coupler extended the upper limit of switching speed. In the case of the MZI-BLD, the carrier density never change between the ON state and the OFF state. Therefore, the switching speed of the MZI-BLD is not limited by the relaxation oscillation frequency any more. The maximum limit is decided by the photon lifetime.

We already discussed about the photon lifetime in Section 5.6. We show the brief summary, again. The photon lifetime are expressed as

$$\frac{1}{\tau_{ph}} = \frac{c}{n_r}\left(\alpha + \frac{1}{2L} ln \frac{1}{R^2}\right) \tag{14}$$

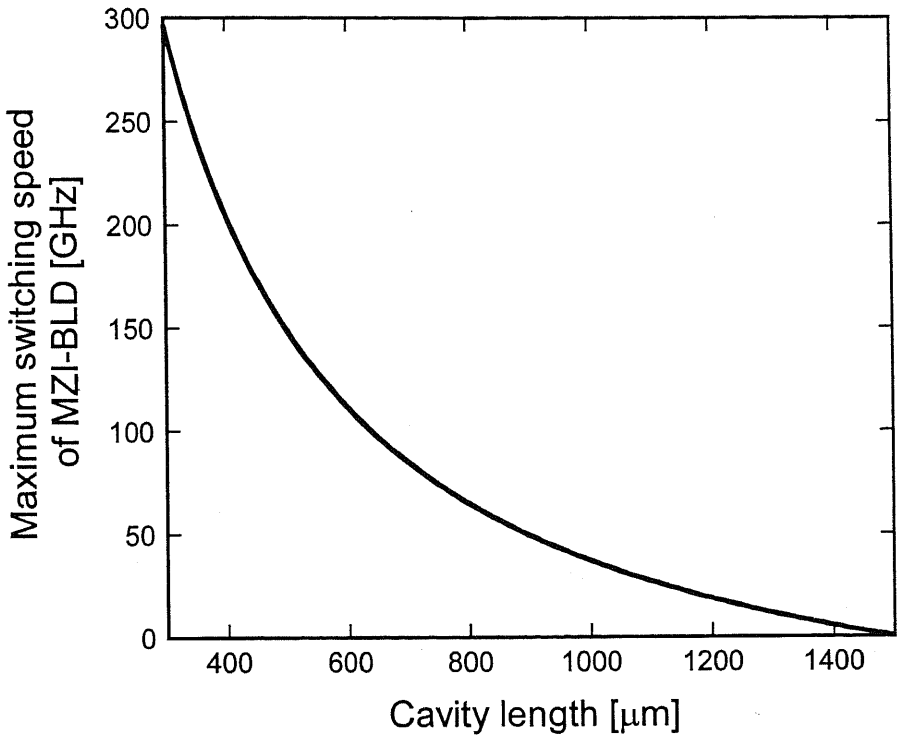

Fig.6.12 The estimated maximum switching speed of the MZI-BLD. The solid line show the limitation by photon lifetime, i.e. $1/\tau_p$ is plotted. If the device size is smaller than 600 μm, the maximum speed is estimated to be more than 100 GHz.

where α internal loss, L is cavity length, R power reflectivity.

The photon lifetime can be calculated using equations (14) and the result is shown in Fig.6.12. We use the almost same parameters in the case of the MMI-BLD, i.e., $c = 3.0 \times 10^{10}$ [cm·s^{-1}], $n_r = 3.25$, and $R = 0.3$. As like the MMI-BLD case, we take -8 [cm^{-1}] as the internal loss α (i.e., small gain) to calculate the photon lifetime from equation (14) by taking account of gain saturation. In this way, we can calculate the photon lifetime during optical switching and estimate the maximum switching speed of the MZI-BLD. The maximum speed ($1/\tau_{ph}$) limited by the photon lifetime with cavity length is plotted in Fig.6.12. The photon lifetime is ultra-fast below 10 psec, if the cavity length is small. From Fig.6.12, $1/\tau_{ph}$ is over 40 GHz if the cavity length is smaller than 1000 μm. Since the MZI cavity length analyzed in this chapter is around 1000 μm, the maximum speed is limited to be around 40 GHz. To obtain faster speed, the cavity length should decrease. If the cavity length is smaller than 600 μm, the maximum switching speed can be obtained to be more than 100 GHz. As shown here, the MMI-BLD has the possibility of high-speed switching more than 40 GHz.

To reduce the cavity length, the high-mesa waveguides should be used for 3-dB MMI coupler. A Ultracompact MMI coupler is proposed using parabolically tapered waveguides, whose length is around 30 μm [33]. In this case, the cavity length of the MZI-BLD can be reduced to be less than 600 μm, and the switching speed more than 100 GHz can be obtained.

6.7 Modal Stability

As mentioned in Section 6.4, any modes expressed by linear combination of mode-1 and mode-2 are able to be the lasing modes of the MZI-BLD. There are no reasons to fix the lasing mode to mode-1 or mod-2. Some fluctuation of 3-dB MMI couplers, the Mach-Zehnder arms, the cleaved facet, etc. lead to the change of the lasing modes. To get the stable switching operation between mode-1 and mode-2, some stabilizer may be needed. In this section, the two suggestions for modal stability are described, i.e. saturable absorber solution, and Bragg grating solution.

A. Saturable absorber

The easy solution to stabilize the lasing mode is to equip saturable absorbers at the end of the cavity as shown in Fig.6.13 (a). As like the MMI-BLD, the strong absorption of the saturable absorber prevent the unfavorable modes from lasing. In this way, the modal stability can be obtained. However, the carrier lifetime of saturable absorber limits the switching speed to around 40 GHz as discussed in Section 5.6.

B. Bragg grating

To avoid the switching speed limitation of the saturable absorbers, another solution is suggested using Bragg grating. It is useful for modal stability to assign mode-1 and mode-2 to different Bragg wavelengths λ_1, λ_2, respectively depicted in Fig.6.13 (b). The two Bragg wavelengths should have the near frequency because the cross-saturation coefficient is significant only around $\lambda_1 = \lambda_2$ and it vanishes otherwise. The phase shifters are also necessary for the tuning Fabry-Perot resonance peak. The two kinds of Bragg grating can be fabricated by a direct electron beam lithography. The leakage of mode-1 to mode2 do not make contribution for mode-2 lasing, because two modes have different Bragg wavelengths. In this case, the switching speed do not decay any more (we need to pay attention to the reflectivities of the Bragg gratings, which affect the photon lifetime of the cavity). The Bragg grating solution also have the advantage of a single-mode operation, which is very important for today's WDM communications.

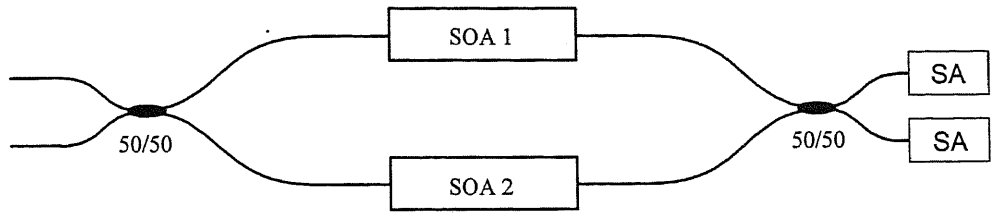

(a) Saturable absorber (SA) solution

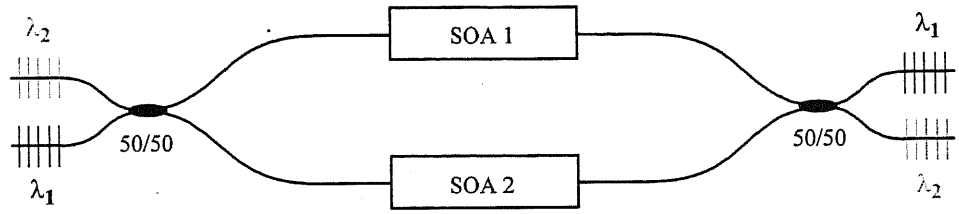

(b) Bragg grating solution

Fig.6.13 Two solutions for modal stability of the MZI-BLD, (a) Saturable absorption solution, (b) Bragg grating solution.

In this section, we discuss the two way for modal stability, the saturable absorber and the Bragg grating solutions. The Bragg grating is preferable because of the advantage of the high speed switching and the single-mode operation. Using this improvement, the stable all-optical flip-flop devices will be achieved.

6.8 Conclusion

We have proposed and investigated a novel BLD with the MZI coupler. The MZI has semiconductor optical amplifiers (SOAs) in its arms. The MZI-BLD has the two orthogonal modes that propagate between the two diagonal cross ports. A bistable switching can be realized between two cross-coupled modes associated with gain saturation. Static characteristics of the MZI-BLD are analyzed using the FD-BPM which includes photon-carrier interaction through the carrier rate equation. This model gives accurate distributions of photon and carrier densities, optical gain and refractive index inside the cavity. From the analyses, it is predicted that the MZI-BLD shows pitchfork bifurcation bistability since the cross-coupled modes have 100 % overlap in the SOA regions. The bistable switching between the two cross-coupled modes by injecting light is predicted. The switching power is around 0 dBm.

We also discuss about the switching speed of the MZI-BLD. There is no change of carrier density between the ON and OFF states, so the switching speed is not limited by the relax-

ation oscillation frequency. In the case of the ridge waveguides, the device length is around 1000 μm, and the switching speed is estimated to be around 40 GHz. If the device length is smaller 600 μm (obtained by the high-mesa waveguides), the switching speed is predicted to be more than 100 GHz.

To get the modal stability, we suggested the two solutions, the saturable absorber solution and the Bragg grating solution. For the high speed switching and the single-mode operation, the Brag grating is preferable to the saturable absorber.

In this way, we have predict the MZI-BLD can be used for an all-optical flip-flop. The MZI-BLD is estimated to show the ultimate high speed switching more than 100 GHz, and this feature will attract the attention of the future high-speed optical communications.

References

[1] S. Nakamura, K. Tajima, and Y. Sugimoto, "High-repetition operation of a symmetric Mach-Zehnder all-optical switch," *Appl. Phys. Lett.,* vol. 66, no. 19, pp. 2457-2459, 1995.

[2] K. Tajima, S. Nakamura, and Y. Sugimoto, "Ultrafast polarization-discriminating Mach-Zehnder all-optical switch," *Appl. Phys. Lett.,* vol. 67, no. 25, pp. 3709-3711, 1995.

[3] K. Tajima, S. Nakamura, Y. Ueno, J. Sasaki, T. Sugimoto, T. Kato, T. Shimoda, M. Itoh, H. Hatakeyama, T. Tamanuki, and T. Sasaki, "Hybrid integrated symmetric Mach-Zehnder all-optical switch with ultrafast, high extinction switching," *Electron. Lett.*, vol. 35, no. 23, pp. 2030-2031, 1999.

[4] J. Leuthold, J. Eckner, Ch. Holtmann, R. Hess, H. Melchior, "All-optical 2 multiplied by 2 switches with 20 dB extinction ratios," *Electron. Lett.*, vol. 32, no. 24, pp. 2235-2236, 1996.

[5] K. Morito, J. Leuthold, H. Melchior, "Dynamic analysis of MZI-SOA all optical switches for balanced switching, " *Proc. ECOC'97*, vol. 2, pp. 81-84, Stevenage, England, 1997.

[6] J. Leuthold, PA. Besse, E. Gamper, M. Dulk, W. Vogt, H. Melchior, "Cascadable MZI all-optical switch with separate ports for data- and control-signals," *Proc. ECOC'98*, vol. 1, pp. 463-464, Madrid, Spain, 1998.

[7] R. Schreieck, M. Kwakernaak, H. Jackel, E. Gamper, E. Gini, W. Vogt, and H. Melchior, "Ultrafast switching dynamics of Mach-Zehnder interferometer switches," *IEEE Photonics. Technol. Lett.*, vol. 13, no. 6, pp. 603-605, 2001.

[8] R. Hess, M. Duelk, W. Vogt, E. Gamper, E. Gini, PA. Besse, H. Melchior, KS. Jepsen, B. Mikkelsen, M. Vaa, HN. Poulsen, AT. Clausen, KE. Stubkjaer, S. Bouchoule, and F. Devaux, "Simultaneous all-optical add and drop multiplexing of 40 Gbit/s OTDM signals using monolithically integrated Mach-Zehnder interferometer," *Electron. Lett.*, vol. 34, no. 6, pp. 579-580, 1998.

[9] S. Nakamura, Y. Ueno, K. Tajima, J. Sasaki, T. Sugimoto, T. Kato, T. Shimoda, M. Itoh, H. Hatakeyama, T. Tamanuki, T. Sasaki, "Demultiplexing of 168-Gb/s data pulses with a hybrid-integrated symmetric Mach-Zehnder all-optical switch," *IEEE Photonics. Technol. Lett.*, vol. 12, no. 4, pp. 425-427, 2000.

[10] S. Nakamura, Y. Ueno, K. Tajima, J. Sasaki, T. Sugimoto, T. Kato, T. Shimoda, M. Itoh, H. Hatakeyama, T. Tamanuki, T. Sasaki, "168 Gbps error-free demultiplexing with hybrid-integrated symmetric Mach-Zehnder all-optical switch," *Proc. OFC'00*, vol. 3, pp. 81-83, Baltimore, USA, 2000.

[11] S. Nakamura, Y. Ueno, J. Sasaki, K. Tajima, "Error-free demultiplexing at 252 Gbit/s and low-power-penalty, jitter-tolerant demutliplexing at 168 Gbit/s with Integrated Symmetric Mach-Zehnder all-optical switch, " *Proc. ECOC'01*, vol. 4, pp. 570-571, Amsterdam, Netherlands, 2001.

[12] K. Tajima, S. Nakamura, Y. Ueno, "Ultrafast all-optical signal processing with Symmetric Mach-Zehnder type all-optical switches," *Optical and Quantum Electron.*, vol. 33, no. 7-10, pp. 875-897, 2001.

[13] St. Fischer, M. Dulk, E. Gamper, W. Vogt, W. Hunziker, E. Gini, H. Melchior, A. Buxens, HN. Poulsen, and AT. Clausen, "All-optical regenerative OTDM add-drop multiplexing at 40 Gb/s using monolithic InP Mach-Zehnder interferometer," *IEEE Photonics. Technol. Lett.*, vol. 12, no. 3, pp. 335-337, 2000.

[14] M. Dulk, St. Fischer, M. Bitter, M. Caraccia, W. Vogt, E. Gini, H. Melchior, W. Hunziker, A. Buxens, HN. Poulsen, and AT. Clausen, "Ultrafast all-optical demultiplexer based

on monolithic Mach-Zehnder interferometer with integrated semiconductor optical amplifiers," *Optical and Quantum Electron.*, vol. 33, no. 7-10, pp. 899-906, 2001.

[15] Y. Ueno, S. Nakamura, K. Tajima, S. Kitamura, "New wavelength converter for picosecond RZ pulses," *Proc. ECOC'98*, vol. 1, pp. 657-658, Madrid, Spain, 1998.

[16] S. Nakamura, Y. Ueno, K. Tajima, "168-GB/s all-optical wavelength conversion with a symmetric-mach-zehnder-type switch," *IEEE Photonics. Technol. Lett.*, vol. 13, no. 10, pp. 1091-1093, 2001.

[17] Y. Ueno, S. Nakamura, J. Sasaki, T. Shimoda, A. Furukawa, T. Tamanuki, T. Sasaki, K. Tajima, "Ultrahigh-speed all-optical data regeneration and wavelength conversion for OTDM systems," *Proc. ECOC'01*, vol. 4, pp. 566-569, Amsterdam, Netherlands, 2001.

[18] M. Dulk, St. Fischer, E. Gamper, W. Vogt, E. Gini, H. Melchior, W. Hunziker, HN. Poulsen, AT. Clausen, A. Buxens, P. Jeppesen, "Efficient regenerative wavelength conversion at 10 Gbit/s over C- and L-band (80 nm span) using a Mach-Zehnder interferometer with monolithically integrated semiconductor optical amplifiers," *Electron. Lett.*, vol. 36, no. 3, pp. 241-243, 2000.

[19] Y. Ueno, S. Nakamura, K. Tajima, "Penalty-free error-free all-optical data pulse regeneration at 84 Gb/s by using a symmetric-Mach-Zehnder-type semiconductor regenerator," *IEEE Photonics. Technol. Lett.*, vol. 13, no. 5, pp. 469-471, 2001.

[20] Y. Ueno, S. Nakamura, K. Tajima, "Penalty-free error-free all-optical data pulse regeneration at 84 Gbps with symmetric-Mach-Zehnder-type regenerator," *Proc. OFC'01*, vol. 54, no. 1, pp. MG5/1-MG5/3, Anaheim, USA, 2001.

[21] S. Fischer, M. Dulk, E. Gamper, W. Vogt, E. Gini, H. Melchior, W. Hunziker, D. Nesset, and AD. Ellis, "3R regenerator for 40 Gbit/s networks, " *Electron. Lett.*, vol. 35, no. 23, pp. 2047-2049, 1999.

[22] H. Kawaguchi, I. H. White, M. J. Offside, and J. E. Carrol, "Ultrafast switching in polarization-bistable laser diodes," *Opt. Lett.*, vol. 17, no. 2, pp. 130-132, 1992.

[23] H. Kawaguchi, T. Irie, and M. Murakimi, "Pitchfork bifurcation polarization bistability in laser diodes with external cavities," *IEEE J. Quantum Electronics*, vol. 31, no. 3, pp. 447-455, 1995.

[24] H. Kawaguchi, I. S. Hidayat, Y. Takahashi, and Y. Yamayoshi, "Pitchfork bifurcation polarisation bistability in vertical-cavity surface-emitting lasers," *Electron. Lett.*, vol. 31, no. 2, pp. 109-111, 1995.

[25] H. Kawaguchi, and I. S. Hidayat, "Gigahertz all-optical flip-flop operation of polarisation-bistable vertical-cavity surface-emitting lasers," *Electron. Lett.*, vol. 31, no. 14, pp. 1150-1151, 1995.

[26] N. Futakuchi, Xueliang Song, D. Miyashita, M. Kato, and Y. Nakano, "Fabrication of InGaAsP/InP Mach-Zehnder interferometer optical amplifier switches by metalorganic vapor phase selective area epitaxy," *Proc. IPRM'01 (Indium Phosphide and Related Materials)*, pp. 583-586, Nara, Japan, 2001.

[27] E. Gini, E. Gamper, W. Vogt, and H. Melchior, "Monolithic integration of passive waveguides with active SOA's and phase shifters for 1550 nm using four step LP-MOVPE growth," *Proc. ECOC'99*, vol. 1, Nice, France, 1999.

[28] C. L. Tang, A. Schremer, and T. Fujita, "Bistability in two-mode semiconductor lasers via gain saturation," *Appl. Phys. Lett.*, vol. 51, no. 18, pp. 1392-1394, 1987.

[29] C. F. Lin, and P. C. Ku, "Analysis of stability in two-mode laser systems," *IEEE J. Quantum Electronics*, vol. 32, pp. 1377-1382, 1996.

[30] H. Kawaguchi, "Bistable laser diodes and their applications: state of the art," *IEEE J. Quantum Electronics*, vol. 3, no. 5, pp. 1254-1270, 1997.
[31] Y. R. Shen, *The Principle of Nonlinear Optics.* New York: Wiley, 1984.
[32] Y. Takahashi, A. Neogi, and H. Kawaguchi, "Polarization-dependence nonlinear gain in semiconductor lasers," *IEEE J. Quantum Electronics*, vol. 34, no. 9, pp. 1660-1682, 1996.
[33] D. S. Levy, R. Scarmozzino, and Y. M. Li, R. M. Osgood, "A new design for ultracompact multimode interference-based 2 × 2 couplers," *IEEE Photonics. Technol. Lett.*, vol. 10, no. 1, pp. 96-98, 1998.

Chapter 7 Conclusion

The purpose of this research is to give the solutions to realize practical all-optical flip-flop devices, that are useful for future optical network functions such as packet buffering, bit-length conversion, and time-division demultiplexing. To overcome the optical turn-off problem of absorptive bistable laser diodes (BLDs), we propose novel BLD structures integrated with nonlinear couplers. By nonlinearities such as cross-phase modulation (XPM), and cross-gain modulation (XGM), all-optical flip-flop operations can be achieved in the BLDs. Three types of waveguide couplers are considered in this paper, i.e., directional couplers (DC), multi-mode interferometer (MMI) couplers, Mach-Zehnder interferometer (MZI) couplers.

In Chapter 2, we developed computer simulators to analyze the bistable characteristics of the proposed BLDs. Two types of numerical models were adopted, i.e., transfer matrix method (TMM) and finite difference beam propagation method (FD-BPM). The TMM model was mainly developed for analyses of the DC-type BLDs, which was extended to treat the behavior of the directional couplers. The spontaneous emission effect was also included in the TMM model. The FD-BPM model was used to analyze the MMI- and MZI-type BLDs. By incorporating the carrier rate equations, the FD-BPM model could treat the photon-carrier interactions. Using this modified FD-BPM, the complex distributions of photon, carrier, refractive index, and gain inside the cavities were analyzed. We also applied this model to analyses of the DC-type BLDs and got the same results as the TMM model.

In Chapter 3, the basic properties of the saturable absorbers were investigated. The optimum condition of the ratio of the saturable absorber length to the device length was obtained experimentally. The maximum limit of the device length to get the hysteresis was also obtained. The optical turn-on characteristics and the effect of the reverse voltage applied to the saturable absorbers were also studied.

In Chapter 4, we proposed the novel all-optical flip-flop device using a directionally coupled bistable laser diode (DC-BLD). From the calculation results by the TMM and FD-BPM models, we predicted that the DC-BLD could be used for an all-optical flip-flop device under the condition of asymmetrical current injection to the directional coupler. We also fabricated

the DC-BLD using the conventional fabrication procedure of LDs. To separate the electrode of the directional coupler, we developed an oblique electron-beam evaporation technique. Using this method, the two adjacent waveguides of the directional coupler were electrically isolated without any lithography. By measuring the fabricated DC-BLD, we made sure that the experimental results and the simulated analyses went together, and we realized an all-optical flip-flop by utilizing the nonlinear effect of the directional coupler. The flip-flop operation was achieved with sufficiently small input optical power level around 0 dBm.

In Chapter 5, we proposed and investigated a novel BLD with active 2×2 MMI coupler cavity designed as input light totally coupled to a cross port. A bistable switching can be realized between the two cross-coupled modes associated with gain saturation. Static characteristics of the MMI-BLD were analyzed using the FD-BPM. The strong coupling condition for two-mode bistability, stability of lasing modes and extinction ratio were investigated. The MMI-BLD with saturable absorbers shown two-mode bistability and could be switched by 0 dBm optical injection, which could be used as all-optical flip-flop or optical memory. We also discussed about the switching speed of the MMI-BLD. The maximum switching speed was estimated to be around 40 GHz limited by the carrier lifetime of the saturable absorber.

In Chapter 6, we proposed a novel BLD with MZI coupler that had semiconductor optical amplifiers (SOAs) in its arms. The MZI-BLD has the two orthogonal modes that propagate between the two diagonal cross ports. A bistable switching can be realized between two cross-coupled modes associated with gain saturation. Static characteristics of the MZI-BLD were analyzed using the FD-BPM model. From the analyses, it was predicted that the MZI-BLD shown pitchfork bifurcation bistability since the cross-coupled modes had 100 % overlap in the SOA regions. The bistable switching between the two cross-coupled modes by injecting light was predicted. The switching power was around 0 dBm. We also discussed about the switching speed of the MZI-BLD. There was no change of carrier density between the ON and OFF states, so the switching speed was not limited by the relaxation oscillation frequency. If the device length was smaller than 600 μm, the switching speed was predicted to be more than 100 GHz.

We believe that the three type of BLDs, DC-BLD, MMI-BLD, MZI-BLD proposed in this paper give the solutions to realize an all-optical flip-flop devices and play an important role in the future optical communications.

Appendix

A. Derivation of the coupled Wave Equations for Directional Coupler

We now derive the differential equations (4.1) that govern the amplitudes $A_1(z)$ and $A_2(z)$ of the coupled modes. When the two waveguides are not interacting they carry optical fields whose complex amplitudes are expressed as

$$\begin{aligned} E_1(y,z) &= A_1 E_1(y) exp(-j\beta_1 z) \\ E_2(y,z) &= A_2 E_2(y) exp(-j\beta_2 z) \end{aligned} \quad (A.1)$$

The amplitudes A_1 and A_2 are then constant. In the presence of coupling, we assume that amplitudes A_1 and A_2 become functions of z but the transverse functions $E_1(y)$ and $E_2(y)$, and the propagation constant β_1 and β_2 are not altered. The amplitudes A_1 and A_2 are assumed to be slowly varying functions of z in comparison with the distance β^{-1} (the inverse of the propagation constant, β_1 or β_2, which is of the order of magnitude of the waveguide of light).

The presence of waveguide 2 is regarded as a perturbation of the medium outside waveguide 1 in the form of a slab of refractive index n_2 - n and width d at a distance $2a$. The excess refractive index (n_2 - n) and the field E_2 correspond to an excess polarization density: $P = (\varepsilon_1 - \varepsilon_2)E_2 = \varepsilon_0(n_2^2 - n^2)E_2$, which creates a source of optical radiation into waveguide 1: $S = -\mu_0 \partial^2 P / \partial t^2$ with complex amplitude

$$\begin{aligned} S_1 &= \mu_0 \omega^2 P_1 = \mu_0 \omega^2 \varepsilon_0 (n_2^2 - n^2) E_2 = (n_2^2 - n^2) k_0^2 E_2 \\ &= (k_2^2 - k^2) E_2 \end{aligned} \quad (A.2)$$

Here ε_1 and ε_2 are the permittivities associated with the refractive indices n_2 and n, and $k_2 = n_2 k_0$. This source is present only in the slab of waveguide 2.

To determine the effect of such a source on the field in waveguide 1, we write the Helmholtz equation in the presence of a source as

$$\nabla^2 E_1 + k_1^2 E_1 = -S_1 = -(k_2^2 - k^2) E_2 . \quad (A.3)$$

We similarly write the Helmholtz equation for the wave in waveguide 2 with a source generated as a result of the field in waveguide 1,

$$\nabla^2 E_2 + k_2^2 E_2 = -S_2 = -(k_1^2 - k^2)E_1, \tag{A.4}$$

where $k_1 = n_1 k_0$. Equations (A.3), (A.4) are two coupled partial differential equations which we solve to determine E_1 and E_2. This type of perturbation analysis is valid only for weakly coupled waveguides.

We now write $E_1(y, z) = A_1(z)e_1(y, z)$ and $E_2(y, z) = A_2(z)e_2(y, z)$, where $e_1(y, z) = E_1(y)\exp(-j\beta_1 z)$ and $e_2(y, z) = E_2(y)\exp(-j\beta_2 z)$ and note that e_1 and e_2 must satisfy the Helmholtz equations,

$$\begin{aligned} \nabla^2 e_1 + k_1^2 e_1 &= 0 \\ \nabla^2 e_2 + k_2^2 e_2 &= 0 \end{aligned} \tag{A.5}$$

where $k_1 = n_1 k_0$ and $k_2 = n_2 k_0$ for points inside the slabs of waveguides 1 and 2, respectively, and $k_1 = k_2 = nk_0$ elsewhere. Substituting $E_1 = A_1 e_1$ into (A.3), we obtain

$$\frac{d^2 A_1}{dz^2} e_1 + 2\frac{dA_1}{dz}\frac{de_1}{dz} = -(k_2^2 - k^2)A_2 e_2. \tag{A.6}$$

Noting that A_1 varies slowly, whereas e_1 varies rapidly with z, we neglect the first term of (A.6) compared to the second. The ratio between these terms is $[(d\psi/dz)e_1]/[2\psi de_1/dz] = [(d\psi/dz)e_1]/[2\psi(-j\beta_1 e_1)] = j(d\psi/\psi)/2\beta_1 dz$ where $\psi = dA_1/dz$. The approximation is valid if $d\psi/\psi << \beta_1 dz$, i.e., if the variation in $A_1(z)$ is slow in comparison with the length β_1^{-1}.

We now substitute for $e_1(y, z) = E_1(y)\exp(-j\beta_1 z)$ and $e_2(y, z) = E_2(y)\exp(-j\beta_2 z)$ into (A.6), after neglecting its first term, to obtain

$$2\frac{dA_1}{dz}(-j\beta_1)E_1(y)e^{-j\beta_1 z} = -(k_2^2 - k^2)A_2 E_2(y)e^{-j\beta_2 z}. \tag{A.7}$$

Multiplying both side of (A.7) by $E_1(y)$, integrating with respect to y, and using the fact that $E^2{}_1(y)$ is normalized so that its integral is unity, we obtain

$$\frac{dA_1}{dz}e^{-j\beta_1 z} = -\kappa_{12}A_2 e^{-j\beta_2 z}, \tag{A.8}$$

where κ_{12} is given by (4.3). A similar equation is obtained by repeating the procedure for waveguide 2. These equations yield the coupled differential equations (4.1).

B. Coupling Length Chart of Directional Coupler

To design a directional coupler, the charts of coupler length are shown. The coupler lengths versus the refractive index of core are calculated from the coupled-mode equation (A.8). The clad index is fixed at 3.24 in these charts. Each chart is calculated with the ridge width 3.0 μm, 2.5 μm, 2.0 μm, 1.5 μm, and 1.0 μm. It needs a caution to use these chart, especially, in the case that the ridge width is 1.0 μm. When the modal overlap between the two waveguides is too large, the couple-mode theory is not correct. So the coupler lengths increase at the small gap region, that is not correct.

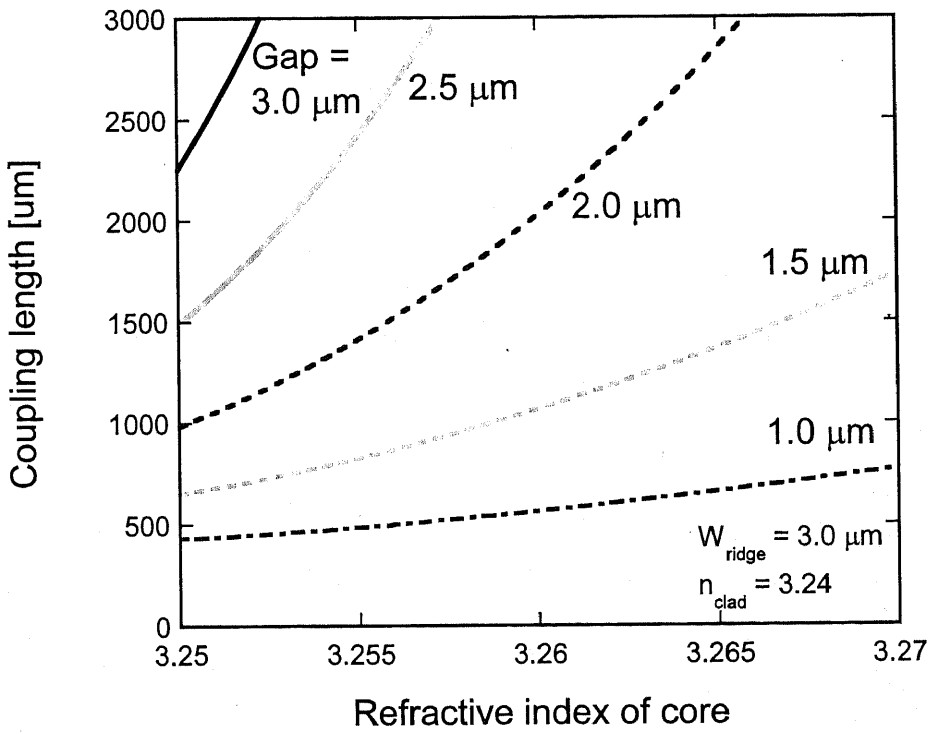

(a) W = 3.0 μm

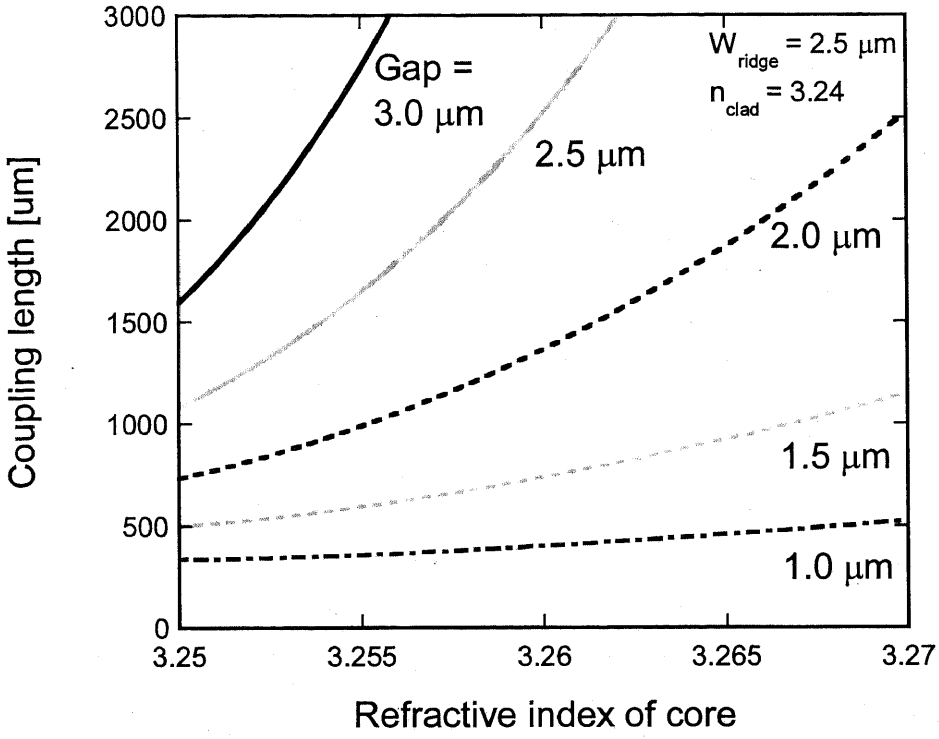

(b) W = 2.5 μm

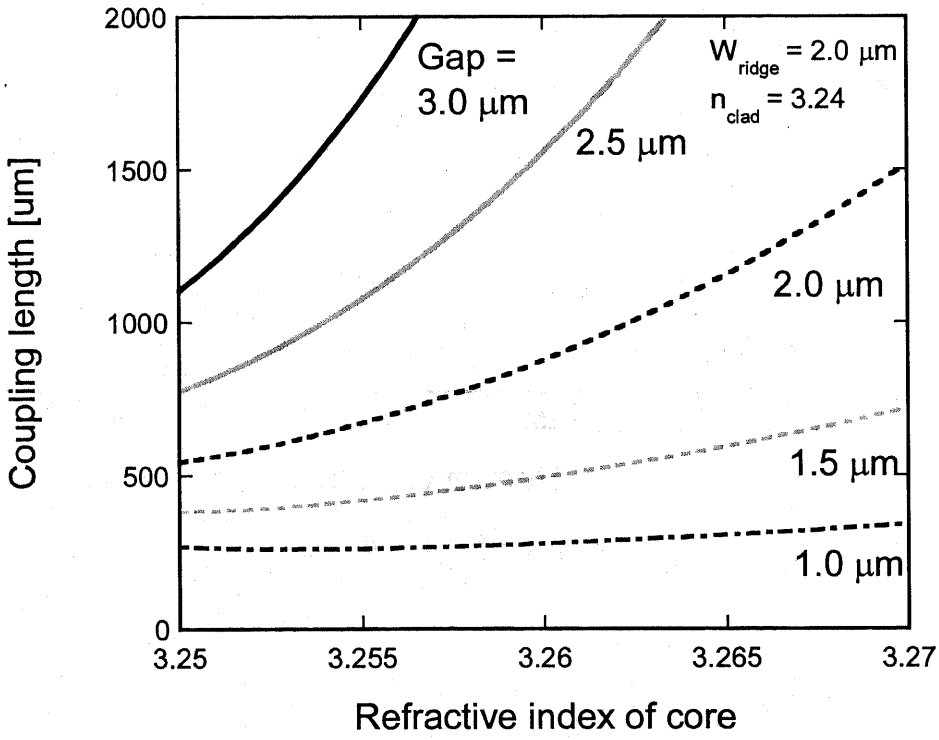

(c) W = 2.0 μm

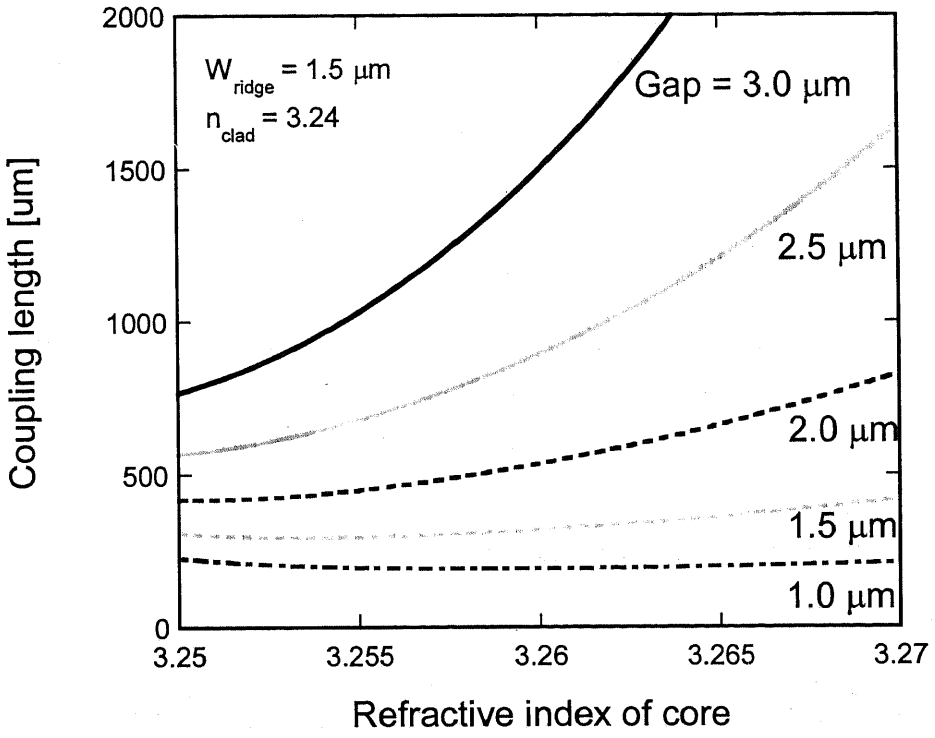

(d) W = 1.5 μm

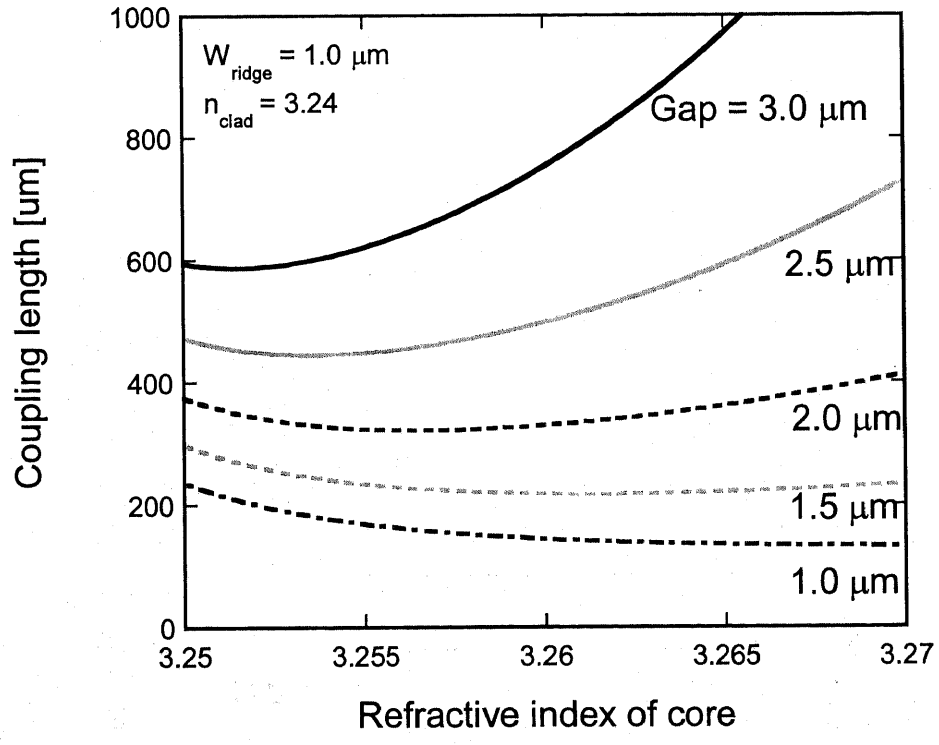

(e) W = 1.0 μm

C. Mode Solver using Matrix Approach

To design various optical waveguide devices, the lateral mode analysis is essential. The calculation methods using matrix approach is most popular to seek effective refractive index. This method can be applied to 1-D multilayer slab waveguides without any approximations.

We consider the slab waveguide shown in the below figure. In this case, the lateral (i.e., x direction) wave vector of i-th layer β_i is expressed as

$$\beta_i = \sqrt{\beta^2 - k_0^2 n_i^2} \tag{C.1}$$

where β is the propagation constant, and k_0 is the wave vector in vacuum.

In general, the electric and magnetic fields of TE modes are expressed by solving Maxwell's equations,

$$\begin{aligned} E_i^y &= A_i exp[\beta_i(x-x_i)] + B_i exp[-\beta_i(x-x_i)] \\ \omega\mu_0 H_i^z &= jA_i\beta_i exp([\beta_i(x-x_i)] - jB_i exp[-\beta_i(x-x_i)]) \end{aligned} \tag{C.2}$$

where the light is propagating to the z-direction.

From equation (C.2), the relation of the electric and magnetic fields as both boundary is expressed as

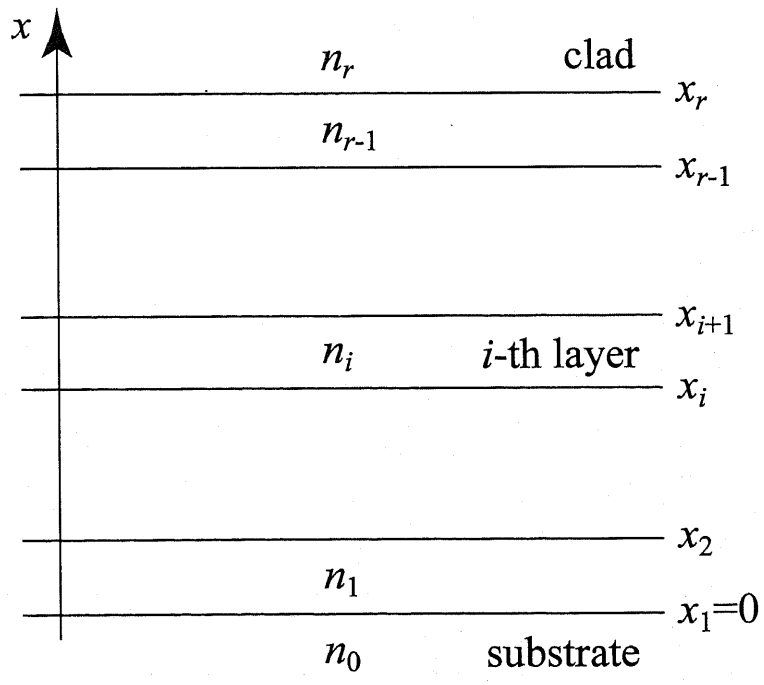

Multi-layer structure of a slab waveguides

$$\begin{bmatrix} E_i^y(x_{i+1}) \\ \omega\mu_0 H_i^z(x_{i+1}) \end{bmatrix} = M_i \begin{bmatrix} E_i^y(x_i) \\ \omega\mu_0 H_i^z(x_i) \end{bmatrix} \tag{C.3}$$

where

$$M_i = \begin{bmatrix} cosh[\beta_i(x_{i+1}-x_i)] & \dfrac{sinh[\beta_i(x_{i+1}-x_i)]}{j\beta_i} \\ j\beta_i sinh[\beta_i(x_{i+1}-x_i)] & cosh[\beta_i(x_{i+1}-x_i)] \end{bmatrix}. \tag{C.4}$$

To taking into account the boundary condition for the TE modes (E^y and H^z are continuous), the electric and magnetic fields of the clad are expressed using that of the substrate,

$$\begin{aligned} \begin{bmatrix} E_{r-1}^y(x_{r-1}) \\ \omega\mu_0 H_{r-1}^z(x_{r-1}) \end{bmatrix} &= M_{r-2} \begin{bmatrix} E_{r-2}^y(x_{r-2}) \\ \omega\mu_0 H_{r-2}^z(x_{r-2}) \end{bmatrix} \\ &= M_{r-2}M_{r-3}\cdots M_1 \begin{bmatrix} E_0^y(x_1) \\ \omega\mu_0 H_0^z(x_1) \end{bmatrix}. \\ &= M \begin{bmatrix} E_0^y(x_1) \\ \omega\mu_0 H_0^z(x_1) \end{bmatrix} \end{aligned} \tag{C.5}$$

If the mode is confined and propagating the waveguide, the electric and magnetic field is converged to be zero at $|x| \to \infty$. Therefore, the electric and magnetic fields of the clad and substrate are expressed as

$$\begin{aligned} E_{r-1}^y(x) &= B_c exp[-\beta_{r-1}(x-x_{r-1})] \\ \omega\mu_0 H_{r-1}^z(x) &= -jB_c\beta_{r-1} exp[-\beta_{r-1}(x-x_{r-1})] \\ E_0^y(x) &= A_s exp[\beta_0(x-x_1)] \\ \omega\mu_0 H_0^z(x) &= jA_s\beta_0 exp[\beta_0(x-x_1)] \end{aligned} \tag{C.6}$$

Substituting equation (C.6) to equation (C.5),

$$\begin{aligned} \begin{bmatrix} B_c \\ -jB_c\beta_{r-1} \end{bmatrix} &= M \begin{bmatrix} A_s \\ iA_s\beta_0 \end{bmatrix} \\ &= \begin{bmatrix} m_{11}A_s + jm_{12}A_s\beta_0 \\ m_{21}A_s + jm_{22}A_s\beta_0 \end{bmatrix} \end{aligned} \tag{C.7}$$

After a bit of algebra, the following equation is obtained,

$$\begin{bmatrix} m_{11}+j\beta_0 m_{12} & -1 \\ m_{21}+j\beta_0 m_{22} & j\beta_{r-1} \end{bmatrix} \begin{bmatrix} A_s \\ B_c \end{bmatrix} = 0. \tag{C.8}$$

For a non-trivial solution, the determinant of the left hand side's matrix of equation (C.8) should be zero. Therefore, we obtain the characteristic equation of TE mode

$$j(m_{11}\beta_{r-1}+m_{22}\beta_0)-m_{12}\beta_0\beta_{r-1}+m_{21} = 0. \tag{C.9}$$

The modal profile and the effective refractive index are obtained by solving equation (C.9). The bisection method or the Newton method are effective to solve equation (C.9).

Similarly, the matrix M_i and the characteristic equation of TM mode are expressed as

$$M_i = \begin{bmatrix} cosh[\beta_i(x_{i+1}-x_i)] & -n_i^2 \dfrac{sinh[\beta_i(x_{i+1}-x_i)]}{j\beta_i} \\ \dfrac{1}{-n_i^2} j\beta_i sinh[\beta_i(x_{i+1}-x_i)] & cosh[\beta_i(x_{i+1}-x_i)] \end{bmatrix} \tag{C.10}$$

$$j\left(m_{11}\frac{\beta_{r-1}}{-n_{r-1}^2} + m_{22}\frac{\beta_0}{-n_0^2} \right) - m_{12}\frac{\beta_0}{-n_0^2}\frac{\beta_{r-1}}{-n_{r-1}^2} + m_{21} = 0. \tag{C.11}$$

List of Publication

Journal

[1] M. Takenaka, and Y. Nakano, "MMI bistable laser diode," *IEEE Photonics. Technol. Lett.*, to be submitted.
[2] M. Takenaka, and Y. Nakano, "Simulation of all-optical functional devices based on semiconductor optical amplifiers," *IEEE J. Select. Topics in Quantum Electronics*, to be submitted, (*invited paper*).
[3] S.-H. Jeong, T. Mizumoto, K. Nakatsuhara, M. Takenaka, Y. Nakano, "Deep-ridge distributed feedback waveguide for polarisation independent all-optical switching," *Electron. Lett.*, vol. 37, no. 8, pp. 498-499, 2001.
[4] S.-H. Jeong, H.-C. Kim, T. Mizumoto, J. Wiedmann, S. Arai, M. Takenaka, Y. Nakano, "Polarization insensitive deep-ridge vertical-groove DFB waveguide for all-optical switching," *Electron. Lett.*, vol. 37, no. 23, pp. 1387-1389, 2001.
[5] S.-H. Jeong, H.-C. Kim, T. Mizumoto, J. Wiedmann, S. Arai, M. Takenaka, and Y. Nakano, "Polarization independent all-optical switching in a nonlinear GaInAsP/InP with vertically etched Bragg reflector," *IEEE J. Quantum Electronics*, to be published.

International Conferences

[6] M. Takenaka, and Y. Nakano, "Self-align electrode separation of directionally coupled semiconductor optical amplifier," *Proc. SPIE*, vol. 4532, pp. 361-368, Denver, August, 2001.
[7] M. Takenaka, and Y. Nakano, "Numerical analysis of directionally coupled bistable laser diode by finite difference beam propagation method for all-optical flip-flop application," *Optical Internet and Photonic in Switching (COIN+PS2002)*, pp. 78-80, Cheju Island, July, 2002.
[8] M. Takenaka, and Y. Nakano, "Realization of all-optical flip-flop using bistable laser diode with nonlinear directional coupler," *18th IEEE International Semiconductor Laser Conference (ISLC '02)*, pp. 121-122, Garmisch-Parternkirchen, September, 2002.
[9] M. Takenaka, and Y. Nakano, "Proposal of an all-Optical flip-flop using a cross-coupled MMI bistable laser diode", *11th European Conference on Integrated Optics (ECIO '03)*, Prague, April, 2003.
[10] M. Saitoh, M. Takenaka, B. Ma, and Y. Nakano, "Demonstration of all-optical wavelength converter based on Fabry-Perot semiconductor optical amplifier," *International conference on solid state devices and materials (SSDM 2000)*, Sendai, August, 2000.

[11] S.-H. Jeong, T. Mizumoto, K. Nakatsuhara, M. Takenaka, and Y. Nakano, "Nonlinear GaInAsP DFB waveguide for polarisation independent all-optical switching," *Optoelectronic Communication Conference (OECC 2001)*, pp. 253-255, Sydney, July, 2001.
[12] S.-H. Jeong, T. Mizumoto, K. Nakatsuhara, M. Takenaka, and Y. Nakano, "Nonlinear DFB waveguide for polarisation independent all-optical switching," *Micro-Optics Conference (MOC 2001)*, pp. 174-177, Osaka, October, 2001.
[13] S.-H. Jeong, H.-C. Kim, T. Mizumoto, J. Wiedmann, S. Arai, M. Takenaka, and Y. Nakano, "Demonstration of polarization insensitive all-optical switching in a highmesa distributed feedback waveguide," *Contemporary Photonic Technologies* (CPT 2002), Tokyo, January, 2002.
[14] S.-H. Jeong, T. Mizumoto, H.-C. Kim, J. Wiedmann, S. Arai, M. Takenaka, and Y. Nakano, "Polarization independent all-optical switching employing nonlinear vertical-groove DFB waveguide," *Optical fiber conference (OFC 2002)*, Anaheim, March, 2002.
[15] S.-H. Jeong, T. Mizumoto, H.-C. Kim, J. Wiedmann, S. Arai, M. Takenaka, and Y. Nakano, "All-optical polarization independent switching in a nonlinear DFB waveguide with vertically etched grating," *Conference on Lasers and Electro-Optics (CLEO/QELS 2002)*, Long Beach, May, 2002.
[16] S.-H. Jeong, T. Mizumoto, M. Takenaka, and Y. Nakano, "All-optical wavelength conversion in a GaInAsP/InP nonlinear DFB-gate," *Optoelectronic Communication Conference (OECC 2002)*, Yokohama, July, 2002.

Technical Meetings

[17] M. Takenaka, Y. Nakano, "Realization of a semiconductor all-optical flip-flop by a directionally coupled bistable laser diode," *Technical report of IEICE 4th PNI meeting,* Osaka, November, 2002
[18] S.-H. Jeong, H.-C. Kim, T. Mizumoto, J. Wiedmann, S. Arai, M. Takenaka, and Y. Nakano, "Polarization insensitive all-optical switch with DFB waveguide," *Technical report of IEICE,* Okinawa, December, 2001.
[19] S.-H. Jeong, T. Mizumoto, K. Nakatsuhara, M. Takenaka, and Y. Nakano, "Nonlinear GaInAsP DFB waveguide for polarization independent all-optical switching," *Technical report of IEICE*, Yonezawa, July, 2001.

Domestic Conferences

[20] M. Takenaka, and Y. Nakano, "Self-align electrode separation of directionally coupled semiconductor optical amplifier," *62the autumn Meeting of the Japan Society Applied Physics*, 13p-Y-12, Nagoya, September, 2001 [In Japanese].
[21] M. Takenaka, and Y. Nakano, "Proposal of all-optical flip-flop using directionally coupled bistable laser diode," *49the spring Meeting on Japan Society Applied Physics*, 29a-ZS-11, Tokyo, March, 2002 [In Japanese].
[22] M. Takenaka, and Y. Nakano, "Realization of a semiconductor all-optical flip-flop having a directionally coupled bistable laser structure," *63the autumn Meeting of the Japan Society Applied Physics*, Nihgata, September, 2002 [In Japanese].
[23] S.-H. Jeong, T. Mizumoto, K. Nakatsuhara, M. Takenaka, and Y. Nakano, "Enlargement of grating coupling coefficient in a polarization independent deep-ridge

DFB waveguide," *62the autumn Meeting of the Japan Society Applied Physics*, 13p-Y-6, Nagoya, September, 2001.

[24] S.-H. Jeong, T. Mizumoto, K. Nakatsuhara, M. Takenaka, and Y. Nakano, "Study of all-optical switching device for polarization independence," *Spring Meeting of IEICE*, C-3-14, pp. 179, Kusatsu, March, 2001.

[25] S.-H. Jeong, T. Mizumoto, K. Nakatsuhara, M. Takenaka, and Y. Nakano, "Highmesa DFB waveguide for polarization independent all-optical switching," *Autumn Meeting of IEICE*, C-4-5, Tokyo, September, 2001.

Acknowledgment

This work could not be accomplished without the fruitful contribution of many people.

First of all, I would like to express my best gratitude to my dissertation supervisor Prof. Y. Nakano for his guidance and constant encouragement during the course of this work. I greatly appreciate valuable and insightful comments from Prof. K. Kikuchi, Prof. Y. Nishimura, Prof. T. Takahashi, Prof. M. Tsuchiya, and Prof. S. Yamashita.

I would like to thank all the members of Nakano laboratory for their discussions and collaborations. Especially, I owe thanks to Mr. Xueliang Song and Mr. Yit Foo Cheong for their contributions to the fabrication and measurement in this work.

I would like to express my thanks to the fellowship of the Japan Society for the Promotion of Science for Japanese Junior Scientists. It supported me financially during three years' research life.

Last but not least, I would like to express my deep gratitude towards my parents and brother for their constant encouragement.

Mitsuru Takenaka

Mitsuru Takenaka

December 16 2002